UNIVERSITY OF
BIRMINGHAM

A MULTI-STAGE MEMBRANE SYSTEM FOR COOLING AND WATER RECOVERY IN HORTICULTURAL GREENHOUSES

By

Paris Pasqualin

A thesis submitted to
The University of Birmingham
for the degree of

Doctor of Philosophy

School of Engineering
College of Engineering and Physical Science
The University of Birmingham
July 2023

Abstract

The increasing issues of water scarcity and food insecurity highlight the necessity to utilise water and produce food more efficiently. Agriculture, which accounts for 70% of global water usage, is related to both these issues. Controlled-environmental greenhouses have been investigated as a potential solution, with liquid desiccant air-conditioning showing promising results. However, controlled-environmental greenhouses face challenges in hot climates. This is because conventional liquid desiccant air-conditioning utilises thermal energy-intensive liquid desiccant regenerators, highlighting the need for an alternative regenerator with lower energy requirements. Thus, a comparison of six membrane-based desalination technologies was conducted, and multi-stage nanofiltration was identified as the most promising for use as a liquid desiccant regenerator (Chapters 1 and 2). After conducting a steady-state investigation on multi-stage nanofiltration regeneration combined with liquid desiccant air-conditioning for greenhouse applications, it was found that the proposed system could achieve better indoor conditions for crops compared to thermal regenerators and conventional cooling technologies (Chapter 3). Consequently, the practical feasibility of nanofiltration regeneration was demonstrated through dead-end filtration experiments using a 1-stage regenerator (Chapter 4) and cross-flow filtration experiments using a 2-stage regenerator (Chapter 5). Additionally, a 2-stage regenerator model was developed and verified with errors below 11% compared to the experimental data (Chapter 5). The verified model was then applied to a dynamic simulation of a greenhouse using the proposed system (Chapter 6). The proposed system enables year-round cultivation and saves 50% of water in desert and semi-arid climates where crop production is challenging, and 30% in tropical climates where agriculture typically overuses water. By reducing water demand and enabling year-round cultivation, the proposed system addresses the issues of water scarcity and food insecurity in hot climates.

Dedicated to Sakura

my beloved wife

and lifelong companion

Acknowledgements

First and foremost, I want to express my gratitude to my supervisor, Prof. Philip Davies, for his exceptional guidance and support, and for his teachings in how to write high-quality academic papers. By giving me this PhD opportunity, you also led me to my amazing wife, whom I want to thank next.

My dearest Sakura, thank you for always believing in and supporting me. You are the light of my life, and your encouragement gave me strength to overcome the inevitable 'lows' I encountered in my PhD journey.

Mum, dad, and Ektor, thank you as well for your support and for visiting me during these years.

I want to also thank Dr. Ryan Lefers and Prof. Mark Tester from Red Sea Farms© for offering me the three month collaboration where I had the opportunity to work on their greenhouse in Saudi Arabia. It was an experience that I never imagined I would have, and the knowledge I gained about greenhouses significantly improved the quality of my thesis.

Furthermore, I want to thank the civil lab technicians and Adam for their assistance in building my rig and sharing their practical skills with me. Finally, I want to acknowledge the School of Engineering for funding my project.

List of papers and abstracts

This thesis is composed of manuscripts that were accepted for publication, that are under review, or that will be submitted to a scientific journal. Abstracts and posters presented during conferences have also been integrated into this thesis. Paris Pasqualin is the first author and main contributor of all the research presented in this thesis.

Publications:

• P. Pasqualin, R. Lefers, S. Mahmoud, and P.A. Davies, Comparative review of membrane-based desalination technologies for energy-efficient regeneration in liquid desiccant air conditioning of greenhouses. Renewable and Sustainable Energy Reviews, 2022. 154: p. 111815.

• P. Pasqualin and P.A. Davies, Concept design of a greenhouse cooling system using multi-stage nanofiltration for liquid desiccant regeneration. Applied Thermal Engineering, 2022. 216: p. 119057.

• P. Pasqualin and P.A. Davies, Experimental and theoretical investigation of nanofiltration membranes for liquid desiccant regeneration in air conditioning applications. Applied Thermal Engineering, 2022. 221: p.119644.

• P. Pasqualin and P.A. Davies, Multi-stage nanofiltration for brine concentration: experimental and modelling study. Desalination, 2023. 566: p.116928

Under Review (original draft submitted to Energy journal on the 5th of September 2023):

• P. Pasqualin and P.A. Davies, Dynamic simulation of a novel liquid desiccant air-conditioning system for greenhouse cooling and water recovery.

Conference Presentations:

• P. Pasqualin and P.A. Davies, Experimental and numerical investigations of LiCl regeneration for greenhouse air conditioning applications. Sixth International Conference on Polygeneration – ICP 2021, 04/10/21.

• P. Pasqualin, R. Lefers, M. Tester, and P.A. Davies, Water conservation in greenhouses using membrane-based desalination technologies for regeneration of liquid desiccants. Desalination for the Environment: Clean Water and Energy, Las Palmas, 22/06/22.

• P. Pasqualin and P.A. Davies, Addressing water and food scarcity through a novel system for greenhouses, experimental validation and model predictions. STEM for BRITAIN 2023 engineering competition, House of Commons, London, 06/03/23.

• P. Pasqualin and P. A. Davies, Multi-stage NF for use in greenhouse cooling and irrigation: experimental results and prospects, Desalination for the Environment: Clean Water and Energy, Limassol, 24/05/2023.

Contents listing

Table of Content

List of Figures

List of Tables

Abbreviations

AC	Conventional air-conditioning
AEMs	Anion-exchange membranes
AGMD	Air gap membrane distillation
ANNs	Artificial neural networks
CEMs	Cation-exchange membranes
COMRO	Cascading osmotically mediated reverse osmosis
COP	Coefficient of performance
CP	Concentration polarisation
DCMD	Direct contact membrane distillation
DS	Draw solution
ECP	External concentration polarisation
ED	Electrodialysis
EDR	Electrodialysis reversal
ERD	Energy recovery device
EvapC	Evaporative cooling
FO	Forward osmosis
HMX	Heat and mass exchanger (dehumidifier)
HX	Heat exchanger
ICP	Internal concentration polarisation
IEMs	Ion-exchange membranes
ILs	Ionic liquids
LCST	Lower critical solution temperature
LD	Liquid desiccant

LDAC	Liquid desiccant air-conditioning
MD	Membrane distillation
MED	Multi-effect distillation
MLDAD	Membrane liquid desiccant air dehumidification
MSF	Multi-stage flash distillation
MVC	Mechanical vapour compressor
NF	Nanofiltration
NF-LDAC	NF combined with LDAC
OARO	Osmotically assisted reverse osmosis
PAFO	Pressure-assisted forward osmosis
PV	photovoltaic
RO	Reverse osmosis
SAR	Sodium adsorption ratio
SGMD	Sweep gas membrane distillation
TR	Thermoresponsive
UCST	Upper critical solution temperature
VCR	Vapour compression refrigeration
VMD	Vacuum membrane distillation
ZLD	Zero liquid discharge

Parameters

A	Area [m^2]
C	Concentration [g/L] (solute per volume of solution)
COP	Coefficient of performance
CP	Concentration polarisation factor
D_w	Diffusion coefficient [m^2/s]
EC	Electric conductivity [mS/cm]
ERH	Equilibrium relative humidity [%]
ET	Crop transpiration rate [kg/s]
ET_c	Crop transpiration [kg/s]
F	Flow parameter
h	Heat loss coefficient [$kW/(m^2\ K)$]
H	Feed spacer [m]
h	Enthalpy [kJ/kg]
h_p	Heat capacity [kJ/(kg K)]
i	van 't Hoff dissociation parameter
I	Current [A]
Irr	Solar radiation [kW/m^2]
J_s	Solute flux [$g/(m^2\ h)$]
J_v	Permeate flux [$L/(m^2\ h)$]
k_c	Crop coefficient
k_s	mass transfer coefficient [m/s]
LAI	Leaf area index [$m^2/\ m^2$]

L_p	Permeability [L/(m^2 h bar)]
m	Tank weight [kg]
M	Molarity [mol/L]
$\dot{m}$	Mass flow [kg/s] (or [kg/min] in Chapter 5)
MM	Relative molecular mass [g/mol]
$MWCO$	Molecular Weight Cut-off [Da]
$Power$	Power [kW]
P_s	Solute permeability [L/(m^2 h bar)]
P_{vap}	Vapour pressure [kPa]
q	Permeate flux coefficient [wt.%$^{-1}$]
$\dot{Q}$	Exchanged heat [kW]
r	Recovery
R	Rejection
r_a	Aerodynamic external resistance [s/m]
r_c	Internal resistance of the canopy [s/m]
Re	Reynold number
Ref_{idx}	Refractive index
RH	Relative humidity [%]
R_n	Radiation above the canopy [kJ/(m^2 h)]
r_{os}	Observed rejection [%]
rpm	Stirring rate [s^{-1}]
r_R	Radiative resistance [s/m]
r_s	True rejection
R_{sc}	Radius of stirred cell

r_{std}	Specified rejection [%]
$\bar{R}_u$	Universal gas constant [J/(K mol)]
Sc	Schmidt number
SEC	Specific energy consumption [kWh/m^3]
Sh	Sherwood number
Speed	Speed [m/s]
T	Temperature [°C] or [K]
t	Simulation time [h]
TDS	Total dissolved solids [g/L]
U	Thermal transmittance [W/(m²K)]
V	Volume [L]
$\dot{V}$	Flow [L/h]
Volt	Voltage [V]
VPD	Vapour pressure deficit [kPa]
V_w	Inverse of the pure water molarity [L/mol]
wt	Weight concentration (percentage of solute per solution) [wt.%]
x	Mass fraction
T	Temperature [°C] or [K]
t	Simulation time [h]
U	Thermal transmittance [W/(m²K)]

Greek letters

α	Absorbance of greenhouse floor with crop
β	Fraction of greenhouse plan area covered by PV collectors
Δ	Slope of the saturation vapour pressure curve [kPa/K]
ΔC	Concentration difference between feed and permeate [g/L]
Δg	Weight difference [g]
ΔP	Applied pressure [bar]
Δt	Time interval
ΔV	Cumulative volume difference [L]
$\Delta \Pi$	Osmotic pressure difference [bar]
ε_{evap}	Effectiveness of the evaporative cooling pad
ζ	Dimensionless coefficient (used in Eq 3-21)
η	Efficiency
λ	Latent heat of evaporation [kJ/kg]
μ	Viscosity of solution [Pa s]
Π	Osmotic pressure [bar]
ρ	Density [kg/m^3]
σ	Reflection factor
$\sigma_{s\text{-}B}$	Constant of Stefan–Boltzmann [W/(m^2 K^4)]
τ	Roof transmittance
ω	Absolute humidity [g_v/kg_a]

Subscripts

0	Starting value
Air	Air
amb	Ambient
b	Brine
c	Crop
CaCl2	Calcium chloride
conc	Concentrated LD
cool	Cooled air leaving the dehumidifier
d	Dried air
e	Effective
el	Electric
end	Exit from the multi-stage regenerator
ERD	Energy recovery device
f	Feed
feed tank	Feed tank
gh	Greenhouse
Hoff	van ‘t Hoff
hyd	Hydraulic
i (from 1 to 4)	i-th stage (from first to forth)
in	Inlet
int	Intermediate
K	Kelvin degree

LD	Liquid desiccant
LiBr	Lithium Bromide
LiCl	Lithium Chloride
m	Membrane
max	Maximum allowable
MgCl2	Magnesium Chloride
m-p	Motor-Pump
n	Net
NF	Nanofiltration
out	Outlet
p	Permeate
pump	Pump
pv	Photovoltaic
reg	Multi-stage regenerator
RO	Reverse osmosis
s	Surface
second feed tank	Second feed tank
system	System
tot	Total
v	Moisture
w	Pure water
ws	Water source

Superscripts

amb	Ambient
deh	Dehumidifier
in	Inlet of the dehumidifier
out	Outlet from the dehumidifier

Energy units

kWh_{el}	Electric energy [kWh]
kWh_{th}	Thermal energy [kWh]

Power units

kW_{el}	Electric power [kW]
kW_{th}	Thermal power [kW]

Chapter 1: General Introduction

Title of published paper: Comparative review of membrane-based desalination technologies for energy-efficient regeneration in liquid desiccant air conditioning of greenhouses.

Paper information: Renewable and Sustainable Energy Reviews, 2022. 154: p. 111815.

Author contributions and affiliations:

- P. Pasqualin[a]: original draft, writing, review, editing, data curation, investigation and visualisation

- R. Lefers[b]: review

- S. Mahmoud[a]: review

- P.A. Davies[a]: conceptualisation, review and editing

[a] School of Engineering, University of Birmingham, Edgbaston, Birmingham B15 2TT, UK.

[b] King Abdullah University of Science and Technology (KAUST), Water Desalination & Reuse Center (WDRC), Biological and Environmental Science and Engineering Division (BESE), Thuwal 1223955-6900, Saudi Arabia.

1.1 Background on liquid desiccant air-conditioning

World population, estimated at 7.7 billion in 2019, is expected to grow to 8.5 billion by 2030 and 9.7 billion by 2050 [1]. Consequently, food production will have to address a greatly increasing demand. A strategy to meet this demand is to cultivate crops in controlled-environment greenhouses which boost productivity and extend cultivation period [2, 3]. Crop cultivation in large-scale greenhouses have been successfully implemented in Mediterranean climates where conventional evaporative cooling is usually adequate. However, hot climates of the tropics and subtropics face design challenges due to high external temperatures and humidities that occur during summer [4]. These extreme conditions limit the cooling and dehumidification effectiveness of evaporative coolers in such climates. Moreover, greenhouses cooled with evaporative coolers consume large quantities of freshwater [5, 6], between 50 and 80% of their total water consumption [7, 8]. The high water requirement also limits the utilisation of evaporative cooling in arid climates where water is typically scarce.

Liquid desiccant air-conditioning (LDAC) was proposed to mitigate the high-water requirement and low-effectiveness of evaporative cooling in hot climates [9]. Advantages of LDAC include high effectiveness when processing large air quantities, prospects to store and utilise the liquid desiccant (LD) on demand, and indoor humidity and temperature control. LDAC depends on constant availability of a low vapour pressure LD, which must be continually reconcentrated or cooled at a substantial energy cost. Compared to evaporative cooling, LDAC achieves lower indoor temperatures in humid climates [10-13] and deals more efficiently with latent loads [14-16].

The LDAC cycle is composed of three components (Figure 1-1A): a dehumidifier (a heat and mass exchanger, HMX), a LD regenerator, and a heat-exchanger (HX). Thus, three processes take place, i.e., dilution (air dehumidification), regeneration, and cooling of the LD

(Figure 1-1B). Air dehumidification represents the moisture transfer from the hot and humid air to the LD, driven by the liquid/air vapour pressure difference [17, 18]. As the LD absorbs vapour, it becomes diluted and must be reconcentrated to its initial state [5]. The LD reconcentration takes place in a process called regeneration. The regeneration process is the opposite compared to vapour absorption during which water is removed from the LD. The LD temperature may increase during the regeneration process, especially when the LD is reconcentrated through thermally driven technologies, meaning a cooling process is typically necessary to restore the LD temperature.

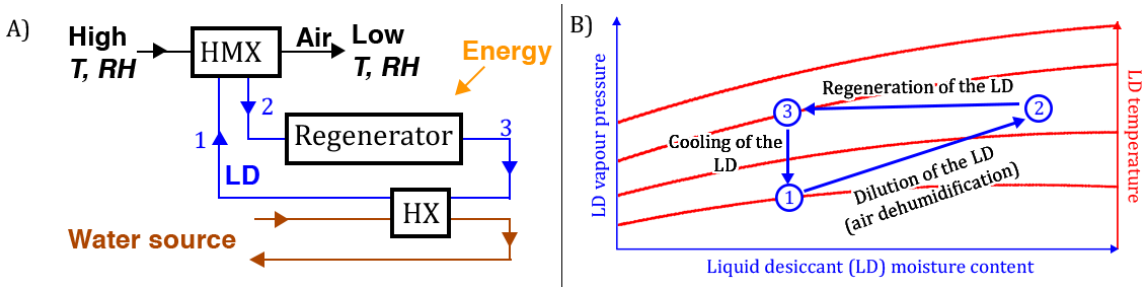

Figure 1-1. A) Schematic of a simplified LDAC system. The regenerator requires energy (such us thermal, pressure, etc). B) Graphical representation of the LD properties in a simplified LDAC system. Isothermal lines are represented in blue. Numbers in A) correspond to those in B).

LDAC employs a LD that is in direct contact with the air that needs to be cooled [19]. LDAC may also employ evaporative cooling which can either be indirect or direct type. On the one hand, indirect evaporative coolers remove sensible heat from the air stream without increasing the absolute humidity of the air [20]. On the other hand, direct evaporative coolers cool the air by spraying water and increase the absolute humidity [20]. Typical efficiency for the indirect type ranges between 60–70% [20] while the efficiency of direct cooling depends on the wet-bulb temperature, with efficiencies reaching 85% [21]. Direct coolers are preferred in hot and dry climates, while indirect coolers in hot and humid climates [20]. Indirect

evaporative cooling reaches lower temperatures compared to direct evaporative cooling. Ideally, the lowest achievable temperature for both types is reached when the relative humidity (*RH*) becomes 100% (i.e., with an efficiency of 100%).

To further decrease the temperature, air must be dehumidified before being directed to an evaporative cooler. Considering air at 25 °C and *RH* of 80%, which are average desired indoor conditions for greenhouses [22, 23], the lowest achievable temperature using direct, indirect, and dehumidification combined with direct evaporative cooling are 22.7, 22.6, and 19.7 °C, respectively (Figure 1-2 is based on the previously mentioned efficiencies of the coolers). These values respectively change to 20.2, 19.6, and 16.8 °C when starting from 25 °C and *RH* of 60% (Figure 1-3 is also based on the previously mentioned efficiencies). Figures 1-2 and 1-3 show that direct and indirect evaporative coolers achieve similar temperatures due to having different efficiencies. The addition of dehumidification always reaches lower temperatures compared to only direct or indirect evaporative cooling.

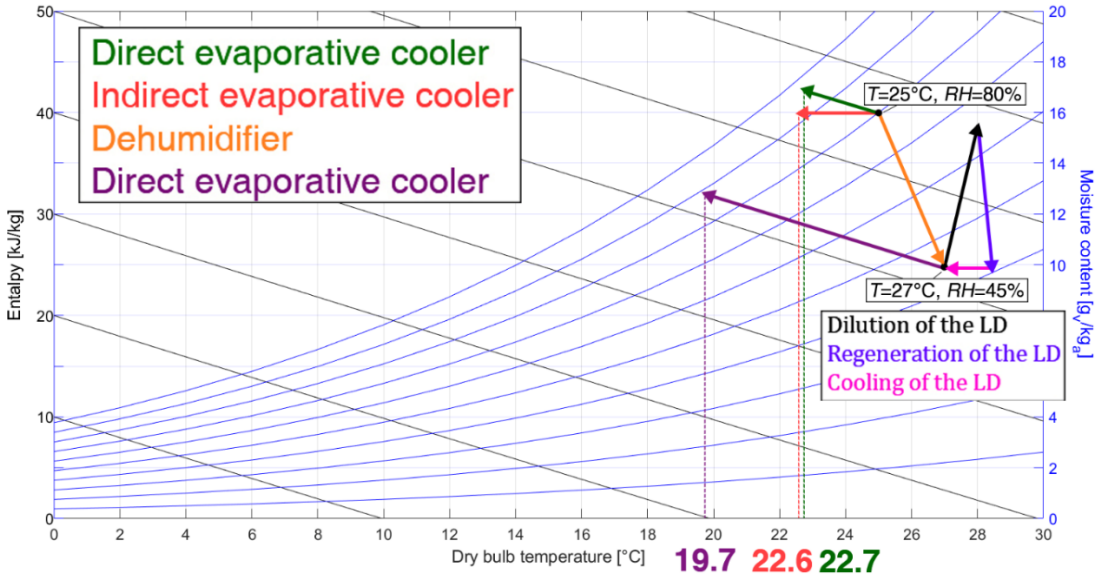

Figure 1-2. Psychrometric chart showing examples of three cooling methods, starting from temperature (T) of 25 °C and relative humidity (RH) of 80%. Points 1, 2, and 3 represent the temperature when air is cooled using direct evaporative cooling, indirect evaporative cooling, and dehumidifier coupled with direct evaporative cooling, respectively.

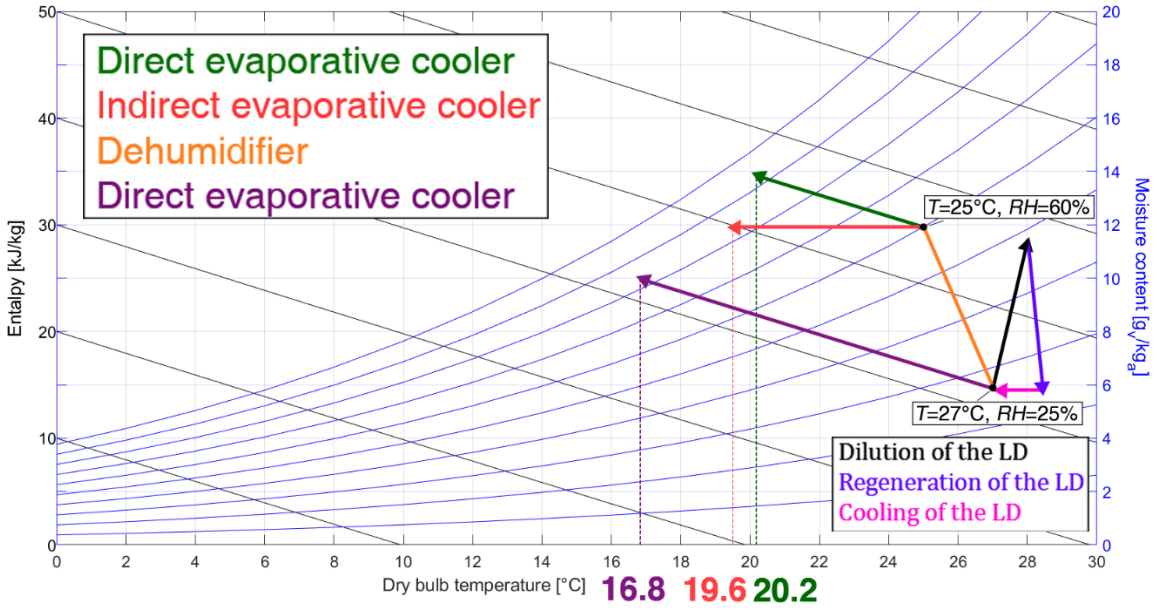

Figure 1-3. Psychrometric chart showing examples of three cooling methods, starting from temperature (T) of 25 °C and relative humidity (RH) of 60%. Points 1, 2, and 3 represent the temperature when air is cooled using direct evaporative cooling, indirect evaporative cooling, and dehumidifier coupled with direct evaporative cooling, respectively.

LDAC systems can operate in three air modes: open ventilation, closed recirculation, and semi-closed recirculation (which is a combination of the other two categories). These modes work at atmospheric pressure by changing the moisture content of the air. Open ventilation cools a conditioned space by cooling and drying an external air stream. The 'open' term indicates that air is taken from (and rejected to) the external environment [19]. Open ventilation requires a constant supply of fresh air which must be provided to the conditioned space.

The requirement of external air in open ventilated greenhouses makes the system vulnerable to the external air conditions. Newer configurations employ closed or semi-closed recirculation which operate without or with less external air. Thus, ambient vulnerability can be overcome by operating with closed/semi-closed recirculation. Closed/semi-closed greenhouses achieve further water savings compared to open greenhouses and have the

advantage of CO_2 enrichment [24]. This is because CO_2 control is easier as Closed/semi-closed greenhouses have zero to low CO_2 losses. Moreover, closed and semi-closed recirculation require fewer equipment (see Figure 1-4). Figure 1-4 depicts air psychometrics for open ventilation, semi-closed, and closed recirculation. Figures 1-5 and 1-6 show a greenhouse operating with open ventilation and semi-closed/closed recirculation, respectively, based on the psychrometric chart in Figure 1-4. In Figures 1-5 and 1-6, The LD is reconcentrated via a generic technology, which separates the LD from the absorbed vapour. Conventional thermal regenerators waste the absorbed vapour by vaporising it into the environment.

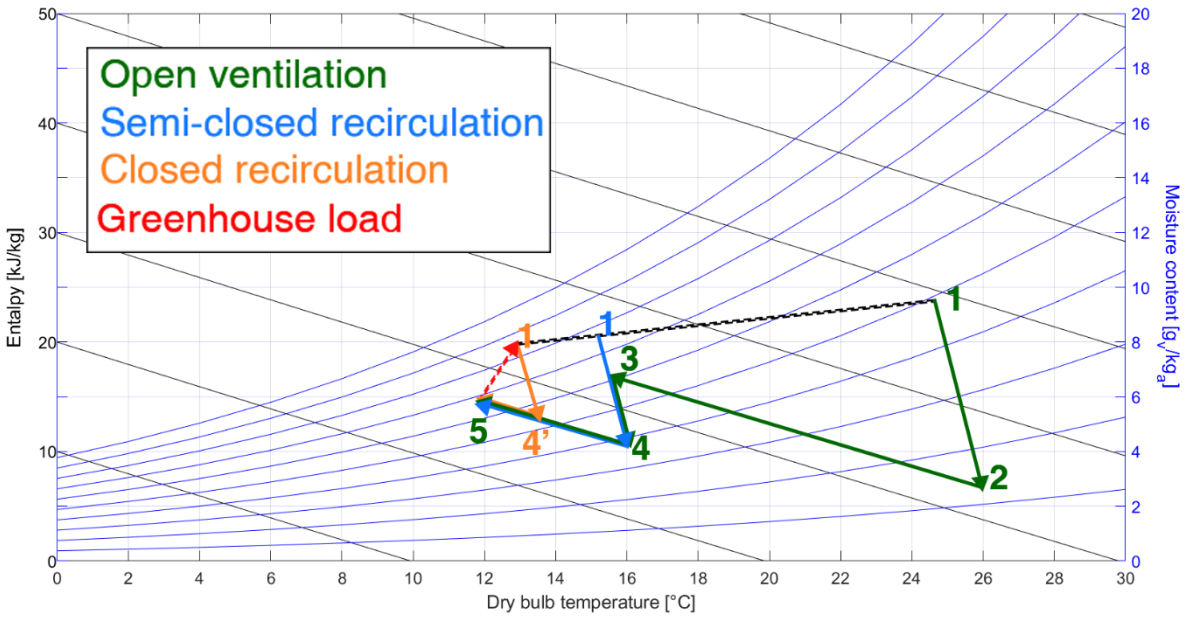

Figure 1-4. Psychrometric chart showing examples of the three ventilation methods, considering external temperature of 28 °C and relative humidity of 65%. Every line represents a component; therefore, open ventilation requires four components while both semi-closed and closed recirculation require only two components. The initial point (i.e., 1) of each ventilation type is not top of the black line.

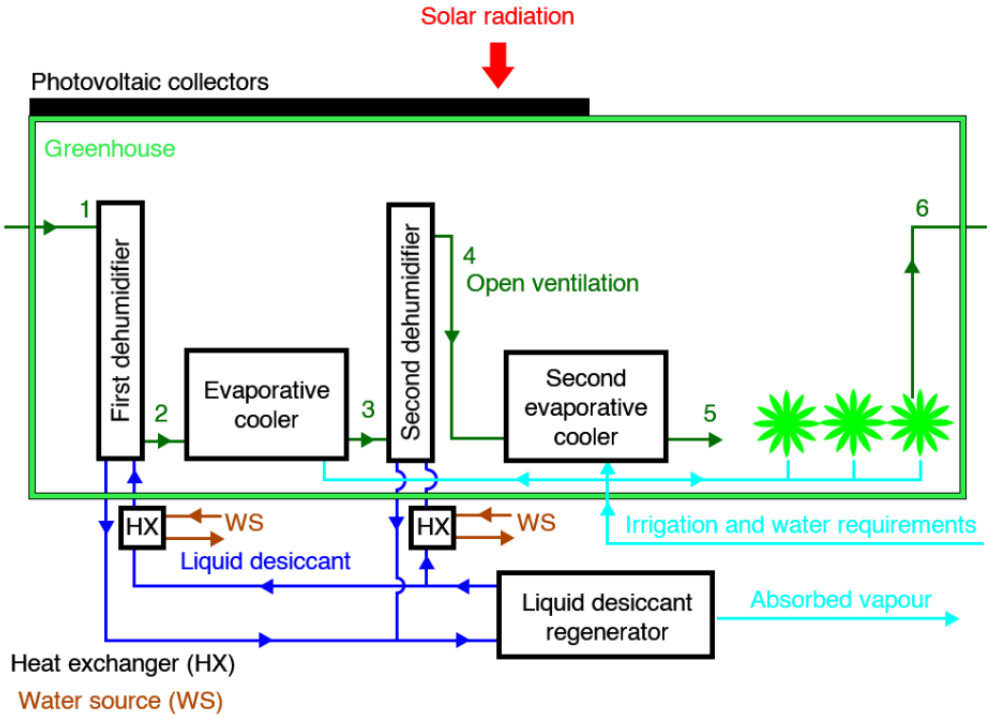

Figure 1-5. Schematic of a greenhouse operating with open ventilation and two dehumidification stages.

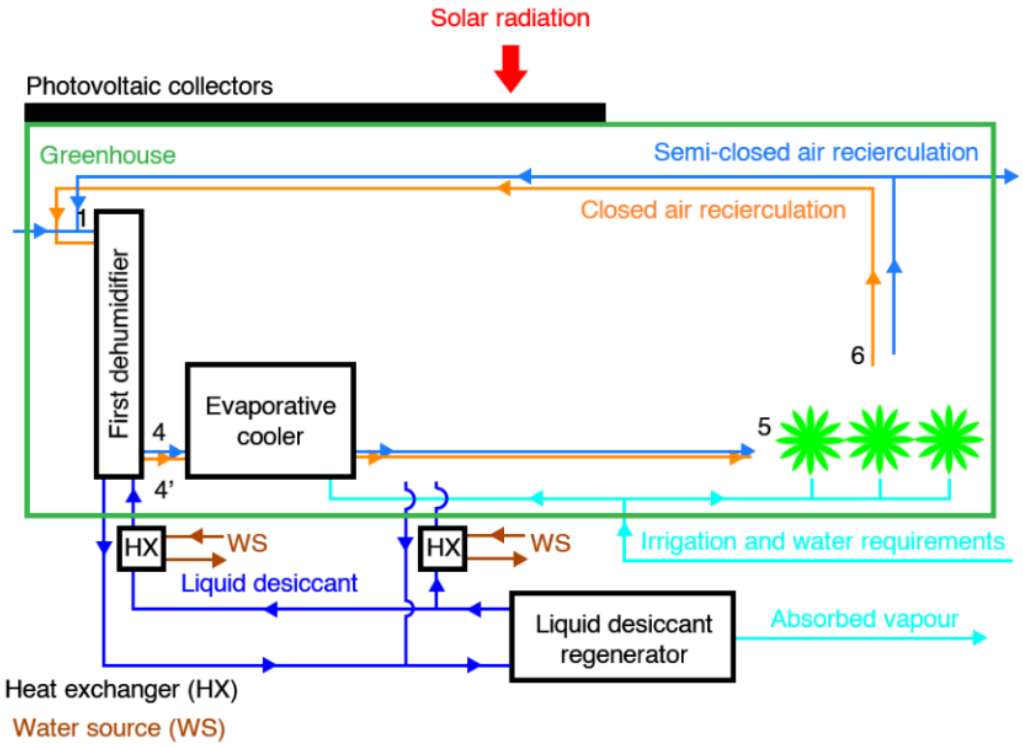

Figure 1-6. Schematic of a greenhouse operating with semi-closed (in blue) and closed (in dark orange) recirculation using one dehumidification stage.

1.2 Liquid desiccants and their properties

The LD properties can significantly affect the LDAC cycle. Thus, an overview of typical LD used in LDAC applications is provided, together with their key properties. An ideal LD should have: high specific heat capacity to avoid high temperature gradient [17], low viscosity and density to decrease the electric consumption [17, 25], no crystallisation tendency at high concentrations to allow employment of highly concentrated solutions, low to zero toxicity [17, 25], low cost [17, 25], and low to zero corrosivity [25].

Common LDs can be divided into two groups, organic and inorganic. Organic desiccants include glycols such as diethylene (DEG), triethylene (TEG), tetraethylene (TREG), dipropylene (DPG), and propylene (PG); while inorganic desiccants include halide salts, such as lithium chloride (LiCl), lithium bromide (LiBr), magnesium chloride ($MgCl_2$) and calcium chloride ($CaCl_2$) [17]. Glycols volatilise due to their low surface vapour pressure which leads to contamination and desiccant losses in the conditioned space, which consequently increases the overall system costs and makes glycols unsuitable for LDAC applications [18, 26]. Inorganic solutions are preferred because they do not volatilise under typical LDAC operating conditions [17]. Among the halide salts, the best are LiBr, LiCl, $CaCl_2$, and $MgCl_2$ due to their low vapour pressures [27]. Several studies [22, 28-35] can be found employing LiBr, LiCl, $CaCl_2$, or $MgCl_2$ for LDAC applications. Among the halide salts, LiCl is the most stable and efficient [36]. LiBr is the second-best, with slightly lower dehumidification efficiency, but with a 20% lower cost than LiCl [37]. $CaCl_2$ and $MgCl_2$ achieve lower dehumidification efficiencies compared to LiCl and LiBr [25], but are even less expensive [38]. $MgCl_2$ is less efficient compared to other desiccants and crystallises at lower concentrations [38] but has other advantages, such as availability and low toxicity [25]. $CaCl_2$ is the most inexpensive halide salt, making it the most readily available choice [37]. However, $CaCl_2$ properties vary

significantly with the inlet air conditions and the LD concentration [37]. Sodium chloride (NaCl) and zinc chloride ($ZnCl_2$) have not been investigated as LDs because they have lower dehumidification efficiencies than the other halide salts [25].

Conventional LDs are corrosive to metals with severe drawbacks regarding the reliability and longevity of the LDAC system [39, 40]. For this reason, alternatives have been proposed such as potassium formate (HCO_2K) [40-42], potassium acetate (CH_3CO_2K) [10], sodium formate (HCO_2Na) [10], and sodium acetate (CH_3CO_2Na) [43]. These alternatives have high solubility and low crystallisation temperature, low density, low corrosivity, low toxicity, and low volatility [37, 44]. Additionally, alternative LDs are more environmentally safe [37]. Among the alternatives, HCO_2K is preferred due to additional benefits, such as lower manufacturing cost and higher vapour pressure, which reduces the energy requirement of the regeneration process [45]. However, high vapour pressure negatively affects the dehumidification process where low vapour pressures achieve high dehumidification efficiency. A drawback of these alternatives is that they achieve the same dehumidification efficiency as conventional LDs at higher concentrations. For example, Zhang et al. [40] found that a concentration of 62 wt.% (880 g/L) HCO_2K was needed to achieve the same dehumidification as 40 wt.% (510 g/L) of $CaCl_2$ and 32 wt.% (380 g/L) of LiCl.

The dehumidification efficiency of LDs is measured based on their equilibrium relative humidity (*ERH*), which must be low to achieve an efficient dehumidification [17, 25]. The *ERH* is proportional to the vapour pressure difference between the air and the LD, which is the driving force for moisture transfer [35]. This means that the *ERH* is directly proportional to the dehumidification effectiveness of the system. The *ERH* also represents the minimum *RH* to which air can be dried when air and LD are at the same temperature [25].

A lower *ERH*, reached at a lower desiccant temperature or higher LD concentration, achieves a higher dehumidification efficiency [18, 46]. Different studies have investigated the *ERH* of LDs. Davies and Knowles [25] showed that open ventilated greenhouses in hot climates, such as Tunis, Jeddah, Abu Dhabi, Mumbai, and Bangkok, require an *ERH* below 50% to achieve an efficient dehumidification.

Since the properties of the LDs depend on several factors, equations have been developed to predict their properties. For example, Conde [47] reviewed different studies and developed interpolating equations for the properties of LiCl and $CaCl_2$. Lychnos and Davies [22] developed equations to calculate the vapour pressure of $MgCl_2$ depending on the LD temperature and concentration. Bouzenada et al. [46] developed a mathematical correlation to calculate the vapour pressure of $CaCl_2$ based on the LD concentration. Regarding LiCl, $CaCl_2$ and their mixtures, Yao et al. [48] experimentally investigated the accuracy of the simple mixing rule and the non-random two-liquid models. Their findings showed that the simple mixing rule is more accurate compared to the non-random two-liquid when the weight concentration of the LD is below 10 wt.% (105 g/L), while the non-random two-liquid model becomes is preferred for weight concentrations above 30 wt.% (350 g/L). Moreover, the authors proposed improvements for the two models to increase their accuracy. Artificial neural networks (ANNs) have also been investigated by Gandhidasan [49] who developed an ANNs model to determine the vapour pressure of $CaCl_2$, LiCl, and LiBr.

1.3 Previous studies on liquid desiccant air-conditioning for greenhouses

The above-mentioned equations have been introduced into models to accurately simulate the LDAC cycles for residential buildings. However, greenhouses have special requirements distinct from those of human residences. While humans require a temperature of 23 °C and

RH of 50% [50], crops require variable temperature according to species. For example, lettuces have an optimal temperature of 17–23 °C, tomatoes and cucumbers of 27–29 °C, and soya beans of 25–30 °C [22]. Compared to humans, crops are less tolerant to a sudden drop of temperature, which can decrease their growth. Moreover, crops are negatively affected by high temperature differences between day and night [23]. Regarding the *RH* in greenhouses, *RH* above 94% results in lower transpiration and in turn in lower yield, while *RH* below 70% can lead to a lower number of fruits per crop and lower growth [23]. Another difference between human residences and greenhouses is their structure. Greenhouses need to admit high amounts of solar radiation as required for photosynthesis. This higher incoming radiation leads to higher thermal loads which must be removed by the cooling system. Moreover, greenhouses operate with air changes of 20–40 times higher than human residences, leading to an increased cooling load to cool a larger volume of air. The high solar load, high cooling load, high moisture removal rate, and small allowable ranges of both temperature and *RH* make LDAC in greenhouses more challenging than in residential buildings.

Consequently, LDAC studies for greenhouse applications are limited. These studies include Davies [9] who theoretically evaluated the temperature reduction in a greenhouse resulting from the integration of open solar collectors, LDAC, and cooling pads for an open ventilated greenhouse. The evaluated system, designed for the Gulf region, achieved an additional 5 °C reduction in indoor temperature compared to conventional evaporative cooling. This extended the optimal growing season for temperate and tropical crops from 3 to 6 and 7 to 12 months per year, respectively. Moreover, Lychnos et al. [33] simulated the cooling performance of a LDAC system using $MgCl_2$ and predicted a temperature drop of 3.4–4.2 °C higher than that achieved with evaporative cooling. This system was further investigated by Lychnos and Davies [22] who theoretically and experimentally investigated a

solar-powered LDAC system using $MgCl_2$ and predicted a temperature drop of 5.5–7.5 °C higher than evaporative cooling.

Closed recirculated greenhouses have also been studied for greenhouse LDAC applications. Lefers et al. [5] were the first to propose a closed greenhouse using LDAC. The authors conducted experiments using hollow fibre vacuum membrane-distillation membranes and $MgCl_2$.

1.4 Limitations of conventional liquid desiccant air-conditioning and alternatives

Although LDAC has advantages over conventional technologies used for cooling in greenhouses, LDAC faces many limitations. These include droplet carryover, corrosiveness, poor wettability, large temperature change, and large heat requirement [17]. When poor wettability occurs, dry zones are formed which limit the heat and mass transfer and reduce the dehumidification performance [51]. These limitations in greenhouses imply that the LDAC must be highly efficient and conventional LDAC do not meet this requirement, making it a necessity to address these limitations. The main components of a LDAC system are the dehumidifier and the LD regenerator; thus, new types of dehumidifiers and regenerators have been proposed, as well as alternative ways to power the system.

Regarding the dehumidifiers, the most common direct contact type is the spray tower where the LD is sprayed to increase the heat exchange surface, which in turn increases the efficiency of the regeneration process [52]. Other direct contact types are the packed bed and the falling film [52]. These direct contact types are thermally driven, making them energy-intensive. Newer direct contact dehumidifiers exist, such as the ultrasonic atomisation desiccant regenerator which utilises ultrasounds [53, 54]. Other types of dehumidifiers have been developed, such as the membrane liquid desiccant air dehumidifiers (MLDAD), to mitigate droplets carryover [39]. MLDAD utilises membranes which allow only water vapour

to pass through, thus avoiding that the LD contaminates or corrodes the MLDAD components [39].

Regarding the LD regenerators, conventional types consist of packed beds powered by thermal energy or open-solar collectors [17]. As a result of being thermally-driven, these regenerators have high energy demands [55], and in turn low coefficient of performance (*COP*). Based on an experimental study [56] investigating different external dry-bulb temperatures and humidities, the *COP* varied from 0.2 to 0.9. Another study [57] evaluated the efficiency of different solar collectors for various climates and found that hotter and more humid locations could produce a maximum *COP* of only 0.51. These *COP* values are low compared to other systems, such as heat pumps which have an average *COP* of 2.5 [58].

Other packed-bed regenerators have been powered by heat pumps, which allow simultaneous heating and cooling, which decrease the amount of equipment needed [59]. Heat pumps can be coupled with liquid-to-air membrane energy exchangers which are not affected by droplet carryover as other dehumidifiers [59]. Although heat pumps can produce both heating and cooling, the matching of the produced heating/cooling to the heating/cooling requirements is a challenging task [59]. A novel matching capacity method was proposed which achieved a maximum *COP* of 5 [60]. Although a high *COP* can be achieved using heat pumps, these do not solve the high-water requirement of greenhouses. Moreover, heat pumps may contribute to global warming due to the high global warming potential of conventional refrigerants. Instead, newer refrigerants such as hydrocarbons may be used which have a very low global warming potential [61]. However, compared to systems using conventional refrigerants, systems using hydrocarbons need to be designed more carefully with better safety controls due to the high flammability of hydrocarbons [61].

Regarding newer types of regenerators, investigations on membrane-based separation processes found higher *COP* values than conventional regenerators [17, 18]. Membrane-based separation processes also have the advantage that the absorbed moisture can be re-utilised for irrigation (e.g., the "absorbed moisture" in Figure 1-6 is rerouted as to "irrigation and water requirements"). A comparison of six desalination technologies – membrane distillation, reverse osmosis, nanofiltration, forward osmosis, thermoresponsive solutions and electrodialysis – was conducted in Chapter 2.

In summary, Chapter 2 found that the high water and energy requirement of greenhouses in hot countries suggests that membrane-based technologies, rather than thermal-based, are more efficient. Membrane-based technologies are promising because they have a lower energy consumption than conventional regeneration methods and simultaneously decrease the irrigation requirements of greenhouses. Forward osmosis, reverse osmosis, and electrodialysis are the least suitable desalination technologies for LD regeneration. The regeneration of the draw solution in forward osmosis is energy intensive when operated with concentrated feed solutions [62]. Moreover, forward osmosis requires another desalination technology to concentrate the LD. Reverse osmosis has burst pressures of 70–80 bar [63] which limit the LD concentration to 70 g/L [55]. As a result, reverse osmosis is not suitable for LDAC applications that require LDs with higher concentrations. Electrodialysis achieves a limited concentration difference between the inlet and outlet LD. This difference cannot exceed a certain limit, otherwise the LD will be diluted instead of concentrated [64]. Another disadvantage of electrodialysis is that it involves three separate liquid flows, namely electrode solution, concentrated, and diluted solutions. While the LD is concentrated, the diluted solution is diluted and needs to be re-concentrated, highlighting the necessity of another desalination technology.

The most promising technologies for LD regeneration are thermoresponsive solutions, membrane distillation, and nanofiltration. Although thermoresponsive solutions have potential due to their rapid change of *ERH* (which can lead to a higher *COP*), investigations are still in a preliminary stage of research and have considered only low concentrations [65]. Membrane distillation can operate with concentrated solutions but their drawback is the high expected energy consumption due to the involvement of phase transition [55]. Theoretically, membrane distillation resisting 100 °C could increase the efficiency of multi-stage membrane distillation systems, but commercial membrane distillation membranes only resists 80 °C [66-72]. Lastly, theoretical nanofiltration studies [73] show potential for high concentration applications when operated in multi-stage systems because the energy consumption decreases as the number of stages increases. Since nanofiltration membranes are readily available, multi-stage nanofiltration for LD regeneration was identified as the most promising and practical option to investigate in this PhD project.

1.5 Aims and structure of thesis

To help addressing the challenges of increasing water scarcity and food demand in hot climates where horticultural greenhouses are used, the concept of a greenhouse LDAC system using a multi-stage nanofiltration as the LD regenerator, namely NF-LDAC, was designed and assessed (Chapter 3). Then, samples of four commercial nanofiltration membranes were investigated to evaluate the practicality of regenerating concentrated LDs in 1-stage dead-end filtration experiments (Chapter 4). It was found that LD regeneration through nanofiltration membranes is possible, but 1-stage does not achieve high concentration differences. Thus, a 2-stage regenerator was built consisting of a nanofiltration membrane and a reverse osmosis membrane operating in cross-flow filtration (Chapter 5). Because NF-LDAC is a novel process introduced in this PhD thesis, there is no existing literature to compare against the

obtained results. Since the multi-stage nanofiltration regenerator is a modification of another multi-stage nanofiltration system used for zero liquid discharge (ZLD), Chapter 5 also investigated multi-stage nanofiltration systems for ZLD. This provides additional validation of the PhD thesis, allowing for a critical comparison to be made between the experimental data and existing literature. The 2-stage regenerator model was verified with errors below 11%. The final aim was to integrate the verified model (including energy and pressure losses), experimental data, datasheets, and realistic operating conditions into a dynamic simulation of a greenhouse using NF-LDAC (Chapter 6). The findings of this PhD thesis provide insights into practical aspects that need to be considered when designing NF-LDAC systems. A general discussion (Chapter 7) concludes this PhD thesis with a summary of the research, limitations encountered, and future research for NF-LDAC, as well as a summary of the main conclusions.

Chapter 2: Comparative review to choose a desalination technology for use as a regenerator[1]

Title of published paper: Comparative review of membrane-based desalination technologies for energy-efficient regeneration in liquid desiccant air conditioning of greenhouses.

Paper information: Renewable and Sustainable Energy Reviews, 2022. 154: p. 111815.

Author contributions and affiliations:

- P. Pasqualin[a]: original draft, writing, review, editing, data curation, investigation and visualisation

- R. Lefers[b]: review

- S. Mahmoud[a]: review

- P.A. Davies[a]: conceptualisation, review and editing

[a] School of Engineering, University of Birmingham, Edgbaston, Birmingham B15 2TT, UK.

[b] King Abdullah University of Science and Technology (KAUST), Water Desalination & Reuse Center (WDRC), Biological and Environmental Science and Engineering Division (BESE), Thuwal 1223955-6900, Saudi Arabia.

[1] The published paper contains additional figures that were excluded from Chapter 2 due to copyright considerations. Subsections 2.7.1 and 2.7.3 were presented in conferences and are not part of the published paper.

LDAC in greenhouses is an emerging technology that could maintain optimal growing conditions for crops while also being self-sustained by solar energy. However, this is not achieved because the regeneration of the LD is a bottleneck in LDAC. This highlights the need for alternative regeneration technologies. Studies using membrane-based separation processes such as membrane distillation (MD), reverse osmosis (RO), and electrodialysis (ED) have already been conducted for LDAC systems [17, 18]. There are also other membrane-based separation processes such as nanofiltration (NF), forward osmosis (FO), and thermoresponsive (TR) solutions that have not been investigated for LDAC.

Thus, a comparative review was conducted for these six desalination technologies – MD, RO, NF, FO, TR solutions, and ED – which may be employed for LD regeneration. The technologies were evaluated and compared based on criteria including achievable LD concentration, energy requirements, system efficiency, and availability of the technology. This comparative review presents the state-of-the-art of these six technologies and studies using them for desalination applications. To date, only MD, RO, and ED have been investigated for LDAC application. Therefore, studies using LDAC are presented only for these three technologies.

A comparison of RO, NF, and ED for agriculture has already been done by Burn et al. [74]. However, the authors focused on the economic feasibility of the technologies. There has been increasing research in membrane-based technologies after the publication of Burn et al. work, as well as research in new technologies that were not covered in their comparison. Since the economic aspect can be found in [74], the focus of the comparison here is regarding the limitation of the membrane-based technologies, with the aim to provide suggestions that could improve their usage as LD regenerators in greenhouse LDAC applications. The comparison includes 29 peer-reviewed selected studies, each investigating one of the

technologies for desalination applications. Among them, 7 are for MD, 4 for RO, 3 for NF, 3 for FO, 6 for TR solutions, and 6 for ED. A second comparison was also performed for 11 studies investigating desalination technologies for LD regeneration. Specifically, 5 studies are for MD, 1 for RO, and 5 for ED. The LD regeneration studies were selected based on the date of publication being in the last decade, with 8 studies being published after 2016. Another requirement for selecting these studies was to treat highly concentrated LD solutions, required for an effective dehumidification.

2.1 Membrane distillation

MD combines thermal evaporation and membrane separation [75]. Partial water vapour pressure is the driving force of the process, driven by a temperature difference between feed side and condensation surface [75]. An aqueous solution is in contact with a microporous hydrophobic membrane that allows only vapour to pass through, which creates a vapour-liquid interface [76]. Vapour is released, due to the heat provided to the feed solution, which diffuses through the membrane pores and condensates on the cooler permeate side.

2.1.1 Types

Direct contact MD (DCMD) is the basic MD configuration, employed in the past to concentrate aqueous solutions in food industries [77, 78] and manufacture acids [79]. However, DCMD drawback is the heat lost by conduction [80]. Other configurations (Figure 2-1 Shows four configurations) include an air gap (AGMD), a sweep gas (SGMD), or a vacuum gap (VMD) on the permeate side to minimise the conduction losses. In AGMD, a portion of the vapour condenses on a condensation surface while the remaining portion is condensed by an external condenser [81]. Similarly to AGMD, the permeate of SGMD is

condensed by an external condenser, required to be of large dimensions due to the small permeate volume that evaporates in a large sweep gas volume [80]. In VMD, vacuum is applied using a vacuum pump. An advantage of VMD is that the temperature of the evaporating fluid can be lower due to the additional driving force of the vacuum applied on the permeate side [82]. Likewise in other MD configurations, vapour in VMD is condensed by an external condenser [75]. More membrane modules can be placed in multi-stage configurations to increase the system efficiency, with decreasing temperature and pressure levels from stage to stage.

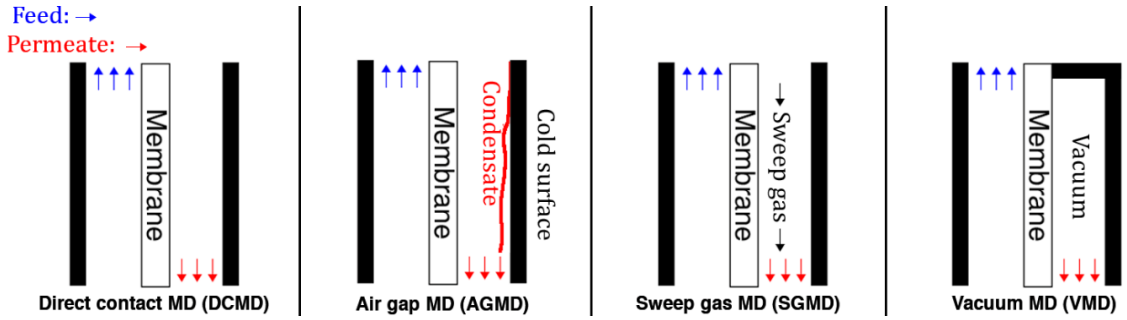

Figure 2-1. Schematic of four membrane distillation (MD) configurations.

VMD performs better compared to the other MD configurations. A comparison between DCMD and VMD was carried out using highly concentrated LiCl solutions as the feed [70]. However, only VMD could operate with positive flux at concentrations approaching saturation. For greenhouse LDAC, Lefers et al. [34] showed that VMD operating with concentrated $MgCl_2$ maintained the greenhouse below 23 °C and the *RH* within 70–90%.

The drawback of MD regeneration is that it requires more energy compared to other membrane-based desalination technologies [83]. This is because MD is a thermally driven process with higher irreversible losses due to the evaporation and condensation of the LD [55]. Consequently, MD has a high thermal specific energy consumption (SEC_{th}). For

example, an AGMD solar desalination system had SEC_{th} of 900–2600 kWh_{th}/m^3 when treating a feed containing 35 g/L of NaCl [84]. The SEC_{th} of AGMD can decrease by employing multi-staging. In fact, the SEC_{th} of single-stage AGMD decreased from 1800 kWh_{th}/m^3 to 290 kWh_{th}/m^3 when employing a 3-stage AGMD [85]. To decrease the SEC_{th} even further, VPD systems must be used which have SEC_{th} of 150–400 kWh_{th}/m^3 when treating a feed containing 35 g/L of NaCl [86]. VMD may be able to have less heat losses and a lower thermal consumption compared to the other MD configurations, but the applied vacuum represents an additional electric consumption. Therefore, when both thermal and electric consumptions are considered, VMD may have a higher overall energy consumption, compared to the other MD configurations.

2.1.2 Membrane distillation for water desalination

MD for water desalination can be operated as DCMD, AGMD, SGMD, or VMD, but the most investigated configurations are DCMD and VMD. Studies regarding DCMD have been conducted by Tun et al. [71] who investigated a DCMD crystallisation process using two aqueous salt solutions: sodium sulphate (Na_2SO_4) and NaCl. The purpose of their study was to recover water and produce salt crystals. The experiments were carried out with feed temperatures of 50 and 60 °C, permeate temperatures of 20 and 30 °C and feed concentrations up to 284 and 263 g/L of Na_2SO_4 and NaCl, respectively. The utilised hydrophobic PVDF membranes were produced from Millipore. The flux gradually decreased due to vapour pressure suppression and concentration polarisation up to a critical point, with rapid vapour flux decline beyond that point. Before saturation, permeate flux between 11.5 and 21 $L/(m^2\,h)$ and 14.5 and 20 $L/(m^2\,h)$ were reported for Na_2SO_4 and NaCl, respectively. The cases with NaCl feed concentration of 263 g/L and feed/permeate temperatures of 50/30 °C and 60/20 °C

achieved recoveries (*R*) of 18 and 20%, respectively. For the same feed/permeate temperatures, Na_2SO_4 achieved *r* of 20 and 32%. Vapour flux was predicted by a heat and mass transfer model, but the authors did not provide information regarding model performance compared to experimental results.

Another study employing concentrated NaCl for a DCMD application was conducted by Yun et al. [72]. Permeate flux was measured depending on different feed concentrations (187–285 g/L), feed flow velocities, feed and permeate temperatures. The tested membranes were fabricated by Perspex. A mathematical model was developed to compare with experimental results; the experiments were initially executed using distillate water, with error between calculated and measured vapour fluxes lower than 5%. The results showed the permeate flux: 1) increased exponentially with feed temperature, 2) had small variations with different permeate temperatures and feed flow velocities and 3) decreased sharply when NaCl concentration reached 302 g/L (saturation concentration). When operating with feed/permeate temperatures of 70/20 °C and NaCl feed of 285 g/L, permeate flux over time formed an inverse "S" shape. Permeate flux decreased from 7 to 0.5 L/(m^2 h) when saturation was reached. The model predictions and experimental results were in good agreement with error lower than 10%.

Continuing with DCMD, Chen et al. [68] investigated crystallisation kinetics using NaCl in a PVDF hollow-fibre module (not commercially available) to quantify scaling formation. A model was developed to compare with experimental results. High permeate flux decline was observed associated with a critical crystal deposition point on the membrane surface, which occurred when the crystal size reached 26 μm. The experiments were carried out with NaCl concentration of 199 g/L, initial feed mass solution of 1200 g, permeate temperature of 19 °C, feed and permeate flowrates of 48 and 12 L/h, respectively. When using feed at 67 °C, the

critical point was observed after 6.6 hours with almost null flux after 8 hours. Crystal median size increased from 11.4 μm (at 6.5 hours) to 349.2 μm (at 7.5 hours), corresponding to a flux drop from 9.58 to 1.95 L/(m^2 h). The authors reported an error below 10% between experimental and simulation results.

Besides DCMD, VMD is also widely used in MD desalination applications. A study regarding VMD employing concentrated solutions was performed by Mericq et al. [69] who simulated an industrial scale VMD coupled with reverse osmosis process to improve *r*. The plant was simulated with a feed flowrate of 4167 m^3/h and *r* of 40%. A model was developed and tested to measure temperature and concentration polarisation for three synthetic concentrated solutions containing NaCl with total dissolved solids of 94 (SW95), 149 (SW150) and 291 g/L (SW300). The study also considered an actual brine with concentration of 64 g/L. A PTFE flat-sheet membrane, namely Fluoropore (produced by Millipore, France) was used for the experiments. Super-saturation of salts led to their precipitation and thus crystallisation was observed, but these phenomena were not taken into consideration by their model. Temperature polarisation effect on flux reduction was higher compared to concentration polarisation, with temperature polarisation contribution being more than 88% for SW95, SW150 and the actual brine. Temperature polarisation had a reduced impact of 62% for SW300, showing that concentration polarisation becomes more relevant for highly concentrated solutions. Permeate flux reduction, due to both polarisations, was higher than 94% for all cases. Scaling occurred mainly due to calcium precipitation at high salt concentrations, with a flux reduction of 24% being reported by the authors.

Mericq et al. [69] also observed that the feed temperature significantly influenced the permeate flux, increasing SW300 from 20 to 70 °C increased permeate vapour flux from 1.33 to 22.3 L/(m^2 h). It must be noted that higher feed temperatures increase permeate flux at the

expense of higher energy consumption because more energy is required to increase the feed temperature to a higher value. To concentrate the brine to 300 g/L under optimal operating conditions, the permeate flux ranged from 7 to 17 L/(m^2 h). The coupling of VMD with the desalination plant increased the *r* from 40% to 89%. Based on mass balance equations considering a flowrate of 4167 m^3/h and feed concentration of 39 g/L, the system produced 1667 m^3/h of permeate (*r* of 40%) with a permeate concentration of 0.06 g/L. The VMD unit produced 2047 m^3/h of permeate (*r* of 82%) with a concentration of 13.3 g/L, which is unsuitable for drinking purposes. This study reports higher permeate flux and lower flux declines compared to previous studies [68, 71, 72], related to the investigation of lower feed concentration.

Another study regarding VMD was conducted by Andrés-Mañas et al. [66] who theoretically investigated a multi-stage VMD unit powered by flat plate collectors to desalinate seawater. The model incorporated solar collectors, thermal storage, a control system, and the VMD unit considering typical weather conditions of Almería (Spain). The thermal storage was integrated to guarantee permeate production during days with unstable or absent solar radiation. A control system was modelled using valves which regulated the flowrates of the system. The solar collectors and the thermal storage were simulated using differential equations. The storage equations considered a thermal stratification of two layers inside the buffer. Although it is a simple model easily integrated in the model, a realistic configuration should consider more layers depending on the height of the storage. The VMD unit model provided outputs via interpolations, based on experimental studies previously done by the authors [67] using a MDS-40B membrane (assembled and manufactured by Aquaver BV). The R^2 deviation of the interpolation equations were low when considering low output

temperatures. For the calculated distillate production, a R^2 deviation of 2.4 L/h was reported, resulting in errors of 5–15% depending on the operating conditions.

The system performance was measured for three VMD feed set-point temperatures (SPT) of 60, 70, and 80 °C. During optimal weather conditions (solar irradiance higher than 1000 W/m^2) at 80 °C SPT, the system produced 7.2 $L/(m^2\ h)$ of distillate water. The energy produced by the solar collectors was higher than the energy requirement by the MD and the remaining energy (34% of total energy collected) was stored in the thermal buffer. During limited weather conditions (solar irradiance lower than 300 W/m^2) at 60 °C SPT, the system produced 2.4 $L/(m^2\ h)$ of distillate water for 4.5 hours using energy from the thermal storage. The results showed that higher SPT allowed the system to utilise more efficiently the solar collectors. At 60 °C SPT, the temperature of the collector would exceed the maximum value of 115 °C, pausing their operation and decreasing the solar input energy to the system. For feed seawater flux of 120 L/h, the annual water productions were 41.7, 68.4, and 70.5 m^3 for the 60, 70, and 80 °C SPT, respectively. An average flux of 5.5±1 $L/(m^2\ h)$ was reported for 70 and 80 °C SPT, which corresponds to *r* of 29.5±5.5%. An average permeate flux of 3±1 $L/(m^2\ h)$ was reported for the 60 °C SPT. The 80 °C SPT was difficult to maintain and was only possible for 2.6% of the operating time during the year. For this reason, the 70 °C SPT was considered the best solution. Higher feed temperatures exponentially increase the permeate flux compared to lower temperatures which is not observed in this study since the 80 °C SPT was not maintained for an extended period. The study included some energy considerations which are not enough to determine the system energy consumption. In another experimental study done by the authors [67] considering the same VMD unit, a SEC_{th} of 207.7 kWh_{th}/m^3 and SEC_{el} varying from 5 to 20 kWh_{el}/m^3 were reported; operated with feed seawater flux of 150.1 L/h and 75 °C SPT.

Regarding MD using solutions containing different salts than NaCl, a comparison between DCMD and VMD was carried out by Quist-Jensen et al. [70] who investigated the feasibility of simultaneous water recovery and crystal formation from highly concentrated LiCl solutions. The membrane modules were purchased from Microdyn-Nadir (MD020CP2N) and Membrana (Accurel S6/2) which were used for the DCMD and the VMD, respectively. LiCl precipitation from single salt solutions requires salinities above 593.5 g/L. Since osmotic pressure is proportional to concentration, high concentration values result in osmotic effects that can overcome the thermal ones, leading to a negative flux. Between DCMD and VMD, only VMD achieved positive flux, approximately 1 L/(m^2 h) for LiCl concentrations higher than 593 g/L while DCMD could not operate with concentrations above 297 g/L. The authors attributed the success of VMD to the minimum temperature polarisation and the reduced resistance to vapour transport within the membrane pores. The reported LiCl production cost of 2.182 $/kg approaches the production cost of 2$/kg from lake water brines. Although an economic analysis was included, no information was presented regarding the energy performance of the system.

In summary, only VMD could operate at high feed concentrations with positive flux for NaCl concentrations approaching saturation. A flux drop due to scaling was observed by most authors [68-72], meaning scaling must be expected in high salinity applications. Nevertheless, scaling in VMD had a limited effect on the flux reduction [70], making it potentially compatible for greenhouse applications. Although, salt precipitations still occurred in VLD, implying the need for cleaning procedures. DCMD studies at high concentration showed rapid flux decline making them unsuitable for greenhouse applications. Most authors [68-72] did not provide the energy consumption, which is expected to be high since MD is a thermally driven separation process [87]. Even though MD can be powered by solar energy, the high

energy consumption would require a high solar collectors' area to produce high feed temperatures, making MD technologies problematic in self-sustainable greenhouse applications. Table 2-1 summarises the selected studies in MD for water desalination considering important parameters, necessary to compare results from different desalination technologies and to evaluate compatibility for greenhouse applications.

Table 2-1. Summary of selected MD studies for desalination applications.

Study	Solute	Concentration [g/L] (wt.%)	Molar fraction	*SEC* [kWh/m^3]	Recovery [%]	Experimental or theoretical	MD technology
[71]	NaCl Na_2SO_4	263 (23) 284.1 (24.15)	0.085 0.039		18–20 20–32	Both	DCMD
[72]	NaCl	284.5 (24.68)	0.092			Both	DCMD
[68]	NaCl	199.3 (18)	0.063			Both	DCMD
[69]	NaCl	64 (6.2)	0.020		82	Theoretical	VMD coupled with RO
[66, 67]	NaCl	35 (3.44)	0.011	208 (Thermal) 5–20 (Electrical)	29.5±5.5	Theoretical	Multi effect VMD
[70]	LiCl	593.5 (45.4)	0.261			Both	DCMD VMD

The main parameters affecting MD performance for water desalination are feed temperature (T_{in}), permeate temperature (T_p), and feed concentration (C_{in}). The effects of these parameters on *COP*, permeate flux (J_v), power requirement (*Power*), and recovery (r) are summarised in Table 2-2.

Table 2-2. Main parameters affecting MD performance in desalination applications based on the selected studies[2]

Operating parameter	*COP*	J_v	*Power*	*r*
↑ T_{in}	↑ [66]	↑ [66, 69, 72]	↑ [69, 72]	↑ [71]
↑ T_p		~ [72]		
↑ C_{in}		↓ [68, 69, 71, 72]		

2.1.3 Membrane distillation for liquid desiccant regeneration

Few studies can be found employing MD for LD regeneration in LDAC systems. The selected studies utilise a MD technology as the LD regenerator to treat highly concentrated desiccants and have been published in the last decade. Regarding DCMD, Duong et al. [88] studied theoretically and experimentally a DCMD process to reconcentrate LiCl. At a feed temperature of 55 °C, the calculated permeate flux varied from 12 to 2.5 L/(m^2 h) when the LiCl concentration increased from 20 to 30 wt.% (from 220 to 355 g/L). The feed temperature was highly affected by the permeate flux, with measured flux at 65 °C being twice the flux at 55 °C. Temperature also influenced the outlet feed concentration, with maximum outlet feed concentrations of 25 and 29 wt.% (of 290 and 340 g/L) at 55 and 65 °C feed temperatures, respectively. The power requirement increased linearly with feed concentration up to a point, called the deflection point, where the energy consumption started increasing almost exponentially. Deflection points at 55, 60, and 65 °C occurred when the outlet feed concentrations increased to 23, 25, and 27 wt.% (260, 290, 315 g/L), respectively. However, these authors did not mention the energy consumption of the system.

AGMD has also been investigated as a LiCl regenerator, Rattner et al. [89] modelled an AGMD and showed that higher feed temperatures increased both the *COP* and the moisture

[2] Arrows indicate the effect on the parameters; an arrow facing upwards (↑) or downwards (↓) means the parameter increases or decreases, respectively. The "~" indicates the parameter has small variations.

removal rate, in agreement with a previous study [88]. Moreover, higher feed flowrates increased the moisture removal rate while the *COP* formed an inverted U-shaped curve. The maximum *COP* of 0.372 was measured for a feed flowrate of 3 L/h which corresponds to a moisture removal rate of 3.5 L/(m^2 h). At a flowrate of 4.5 L/h, a *COP* of 0.362 and a moisture removal rate 5 L/(m^2 h) were achieved, meaning that the *COP* decreased as dehumidification improved. The *COP* also increased with lower feed concentration, with a *COP* of 0.56 being reported for a feed concentration of 23 wt.% (260 g/L). The base case study required 0.348 kW to operate with feed concentration of 38 wt.% (470 g/L), flowrate of 3 L/h, and temperature of 135 °C. The outputs for the base case were *COP* of 0.372, moisture removal rate of 3.45 L/(m^2 h), and outlet permeate concentration of 0.4 wt.% (4 g/L). This high feed temperature means the feed must be pressurised to avoid boiling.

Among the few MD studies for LDAC applications, the majority utilise VMD. Lefers et al. [90] tested VMD to reconcentrate $MgCl_2$. Experiments were executed with feed concentration varying from 15 to 35 wt.% (from 165 to 440 g/L), vacuum pressure from 0.025 to 0.1 bar, and feed flowrate from 0.71 to 1.12 L/h. Similarly to the previous study [88], higher fluxes were obtained with higher feed temperatures, which decreased as the feed concentration increased. Feed velocity had low influence on flux. Specifically, flowrates of 0.71, 0.92, and 1.12 L/h resulted in similar permeate fluxes at fixed feed concentration. In contrast, permeate flux was greatly influenced by the feed concentration. Feed concentrations of 20.7, 27.3, and 31.7 corresponded to permeate fluxes of 13, 9.7, and 7 L/(m^2 h), respectively. The study also found that higher permeate fluxes were achieved by applying more vacuum. At 26.8 wt.% (315 g/L) of $MgCl_2$ concentration, vacuum-side pressures of 0.025, 0.05, and 0.1 bar achieved permeate fluxes of 9.7, 7, and 1 L/(m^2 h), respectively.

Zhou et al. [91] also conducted studies regarding VMD in LDAC applications. The authors analysed the performance of VMD to reconcentrate LiCl. They found that feed outlet temperature and concentration increased linearly with feed temperature, as observed also from a previous study [88]. Feed temperatures of 50–100 °C corresponded to outlet temperatures, concentrations, and regeneration costs of 38–47 °C, 38.3–44.8 wt.% (475–580 g/L), and $40.5–99, respectively. Regarding the feed flowrate, increasing it from 3.6 to 111.6 L/h increased the feed outlet temperature from 23.2 to 59.3 °C and decreased the outlet concentration from 42 to 37.7 wt.% (535 to 470 g/L). When the LD inlet concentration increased from 30 to 40 wt.% (from 355 to 500 g/L), the outlet temperature increased from 33 to 47 °C and the outlet concentration from 33.3 to 42.3 wt.% (from 400 to 540 g/L). A drop in the LD concentration difference between inlet and outlet was expected when increasing the feed concentration because higher concentrations result in lower *ERH*, which is negative for the regeneration process. Vacuum pressure also affected the outlet feed concentration; by decreasing it from 0.1 to 0.01 bar, the outlet temperature and concentration varied from 61 to 36 °C and from 37.2 to 40.7 wt.% (460 to 515 g/L), respectively, in agreement with a previous study [90] stating that a higher regeneration performance is achieved at higher pressurisation.

Zhou et al. [92] continued their studies by investigating, theoretically and experimentally, LiCl regeneration via VMD. Two outlet concentrations of 20 and 30 wt.% (220 and 355 g/L) were investigated; with 30 wt.% requiring an additional 7 °C for the LD regeneration than 20 wt.%. Their findings showed that the feed temperature greatly affects the regeneration performance; with higher regeneration performance being achieved at higher regeneration temperatures [92]. Although the study was proposed for a LDAC system, it did not provide the energy requirements for the regeneration process.

In summary, MD can treat highly concentrated LD, but has high energy requirements. A way to decrease the energy consumption is through the feed temperature. Feed temperatures for all types of MD do not exceed 80 °C [66-72], but a theoretical study done by Davies and Zaragoza [93] suggests that feed temperature above 100 °C and more selective collectors could lead to a more effective multi-stage MD system for use in greenhouse cooling. Feed MD temperatures above 80 °C have not yet been experimentally investigated, highlighting potential for experimental studies. Table 2-3 summarises the selected studies showing important parameters necessary to compare results from different desalination technologies and to evaluate compatibility for greenhouse applications.

Table 2-3. Summary of selected MD studies for LDAC applications.

Study	Solute	Inlet concentration [wt.%] (g/L)	Outlet concentration [wt.%] (g/L)	Inlet molar fraction	Outlet molar fraction	*COP*	Experimental or Theoretical	Technology
[88]	LiCl	20 (220)	29 (340)	0.096	0.148		Both	DCMD
[89]	LiCl	38 (470)	40.5 (510)	0.207	0.224	0.37	Theoretical	AGMD
[90]	$MgCl_2$	31.7 (385)		0.081			Experimental	VMD
[91]	LiCl	40 (500)	42.3 (540)	0.221	0.238		Both	VMD
[92]	LiCl		20 (220) 30 (355)		0.096 0.154		Both	VMD

2.2 Reverse osmosis

RO is a pressure-driven membrane separation process employing membranes that allow water to permeate while rejecting dissolved substances. Water contained in the feed flows through the membrane due to an applied pressure [63], which must overcome the osmotic pressure difference between the brine and the permeate sides to achieve positive fluxes [94]. RO desalination removes most naturally occurring salts [74], which must be added back to produce potable and irrigation water, highlighting the necessity to include post-treatment for

RO applications. Moreover, RO membranes are sensitive and easily affected by particles, scaling, biofouling, and other foulants [95]. Therefore, pretreatment of the feed is necessary to prevent membrane fouling [74], which increases the lifespan of RO membranes and decreases the cost of the system [95]. These pre- and post- treatments hinder the use of RO in regeneration of hypersaline solutions. However, the main issue of hypersaline regeneration is due to the pressure limitations of RO membranes.

2.2.1 Pressure limitations

Typical applications of RO are in seawater desalination which require applied pressures of 50–80 bar for feed concentrations of around 35 g/L [63]. The applied pressure must not exceed the membrane burst pressure, typically around 70–80 bar [63]. This imposes an upper limit on the feed concentration which makes RO unsuitable for hypersaline desalination [63, 96]. Therefore, RO is efficient and economical for seawater treatment (typical concentration of 35 g/L) but it becomes less energy and cost efficient at concentrations above 45 g/L [97, 98].

Hypersaline solutions with concentrations above 70 g/L are usually desalinated through thermal processes [55], because the required applied pressure in hypersaline desalination exceeds the maximum operating pressure of conventional RO membranes. RO membranes could be employed for hypersaline desalination if able to operate at higher pressures. Few studies can be found employing high-pressure RO applications with maximum tested pressure of 200 bar [99, 100]. RO membranes with burst pressure above 80 bar can be found in the market [101]; for example, DuPont [102] and Pall corporation [103] have produced membranes with maximum operating pressure of 120 and 160 bar, respectively (Table 2-4).

High applied pressure may lead to either severe compaction (which results in loss of permeability due to the formation of an impermeable film) or rupture (which decreases the rejection of the membrane) [101]. Although, membranes are more likely to rupture above a certain pressure limit [101]. High applied pressures also deteriorate the membranes and negatively affect the membrane transport properties [80, 100, 104-106].

Table 2-4. Maximum operating pressures and temperatures of selected commercial RO membranes.

Company	Model	Maximum operating pressure [bar]	Maximum operating temperature [°C]	Product type
DuPont [102]	XUS180808	120	30	Spiral Wound
Pall corporation [103]	DTSE	75	40	Disc Tube
	DTSE-MP	90	40	Disc Tube
	DTGE	75	40	Disc Tube
	DTGE-MP	90	40	Disc Tube
	DTSE-HP	120	40	Disc Tube
	DTGE-HP	120	40	Disc Tube
	DTGE-HHP	160	40	Disc Tube
Dow [107]	TW30-1812	21	45	Spiral Wound
	TW30-4014	41	45	Spiral Wound
	TW30-4021	41	45	Spiral Wound
	SW30HR-380	69	45	Spiral Wound
Hydranautics [108]	SWC4 MAX	83	45	Spiral Wound
Toray [108]	TM820M	83	45	Spiral Wound

The RO rejection depends on the utilised membrane, but usually ranges from 98 to 99.5% [109]. The drawback of RO membranes is their low life cycles between 2 and 5 years [110]. The advantage of RO is that it requires the lowest energy among the membrane-based technologies for seawater and brackish water desalination [63, 96, 111]. Including pretreatment, the maximum energy consumption for seawater is 12 kWh_{el}/m^3, and 4 kWh_{el}/m^3 when employing an energy recovery device [112]. Typically, the SEC_{el} of RO is between 2.2 and 2.8 kWh_{el}/m^3 with a minimum theoretical SEC_{el} for seawater of 1.09 kWh_{el}/m^3, calculated

with feed containing 35 g/L of NaCl at 25 °C [112]. Pressure driven processes are able to approach this minimum achievable energy requirement, while thermally driven processes require much higher energy requirements due to the involvement of phase transition [87]. This occurs because water has a latent heat of evaporation of around 2.260 kJ/kg [113], meaning that 2.260 kJ of heat must be provided to vaporise one kilogram of water. Pressure driven membrane-based technologies, such as RO, can separate water from the feed without requiring this extensive heat, making RO more energy efficient compared to thermally driven desalination technologies. However, higher feed concentrations increase the energy requirements of conventional single-stage RO and thus hypersaline treatment is expected to be more energy intensive [111].

These considerations show that conventional RO applications are limited by the maximum operating pressure of the membranes. Different technologies have emerged to address this limitation, such as the osmotically assisted reverse osmosis (OARO) and the cascading osmotically mediated reverse osmosis (COMRO) processes as developed by Bartholomew et al. [94] and Chen et al. [114], respectively. However, these technologies face technological limitations. These limitations include requirement of loose spacers in both the feed and permeate channels to enhance the permeate flux, which weakens the structure of the membrane and may lead to severe deformation [73]. To avoid deformation, denser spacers should be employed, resulting in large parasitic pressure losses and high energy consumption [73]. Moreover, OARO and COMPRO are affected by concentration polarisation on both sides since both sides are in contact with a concentrated solution. As a result, osmotically mediated processes are affected by internal and external concentration polarisation (ICP and ECP) which hinders their performance [73].

The intensity of ICP is usually measured through the structure parameter of the support layer [115]. Although a low structure parameter results in more diffusion which decreases the ICP, it also results in less structural support which is required by the membrane [115]. Different options have been proposed to decrease the high ICP in forward osmosis membranes, such as fabrication of porous polyketone support membranes with low structure parameter and high pressure resistance [116], membrane chemical treatments [117], and system modifications like closure of the feed valve at regular intervals [115]. These options were investigated for forward osmosis membranes and similar approaches could be implemented also for RO membranes.

2.2.2 Reverse osmosis for water desalination

RO is not an efficient desalination technology for concentrations higher than 45 g/L [97, 98]. This limitation is correlated to the maximum operating pressure of conventional RO membranes, around 70–80 bar [63]. A study considering membranes with higher burst pressure was done by Davenport et al. [101] who investigated a high-pressure reverse osmosis (HPRO) to desalinate hypersaline brines. HPRO is defined as a RO process operating with hydraulic pressures higher than 100 bar, which implies the necessity of membranes with equally high operational pressure. The authors modelled a hybrid HPRO coupled with mechanical vapour compression, operated at 150 bar treating waste seawater with concentration of 70 g/L. The feed was concentrated to 250 g/L, achieving a r of 72% and a relatively high SEC_{el} of 12 kWh_{el}/m^3.

Different technologies have emerged to address the pressure limitation of RO membranes. Park et al. [118] developed a theoretical model for a draw solution assisted reverse osmosis (DSARO) process. During operation, seawater was the feed to the 1st RO stage while the draw

solution circulated on the permeate side of the 1st RO. The draw solution was then pressurised and pumped on the 2nd stage (this time as feed) and fresh water was produced on the permeate side of the 2nd stage.

The overall osmotic pressure difference was reduced by employing a draw solution having a concentration higher than pure water and lower than seawater. A compatible draw solution is NaCl, which was used in their study. To reach *r* of 40%, an applied pressure (ΔP) of 35 bar on the 1st stage and 30 bar on the 2nd stage were required. The energy efficiency of the DSARO process was lower compared to a conventional RO system, but DSARO could operate with lower pressures and in turn achieve lower installation and membrane replacement costs. The calculated specific cost to produce water with SDARO was 10% lower compared to a conventional RO process.

Another draw solution assisted process was proposed by Bartholomew et al. [94] who developed the OARO technology to desalinate highly concentrated brines using readily available membranes and equipment. A series of stages were used to gradually reduce the feed concentration until a conventional RO stage could be utilised, requiring relatively low pressure and low energy to produce clean water. NaCl was used as the draw solution, similarly to the previous study [118]. The system was composed of closed draw solution circuits between the stages, with decreasing draw solution concentration from circuit to circuit (going toward the RO stage). The draw solutions within each circuit were pressurised when the draw solution was employed to reject water and depressurised when the draw solution was employed to absorb water. For the process to be a RO application, the feed concentration must be higher than the draw solution concentration. This study also considered cases with feed concentrations lower than the draw solution, meaning the system operated as a pressure-assisted forward osmosis process. The cases with draw solution concentration up to 125 g/L

are OARO processes, while the cases with higher draw solution concentration should be called pressure-assisted forward osmosis, which is not mentioned by the authors.

The case having a draw solution with zero concentration (conventional RO application) and feed concentration of 35 g/L had a *r* of 54%, in agreement with the expected performance of conventional RO. However, the *r* dropped to 4% when the feed concentration increased to 75 g/L, showing the necessity of a saline draw solution when treating hypersaline feeds. With feed and first stage draw solution concentrations of 145 and 200 g/L, respectively, the *r* was higher than 30%. When considering a feed with concentration of 125 g/L, increasing the 1st stage draw solution concentration from 100 to 225 g/L increased the *r* from 17 to 42%, the number of modules from 3 to 7, and the energy consumption from 5.7 to 14 kWh_{el}/m^3. A higher 1st stage draw solution concentration required more stages to sufficiently dilute the feed of the final RO stage. More stages required more energy while maintaining the same number of stages would result in higher feed concentration in the last RO stage, making permeate production more energy intensive. The estimated *r* ranged between 35 and 50% and the energy consumption between 6 and 19 kWh_{el}/m^3 when employing a draw solution with concentration between 100 and 140 g/L.

Another multi-stage process was proposed by Chen et al. [114] who developed the COMRO technology. To desalinate a hypersaline feed of 70 g/L, COMRO could operate with a pressure of 68 bar, compared to 137 bar required by a conventional RO process. The feed was diluted through a series of bilateral counter-current (BCC) reverse osmosis stages before passing through a final conventional RO stage. The diluted feed from the BCC stages was pressurised by a high-pressure pump before being directed to the final RO stage. The brine from the conventional RO stage remained pressurised in the BCC stages via booster pumps (one on every stage). The brine effluent became more concentrated while it absorbed water

from the saline feed. The effluent hypersaline brine was depressurised through an energy recovery device prior post-treatment to improve the energy performance of the system.

To treat a hypersaline feed with concentration of 70 g/L and *r* of 50%, a conventional RO stage would require 3.79 kWh_{el}/m^3. Using COMPRO, this energy decreases to 3.79, 3.35, 3.22, and 3.16 kWh_{el}/m^3 for one, two, three, and four BCC stages, respectively. COMRO at a recovery of 70% required 2.11 kWh_{el}/m^3, which is 33% less compared to a conventional RO process. COMRO could also be used for higher feed concentrations, 2-stage COMRO at a *r* of 20% could operate with a feed concentration up to 150 g/L, but the authors did not provide the energy consumption for this case. Membranes with lower salt selectivity could be employed in the BCC stages because the water passing through the BCC stages was not the final freshwater product, meaning membrane cost could be lower compared to conventional RO systems.

In summary, RO used for brackish water desalination with feed concentrations ranging from 0.1 to 10 g/L [110] has an average SEC_{el} of 2–6 kWh_{el}/m^3 [119]. For seawater desalination, RO has an average SEC_{el} of 4–8 kWh_{el}/m^3 [120]. Davenport et al. [101] study was expected to be more energy intensive compared to conventional RO due to the high applied pressure. The maximum operating temperatures of high-pressure RO membranes between 30 [102] and 40 °C [103] means these applications are unsuitable, especially the first one, for greenhouse applications in hot climates. The most energy-intensive process is OARO having a SEC_{el} of 19.3 kWh_{el}/m^3 (with feed concentration of 140 g/L and *r* of 50% [94]), while the least energy-intensive process is COMRO having a SEC_{el} of 3.16 kWh_{el}/m^3 (with feed concentration of 70 g/L and *r* of 50% [114]). Among the selected studies, COMRO seems the most promising process for greenhouse applications, especially for the possibility to work with high concentration and low *r*. However, COMPRO is expected to be affected by

concentration polarisation on both feed and the permeate sides, which would reduce the permeate flux and deform the membranes [73]. Therefore, experimental validation of COMPRO practicality is required.

Table 2-5 summarises the selected studies in RO for water desalination considering important parameters, necessary to compare results from different desalination technologies and to evaluate compatibility for greenhouse applications.

Table 2-5. Summary of selected RO studies for desalination applications.

Study	Solute	Concentration [g/L] (wt.%)	Molar fraction	SEC_{el} [kWh_{el}/m^3]	Recovery [%]	Experimental or Theoretical
[101]	NaCl	70 (6.75)	0.040	12	72	Theoretical
[118]	NaCl	30 (3)	0.009	3.25	40	Theoretical
[94]	NaCl	140 (13)	0.044	6–19	35–80	Theoretical
[114]	NaCl	150 (13.9)	0.047		20	Theoretical

The main parameters affecting RO performance for water desalination are applied pressure (ΔP), number of stages (N_{stages}), feed concentration (C_{in}), and DS concentration (DS_{conc}). The effects of these parameters on the required applied pressure (ΔPr), Power requirement (*Power*), and recovery (r) summarised in Table 2-6.

Table 2-6. Main parameters affecting RO performance in desalination applications based on the selected studies[3]

Operating parameter	ΔPr	*Power*	*r*
↑ ΔP		↑ [101]	
↑ N_{stages}	↓ [118]	↓ [114]	
↑ C_{in}			↓ [94]
↑ DS_{conc}		↑ [94]	↑ [94]

2.2.3 Reverse osmosis for liquid desiccant regeneration

Only one study can be found employing RO for desiccant regeneration in LDAC systems. Al-Sulaiman et al. [121] modelled a 2-stage evaporative cooling system using RO for $CaCl_2$ regeneration. The external conditions were fixed at 40 °C and relative humidity (*RH*) of 60% with target inlet conditions of 26 °C and *RH* of 57%. A RO process was utilised to reconcentrate the desiccant at 45 wt.% (590 g/L). During the regeneration, the LD temperature increased to 40 °C and needed to be cooled to 30 °C before being directed to the dehumidification stage. The RO process operated with a *r* of 3%, corresponding to 56.3 L/h of water production. Two evaporative coolers were required which consumed 26.8 L/h of water. This water requirement was provided by the permeate of the RO regenerator. The authors also reported a *COP* of 1.2 for the base case study. They also reported an osmotic pressure difference across the membrane of 244 bar, meaning the system cannot exist in practice since commercially available membranes can only withstand pressures of 160 bar [103]. The 244 bar may be a miscalculation since the osmotic pressure difference should be higher than 1500 bar based on Gibbs energy.

In summary, RO cannot operate in LDAC applications because the high LD concentration, required for the dehumidification process, increases the osmotic pressure difference to values

[3] Arrows indicate the effect on the parameters; an arrow facing upwards (↑) or downwards (↓) means the parameter increases or decreases, respectively.

higher than the maximum burst pressure of commercial RO membranes. Table 2-7 summarises the study of Al-Sulaiman et al. [121] by presenting key parameters for the comparison of the technologies.

Table 2-7. Summary of the key parameters from the selected RO study [139] for a LDAC application.

Study	Solute	Inlet concentration [wt.%] (g/L)	Outlet concentration [wt.%] (g/L)	Inlet molar fraction	Outlet molar fraction	*COP*	Experimental or Theoretical
[121]	$CaCl_2$	44 (575)	45 (590)	0.113	0.117	1.2	Theoretical

Another promising approach for hypersaline LD regeneration based on RO is the utilisation of low-salt-rejection reverse osmosis membranes; such membranes include end-of-life RO membranes and nanofiltration membranes.

2.3 Nanofiltration

NF is a pressure-driven membrane separation process with higher rejection compared to ultrafiltration, but lower compared to RO [122]. NF membranes remove turbidity, micro-organisms, hardness, and a fraction of dissolved salts [123]. NF membranes are distinguished for their low rejection of monovalent ions (around 10–50%) and high rejection of divalent ions (above 50%) [124-129]. The low rejection allows NF to operate at lower operating pressures and achieve higher *COP*, compared to RO. Other advantages are relatively low investment, operation and maintenance costs [123].

Interfacial polymerisation, nanoparticles incorporation, and UV treatment have improved NF by increasing rejection and decreasing fouling [130]. NF has mainly received attention to treat feeds with low concentrations, such as brackish water [131]. Aside from seawater and

wastewater desalination treatment, NF has been employed for applications related to biotechnology, food and pharmaceutical industries [130].

2.3.1 Nanofiltration for water desalination

Theoretical studies have been proposed employing NF membranes in multi-stage systems. Altaee and Sharif [132] compared a dual-stage NF seawater desalination plant with a NF-brackish water RO process. The electric specific power consumption (SEC_{el}) to treat a feed with a concentration of 43 g/L was 4.58, 4.2, and 3.86 kWh_{el}/m^3 for conventional RO, NF-NF, and NF-brackish water RO, respectively. NF-NF at feed of43 g/L achieved a permeate concentration of 0.359 g/L and *r* of 22%. When operating with feed of 35 g/L, NF-NF operated with pressures of 28–35 bar on the 1st stage and 14–21 bar on the 2nd stage, achieving a *r* of 30%, permeate concentration of 0.254 g/L, and SEC_{el} of 3.35 kWh_{el}/m^3. The results showed that the employment of highly concentrated feeds reduced the *r* due to the increased osmotic pressure. To increase *r*, the operating pressure should increase up to the maximum operating limit.

Moreover, Wang et al. [73] modelled an N-stage made of low-salt-rejection RO stages, i.e., "loose" RO or NF stages. The maximum output concentration depended on the maximum operating pressure of the stages. With only one RO stage, seawater was concentrated from 35 to 82 g/L, considering a maximum operating pressure of 70 bar. It was possible to further increase the feed concentration by connecting more stages. The connections were done by recirculating and mixing the produced permeate of a stage with the input of the previous stage. Therefore, seawater was concentrated from 35 to 233 g/L by employing a first RO membrane, with 100% rejection, followed by three NF stages having rejection of 46, 29, and 16%. To concentrate the feed to a certain concentration, the SEC_{el} decreased by employing

more stages. Specifically, to concentrate seawater from 60 to 233 g/L, the SEC_{el} decreases from 15.7 to 8 kWh_{el}/m^3 by employing a 3-stage and a 4-stage system, respectively. This configuration allows the system to concentrate low concentrations feeds up to highly concentrated brines, but it is impractical for highly concentrated feed, required for LDAC applications. To overcome this limitation, the system must be modified to re-circulate the concentrated brines instead of the permeates and by inverting the stages so that RO is the last stage.

Regarding NF investigation of single membranes, Hilal et al. [133] investigated three commercial nanofiltration membranes, namely NF90, NF270, N30F, to treat feed with NaCl concentration up to 25 g/L. The Spiegler-Kedem model was used to validate the experimental results, which were in good agreement for the NF90 and the NF270 membranes for all NaCl concentrations. However, it did not fit well with the results of the N30F membrane, especially for flux below 10 L/(m^2 h). The authors correlated this high error with the low rejection of the N30F membrane and suggested using the Donnan steric-pore model for low rejections membranes. The experiments were carried out with applied pressures of 2–9 bar and NaCl concentration of 5–25 g/L. When operating with NaCl concentration of 5 g/L and 9 bar, the NF90 membrane achieved a rejection of 95%, which dropped to 41% when operating at NaCl concentration of 25 g/L and 9 bar. For NaCl concentration of 5–25 g/L, the rejections of the NF270 and the N30F membranes were 11–29% and 3–6%, respectively. Although the NF270 membrane operated at lower rejection compared to NF90, NF270 achieved permeate flux between 20 and 100 L/(m^2 h), higher than those of NF90 between 5 and 40 L/(m^2 h). The authors did not mention the economic or energetic performance of the system.

Regarding NF used in desalination plants, Eriksson et al. [134] reported results from a RO plant at Umm Lajj, Saudi Arabia coupled with NF membranes. The NF pretreatment reduced

total hardness from 7.5 to 0.22 g/L and feed concentration entering the RO plant from 45.5 to 28.2 g/L. The stand-alone RO plant operated at 65 bar with a recovery of 30%. With the NF integration, an overall *r* of 36.4% was achieved. Specifically, the NF unit operated with a *r* of 65% and operating pressure of 25 bar while the RO plant with a *r* of 56% and operating pressure of 54 bar. The study provided some basic economic calculations but did not mention the energy requirement of the system.

In summary, the pressure limitation of RO can be mitigated by combining RO with multiple NF stages. RO typically has rejection near 100% while NF in the range of 10–50% [124-126, 128, 129]. Thus, the total osmotic pressure difference can be "divided" among the NF stages, resulting in lower required pressure in each NF stage. More stages result in lower required applied pressures and lower energy requirements. Table 2-8 summarises the selected studies in NF for water desalination considering important parameters, necessary to compare results from different desalination technologies and to evaluate compatibility for greenhouse applications.

Table 2-8. Summary of selected NF studies for desalination applications.

Study	Solute	Concentration [g/L] (wt.%)	Molar fraction	SEC_{el} [kWh_{el}/m^3]	Recovery [%]	Experimental or Theoretical
[133]	NaCl	25 (2.5)	0.0077			Both
[134]	NaCl	45.5 (4.45)	0.0141		36.4	Experimental
[132]	NaCl	43 (4.25)	0.0133	4.2	22	Theoretical
[73]	NaCl	60 (1)	0.0181	7.98	47	Theoretical

The main parameters affecting NF performance for water desalination are the number of stages (N_{stages}) and the feed concentration (C_{in}). The effects of these parameters on the rejection (*R*), power requirement (*Power*), and recovery (*r*) are summarised in Table 2-9.

Table 2-9. Main parameters affecting NF performance in desalination applications based on the selected studies[4]

Operating parameter	*R*	*Power*	*r*
↑ N_{stages}		↓ [73]	
↑ C_{in}	↓ [133]	↑ [132]	↓ [132]

2.4 Forward osmosis

FO studies have recently increased in number, because of the potential to operate at higher feed concentration than conventional RO with low energy requirements [135-137]. Instead of using electric energy, FO exploits the natural osmotic process to draw water through a semipermeable membrane from a concentrated feed to a more concentrated solution, which is referred to as the draw solution (DS) [138]. During water permeation, the DS gets diluted as it absorbs water, meaning another separation process is required to reconcentrate the DS (see Figure 2-2) [139]. This additional process negatively affects the overall cost and increases the system energy demand. Consequently, the "low energy requirement" may only be suitable for those applications where further pretreatment or post-treatment is not required for the DS [140]. Common DS for FO are $MgCl_2$, $MgSO_4$, NaCl, KCl, $KHCO_3$, $Ca(NO_3)_2$, and NH_4HCO_3 [141, 142]. Since the concentration difference between feed and DS is the driving force of FO [143], high DS concentration is required to obtain high permeate fluxes when the feed concentration is also high. However, high DS concentration leads to a high energy consumption for the DS regeneration [62] making current FO technology unsuitable for self-sustained greenhouse applications.

[4] Arrows indicate the effect on the parameters; an arrow facing upwards (↑) or downwards (↓) means the parameter increases or decreases, respectively.

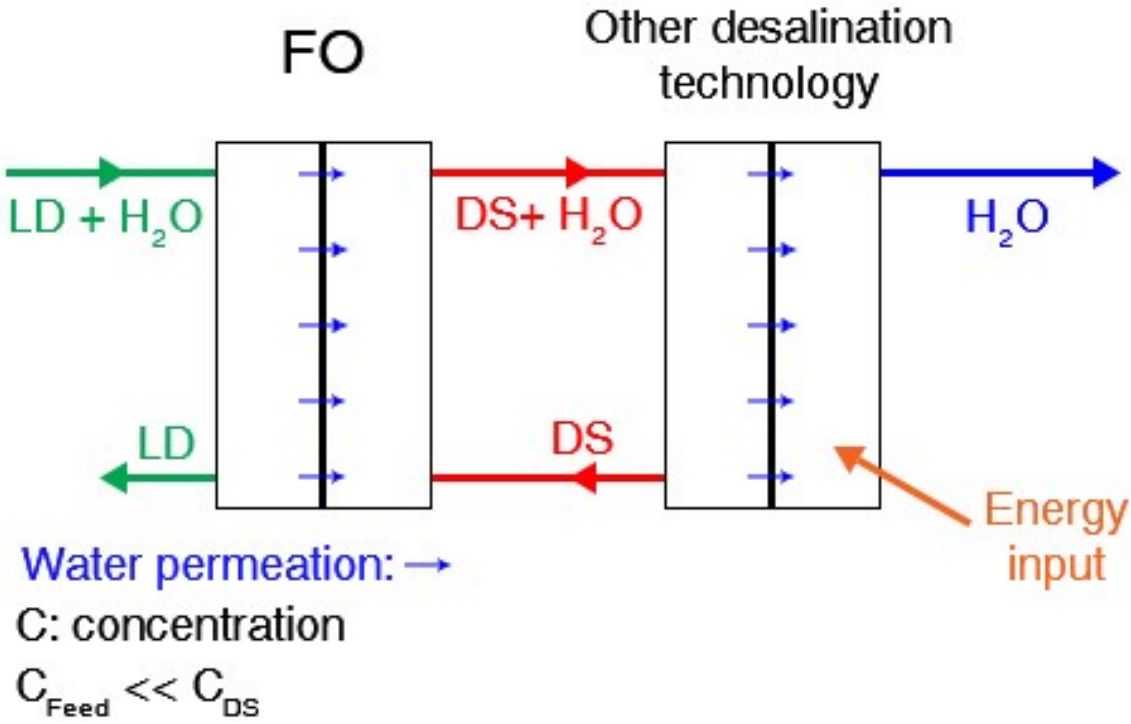

Figure 2-2. Schematic representation of a forward osmosis (FO) system for liquid desiccant (LD) regeneration. "Feed" stands for feed and "DS" for draw solution.

FO has been employed for industrial waste treatment [144], food industry [145], bioreactor membrane [146], concentration of digested biomasses [147], dilution of fertilisers [148, 149], food and beverage concentration [144], and pharmaceutical products [144]. FO has also been employed for energy production by exploiting the osmotic pressure difference between seawater and freshwater [150]. Theoretically, FO could also be used to reconcentrate LD solutions [18] but experimental studies are required to validate the theory.

FO technology suffers from technological limitations, such as lack of suitable membranes [151]. Commercial RO membranes were proven not to be suitable for FO processes due to internal concentration polarisation (ICP) decreasing the efficiency [138, 152, 153]. FO is severely affected by ICP which lowers the permeate flux compared to the expected values [135, 154-157]. High DS flowrate is required to minimise ICP, but high DS flowrate increases

pressure drop [158]. ICP may be mitigated by a more open membrane substrate structure, but this also tends to reduce the allowable transmembrane pressure to avoid crushing the membrane. In addition to ICP, other parameters affecting the efficiency of the system are external concentration polarisation (ECP), scaling, hardness, and solid materials existing in the feed [154]. Moreover, reverse salt flux decreases the osmotic pressure difference across the membrane [159], and in turn the *r*. The *r* is also limited by the DS concentration and large amounts of DS are required to achieve high *r* [160]. Other limitations are related to the mass transfer which is more negatively affected in FO membranes compared to other types of membranes [161]. Additionally, reverse solute flux (going from the permeate to the feed side) is an Important limitation in FO [162-164].

Pressure-assisted forward osmosis (PAFO) is an advanced FO technology aiming to overcome the limitations of conventional FO. By applying pressure to the feed, PAFO aims to increase water permeation through the membrane using a less concentrated DS [144]. The permeate flux increases because it is driven by the combination of osmotic and hydraulic forces [154]. PAFO can either decrease the required membrane surface area or reduce the membrane cost, compared to conventional FO [165, 166]. However, the applied pressure increases fouling and energy consumption [167]. PAFO membranes must be more robust, compared to FO, to resist compaction due to the applied pressure. However, increasing the membrane support layer thickness also increases the ICP which in turn decreases the permeate flux, thereby contrasting the aim of PAFO to increase the permeate flux.

Fouling has been found to be less severe in FO compared to PAFO, due to the absence of external pressure, resulting in a less resistant fouling layer formed under the only effect of osmotic pressure [168]. This layer can be partially removed through simple physical cleaning [168-171]. In PAFO, a more resistant fouling layer is formed due to the applied pressure

[168]. The membranes deteriorate under higher applied pressure which shortens their replacement cycle, decreases water production, and increases the overall cost [172].

2.4.1 Forward osmosis for water desalination

Few studies can be found in the literature investigating high salinity FO or PAFO applications. The selected studies have feed concentrations above 2 g/L. Lee et al. [167] investigated an intermittent pressure-assisted forward osmosis (I-PAFO) operation for organic fouling mitigation. I-PAFO was compared to both FO and PAFO in terms of permeate flux, *r*, fouling propensity, energy consumption, and required membrane area. The feed contained 2 g/L of NaCl, the foulant contained 0.25 g/L of sodium alginate, and the DS contained 35 g/L of NaCl. Consecutive batch tests were carried out with physical cleaning in between them. The utilised membrane, namely CSM FO-8040, was fabricated by Toray Chemical Korea Inc. The results showed that FO and PAFO had similar permeate fluxes at the end of every batch test, around 15 L/(m^2 h), while I-PAFO around 20.8 L/(m^2 h). After scaling was formed, permeate fluxes declined to 50% and 30% of their nominal values for FO and both PAFO technologies, respectively. These results agree with a previous study [168] stating that FO is less affected by fouling than PAFO. During PAFO operation, the *r* returned to approximately 60% of the initial value after the first physical cleanings and to 50% after consecutive physical cleanings. During I-PAFO operation, the *r* returned to approximately 75% for all batch tests. I-PAFO displayed benefits in terms of reducing membrane area requirements compared to PAFO. The energy consumption of FO was zero, I-PAFO around 0.03 kWh_{el} for all batch tests while PAFO consumed 0.05, 0.06, and 0.07 kWh_{el} at the 1st, 2nd, and 3rd batch test, respectively. The energy consumption was provided by the authors in [kWh_{el}] without

being correlated to the permeate volume, making it impossible to compare their SEC_{el} with those of other studies.

More investigations on PAFO was performed by Yun et al. [173] who investigated a PAFO process working with synthetic seawater feed with concentration of 35 g/L, $MgCl_2$ as DS, and sodium alginate and humic acid as foulants. FO-RO and PAFO performances were analysed using a theoretical model incorporating internal and external concentration polarisation. The membranes were created in a laboratory (not commercially available). A pure water permeability of 0.61 L/(m^2 h bar) was reported with a ΔP of 13 bar. PAFO achieved permeate fluxes of 4–8 L/(m^2 h) for ΔP of 0–9 bar, which was higher compared to FO-RO. These results indicate that the combined effect of the hydraulic and osmotic pressures in PAFO can substantially increase the flux. The authors also stated that the hydraulic pressure does not affect fouling in short term FO operations, adding that further investigations for long-term operations are required to evaluate the fouling effect of hydraulic pressure on FO membrane.

FO has also been investigated for natural gas extraction operations by McGinnis et al. [62] who experimentally investigated FO combined with a membrane brine concentrator to produce water from extraction of natural gas. The system operated with average feed concentration of 73±4.2 g/L, average NH_3/CO_2 (used as the DS) concentration of 97.9±4.3 g/L, and average $CaCO_3$ (used as hardness) concentration of 17±3 g/L. The system produced an average brine concentration of 180±19 g/L and average permeate concentration of 0.3±0.115 g/L. The brine from the system was directed to a brine stripper, which removed the DS that was introduced in the feed due to reverse salt flux. During a 100-hour period, no DS was added to the system, showing absence of DS leakage. The permeate from the system was directed to a conventional RO unit to produce water with a concentration lower than 0.5 g/L.

The system operated with an average permeate flux of 2.6±0.12 L/(m^2 h) and *r* of 64±2.2%. The SEC_{th} was 275±12 kWh_{th}/m^3 (including the distillation columns and the brine stripper) while the pilot system required an additional electric energy of 8.5 kWh_{el}/m^3 to power up the primary and supporting processes. For a similarly configured conventional evaporative brine concentrator, the authors state that a SEC_{th} of 633 kWh_{th}/m^3 would be required, meaning 2.3 times higher than the energy consumption of FO combined with a membrane brine concentrator.

In summary, FO is suitable as a pretreatment method for other desalination technologies [140], but not suitable for greenhouse applications which require highly concentrated solutions. With higher feed concentration at a fixed DS concentration, a higher applied pressure is required during the PAFO process, which increases concentration polarisation and fouling [173]. McGinnis study [62], which treated highly concentrated feed, had extremely high energy requirements. FO technologies could be viable only if a high thermal waste energy source is freely provided from a plant whose wastewater requires treatment [62], but this is not the case for greenhouse applications. Table 2-10 summarises the selected studies in FO for water desalination considering important parameters, necessary to compare results from different desalination technologies and to evaluate compatibility for greenhouse applications.

Table 2-10. Summary of selected FO studies for desalination applications.

Study	Solute	Concentration [g/L] (wt.%)	Molar fraction	*SEC* [kWh/m^3]	Energy input	Experimental or Theoretical
[167]	NaCl	2.29 (0.5)	0.001		Electrical	Experimental
[173]	NaCl	35 (3.44)	0.011		Electrical	Both
[62]	Natural gas extraction waste	73±4.2		275±12 8.5	Thermal Electrical	Experimental

2.5 Thermoresponsive draw solutions

The main limitation of FO/PAFO desalination is the high energy required to reconcentrate the DS [174]. Conventional inorganic (like NaCl, $MgCl_2$, $CaCl_2$, $NaHCO_3$, KBr, K_2SO_4, and NH_4HCO_3) [65, 141] and organic salts (like hydroacid complexes and zwitterions) [65, 175, 176] achieve high permeate fluxes but are energy intensive to reconcentrate [65]. Moreover, they exhibit high inverse salt fluxes, which negatively affects the permeate quality and increases the membrane replenishment cost [141, 160].

To overcome the limitations of FO/PAFO, TR solutions employed as DS have emerged as a new technology due to their unique response to temperature. TR solutions are characterised by their lower and upper critical solution temperature (LCST and UCST) [177]. LCST is defined as the temperature where the solution transmittance is below 5% [178]. Water rejection is observed for a TR solution when the temperature is higher/lower than the UCST/LCST (meaning that the TR solution has low *ERH*). Outside the absorption range, the TR solution absorbs water (meaning that the TR solution has high *ERH*). The following paragraphs discuss only LCST because few studies can be found regarding UCST.

During heating, chemical chains become insoluble in water due to hydrophilic/hydrophobic transition [179]. Therefore, water is recovered by heating the diluted TR solution above its LCST [180]. The LCST can be controlled by modifying the chemical structure of the solution and thus, the energy consumption to reconcentrate the DS can decrease by choosing low LCST [181]. TR solutions have attracted attention due to DS regeneration by renewable sources, such as solar thermal energy [182].

Several studies [153, 180, 183-188] agree that the ideal DS should meet six requirements: 1) high osmotic pressure below LCST to achieve high permeate flux, 2) low energy requirement to reconcentrate the DS, 3) low membrane diffusivity to minimise reverse salt

flux and in turn decrease the replenishment costs, 4) ability to maintain its properties over time, 5) low viscosity to decrease ICP, and 6) to be environmentally safe and non-toxic. High osmotic pressures can be achieved by using TR solutions with high solubility and low relative molecular mass [188]. Higher viscosity increases the pressure loss in the membrane module, therefore, TR applications require low viscosity [186]. Researchers have developed different TR solutions based on the above criteria, namely ionic liquids (ILs) [189, 190], hydrogels [191], magnetic nanoparticles [192-194], TR materials [190, 194-196], linear polyelectrolytes [197-200], and branched polymers [201, 202].

Organic Ils characteristics include high ionic conductivity [65, 203, 204], low vapour pressure [65, 190], and high thermal stability [65, 190, 203]. These highlight the potential for Ils to be employed as DS. Ils generate high osmotic pressures with low reverse salt fluxes due to their moderate molecular sizes [203, 204]. Ils have the drawback that they are hard to reconcentrate [205]. For this reason, Ils such as $[P_{4444}]$DMBS, $[P_{4444}]$TMBS, and $[P_{4448}]$Br have been developed to overcome the regeneration limitation [205], but findings are in preliminary stages despite their potential [65].

Stimuli-responsive hydrogels have also been proposed for low energy desalination applications [206-208]. Hydrogels are polymers able to swell and shrink reversibly when stimulated; the stimuli can be temperature, pH, magnetic force, ions concentration, or light [142]. As temperature increases above the LCST, hydrogels shrink significantly [209] and release up to 70% of the absorbed water [142]. Although stimuli-responsive hydrogels have low reverse salt fluxes, the *r* is lower compared to other types of TR solutions, which could be caused due to inefficient membrane contact [210, 211]. Furthermore, hydrogels form a dense skin during heating which further decreases the *r* [212]. Composite hydrogels incorporated with inorganic nanoparticles have been developed to improve the hydrogel performance [142,

213, 214]. These composite hydrogels achieved high permeate fluxes and high *r*, but water is mostly recovered as vapour [142], meaning an additional condensation unit is required to reconcentrate the hydrogels, thereby increasing the overall cost of the system.

Further developments on hydrogels shifted interest towards microgels. TR microgels have shown improved permeate flux, *r*, and permeate flux compared to hydrogels [174]. TR microgels achieve improved membrane contact and increased performance due to their small sizes and large surface area [185]. TR copolymer microgels of N-iso-propylacrylamide and acrylic acid have been developed to overcome limitations of TR hydrogels, with acrylic acid improving both permeate flux and regeneration performance [142, 185]. Although microgels showed improvements regarding permeate flux, their weak swelling kinetic negatively affects the overall performance of the process [174]. Therefore, further studies are required to improve the TR microgels swelling kinetic and to achieve high permeate fluxes [174]. Microgels can also be stimulated using gases [215]. Gas-responsive microgels have been investigated as DS for FO applications due to their advantage to absorb and reject water at room temperature [215]. This decreases the energy requirements, compared to TR solutions, and leads to a more energy efficient regeneration.

Moreover, TR magnetic nanoparticles (MNPs) have been studied to produce water from brackish water or seawater [194]. MNPs can be efficiently reconcentrated via heat-facilitated magnetic separation at relatively low energy expenses [216-222] with high *r* [194]. Small MNPs with high specific surface area can absorb water more efficiently, but smaller MNPs (dimension <15 nm) are hard to capture using a magnetic separator [218]. To efficiently capture small MNPs, the small MNPs must aggregate to form “bigger” MNPs [194]. Reversible aggregation can be achieved by temperature-sensitive polymer functionalization [219, 223].

TR polyelectrolyte DS have also been investigated as they absorb high quantities of water from seawater at high temperatures [219, 223, 224]. These polyelectrolytes have high relative molecular masses and achieve low reverse salt fluxes when reconcentrated by ultrafiltration or MD [225].

Other TR solutions include polyalkylene glycols [186]. Different polyalkylene glycols have been investigated as TR, such as polypropylene glycol (PPG400), di(ethylene glycol) n-hexyl ether, di(propylene glycol) n-propyl ether, propylene glycol n-butyl ether, and ethylene oxide-propylene oxide copolymer [196, 226, 227].

Based on their properties, TR solutions have potential for LD regeneration due to their ability to rapidly change their *ERH* and the possibility to reach an *ERH* close to zero [39]. By changing their *ERH*, TR solutions work with high *COP* during both dehumidification and regeneration processes. Gas-responsive microgels also have potential due to the possibility to reconcentrate the LD at room temperature [215], removing the energy cost required to heat/cool the TR solution. However, thermo- and gas- responsive investigations are in a preliminary stage and more research is required in LDAC applications.

2.5.1 Thermoresponsive solutions for water desalination

The majority of TR studies are still in a preliminary stage with most researchers utilising distilled water as the feed [65]. Some studies with higher concentration can be found, with concentrations up to 45 g/L. Zhao et al. [194] experimentally investigated a multifunctional Fe_3O_4 MNPs grafted with copolymer poly(sodium styrene-4-sulfonate)-co-poly(N-isopropylacrylamide) (PSSS-PNIPAM) used as the DS. This copolymer combines a poly(sodium styrene-4-sulfonate) (PSSS) polyelectrolyte that provides high osmotic pressure with a TR co-poly(N-isopropylacrylamide)(PNIPAM) that facilitates DS regeneration via

particle aggregation at temperatures above its LCST. Two MNPs sizes of 4.9 and 9.4 nm were investigated, namely MNP5 and MNP9, respectively. The MNPs were subsequently functionalized with PSSS-PNIPAM copolymers to create the MNP5-15SN and MNP9-15SN TR solutions. The chemicals and solvents were purchased from Sigma-Aldrich Japan Co. (Tokyo, Japan). The MNP5-15SN solution achieved a higher osmotic pressure compared to the MNP9-15SN. When using a feed with a concentration of 35 g/L, permeate fluxes of 1.7 and 3.7 L/(m^2 h) were measured using the MNP9-15SN and MNP5-15SN, respectively. The study did not mention their energy consumption.

Zhao et al. [178] continued their TR studies on poly(sodium styrene-4-sulfonate-co-n-isopropylacrylamide) (PSSS-PNIPAM) employed as DS combined with a lab-scale setup of a multi-bore PVDF hollow fibre MD to reconcentrate the DS. Four PSSS-PNIPAM copolymers were prepared with SSS contents of 5, 10, 15, and 20 wt.%, namely 5SN, 10SN, 15SN, and 20SN, respectively. It was found that PSSS-PNIPAM copolymer with SSS content higher than 20 wt.% could not be used as a DS. PSSS-PNIPAM with 15 wt.% of SSS exhibited the best performance among the investigated SSS contents.

Inada et al. [180] developed a series of glycerol-oligo(ethylene oxide)-block-oligo(butylene oxide) (GEB) to utilise as the DS. The average degrees of polymerisation of ethylene oxide (m) and butylene oxide (n) units of GE_mB_n were varied to control the hydrophilic/hydrophobic molecule balance and in turn regulate the LCST. The materials were purchased from Sigma-Aldrich Japan Co. (Tokyo, Japan). Two values of 7 and 9 for "m" were considered; GE_7B_n and GE_9B_n exceeded seawater osmotic pressure at concentrations of 50–70 wt.% (0.48–1.51 mol/kg and 0.44–1.3 mol/kg for GE_7B_n and GE_9B_n, respectively). An osmotic pressure of 74 bar was reached with GE_7B_3 having a concentration of 68 wt.% (which was the highest among the tested solutions). GE_7B_3 had the lowest viscosity among the

solutions. When heated at 60 °C, GE_7B_3 concentration and osmotic pressure decreased to 6.9 wt.% (0.044 mol/kg) and 2 bar, respectively. The experiments were conducted with seawater as the feed for two operational modes, namely AL-FS (active layer facing feed solution) and AL-DS (active layer facing DS). Permeate fluxes of 1.56 and 4.81 L/(m^2 h) were reported for GE_7B_3 operating with AL-FS and AL-DS, respectively. AL-DS was expected to perform better compared to AL-FS during FO due to less ICP effect.

The permeate flux and inverse salt flux of GE_7B_3 were compared to NaCl, PPG400, PEG1540, and $[P_{4444}][TMBS]$. The results showed higher permeate fluxes for NaCl, PPG400, and PEG1540 compared to GE_7B_3 while the reverse salt flux of GE_7B_3 was the lowest among the solutions. Even though GE_7B_3 was chosen based on its low viscosity, GE_7B_3 viscosity of 56 mPa-s was the highest among the investigated solutions. The membrane performance, defined as the ratio between inverse salt and permeate fluxes (higher performance is achieved for lower ratio values), was measured for all DS. AL-DS GE_7B_3 ratio of 0.28 g/L was higher than NaCl of 0.2 g/L, meaning that NaCl as a DS was more efficient. Moreover, GE_7B_3 has a relative molecular mass of 1660 g/mol, which contradicts the criteria of low molecular mass to produce high osmotic pressure. Finally, the energy consumption of the system was not mentioned.

Ahmed et al. [226] investigated the technical feasibility of a FO desalination pilot scale integrated with a TR ethylene oxide-propylene oxide copolymer (TL-1150-1) as a DS to produce 10 m^3/day of pure water. The utilised spiral wound hollow-fibre FO membranes, with effective membrane area of 336 m^2, were purchased from Toyobo (Japan) while the DS was developed from Trevi systems Inc. (USA) with a LCST of 85 °C. The relative molecular mass and LCST of the DS were chosen to decrease inverse salt flux. The DS was heated above the LCST to produce water and to reconcentrate the DS. The DS was then cooled to 40 °C before

returning to the FO membrane. During experiments, the feed was taken directly from the sea with an average concentration of 35.8 g/L. The *r* was measured for a feed flowrate of 961 L/h and a DS flowrate ranging from 486 to 1087 L/h. The highest *r* of 31.2% was achieved with a DS flowrate of 727 L/h. The reliability of the FO pilot plant was proved over 30 days continuous operation without observing any severe fouling. The plant included NF post-treatment to produce permeate based on the WHO standards (concentration less than 0.5 g/L). A permeate concentration of 0.14 g/L and *r* of 30% were reported, meaning the system operated with a permeate flux of 0.37 L/(m^2 h). The SEC_{el} was between 35 and 40 kWh_{el}/m^3 while the remaining components required an additional 2.4 kWh_{el}/m^3. Like the previous study [180], a DS with high relative molecular mass and high LCST was selected to decrease the inverse permeate flux.

Zeweldi et al. [65] investigated a monomeric TR ILs, namely $[N_{4444}]$2,4,6-$MeBnSO_3$ with LCST, relative molecular mass, density, and van 't Hoff factor of 57 °C, 441.07 g/mol, 1.016 g/cm^3, and 1.21, respectively. The DS with concentrations between 220.5 and 882 g/L generated an osmotic pressure between 14 and 59 bar. Around 98% of the dissolved solids of the DS were retrieved via thermal precipitation at 60 °C. The remaining 2% had to be recovered through RO or MD to produce water with Ils concentrations below 0.1 g/L. This high *r* is necessary due to the high DS concentration. The DS was tested with seawater as the feed for both AL-FS and AL-DS operational modes; AL-DS showed better performance compared to AL-FS. When using a DS with concentration of 882 g/L, a permeate flux of 12.3 L/(m^2 h) and a reverse salt flux of 2.65 g/(m^2 h) where measured, which means a flux ratio of 0.215 g/L. However, the flux ratio of 0.2 g/L when using NaCl as the DS shows that a conventional DS is more efficient. The estimated SEC_{th} for thermal precipitation was 7.7

kWh_{th}/m^3 while the overall SEC_{th} was 8.8 and 9.95 kWh_{th}/m^3 considering RO and MD post-treatments, respectively.

TR solutions have also been studied for non-FO seawater desalination applications. Peters and Hankins [188] theoretically compared FO and OARO for a zero liquid discharge process integrating NH_3/CO_2 as the DS. A parametric analysis was carried out varying FO/OARO membrane feed flowrate ($\dot{V}$) from 3000 to 7000 L/h, membrane operating pressure (ΔP) from 1 to 48.3 bar, draw to feed flowrate ratio from 0.3 to 0.7, seawater concentration from 25 to 65 g/L and ammonia to carbon dioxide ratio from 2 to 2.8. The energy requirement of OARO increased when the feed concentration increased and remained approximately constant when varying the other parameters. Similarly to OARO, the energy consumption of FO increased as the feed concentration increased with small variations when varying the other parameters. To achieve a brine concentration of 245 g/L when starting with seawater at 45 g/L, the optimal parameters for $\dot{V}$, ΔP, draw to feed flowrate ratio, and ammonia to carbon dioxide ratio were 5 m^3/h, 48.3 bar, 0.5, and 2.4, respectively. The membrane brine concentrator was composed of three FO/OARO stages. Average first stage permeate fluxes of 20.45 and 17.34 $L/(m^2\ h)$ were reported for the FO and OARO cases, respectively. The permeate fluxes declined to 10 and 5.18 $L/(m^2\ h)$ for the second and third OARO stages and to 10.44 and 6 $L/(m^2\ h)$ for the second and third FO stages.

The optimal FO and OARO cases had SEC_{el} values of 14.5 and 12.93 kWh_{el}/m^3, respectively. With low-grade waste heat integration, the SEC_{el} decreased to 4.5 and 5.2 kWh_{el}/m^3 with FO and OARO, respectively. Even though OARO requires high-pressure pumps (absent in FO), their additional energy requirement is neglected due to the highly energy-intensive processes of heating and cooling the DS. A higher energy consumption for FO was expected because it operated with a DS concentration higher than the feed solution,

required to produce positive permeate flux, while OARO operated with a DS concentration lower than the feed solution because the driving force to generate a positive permeate flux was obtained from the applied pressure. For this reason, OARO reconcentrated the DS at a 12 °C lower temperature and required 23% less energy compared to FO. The system required a brine stripper to reduce the traces of ammonia from the brine, which inevitably increased the overall energy consumption. The study also included economic evaluations with OARO cost being 15.5% lower compared to FO.

The FO and OARO cases were further investigated by comparing them with a low-salt-rejection RO and a conventional NaCl OARO process to concentrate seawater from 35 to 233 g/L. The calculated SEC_{el} of FO, TR OARO, low-salt-rejection RO, and NaCl OARO were 11, 9.3, 5.1, and 3.9 kWh_{el}/m^3, respectively. The low-salt-rejection RO and NaCl OARO cases were less energy-intensive because they do not require any cooling or heat transfer equipment. In case of a low-grade waste heat freely available, the energy consumptions of FO and TR OARO decrease to 2.9 and 3.5 kWh_{el}/m^3, respectively, while the equivalent electric energy consumptions of low-salt-rejection RO and NaCl OARO remain the same because these processes cannot be powered by a low-grade waste heat. These results indicate that FO and TR OARO are better than conventional processes only when a free thermal energy is available.

In summary, TR solutions need to be cooled and heated to absorb and reject water, which increases the energy requirement of the system. The review of TR for water desalination shows that TR solutions achieve lower energy consumption only when a low-grade waste heat is freely available [178, 188]. Although TR aims to decrease the energy consumption compared to conventional DS, their values are still high compared to other technologies, such as RO. The TR solutions require low salt fluxes to produce non-toxic water because some

TRs are toxic [65]. The studies [65, 180] which evaluated the FO performance by considering the ratio between reverse salt and permeate fluxes, minimised this ratio to achieve higher membrane performance by employing solutions with a high relative molecular mass and high LCST. Based on this ratio, however, the performance of TR solutions was lower compared to NaCl used as a DS. Thus, further research is required for TR solutions to be competitive against conventional alternatives. Most researchers have experimentally evaluated TR solutions mainly for FO systems. The theoretical study of Peters and Hankins [188] shows the potential of NH_3/CO_2 as DS coupled with other desalination methods, such as OARO, but more experimental studies are required to properly evaluate their theoretical model. Numerous studies employing NH_3/CO_2 for refrigeration can be found in the literature from the early 2000s [62, 228-233]. Therefore, future improvement of this study could consider more recent TR solutions, such as ILs or MNPs.

TR studies until now have been employed for low salinities [65, 178, 188, 194, 226] which does not satisfy high feed concentration criteria of greenhouse applications. Additional research should be done employing higher concentrated feeds to test the concentration limits of TR and risk of fouling. Table 2-11 summarises the selected studies in TR used as DS for water desalination considering important parameters, necessary to compare results from different desalination technologies and to evaluate compatibility for greenhouse applications.

Table 2-11. Summary of selected TR studies for desalination applications.

Study	Solute	Concentration [g/L] (wt.%)	Molar fraction	*SEC* [kWh/m^3]	Energy input	Experimental or Theoretical
[194]	NaCl	35 (3.44)	0.0108			Experimental
[178]	NaCl	35 (3.44)	0.0108	0.5 29	Electrical Thermal	Experimental
[180]	NaCl	35 (3.44)	0.0108			Experimental
[226]	NaCl	35.8 (3.5)	0.0111	37–42	Electrical	Experimental
[65]	NaCl	35 (3.44)	0.0108	8.8–9.95	Electrical	Experimental
[188]	NaCl	45 (4.4)	0.014	5.24 109.24 87.93	Electrical Thermal Cooling load	Theoretical

2.6 Electrodialysis

ED is a membrane separation process where charged species are separated from uncharged solutions through ion-exchange membranes (IEMs) [74]. IEMs are arranged in series between a cathode electrode and an anode electrode [234, 235]. Due to the applied electrical potential, cationic species (such as Na^+, K^+, and NH_4^+) pass through cation-exchange membranes (CEMs) to reach the cathode electrode, while anion species (such as PO_4^{3-}, SO_4^{2-}, and Cl^-) pass through anion-exchange membranes (AEMs) to reach the anode electrode [74]. CEMs and AEMs allow only positive and negative species to pass through, respectively [74]. AEMs and CEMs are arranged in an "Anode-CEM-AEM-//-CEM-AEM-Cathode" configuration [235].

2.6.1 Fouling mitigation and conventional use

Like all membrane processes, ED is affected by fouling. Foulants depend on the feed composition, but commonly are calcium and magnesium carbonates, sulphates, or phosphates

[74]. Fouling occurs mainly for negative charged organic foulants that attach to the AEMs [236]. Thus, ED without AEMs has been studied to decrease fouling compared to conventional ED [236]. Moreover, electrodialysis reversal (EDR) has been adopted to reduce the tendency of IEMs fouling [237]. EDR consists in periodic reversal of the current direction through the ED stack which removes accumulated foulants from the membranes [238].

ED is mainly used for feeds having low concentrations, with economic advantage over conventional RO for concentrations below 10 g/L [234]. For example, industrial scale ED studies process concentrations of 2.5–3 g/L and obtain recoveries of 85% [239]. ED has also been employed for brackish water with concentrations above 15 g/L [240]. Other ED applications include chemical conversion into electricity, hydrogen production, and chemical synthesis [235].

2.6.2 Electrodialysis for water desalination

Few studies can be found in literature regarding ED for water desalination with hypersaline feeds. The selected studies have feed concentrations between 35 and 300 g/L. Desai et al. [241] investigated a hybrid flow battery with reversible operation to simultaneously desalinate hypersaline brines and produce electrical energy. Two feeds with NaCl concentration of 35 and 100 g/L were theoretically and experimentally investigated. The permeate had a concentration of 4.8 and 13.4 g/L when using a feed with 35 and 100 g/L, respectively, which corresponded to rejections of 85% and 86%. For feed concentrations of 35 and 100 g/L, the SEC_{el} was 2.1 and 12.7 kWh_{el}/m^3, respectively, with errors between experimental and modelling results below 10%. Compared to a conventional one-stage RO operating at 69 bar, ED required the same energy to treat a feed concentration of 35 g/L, but ED required less energy to treat a feed concentration of 100 g/L.

Tian et al. [242] developed a bipolar membrane ED to treat hypersaline industrial wastewaters. Bipolar membrane ED is widely applied for wastewater treatment due to both phase change and pollution absence [243, 244]. The model was created with Aspen HYSYS software. Experiments were performed to compare with simulation results. A wastewater feed with a concentration of 87 g/L of Na_2SO_4 was treated by the system. The system produced three outputs, i.e., sodium hydroxide, sulfuric acid, and treated wastewater. Sodium hydroxide and sulfuric acid solutions were recycled until the Na_2SO_4 outlet concentration decreased to 4 g/L. By considering an average Na_2SO_4 density of 2.66 g/mL, the system had a SEC_{el} of 7.1 kWh_{el}/m^3 (Na_2SO_4 based).

Most hypersaline ED studies focus on economic feasibility. Kim et al. [245] investigated the technical and economic feasibility of ED without AEMs to treat brine with concentration up to 100 g/L and salt rejections up to 70%. The system removed salts and suspended solids while being less susceptible to membrane fouling/scaling due to operation without AEMs. The NaCl feed concentration varied from 6 to 100 g/L while Na_2SO_4 was used as the rinsing solution in the electrode channels. To reach a recovery of 50%, the SEC_{el} increased exponentially with feed concentration. Specifically, the SEC_{el} for feed concentrations of 60 and 100 g/L were 12 and 45 kWh_{el}/m^3, respectively.

Further studies regarding ED without AEMs were conducted by Kim et al. [246] for partial desalination of hypersaline brines with concentrations of 70 g/L. A lab scale on system was created considering feed flow velocities of 0.24–4.0 mm/s and rejections of 10, 30, 50, and 70%. To achieve a *r* of 50%, the SEC_{el} ranged from 6 to 213 kWh_{el}/m^3 for feed flow velocities from 0.24 to 4.0 mm/s, respectively. The authors included economical evaluations, reporting a water cost production of $\$3.08/m^3$ for a *r* of 50%.

Other studies regarding ED process were performed by McGovern et al. [247] who investigated energy and equipment size for hypersaline desalination with seawater reaching concentrations up to 195 g/L. The experiment replicated the performance of a ten-stage continuous flow ED system which produced permeate with a concentration of 0.24 g/L. The cost per unit of salt removed was significantly lower when removed from a high salinity compared to low salinity feed, highlighting potential of partial desalination ED for highly concentrated solutions. However, the authors provided energy consumptions and recoveries for other studies without mentioning their own.

Tufa et al. [248] investigated a conventional seawater RO (SWRO) coupled with DCMD and reverse electrodialysis to simultaneously produce water and electric energy. The system performance, based on lab-scale tests, was evaluated for three cases: without pressure exchanger, with pressure exchanger, and pressure exchanger combined with reverse electrodialysis. The system was also evaluated for three different feed temperatures, i.e., 40, 50, and 60 °C, and *r* from 75 to 90%. The SWRO was design to operate at a *r* of 50% with a rejection of 100% when treating seawater with a concentration of 29 g/L. The SWRO brine was directed to a heating system, which raised the feed temperature to 40, 50, or 60 °C before been directed to the DCMD.

For the simulations, *r* was fixed and independent from the feed temperature. However, a DCMD working with higher temperature should produce higher permeate flux and in turn obtain a higher *r*. A *r* higher than 80% was predicted for DCMD achieving brine concentrations of 175–292 g/L. The authors stated that *r* above 80% were calculated because osmotic phenomena do not limit the DCMD. Permeate fluxes of 1.4–4.3 L/(m^2 h) and 0.5–2.3 L/(m^2 h) were estimated for DCMD brine concentrations of 117 and 292 g/L, respectively, at

different feed temperatures with higher permeate fluxes corresponding to higher feed temperatures.

The SEC_{el} was evaluated for all configurations. For example, r of 90% and 60 °C DCMD temperature had SEC_{el} of 6.5, 5.8, and 5.5 kWh_{el}/m^3 when operating without pressure exchanger, with pressure exchanger, and pressure exchanger combined with reverse electrodialysis, respectively. For the same r but at 40 °C DCMD temperature, SEC_{el} of 3.9, 3.1, and 2.9 kWh_{el}/m^3 were reported. The SEC_{el} should increase with r, however, a SEC_{el} at higher r indicates that the permeate volume increased faster than the required energy. The authors also evaluated exergetic efficiency with a maximum value of 54% for a r of 75% and a DCMD temperature of 40 °C. To reach a r of 90%, exergetic efficiencies of 49, 44, and 39% were reported for the 40, 50, and 60 °C DCMD temperatures, respectively. Finally, the authors provided economic considerations, showing similar membrane costs at different DCMD temperatures and recoveries.

In summary, ED can be economical to treat hypersaline solutions for partial desalination [241, 247, 249]. Typical SEC_{el} for ED should range from 6 to 11 kWh_{el}/m^3 according to Silva et al. [250] and from 1 to 12 kWh_{el}/m^3 according to Zhao et al. [119]. The selected ED studies are within these ranges for typical desalination processes. However, the SEC_{el} increases beyond these ranges when employing hypersaline solutions [245] or high feed flow velocities [246]. ED is a promising technology for greenhouse application being able to operate with high feed concentration, limited fouling (for operations such as EDR or ED without AEMs) and low r requirements. However, bipolar membrane ED [242] and ED without AEMs [245, 246] technologies produce effluents, aside from the treated solution, which derive from combinations between feed and rinsing solutions. The rinsing solution is required to avoid gasification of Cl^- ions, meaning a small amount of solution is lost. Table 2-12 summarises

the selected studies in ED for water desalination considering important parameters, necessary to compare results from different desalination technologies and to evaluate compatibility for greenhouse applications.

Table 2-12. Summary of selected ED studies for desalination applications.

Study	Solute	Concentration [g/L] (wt.%)	Molar fraction	SEC_{el} [kWh_{el}/m^3]	Experimental or Theoretical	ED Technology
[241]	NaCl	100 (9.5)	0.031	12.7	Both	Hybrid flow battery
[242]	Na_2SO_4	87 (8.2)	0.011	7.1	Both	Bipolar membrane ED
[245]	NaCl	100 (9.5)	0.031	45	Both	ED without AEMs
[246]	NaCl	70 (6.75)	0.022	5.6–213	Both	ED without AEMs
[247]	NaCl	195 (17.7)	0.062		Both	Ten-stage ED
[248]	NaCl	292 (25.25)	0.094	5.53	Theoretical	SWRO-DCMD-ED

The main parameters affecting ED performance for water desalination are feed temperature (T_{in}), concentration (C_{in}), feed flow velocity ($Speed_f$), and recovery (r). The effects of these parameters on permeate flux (J_v), production cost ($Prod_{Cost}$), power requirement ($Power$), r, and exergetic efficiency (Ex_{eff}) are summarised in Table 2-13.

Table 2-13. Main parameters affecting ED performance in desalination application based on the selected studies[5]

Operating parameter	J_v	$Prod_{Cost}$	$Power$	r	Ex_{eff}
↑ T_{in}	↑ [248]	~ [248]	↑ [248]	~ [248]	↓ [248]
↑ C_{in}		↓ [247]	↑ [241]	~ [241]	
↑ $Speed_f$			↑ [246]		
↑ r			↓ [248]		

[5] Arrows indicate the effect on the parameters; an arrow facing upwards (↑) or downwards (↓) means the parameter increases or decreases, respectively. The "~" indicates the parameter has small variations.

2.6.3 Electrodialysis for liquid desiccant regeneration

Although ED has been used mostly for treatment of feeds with low concentrations, ED studies for LD concentration can also be found. The selected ED studies utilise ED as the LD regenerator to treat highly concentrated desiccants and have been published in the last decade.

Cheng and Pei [251] performed a theoretical comparison between LiCl and LiBr which were concentrated by ED. The vapour pressure of the two desiccants were calculated using empirical interpolations [47, 252]. In the concentration range of 20–42 wt.% (220–535 g/L) and temperature of 10–50 °C, the vapour pressure of LiCl was higher than LiBr, which contradicts with other studies [25, 39] stating the opposite. These authors showed how different parameters affect ED. Increasing the desiccant temperature from 20 to 30 °C increased the moisture removal rate from 5 to 13 L/h using LiCl and from 5 to 11 L/h using LiBr. Higher feed temperature was beneficial also for the *COP*. Specifically, increasing the feed temperature from 20 to 30 °C increased the *COP* from 1 to 2.8 for LiCl and from 2.5 to 5.8 for LiBr. In contrast, the initial desiccant concentration had the opposite effect, with higher initial concentration corresponding to lower *COP*. These results show that higher concentration is beneficial for the dehumidification process but disadvantageous for the overall system.

Pei et al. [253] conducted experiments on LiBr regeneration via ED. They investigated the effect of feed flowrate on different parameters. For example, LiBr with feed concentration of 45 wt.% (660) had an outlet concentration that increased by 0.34, 0.42, and 0.48 wt.% (3, 4, and 5 g/L) with flowrates of 80, 120, and 160 L/h, respectively. These authors observed desiccant losses during experiments which occurred due to chemical interactions of the feed with the electrode solution. It was found that higher flowrates decreased the desiccant losses. Specifically, flowrates of 80, 120, and 160 L/h corresponded to desiccant losses of 0.05%,

0.04%, and 0.03%, respectively. Moreover, by increasing the feed concentration from 45 to 55 wt.% (660 to 900 g/L), the *COP* decreased from 0.97 to 0.32. Regarding the flowrate, increasing it from 80 to 160 L/h increased the *COP* from 1.32 to 1.67. Although increasing the flowrate increased the energy consumption, the increment was modest. Contemporary, high flowrate led to a more efficient system by increasing the *COP*, similarly to a previous study [251]. Increasing the applied current from 3 to 8 A decreased the *COP* from 4.26 to 0.97. Considering a LiBr initial concentration of 45 wt.% (660 g/L) and an applied current of 3 A, ED achieved a maximum current efficiency of 30.36% and a *COP* of 4.26.

According to previous studies [25, 39], LiCl should be the best LD. Different studies can be found employing LiCl combined with ED as the regeneration process. Sun and Zhang [254] carried out experiments to investigate the performance of an ED system used to reconcentrate LiCl with an initial concentration varying from 7 to 25 wt.% (70 to 290 g/L). The system included three closed loop circuits, i.e., LD, electrode solution, and diluted solutions. As the ED operating time proceeded, the outlet LD concentration increased up to a maximum value. Feed concentrations of 10.6, 15.46, 19.87, and 24.69 wt.% (112, 168, 221, 283 g/L) increased to 12.4, 16.8, 20.6, and 25.4 wt.% (132, 184, 230, and 292 g/L), respectively. As the feed concentration increased, the permeate flux and current efficiency decreased. Moreover, higher brine concentrations were achieved with higher applied currents. Specifically, applied currents of 10 and 20 A corresponded to concentration increments of 0.7 and 1.3 wt.% (7 and 13 g/L), respectively. Higher feed concentration leads to a more efficient regeneration, however, increasing the feed concentration from 10.56 to 24.69 wt.% (112 to 283 g/L) also increased the SEC_{el} from 3.3 to 10 kWh_{el}/m^3, respectively.

Another study using LiCl was conducted by Guo et al. [64] who experimentally investigated an ED system consisting of ten cell pairs of ion-exchange membranes. A

concentrated feed with concentration of 28.8 wt.% (338 g/L) and flowrate of 100 L/h could increase its concentration if the concentration difference between the concentrated and diluted feeds was below 5.86 wt.% (60 g/L). This maximum concentration could be explained as an electrochemical potential, created by the concentration difference between the two feeds which prevents the concentrated feed from being further concentrated.

Moreover, Al-Jubainawi et al. [255] investigated the mass transfer mechanisms and performance of ED for LiCl regeneration. They observed that the permeate flux decreased during operation and reached a stable value towards the end of the simulation. Although lower concentration differences between inlet and outlet achieved stable fluxes through the entire operation, the permeate flux decreased at lower concentration differences. This difference is limited due to the electrochemical potential between inlet and outlet, as seen from a previous study [64]. The applied current also affected the system; a concentrated feed of 18 and 30 wt.% at 100 L/h flowrate and applied current of 12 A achieved fluxes of 1.08 and 0.5 L/(m^2 h), respectively, compared to fluxes of 0.3 and 0.13 L/(m^2 h) for an applied current of 3 A.

In summary, the selected studies show that the applied current is a critical operating parameter. High applied current has the disadvantage of increasing the energy requirement which lowers the *COP* [255], but has the advantage of increasing the permeate flux [255] and the dehumidification and regeneration efficiencies [254, 255]. Therefore, an optimal value of the current efficiency can be found based on the operating conditions, taking into consideration the *COP* and the dehumidification and regeneration efficiencies. However, ED is limited by the concentration difference between the concentrated and diluted solutions. This difference cannot exceed 6 wt.% (60 g/L), which may be low for LDAC applications. Moreover, the regeneration of the diluted solution implies the requirement of another desalination technology, highlighting that stand-alone ED cannot operate in LD regeneration.

Table 2-14 summarises key parameters, from the selected studies, for comparing different technologies.

Table 2-14. Summary of selected ED studies for LDAC applications.

Study	Solute	Inlet concentration [wt.%]	Outlet concentration [wt.%]	Inlet molar fraction	Outlet molar fraction	*COP*	Experimental or Theoretical
[251]	LiCl		38		0.207	1–2.8	Theoretical
	LiBr		55		0.202	2.5–5.8	
[253]	LiBr	45	45.622	0.145	0.148	1.3–4.3	Experimental
[254]	LiCl	24.69	25.4	0.122	0.126		Experimental
[64]	LiCl	28.9	29.97	0.147	0.154		Experimental
[255]	LiCl		30		0.154		Both

2.7 Comparison of the technologies

This Section compares MD, RO, NF, FO, TR solutions, and ED for desalination, LD regeneration, and water irrigation applications.

2.7.1 Comparison for water desalination

Most of the selected studies for water desalination applications employed seawater as the feed, which can be seen as a desiccant solution containing NaCl, which can reach *ERH* values down to 75% [25]. Since greenhouses require relative humidities of 70–90%, NaCl may also be employed for greenhouse applications. The six desalination technologies, i.e., MD, RO, NF, FO, TR solutions, and ED can either be thermally or electrically driven. Figure 2-3 Was created by plotting the *SEC* against the feed concentration of the selected studies. Figure 2-3 Shows that the thermally driven processes (involving phase transition) have higher *SEC* compared to the electrically driven.

Based on the possibility to operate with high feed concentrations, the most suitable desalination technologies for greenhouse cooling and dehumidification are MD, ED, and RO. ED and RO operated with concentrations ranging from 7 to 25 wt.%, equivalent to 70 to 290 g/L, while MD operated with concentration up to 45 wt.%, equivalent to 585 g/L, (Figure 2-4). Figure 2-4 Was created by plotting the permeate flowrate against the feed concentration of the selected studies. MD with high feed concentrations is not visible in Figure 2-3 Because the 45 wt.% (585 g/L) MD study did not provide its *SEC*. The regeneration process efficiency can be measured from the permeate flux. For feed concentrations of 20–45 wt.% (220–585 g/L), MD achieved the highest permeate flux (Figure 2-4). Figure 2-5 Shows the desalination studies over the last 20 years. The recent research focuses on TR solutions, but the studies are still in preliminary stages considering feeds with low concentrations. Recent investigations also include RO (specifically osmotically assisted configurations) and ED.

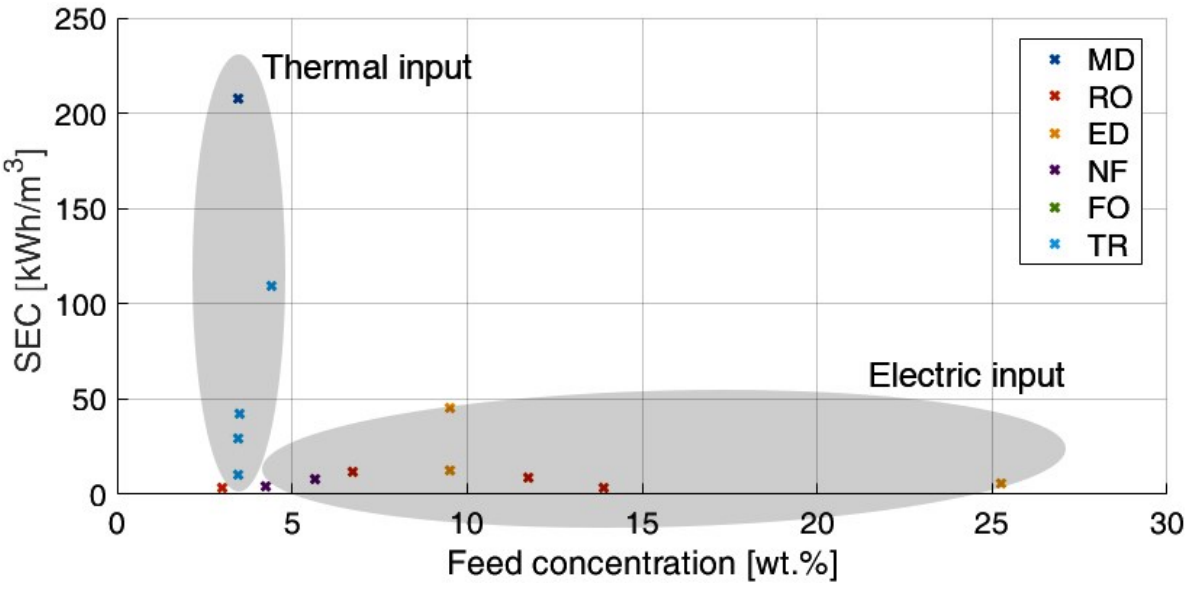

Figure 2-3. Specific energy consumption (SEC) against feed concentration of selected desalination studies.

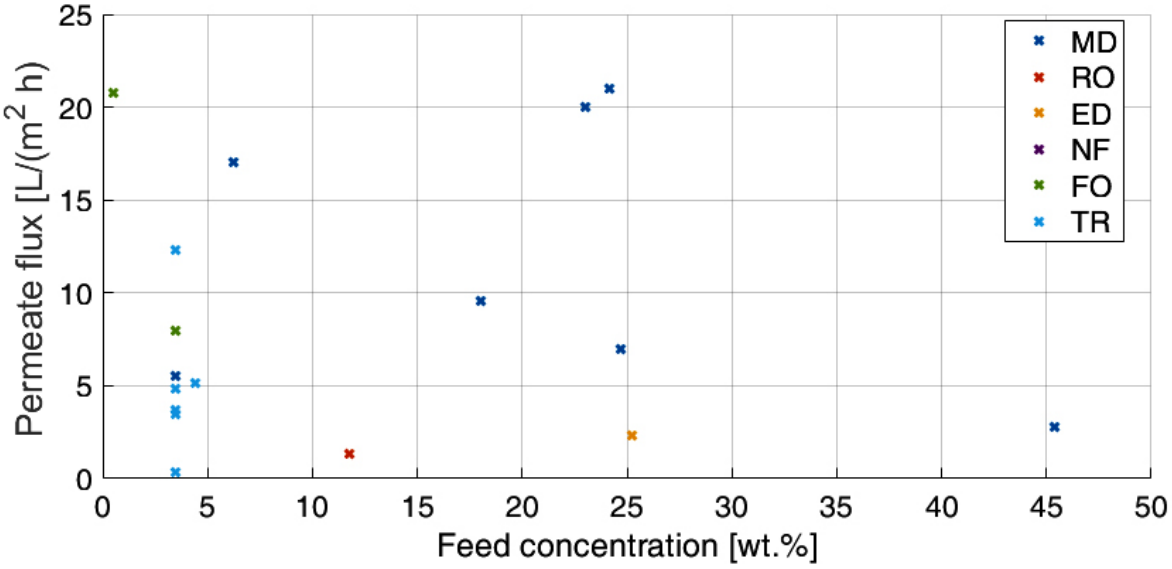

Figure 2-4. Permeate flux against feed concentration of selected desalination studies.

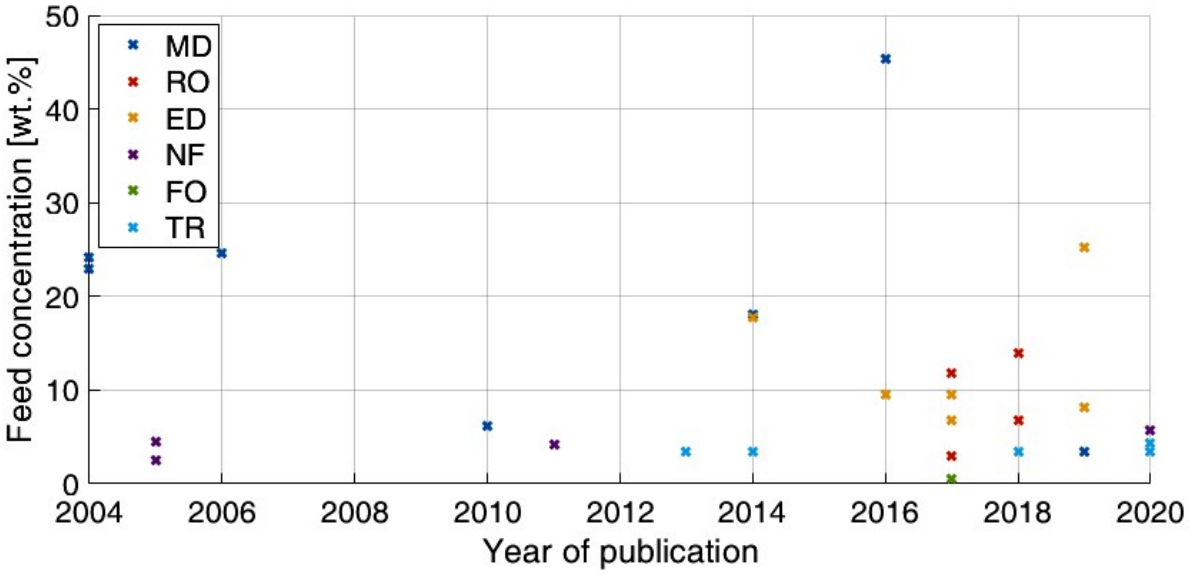

Figure 2-5. Feed concentration against year of publication of selected desalination studies.

2.7.2 Comparison for liquid desiccant regeneration

Conventional MD, RO, and ED technologies employed for LDAC applications are not efficient for highly concentrated desiccant regeneration, with MD being the only one with potential to improve if operated with feed temperatures higher than 80 °C and more selective

collectors [93]. A detailed comparison of MD, RO, and ED employed for LD regeneration is firstly presented based on the selected studies. Then, the comparison is extended to all six desalination technologies.

To compare the desiccants used in the selected studies, Figure 2-6 Plots the outlet feed concentration [wt.%] against the outlet molar fraction of LiCl, LiBr, and $CaCl_2$ ($MgCl_2$ is not included because the data on outlet concentration was not provided by the authors [90]). LiCl achieved higher molar fractions at lower concentrations compared to the other desiccants because LiCl has the lowest atomic mass. Figure 2-6 Also shows that if concentration is considered as weight percentage [wt.%], then the highest concentrations are achieved using LiBr and $CaCl_2$. Whereas if concentration is considered as molar fraction, the highest concentration is achieved using LiCl. This occurs because at a given weight concentration, the molar concentration is higher for LD with lower atomic masses. In fact, LiCl achieves a higher molar fraction at a lower weight concentration compared to the other desiccants because LiCl has a relative molecular mass of 42.38 g/mol while $CaCl_2$ and LiBr have relative molecular masses of 110.98 and 86.845 g/mol, respectively.

Regarding the maximum LD concentrations achieved by MD, RO, and ED, Figure 2-7 Plots the outlet feed concentration [wt.%] against the feed concentration [wt.%], while Figure 2-8 Plots the outlet molar fraction against the inlet molar fraction of the selected studies. These two Figures show that the maximum outlet LD concentration of 45.6 wt.% (595 g/L) was achieved using ED when the concentration was measured as weight percentage [wt.%], and 0.234 using MD when the concentration was measured as molar fraction. The concentration difference between the inlet and outlet LD shows that small concentration variations are required for the LD regeneration process. High feed concentration leads to membrane fouling for all the seawater desalination applications, which does not occur in these

studies because the regeneration units operated with highly concentrated LD solutions prepared in the laboratory with low propensity for fouling. Moreover, MD achieved a higher dehumidification efficiency than ED. Specifically, the average concentration difference for MD between inlet and outlet LD was 2.4 wt.% (25 g/L), compared to 0.85 wt.% (8 g/L) for ED

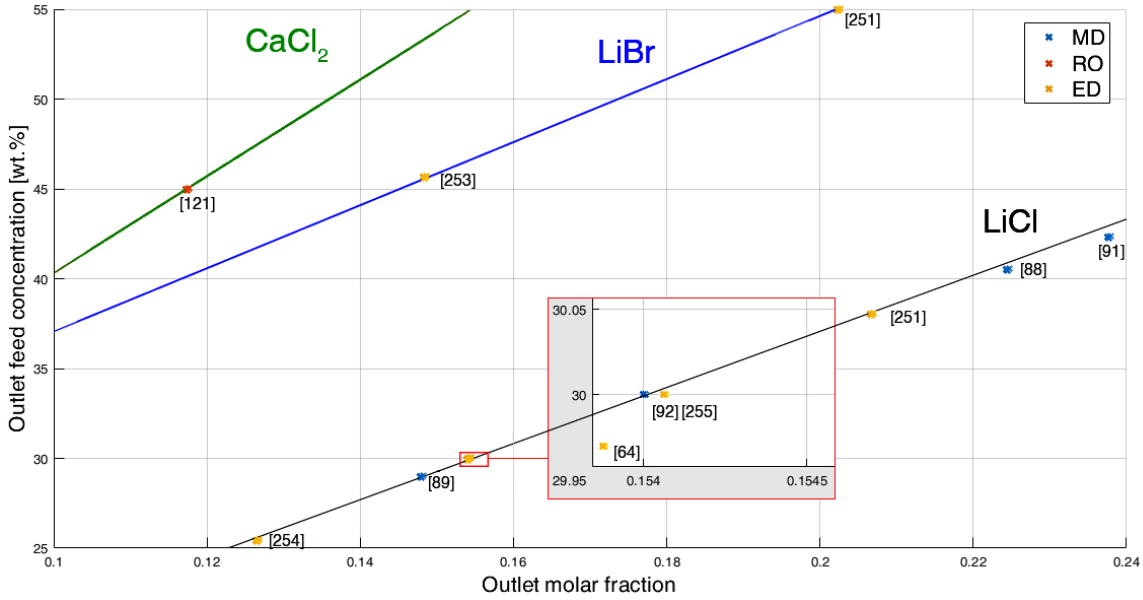

Figure 2-6. Outlet feed concentration against outlet molar fraction. Studies on the green line utilise $CaCl_2$, on the blue line utilise LiBr, and on the black line utilise LiCl. Numbers on the graph represent the references of the selected LD studies.

Regarding the research done in MD, RO, and ED as LD regenerators, Figure 2-9 Plots the outlet molar fraction against the year of publication of the relevant studies. All the research focus over the last 10 years has been on MD and ED with feed concentrations of 30–45 wt.% (355–585 g/L). Regarding the energy consumption, ED was expected to require less energy than MD due to phase transition absence (which occurs in the MD process [55]). This can be seen also from the *COP*; The ED studies reported *COP* values of 1–5.8, whereas only one MD study reported their *COP*, equal to 0.372. Since the *COP* is inversely proportional to the

required power to drive the system, ED requires from 2.5 to 15.5 times less energy compared to MD. The negative aspect of ED is the higher complexity compared to MD. ED has an additional recirculating circuit for the electrode solution and is affected by more parameters, such as applied current, current efficiency, and concentration difference between concentrated and diluted feeds. If the required energy of the system can be provided from both solar (thermal energy for MD) and photovoltaic (electric energy for ED) collectors, then MD is preferred over ED. However, the negative aspect of MD is that the LD exits the regeneration cycle hot which needs to be cooled before it can be used for dehumidification, adding extra steps in the whole process.

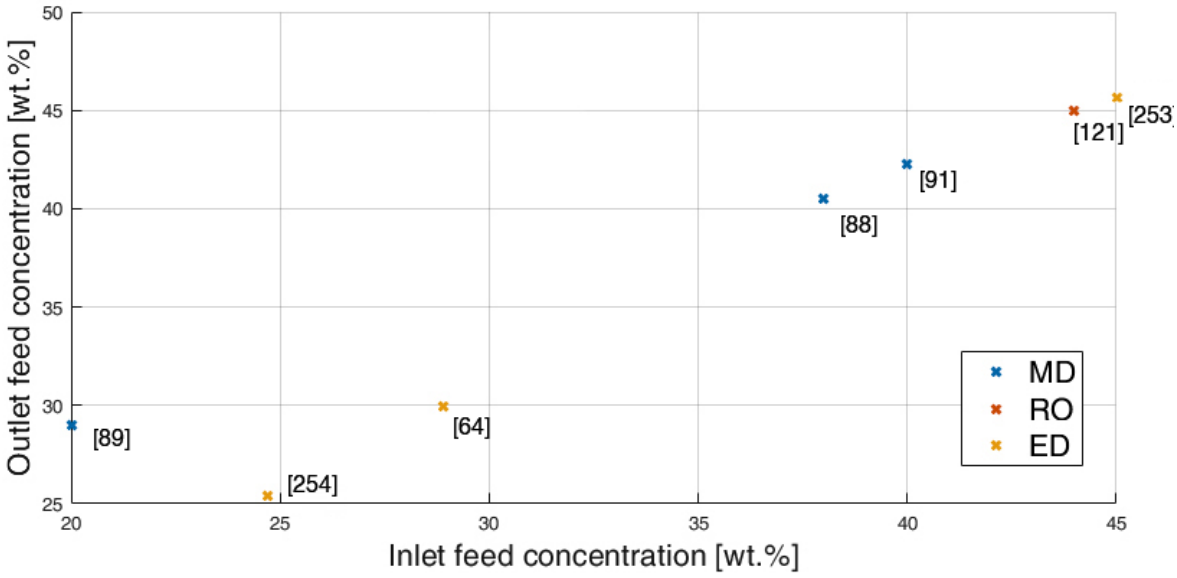

Figure 2-7. Outlet feed concentration against feed concentration. Numbers on the graph represent the references of the selected LD studies.

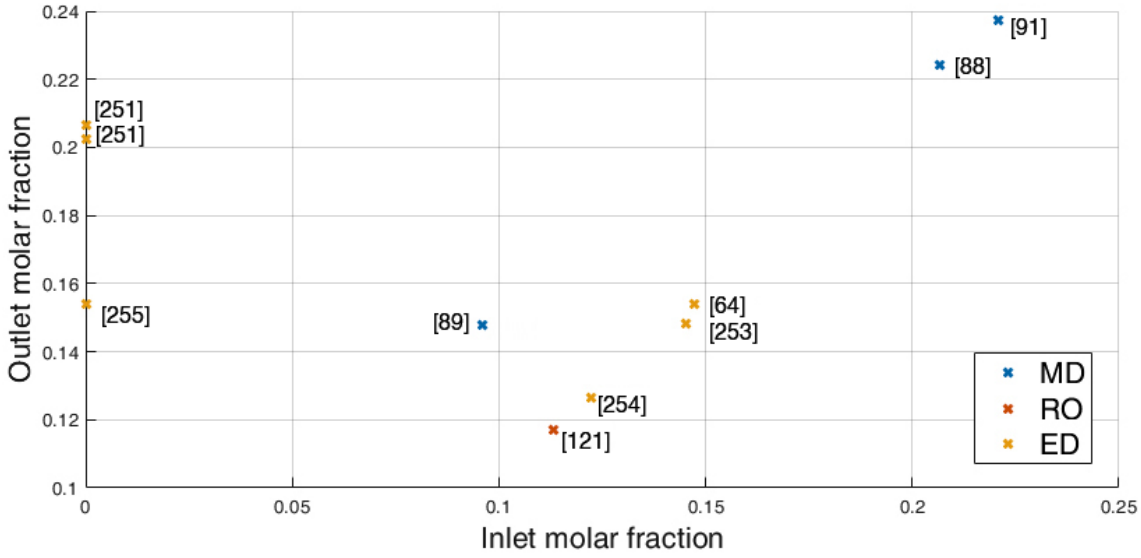

Figure 2-8. Outlet molar fraction against feed concentration. Numbers on the graph represent the references of the selected LD studies.

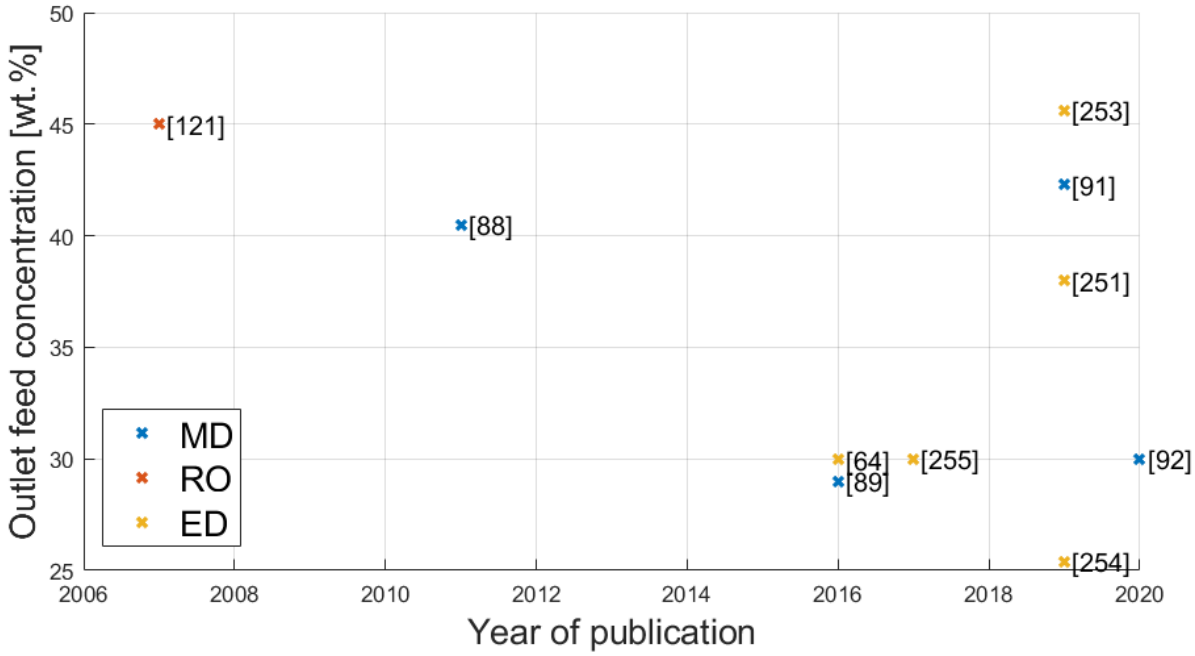

Figure 2-9. Outlet feed concentration against year of publication. Numbers on the graph represent the references of the selected LD studies.

The main parameters affecting the performance of MD for LD regeneration are feed temperature (T_{in}), feed concentration (C_{in}), and feed flowrate ($\dot{V}_{in}$). VMD is also affected by

the vacuum applied pressure (VP_{app}). The main parameters affecting the ED performance for the LD regeneration are T_{in}, C_{in}, $\dot{V}_{in}$, applied current (I_{app}), and concentration difference between concentrated and diluted feeds (C_{conc}-C_{del}). The effects of these parameters on dehumidification process (*Deh*), *COP*, permeate flux (J_v), outlet concentration (C_{out}), power requirement (*Power*), regeneration temperature (T_{reg}), outlet temperature (T_{out}), regeneration cost ($Cost_{reg}$), concentration difference between inlet and outlet feed concentrations (C_{out}-C_{in}), current efficiency (I_{eff}), and desiccant losses (Des_{loss}) are summarised in Tables 2-15 And 2-16.

Table 2-15. Main parameters affecting MD performance in LDAC applications based on the selected studies.[6]

Operating parameter	*Deh*	*COP*	J_v	C_{out}	*Power*	T_{reg}	T_{out}	$Cost_{reg}$
↑ T_{in}	↑ [89]	↑ [89]	↑ [88, 90]	↑ [88, 91]	↑ [88]	↑ [92]	↑ [91]	↑ [91]
↑ C_{in}	↓ [88, 89]	↓ [89]	↓ [88, 90]					
↑ $\dot{V}_{in}$	↑ [89]	↗↘ [89]						
↑ VP_{app}			↑ [90]	↑ [91]	↑ [90, 91]		↓ [91]	

Table 2-16. Main parameters affecting ED performance in LDAC applications based on the selected studies.[11]

Operating parameter	*Deh*	*COP*	J_v	C_{out}	*Power*	C_{out}-C_{in}	I_{eff}	Des_{loss}
↑ T_{in}	↑ [251]	↑ [251]						
↑ C_{in}		↓ [251, 253]	↓ [254, 255]		↑ [254]	↓ [253]	↓ [254]	
↑ $\dot{V}_{in}$		↑ [253]		↑ [253]	↑ [253]			↓ [253]
↑ I_{app}	↑ [255]	↓ [255]	↑ [255]	↑ [254]	↑ [255]			
↑ C_{conc}-C_{del}			↑ [255]			↓ [64]		

[6] Arrows indicate the effect on the parameters; an arrow facing upwards (↑), downwards (↓), or both (↗↘) means the parameter increases, decreases, or it has an inverse U-shaped trend, respectively. Parameters in a slightly grey shading appear on both Tables A1-15 and A1-16. Numbers on the tables represent the referenced studies.

Based on Table 2-15 and Table 2-16, the dehumidification efficiency and *COP* increase with feed temperature for MD [89] and ED [251], but also the energy consumption increases to heat the LD [88]. For MD, higher $\dot{V}_{in}$ increases the dehumidification efficiency while *COP* has an inverse U-shape trend [89]. Increasing the feed temperature also increases the water flowrate [88, 90], the outlet concentration [88, 91], the outlet temperature [91], the regeneration temperature [92], and the regeneration cost [91]. In the case of VMD, more vacuum increases the outlet feed concentration [90] and the permeate flux [91] at the expense of higher energy requirements [90, 91]. Moreover, a higher applied vacuum pressure decreases the outlet feed temperature [91] and decreases the required energy to cool the LD.

For ED, the *COP* increases with $\dot{V}_{in}$ [253] while a higher concentration difference between inlet and outlet concentrations increases the permeate flux [255] and decreases the outlet concentration and the regeneration efficiency [64]. However, higher $\dot{V}_{in}$ increases the outlet concentration, the energy requirements, and the desiccant losses [253].

The feed concentration is a key parameter for both MD and ED. For MD, higher feed concentration is advantageous for the dehumidification efficiency [88, 89], but disadvantageous when considering the overall LDAC process, with lower *COP* values [89] and permeate fluxes [88, 90]. Similar results are reported for ED, with higher feed concentrations decreasing the *COP* [251, 253] and the permeate fluxes [254, 255]. Moreover, higher feed concentration for ED also increases the SEC_{el} [254], decreases the current efficiency [254], and decreases the difference between inlet and outlet feed concentrations [253]. A higher feed concentration provides a lower *ERH* which is beneficial for the dehumidification efficiency, while the regeneration process requires high *ERH* to produce high permeate fluxes. Therefore, an optimal value of the LD concentration exists for the overall system performance, but since the objective in greenhouses is to maintain optimal

internal conditions for the crops, the system must operate at high LD concentrations with lower *COP*.

2.7.3 Comparison for irrigation

So far in this thesis, it has been mentioned that the permeate from the desalination technologies employed for LD regeneration can be re-utilised for irrigation. This concept is further investigated here by considering the parameters that affect the soil.

The properties of the irrigated water can affect the soil and thus the crops in a greenhouse. The effects of the irrigated water can be measured based on different parameters, such as the sodium adsorption ratio (*SAR*), the salinity, the concentrations of ions and cations and the pH of the irrigation water. *SAR* is one of the most used parameter, according to Sposito et al. [256] it is defined as:

$$SAR = \frac{[Na^+]}{([Ca^{2+}] + [Mg^{2+}])^{0.5}} \quad (1\text{-}1)$$

where $[Na^+]$, $[Ca^{2+}]$ and $[Mg^{2+}]$ represent the concentrations in [mmoles/L] of sodium, calcium, and magnesium, respectively, present in the irrigated water. *SAR* can be seen as the chemical interaction between the soil and the cations in the irrigated water [256]. High *SAR* decreases the aggregate stability of the soil causing its deterioration or destruction [257]. Consequently, the *SAR* of the irrigation water must be correctly balanced to preserve the properties of the soil and the crops in a greenhouse.

The most popular guideline for irrigation, proposed by Ayers and Westcot [258], summarises the threshold limits for electric conductivity (*EC*) [mS/cm], total dissolved solids (*TDS*) [g/L], water infiltration (which accounts for both threshold values of *SAR* and *EC*), specific toxicity as concentrations of sodium (Na) and chloride (Cl) [mEq/L], specific toxicity

of boron (B) [mg/L], miscellaneous effects of nitrogen (NO_3 – N) [mg/L] and bicarbonate (HCO_3) [mEq/L], and pH of water (Table 2-17).

Based on Table 2-17, *EC* should be below 0.7 mS/cm and *SAR* in the range of 0–3, whereas optimal *EC* and *TDS* should be around 0.7 mS/cm and 0.45 g/L, respectively. From the selected studies, only RO, ED, and NF produced permeates with *TDS* lower than 0.45 g/L (see Figure 2-10).

Table 2-17. Guideline of water quality for irrigation taken from Ayers and Westcot [258].

Potential Irrigation problem	Parameter	Effect on the soil			Unit
		None	Slight to moderate	Severe	
Concentration					
	EC	< 0.7	0.7–3.0	> 3.0	mS/cm
	TDS	< 0.45	0.45–2	> 2	g/L
Water infiltration					
	SAR = 0–3 and *EC* =	> 0.7	0.7–0.2	< 0.2	mS/cm
	SAR = 3–6 and *EC* =	> 1.2	1.2–0.3	< 0.3	mS/cm
	SAR = 6–12 and *EC* =	> 1.9	1.9–0.5	< 0.5	mS/cm
	SAR = 12–20 and *EC* =	> 2.9	2.9–1.3	< 1.3	mS/cm
	SAR = 20–40 and *EC* =	> 5.0	5.0–2.9	< 2.9	mS/cm
Specific toxicity					
Na surface irrigation	*SAR*	< 3	3–9	> 9	
Na sprinkler irrigation	concentration	< 3	> 3		mEq/L
Cl surface irrigation	concentration	< 4	4–10	> 10	mEq/L
Cl sprinkler irrigation	concentration	< 3	> 3		mEq/L
B	concentration	< 0.7	0.7–3	> 3.0	mg/L
Miscellaneous effects					
NO_3 – N	concentration	< 5	5–30	> 30	mg/L
HCO_3	concentration	< 1.5	1.5–8.5	> 8.5	mEq/L
pH of water		Recommended range 6.5–8.4			

Thus, the *SAR* needs to be considered together with *TDS*, but none of the selected studies for water desalination considered the *SAR*. In theory, the RO permeate is suitable for

irrigation because RO removes all the sodium, calcium, and magnesium ions. For example, 0.001 mmoles/L of sodium, calcium, and magnesium results in a *SAR* of 0.03. NF permeate is not suitable for irrigation because its high rejection for divalent ions and low rejection for monovalent ions results in a high *SAR*. For example, 0.001 mmoles/L of calcium and magnesium and 1 mmoles/L of sodium results in a *SAR* of 31.6. In this case, adding 0.22 mmoles/L of calcium as a post-treatment would decrease the *SAR* to 3. Regarding ED, monovalent selective membranes have been fabricated which remove sodium and potassium with precise rejection rates, allowing to control the *SAR* [74]. However, ED does not perform well for LDAC applications

Although stand-alone RO was proven to be unsuitable for LD regeneration, RO can be combined with NF. Thus, multi-stage NF having a last RO stage is a feasible solution for LD regeneration that does not require post-treatment. Consequently, among the six technologies, multi-stage NF having a last RO stage is the most suitable technology for greenhouse irrigation.

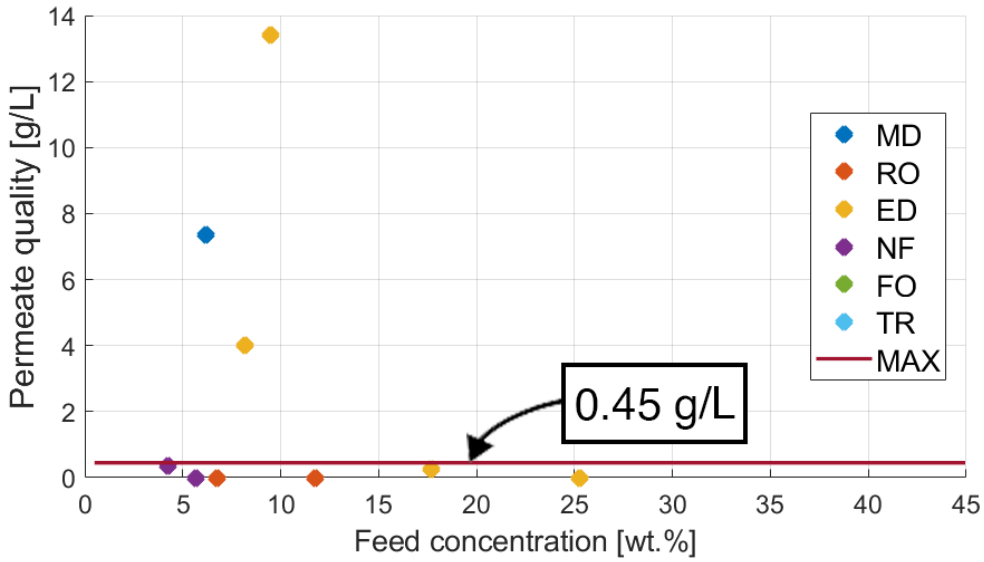

Figure 2-10. Permeate quality against feed concentration of the selected desalination studies. The "MAX" line represents the threshold of 0.45 g/L taken from the guidelines of water quality for irrigation based on Ayers and Westcot [258].

Chapter 3: Concept design of a greenhouse cooling system using multi-stage nanofiltration for liquid desiccant regeneration

Title of published paper: Concept design of a greenhouse cooling system using multi-stage nanofiltration for liquid desiccant regeneration

Paper information: Applied Thermal Engineering, 2022. 216: p. 119057.

Author contributions and affiliations:

- P. Pasqualin: original draft, writing, review, editing, modelling, data curation, investigation and visualisation

- P.A. Davies: conceptualisation, review and editing

School of Engineering, University of Birmingham, Edgbaston Birmingham B15 2TT, UK.

3.1 Introduction

Greenhouses in hot climates often struggle to produce crops during summer because the temperature inside the greenhouse rises above the acceptable range for cultivation [9]. To enable cultivation year-round, cooling technologies are needed, but conventional technologies such as vapour compression and evaporative cooling have significant downsides. Vapour compression requires large amounts of energy and typically utilises refrigerants that contribute to global warming; and evaporative cooling is only suitable for locations with abundant supplies of water. Therefore, resource-efficient greenhouses are not yet available for hot climates with limited water availability [259]. To address this important gap, there is a need for improved processes with low water demands.

LDAC has the potential to replace conventional cooling because it is more energy efficient and environmentally friendly [260], and allows storage of the LD for use when needed [10]. Another advantage is that LDAC provides simultaneous cooling and dehumidification.

Dehumidification is especially important for greenhouses, where crops continually release water vapour by transpiration [23]. Because of transpiration, the cooling system must remove large amounts of vapour, especially when operated in closed recirculation. Closed recirculation has several advantages over open ventilation, usually resulting in higher quality and yield of crops [24]. Moreover, it allows CO_2 enrichment without losing CO_2 to the surroundings; and it protects against insects and pests [24]. Closed recirculation can also decrease energy and water demands [24].

For effective vapour absorption using LDAC, high LD concentrations are required [18, 46]. The absorbed moisture must be removed from the LD in a process called regeneration [5]. LDAC presents several challenges, but the high energy requirement of regeneration is the most critical [17]. Some early studies focused on open evaporative regenerators which is an

energy-intensive and inefficient approach [55]. For example, one study found that open evaporative regenerators would occupy an area up to four times the plan area of the greenhouse [22]. Therefore, there is a need for more efficient and compact LD regeneration.

Membrane-based desalination technologies have been proposed as alternative LD regenerators. These technologies include membrane distillation [88-92], reverse osmosis (RO) [121], and electrodialysis [64, 251, 253-255]. In general, membrane-based desalination technologies can be pressure-driven (such as reverse osmosis and nanofiltration) or thermally-driven (such as membrane distillation). Several studies found that pressure-driven are more efficient than thermally-driven membrane processes for seawater and brackish water desalination [63, 96, 111]. Therefore, it is reasonable to expect that pressure-driven membrane processes may also be more efficient for LD regeneration. So far, however, high LD concentrations have prevented the use of pressure-driven membrane processes because the burst pressure of the membrane would be exceeded.

To overcome the burst pressure limitation, multi-stage NF can be used. Multi-stage NF has received interest as an energy-efficient membrane process for highly concentrated solutions. In contrast to RO, NF membranes operate with a total osmotic pressure difference higher than the burst pressure of a single membrane. This is because the NF membranes have lower rejections than commercial RO membranes (the rejection of which is about 98% [107, 108]), allowing the NF membranes to gradually decrease the LD concentration via several stages. As a result, the feed osmotic pressure is divided among the stages, allowing the osmotic pressure difference across each membrane to be lower than its burst pressure.

Though not yet used in LDAC, multi-stage NF systems have been investigated theoretically for concentration of seawater. For example, Altaee and Sharif [132] modelled a 2–stage NF system and predicted permeate qualities of 0.254 and 0.359 g/L when treating

seawater with concentrations of 35 and 43 g/L, respectively. More recently, Wang et al. [73] modelled a multi-stage NF system capable of obtaining highly concentrated brines for crystallisation applications in zero liquid discharge systems. These authors studied a 3-stage system (consisting of an initial RO stage, followed by 2 NF stages and then an energy recovery device) which concentrated seawater feed from 60 to 233 g/L and predicted an electric specific energy consumption (SEC_{el}) of 15.7 kWh_{el}/m^3 (electrical input per volume of permeate produced). They also modelled a 4-stage system, based on the same concept, and predicted a SEC_{el} of 8 kWh_{el}/m^3, thus showing that the SEC_{el} decreased as more stages were added. Compared to conventional alternatives such as mechanical vapour compression which has a SEC_{el} of 20–25 kWh_{el}/m^3 [101], the SEC_{el} of 8 kWh_{el}/m^3 is at least 2.5 times lower.

Although NF has not yet been experimentally investigated to concentrate highly concentrated LDs, it has been investigated using conventional LDs at lower concentrations. For example, Afonso and de Pinho [261] investigated the transport of $MgCl_2$ across an amphoteric NF membrane and reported rejections in the range of 10–30% using concentrations up to 1.05 wt.% (10.5 g/L). Murthy and Chaudhari [262] investigated the rejection of the NF-300 membrane (made by Applexion) using $CaCl_2$ and $MgCl_2$ at concentrations up to 1 wt.% (10 g/L). Their results showed that $CaCl_2$ rejection was between 70 and 80%, whereas $MgCl_2$ rejection was between 80 and 90%. Another study [263] investigated LiCl and $MgCl_2$ rejections using composite NF membranes with positively charged skin layers. The authors reported average LiCl and $MgCl_2$ rejections of 70 and 83%, respectively, for LD concentrations of 0.2 wt.% (2 g/L).

The above-mentioned studies showed that the NF membranes partially rejected LiCl, $CaCl_2$, and $MgCl_2$ which is the requirement for a multi-stage regeneration process. However, the concentrations were too low for LDAC applications. It should be noted that, although LiCl

and LiBr are often considered the best LD as they absorb large amounts of moisture [25], they are also very toxic [264, 265]. For example, a concentration above 0.1 g/L can be life-threatening for humans [266]. For this reason, this study prefers $CaCl_2$ as it has good dehumidification performance and is much less toxic [267].

The aim of this Chapter is to analyse a concept of a closed recirculated greenhouse cooled and dehumidified by a LDAC system using a multi-stage NF regenerator (namely *closed: NF-LDAC*). While previous studies considered LDAC for greenhouses using less efficient means of regeneration [9, 22, 268, 269], this concept is novel in that it assesses the potential of NF-LDAC to provide a compact and efficient solution.

The main location investigated is Mecca (Saudi Arabia) with the Red Sea being the heat sink of the system. In total, three types of climates are considered – *hot and humid* (Mecca), *hot and arid* (Timbuktu), *semi-hot and semi-arid* (Cairo). Realistic climatic data for Mecca, Timbuktu, and Cairo were taken from TRNSYS® software. For consistency, the same sink temperature is considered for all climates even though Timbuktu and Cairo are not near the Red Sea, as the aim of this study is to compare different climates and not the specific cities.

The structure of Chapter 3 is as follows: first, the concept design of *closed: NF-LDAC* is explained. Next, equations are provided to model the multi-stage NF regenerator and to calculate the temperature (T_{gh}) and relative humidity (RH_{gh}) of the greenhouse. Then, T_{gh} results are plotted for different operating conditions and locations, showing the improvement of *closed: NF-LDAC* against conventional cooling technologies for greenhouses. The monthly *COP* of *closed: NF-LDAC* and the monthly power requirement of the multi-stage regenerator are also presented. The main design parameters are varied to give a better understanding of the system. Finally, the results and future improvements of *closed: NF-LDAC* are discussed.

3.2 Theory

The design of *closed: NF-LDAC* is shown in Figure 3-1. Unlike in the open ventilated greenhouse proposed earlier [9, 269, 270], evaporative cooling is no longer needed for three reasons. First, evaporative cooling requires large amounts of water [5, 6], which might be unavailable in hot climates. Second, closed recirculation achieves low indoor temperatures without the need of an evaporative cooling pad. Third, evaporative cooling would risk increasing the RH_{gh} above 90%, which is the maximum recommended for typical crops [23], such as tomatoes, peppers, and cucumbers. Without the evaporative cooling pad, however, there is a risk of overheating at the early stages of cultivation, e.g., sprout and seedling, when the crops are small and transpire less – such that RH_{gh} may fall below 70% which is the minimum recommended for typical crops [23]. Since transpiration assists cooling by converting sensible into latent heat, such decreased transpiration could lead to T_{gh} above 32 °C which is the maximum recommended for typical crops. Nonetheless, this risk can be addressed by using additional shading during the early-stages of cultivation or by using misting to enhance cooling, such that the evaporative cooling pads are avoided.

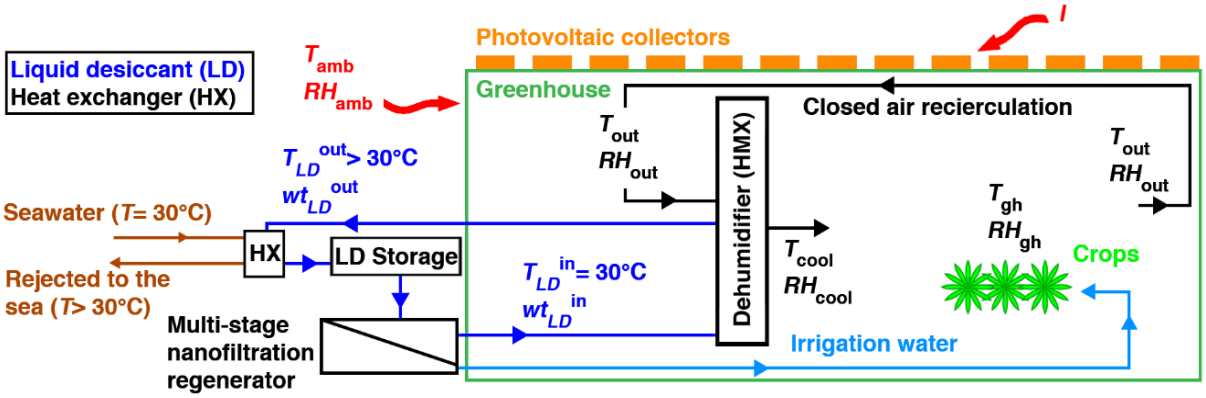

Figure 3-1. Schematic of a greenhouse operating with closed: NF-LDAC. A multi-stage nanofiltration regenerator is used to reconcentrate the liquid desiccant (LD). The greenhouse absorbs heat from the air entering the dehumidifier (HMX) and rejects this heat to the sea (assumed with a temperature equal to 30 °C) through a liquid-to-liquid heat exchanger (HX). Photovoltaic collectors are assumed to be uniformly distributed on top of the greenhouse. The names of the LD parameters are explained in Appendix 1.

The dehumidifier can be a wetted pad (similar in construction to an evaporative cooling pad), with LD flowing over it, absorbing moisture and heat from the incoming air. The cooled and dehumidified air is then directed to the crops. Inside the greenhouse, T_{gh} and the absolute humidity of the greenhouse (ω_{gh}) increase. T_{gh} increases due to the solar radiation and heat transferred through the cladding, while ω_{gh} due to crop transpiration. The hot and humid air leaving the crops is directed to the dehumidifier.

As the LD passes through the dehumidifier, its temperature (T_{LD}) increases. The LD can be cooled using seawater from the Red Sea near Mecca which is assumed to have a maximum temperature of 30 °C during the year, meaning it is possible to cool the LD to 30 °C year-round.

As the LD absorbs moisture from the air, it becomes diluted and needs to be reconcentrated. Figure 3-2 shows the proposed multi-stage NF regenerator. The input of the first stage is the LD from the dehumidifier. Every stage has two outputs, i.e., the permeate (which is less concentrated than the feed) and the brine (which is more concentrated than the feed). Every stage has a specific rejection which is in the range of 10–50% for most commercial NF

membranes [10, 53, 54, 57, 271, 272]. Therefore, the permeate of each stage contains a certain amount of LD. Due to the high concentration of the inlet LD (which is high even though the inlet is referred to as “diluted LD” in comparison to the outlet “concentrated LD” in Figure 3-2), as required for an efficient dehumidification, the osmotic pressure is high at the first stage. To avoid that the osmotic pressure difference across the first NF stage is higher than its burst pressure, the first stage must have a low rejection. The LD entering the following stage is less concentrated, and thus, the rejection can be higher than in the previous stage. Consequently, the NF stages should be arranged with increasing rejections until the permeate is sufficiently diluted to operate with nearly 100% rejection, e.g., using a RO stage. The brine of the first stage is the outlet reconcentrated LD, while the brine of each subsequent stage must be recirculated to the input of the respective upstream stage to avoid desiccant losses. The final RO stage produces pure water; its flowrate should be equal to the moisture that the LD absorbed in the dehumidifier. Therefore, the NF rejections should also be adjusted based on the absorbed moisture. Moreover, the permeate from the multi-stage system may be used for irrigation, thus closing the water cycle by directing the permeate to the crops. The multi-stage regenerator requires power for the pump upstream of each stage. The power requirement is approximately proportional to the number of stages. On the one hand, a small number of stages may not be able to reconcentrate the LD due to the high osmotic pressure. On the other hand, many stages can concentrate the LD, but with too many stages the power requirement may increase with little benefit. Therefore, an optimal number of stages must exist that minimises the power requirement for a given LD concentration. As a rule, the rejections of the NF membranes should be as high as possible but should also be chosen based on the target moisture removal rate.

The power requirement can be decreased by using an energy recovery device (ERD) to capture the high pressure of the concentrated LD and transfer its energy to the inlet diluted LD, thus avoiding wastage of this energy [273]. The proposed NF-LDAC system has photovoltaic (PV) collectors on top of the greenhouse to generate electricity to power the multi-stage regenerator. The PV collectors also provide shading which reduces the heat load entering the greenhouse. However, the shading factor should not be too high, otherwise photosynthesis will be slowed down.

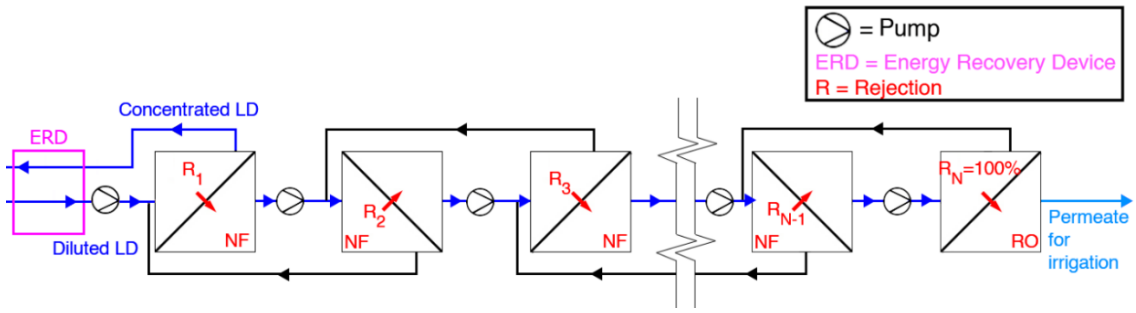

Figure 3-2. Schematic of a N-stage nanofiltration (NF) regenerator. The diluted liquid desiccant (LD) enters the system while the outputs are the concentrated LD and the permeate for irrigation. The system is composed of N-1 NF stages with rejections R_i, where "i" indicates the positioning number of the stage. The last stage is a reverse osmosis (RO) with a rejection of 100%. The NF stages have rejections in the range of 10–50%. The system includes an energy recovery device (ERD) that decreases the energy consumption of the system by recovering the pressure energy of the concentrated LD. A pump is placed before every stage which pressurises the feed to the desired pressure. In industrial applications, NF operates at 40 bar while RO at 70 bar.

The *closed: NF-LDAC* model includes the multi-stage NF regenerator, the dehumidifier, and the greenhouse. The modelling of the NF regenerator is first developed for a 1- stage regenerator, and then as a multi-stage regenerator by considering mass and flow balances among the stages. Following the approach of Wang et al. [73], this study also assumes that the pressure applied to each membrane equals the transmembrane osmotic pressure. This means that the model does not consider pressure losses. Moreover, the assumption of applied pressure being equal to the transmembrane osmotic pressure is ideal, but in practice the stages would not produce any permeate. Unlike in Wang et al. [73], the osmotic pressure here is

calculated using the Gibbs energy rather than the van 't Hoff equation which is an approximation valid only for dilute solutions. Since the LD must be highly concentrated in LDAC applications, such an approximation would be invalid for LDAC systems. Also, in contrast to Wang et al., the proposed design utilises the RO membrane in the last rather than the first stage. Due to the high concentration of the inlet LD, a first RO stage would not produce any permeate since the osmotic pressure difference to overcome would be higher than its burst pressure.

Then, a dehumidifier model is used to calculate the output conditions of the air and the LD passing through the dehumidifier. This dehumidifier model is based on the vapour pressure difference which is the driving force of moisture absorption. It calculates how much moisture must be absorbed by the LD to equilibrate the vapour pressures, while also accounting for energy balance. The dehumidifier model is presented in detail and validated with experiments in Appendix 1. Finally, the greenhouse is modelled by accounting for the solar radiation, the effect of the ambient conditions, and the crop transpiration.

The multi-stage NF regenerator and greenhouse models, though not validated directly in this Chapter (the multi-stage NF regenerator model is validated later in Chapter 5), have been validated elsewhere. The multi-stage NF regenerator model is based on the seminal work of Wang et al. [73] and is based on mass and flow conservation equations and thermodynamic principles. Compared to Wang et al., the multi-stage NF regenerator model here has been further developed by introducing the Gibbs energy equation to calculate the osmotic pressure more accurately at high concentrations. The greenhouse model is similar to Davies' model [9] which was experimentally validated by Abu-Hamdeh and Almitani [269] who investigated a 300 m^2 in Saudi Arabia and found errors below 6% using air mass flows of 3–30 kg/s. The greenhouse model also includes a refinement in the calculation of crop transpiration, by using

the equation proposed by Stanghellini [274]. Although there are different crop transpiration equations, comparative experimental studies found Stanghellini equation to be the most accurate for greenhouses [275, 276].

3.2.1 Modelling of the multi-stage regenerator

A schematic of the 1-stage regenerator with its input and outputs is shown in Figure 3-3. A single stage must satisfy the flow and mass conservation equations and the equation of rejection. Regarding the flow conservation, the feed flowrate entering a stage ($\dot{V}_\mathrm{f}$) [L/h] must be equal to the sum of the output flowrates of the brine ($\dot{V}_\mathrm{b}$) [L/h] and the permeate ($\dot{V}_\mathrm{p}$) [L/h], as described in Eq. 2-1.

$$\dot{V}_\mathrm{f} = \dot{V}_\mathrm{b} + \dot{V}_\mathrm{p} \tag{2-1}$$

Regarding the mass conservation, the product of the feed concentration (C_f) [g/L] and feed flowrate must be equal to the product of the brine concentration (C_b) [g/L] and brine flowrate plus the product of the permeate concentration (C_p) [g/L] and permeate flowrate, as described in Eq. 2-2.

$$\dot{V}_\mathrm{f} C_\mathrm{f} = \dot{V}_\mathrm{b} C_\mathrm{b} + \dot{V}_\mathrm{p} C_\mathrm{p} \tag{2-2}$$

Lastly, the rejection (R) is defined as 1 minus the permeate concentration which is divided by the feed concentration:

$$R = 1 - \frac{C_\mathrm{p}}{C_\mathrm{f}} \tag{2-3}$$

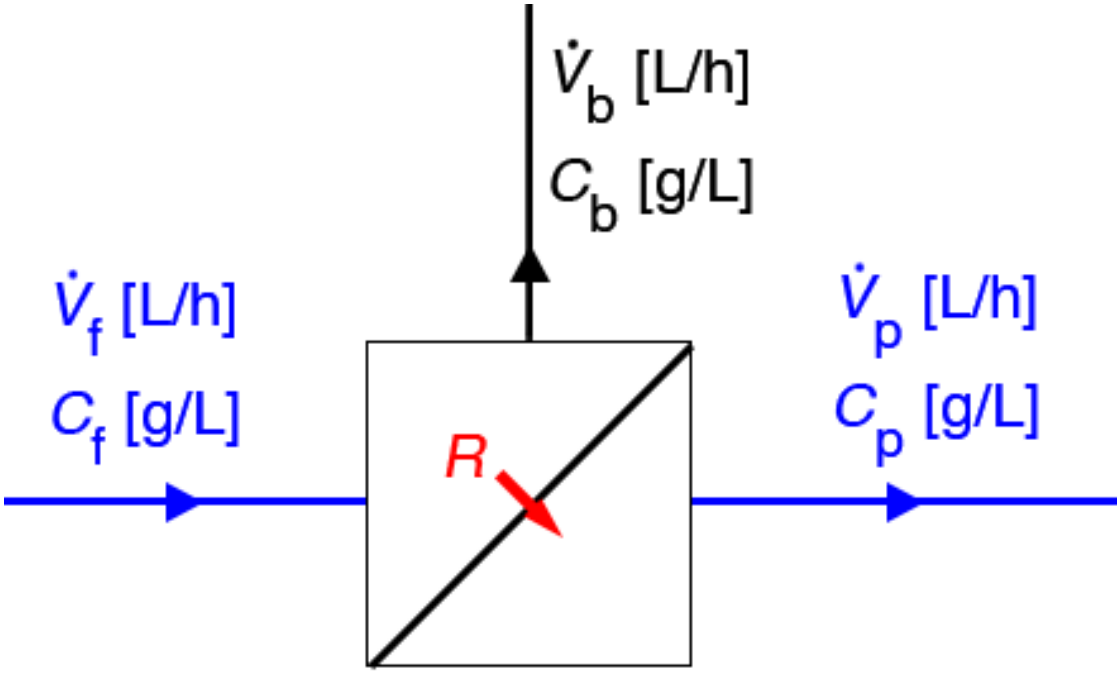

Figure 3-3. Schematic of the 1-stage regenerator. The "$\dot{V}$" values represent flowrates, "C" concentrations, and "R" the rejection. The subscript letter "f" represents the feed, "b" represents the brine, and "p" the permeate.

The osmotic pressure difference ($\Delta\Pi$) based on Gibbs energy [bar] can be calculated as (adapted from Smith [277]):

$$\Delta\Pi = \frac{T_K \bar{R}_u \left[\ln(ERH_p) - \ln(ERH_b)\right]}{V_w} \tag{2-4}$$

where $\Delta\Pi$ is assumed equal to is the applied pressure (ΔP) [bar], $\bar{R}_u$ = 8.314 J/(K mol) is the universal gas constant, which must be converted to 0.0832 (L bar)/(K mol) for consistency with the units of the other parameters, T_K is the temperature [K], V_w =0.018 L/mol is the inverse of the pure water molarity, ERH_p and ERH_b are the equilibrium relative humidities of the permeate and brine, respectively. Conde et al. [47] measured the ERH of $CaCl_2$ (ERH_{CaCl2}) for various concentrations; these data were used to create a polynomial fit of ERH_{CaCl2} as function of concentration:

$$ERH_{\mathrm{CaCl2}} = 26.96x^4 - 19.23x^3 + 0.6232x^2 - 0.4079x + 1 \quad (2\text{-}5)$$

where x is the $CaCl_2$ mass fraction per mass of solution. The outputs of a single stage can be calculated by rearranging equations 2-1, 2-2, 2-3, and 2-4. Thus, the concentration of the permeate of the stage can be calculated as:

$$C_{\mathrm{p}} = C_{\mathrm{f}}(1 - R) \quad (2\text{-}6)$$

The ERH of the brine can be calculated as:

$$ERH_{\mathrm{b}} = \exp\left[\ln\left(ERH_{\mathrm{p}}\right) - \frac{\Delta P\, V_{\mathrm{w}}}{T_{\mathrm{K}}\bar{R}_{\mathrm{u}}}\right] \quad (2\text{-}7)$$

where the weight concentration (percentage of solute per solution) of the brine (wt_{b}) [wt.%] can be calculated by inverting Eq. 2-5 as:

$$wt_{\mathrm{b}} = -498\, ERH_{\mathrm{b}}{}^4 + 1091\, ERH_{\mathrm{b}}{}^3 - 853.6\, ERH_{\mathrm{b}}{}^2 + 236\, ERH_{\mathrm{b}} + 25.46 \quad (2\text{-}8)$$

where wt_{b} is converted to C_{b} [g/L] using the following equation:

$$C_{\mathrm{b}} = \frac{\frac{wt_{\mathrm{b}}}{10^2 - wt_{\mathrm{b}}}}{10^{-3} + \frac{wt_{\mathrm{b}}/\rho_{\mathrm{CaCl2}}}{10^2 - wt_{\mathrm{b}}}} \quad (2\text{-}9)$$

where ρ_{CaCl2} is the density of pure solid anhydrous $CaCl_2$ equal to 2150 kg/m^3. The output flowrates of the single stage are calculated by rearranging equations 2-1 and 2-2, thus:

$$\dot{V}_{\mathrm{b}} = \dot{V}_{\mathrm{f}}\frac{C_{\mathrm{f}} - C_{\mathrm{p}}}{C_{\mathrm{b}} - C_{\mathrm{p}}} \quad (2\text{-}10)$$

$$\dot{V}_{\mathrm{p}} = \dot{V}_{\mathrm{f}} - \dot{V}_{\mathrm{b}} \quad (2\text{-}11)$$

Figure 3-4 shows how the recovery, i.e., $\dot{V}_{\mathrm{p}}/\dot{V}_{\mathrm{f}}$, of the 1-stage varies with R, C_{f}, and ΔP.

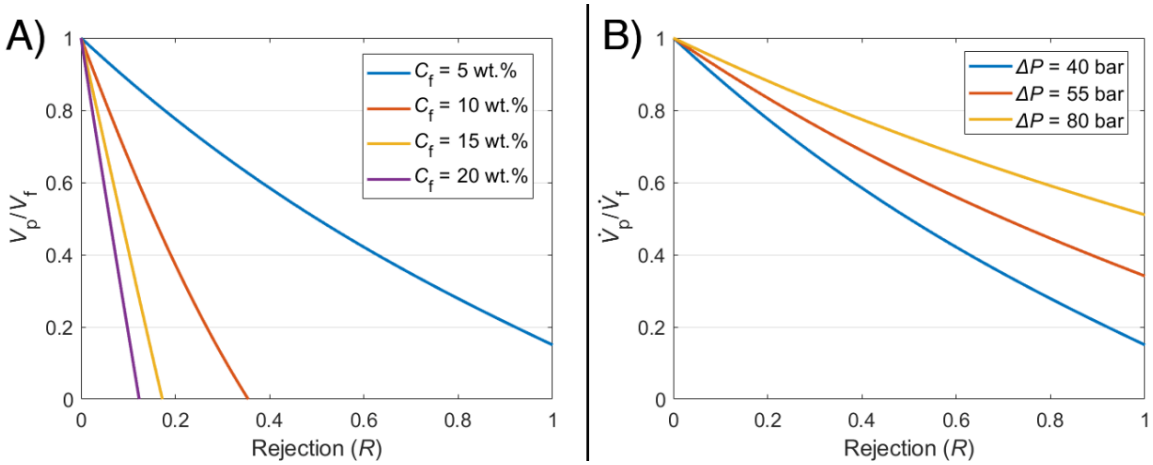

Figure 3-4. A) Recovery of the 1-stage regenerator against rejection (R) for $CaCl_2$ concentrations (C_f) of 5, 10, 15, and 20 wt.% (equivalent to 50, 105, 165, and 225 g/L), ΔP of 40 bar, and T of 25 °C. B) Recovery of the 1-stage regenerator against R for applied pressures (ΔP) of 40, 55, and 80 bar, C_f of 5 wt.% (50 g/L), and T of 25 °C.

In the multi-stage NF regenerator, the inputs and outputs of the stages are related to each other. For a *N*-stage regenerator composed of N-1 NF stages and a last RO stage, the feed flowrate of the j^{th} NF stage ($\dot{V}_{f,j}$) [L/h] is equal to the sum of the permeate flowrate of the previous stage ($\dot{V}_{p,j-1}$) [L/h] and the brine flowrate of the next stage ($\dot{V}_{b,j+1}$) [L/h], as described by Eq. 2-12.

$$\dot{V}_{f,j} = \dot{V}_{p,j-1} + \dot{V}_{b,j+1} \tag{2-12}$$

Similarly, the feed concentration of the j^{th} NF stage ($C_{f,j}$) [g/L] is given by:

$$C_{f,j} = \frac{\dot{V}_{p,j-1} C_{p,j-1} + \dot{V}_{b,j+1} C_{b,j+1}}{\dot{V}_{f,j}} \tag{2-13}$$

Equations 2-12 and 2-13 are valid for j from 1 to N-1. For j=N, since there is no brine recirculation in the last RO stage, the feed flowrate ($\dot{V}_{f,N}$) [L/h] and concentration ($C_{f,N}$) [g/L] at the RO stage are given by:

$$\dot{V}_{\mathrm{f,N}} = \dot{V}_{\mathrm{p,N-1}} \tag{2-14}$$

$$C_{\mathrm{f,N}} = \frac{\dot{V}_{\mathrm{p,N-1}} C_{\mathrm{p,N-1}}}{\dot{V}_{\mathrm{f,N}}} \tag{2-15}$$

The electric power requirement of the N-stage regenerator ($Power_{\mathrm{reg}}$) [kW_{el}] is given by the sum of the electric power requirements of the pumps $Power_{\mathrm{pump,j}}$ [kW_{el}] preceding each stage. For j from 1 to N, $Power_{\mathrm{pump,j}}$ is calculated as:

$$Power_{\mathrm{pump,j}} = \frac{\Delta P \, \dot{V}_{\mathrm{p,j-1}}}{36 \times 10^3 \, \eta_{\mathrm{pump}}} \tag{2-16}$$

where $\dot{V}_{\mathrm{p,N-1}}$ is the flowrate [L/h] entering the pump before the j^{th} stage. For the first stage (j=1), $\dot{V}_{\mathrm{p,0}}$ is equal to $\dot{V}_{\mathrm{f,1}}$. η_{pump} is the efficiency of the pump, assumed equal to 0.85 based on manufacturer datasheets [278]. ΔP is set to 40 bar for the NF stages [124-126, 128] and 70 bar for the RO stage [63]. An ERD can be used to save energy ($Power_{\mathrm{ERD}}$) [kW_{el}] that would be wasted otherwise, calculated as:

$$Power_{\mathrm{ERD}} = \frac{\Delta P \, \dot{V}_{\mathrm{b,1}} \, \eta_{\mathrm{ERD}}}{36 \times 10^3} \tag{2-17}$$

where $\dot{V}_{\mathrm{b,1}}$ is the flowrate of the concentrated LD and η_{ERD} is the efficiency of the ERD assumed equal to 0.9 (isobaric pressure exchanger [279] with 5% friction losses). Therefore, $Power_{\mathrm{reg}}$ is calculated as:

$$Power_{\mathrm{reg}} = \sum_{j=1}^{N} Power_{\mathrm{pump,j}} - Power_{\mathrm{ERD}} \tag{2-18}$$

The electric specific energy consumption (SEC_{el}) [kWh_{el}/m^3] of the multi-stage NF regenerator is given by dividing $Power_{reg}$ with the outlet permeate flowrate ($\dot{V}_{p,end}$) [L/h]:

$$SEC_{el} = 3.6 \frac{Power_{reg}}{\dot{V}_{p,end}} \tag{2-19}$$

The main case – LD mass flow of 20 kg/s, LD concentration of 15 wt.% (165 g/L) and LD temperature of 30 °C – has a SEC_{el} of 86 kWh_{el}/m^3.

Due to the brine recirculation, the above equations initially indicate time-varying feed flowrates at each stage, which converge to steady values after a certain simulation time. Since a high number of stages is required for concentrated LDs, the system is complex and can be solved using software, such as Matlab-Simulink® (release 2022a, Natick, Massachusetts: The MathWorks Inc). For instance, $CaCl_2$ with a concentration of 15 wt.% (165 g/L) requires at least 9 stages. This concentration was used for the main case because it maintains the RH_{gh} within optimal range of 70–90%.

3.2.2 Modelling of the greenhouse

To calculate T_{gh} [°C], the following heat balance equations can be used (taken from Davies [9]):

$$\dot{Q}_{gh} = \dot{m}_{Air}\, c_{p,Air}(T_{out} - T_{cool}) + hA_s(T_{gh} - T_{amb}) + ET_c\lambda \tag{2-20}$$

$$\dot{Q}_{gh} = IrrA_{gh}\tau\alpha(1-\beta) \tag{2-21}$$

$$T_{gh} = \frac{T_{cool} + T_{out}}{2} \tag{2-22}$$

where $\dot{Q}_{gh}$ is the exchanged heat in the greenhouse [kW_{th}], $\dot{m}_{Air}$ is the air mass flow [kg/s], $h_{p,Air}$ is the air heat capacity [kJ/(kg K)], h is the heat loss coefficient [kW/(m^2 K)], A_s is the

greenhouse surface area of the walls [m^2], Irr is the solar radiation [kW/m^2], A_{gh} is the greenhouse plan area [m^2], τ is the roof transmittance, α is the absorbance of greenhouse floor with crop, β is the fraction of A_{gh} covered by PV collectors, ET_c is the crop transpiration rate [kg/s] and λ is the latent heat of evaporation [kJ/kg]. T_{gh} is assumed equal to the average of the cool air directed to the crops (T_{cool}) and the air temperature at the end of the greenhouse (T_{out}).

The performance of *closed: NF-LDAC* is compared against three conventional open ventilated cooling technologies: simple fan ventilation (*Ventilation*), evaporative cooling (*EvapC*), and evaporative cooling combined with LDAC (*EvapC+LDAC*). For these four cooling technologies, T_{cool} is calculated as:

a) *Ventilation*: $T_{cool} = T_{amb}$

b) *EvapC*: $T_{cool} = T_{amb} - \varepsilon_{evap}(T_{amb} - {T_{wb}}^{amb})$

c) *EvapC+LDAC*: $T_{cool} = {T_{out}}^{deh} - \varepsilon_{evap}({T_{out}}^{deh} - {T_{wb}}^{deh})$

d) *closed: NF-LDAC*: $T_{cool} = {T_{out}}^{deh}$

where ${T_{wb}}^{amb}$ is the wet-bulb temperature of the ambient air, ε_{evap} is the effectiveness of the evaporative cooling pad, ${T_{out}}^{deh}$ is the outlet air temperature from the dehumidifier and ${T_{wb}}^{deh}$ is the wet-bulb temperature of the air at the exit of the dehumidifier. ${T_{out}}^{deh}$ is calculated using Eq. 1-1 to Eq. 1-14, as described in Appendix 1.

The temperature parameters used in Eq. 2-20 to Eq. 2-22 can be seen in Figure 3-1 for a better understanding. The combination of Eq. 2-20 to Eq. 2-22, yields:

$$T_{\mathrm{gh}} = \frac{Irr A_{\mathrm{gh}} \tau\alpha(1-\beta) - ET_{\mathrm{c}}\lambda + 2\dot{m}_{\mathrm{Air}} c_{\mathrm{p,Air}} T_{\mathrm{cool}} + hA_{\mathrm{s}} T_{\mathrm{amb}}}{2\dot{m}_{\mathrm{Air}} c_{\mathrm{p,Air}} + hA_{\mathrm{s}}} \quad (2\text{-}23)$$

$$T_{\mathrm{out}} = 2T_{\mathrm{gh}} - T_{\mathrm{cool}} \quad (2\text{-}24)$$

Since the model assumes closed recirculation, it is necessary to calculate the absolute humidity increment resulting from the crop transpiration (ET_{c}). ET_{c} [kg/s] is calculated as [274]:

$$ET_c = \frac{2k_c LAI}{\lambda} \frac{\frac{\Delta\, R_{\mathrm{n}}}{3600} + \frac{\left(VPD\, \rho_{\mathrm{Air}} c_{\mathrm{p,Air}}\right)}{r_{\mathrm{R}}}}{\Delta + 0.06735\left(1 + {}^{r_{\mathrm{c}}}/_{r_{\mathrm{a}}}\right)} A_{\mathrm{gh}} \quad (2\text{-}25)$$

where k_{c} is the crop coefficient, LAI is the leaf area index [m^2/m^2], Δ is the slope of the saturation vapour pressure curve [kPa/K], R_{n} is the net radiation above the canopy [kJ/(m^2 h)], VPD is the vapour pressure deficit of the air [kPa], ρ_{Air} is the density of the air [kg/m^3], r_{R} is the radiative resistance [s/m], r_{c} is the internal resistance of the canopy [s/m], and r_{a} is the aerodynamic external resistance [s/m]. The equations to calculate these parameters are provided in Appendix 2. The absolute humidity at the end of the greenhouse (ω_{out}) [$g_{\mathrm{v}}/kg_{\mathrm{a}}$] can be calculated as:

$$\omega_{\mathrm{out}} = 10^3 \frac{\dot{m}_{\mathrm{v,cool}} + ET_{\mathrm{c}}}{\dot{m}_{\mathrm{d,cool}}} \quad (2\text{-}26)$$

where $\dot{m}_{\mathrm{v,cool}}$ is the moisture mass flow at the exit of the dehumidifier [kg/s] and $\dot{m}_{\mathrm{d,cool}}$ is the mass flow of dried air at the exit of the dehumidifier [kg/s]. Once T_{out} and ω_{out} are calculated, the air conditions at the end of the greenhouse are fully determined. This air is directed to the dehumidifier.

Generally, the *COP* is calculated as the heating or cooling power output divided by the required input electric power [280]. In this case, the COP is calculated as the produced cooling power [kW_{th}] divided $Power_{reg}$ [kW_{el}]:

$$COP = \frac{\dot{Q}_{gh}}{Power_{reg}} \tag{2-27}$$

The multi-stage regenerator is assumed to be powered by PV collectors with power output P_{PV} [kW_{el}] given by:

$$P_{PV} = \eta_{PV} I \beta A_{gh} \tag{2-28}$$

where η_{PV} is the efficiency of the PV collectors, assumed equal to 18% based on commercial PV collectors [281]. The P_{PV} values are calculated using maximum solar radiations. Since the solar radiation varies based on time and climate, it is assumed that the PV collectors also include a solar battery storage. Thus, the multi-stage NF regenerator absorbs the required electric power from the solar battery storage when the power is needed.

Equations from 2-20 to 2-27 are used in an iterative method to simulate the closed recirculation of the greenhouse. The model is steady state, corresponding to 7 iterations as required for the convergence of T_{gh} (iterations were repeated until the percentage difference was below 0.02%).

Due to their high thermal inertia, residential buildings usually require dynamic modelling for accurate predictions. For greenhouses, however, steady-state models may be sufficient. For example, Kittas et al. [270] investigated a commercial greenhouse with an evaporative cooling system and found good agreement between their steady-state model and experimental results. The authors measured the temperature at the middle of the greenhouse with an error of

6% compared to their model. They also measured the temperature at the end of the greenhouse with an error of 3% compared to their model. Moreover, Abu-Hamdeh and Almitani [269] experimentally investigated a 300 m^2 greenhouse and compared their results using the steady-state model of Davies' study [9] (the model in this Chapter is also based on Davies' study). The authors measured the greenhouse temperature with air mass flows of 3–30 kg/s using *EvapC+LDAC* and found the steady-state model to be accurate (error below 6%). At the design phase, steady-state models give reliable results for greenhouses. For the steady-state model of *closed: NF-LDAC*, all parameters are considered constant. However, parameters such as k_c, *LAI*, and air flows are time dependent. At the performance phase, dynamic modelling could point out how to maximise the performance of *closed: NF-LDAC* based on climate and operating conditions. Such predictions require dynamic modelling based on time dependent parameters.

The values of the constant parameters used for the idealised steady-state model are summarised in Table 3-1. The values regarding the greenhouse dimensions and materials are based on typical greenhouses, taken from Davies [9]. The values for the maximum monthly solar radiations, maximum monthly ambient temperatures and average monthly ambient relative humidities for Mecca (hot and humid), Timbuktu (*hot and arid*), and Cairo (*semi-hot and semi-arid*) are shown in Table 3-2. The weather data was taken from TRNSYS® software (which generates the weather data using Meteonorm version 5.0.13).

Table 3-1. Values of constant parameters used for the greenhouse model. Values with an "" are taken from Davies [9].*

Parameter	Value	Unit	Full name of parameter
α	0.7*		Absorbance of greenhouse floor with crop
β	0.5*		Fraction of roof area covered by PV collectors
τ	0.8*		Roof transmittance
h	0.0042*	kW/(m^2 K)	Heat loss coefficient
A_{gh}	250*	m^2	Floor area of the greenhouse
A_{s}	450*	m^2	Surface area of the greenhouse
$\dot{m}_{\mathrm{Air}}$	20	kg/s	Air mass flow
$h_{\mathrm{p,Air}}$	1.013	kJ/(kg K)	Heat capacity of the air
LAI	0.8	m^2/m^2	Leaf area index
k_{c}	0.45		Crop coefficient
$\dot{m}_{\mathrm{LD}}$	20	kg/s	Liquid desiccant mass flow
η_{PV}	0.18		Efficiency of the photovoltaic collectors
η_{pump}	0.85		Efficiency of the pump
$\varepsilon_{\mathrm{evap}}$	0.8		Effectiveness of the evaporator

Table 3-2. Maximum monthly solar radiations, maximum monthly ambient temperatures, and average monthly ambient relative humidities for A) Mecca (hot and humid), B) Timbuktu (hot and arid), and C) Cairo (semi-hot and semi-arid).

Maximum ambient temperature [°C]												
A	34.7	35.15	39.05	41.2	44.75	45.45	46.35	44	43.9	41.4	37.3	34.85
B	33.1	36.05	38.65	41.55	42.6	42.25	42.35	38.85	39.65	39.3	35.3	31.6
C	22.4	25.65	31.15	36.5	37.5	38.65	39.15	35.9	36.3	33.15	28.5	23.95
Maximum solar radiation [kW/m^2]												
A	0.820	0.953	1.004	1.039	1.053	1.057	1.054	1.027	1.012	0.993	0.890	0.787
B	0.843	0.940	0.995	1	0.997	0.970	0.973	0.976	0.968	0.933	0.866	0.820
C	0.658	0.786	0.909	0.976	0.988	1.010	0.989	0.951	0.906	0.822	0.695	0.593
Average ambient relative humidity [%]												
A	77.5	78.5	72	64	63	59	62	70.5	74	74.5	81	89
B	33.16	25.85	26.42	34.93	42.36	49.65	56.24	68.03	65.91	55.66	38.17	36.14
C	59.4	52.57	49.74	43.63	41.62	46.54	55.25	58.85	58.58	56.96	61.08	62.59

3.3 Results

The four technologies, namely *Ventilation*, *EvapC, EvapC+LDAC,* and *closed: NF-LDAC* have different equations for T_{cool}, from which T_{gh} is calculated. Figure 3-5 shows T_{gh} results for the four technologies. The seventh (i.e., final and convergent) iteration is shown for *closed: NF-LDAC*.

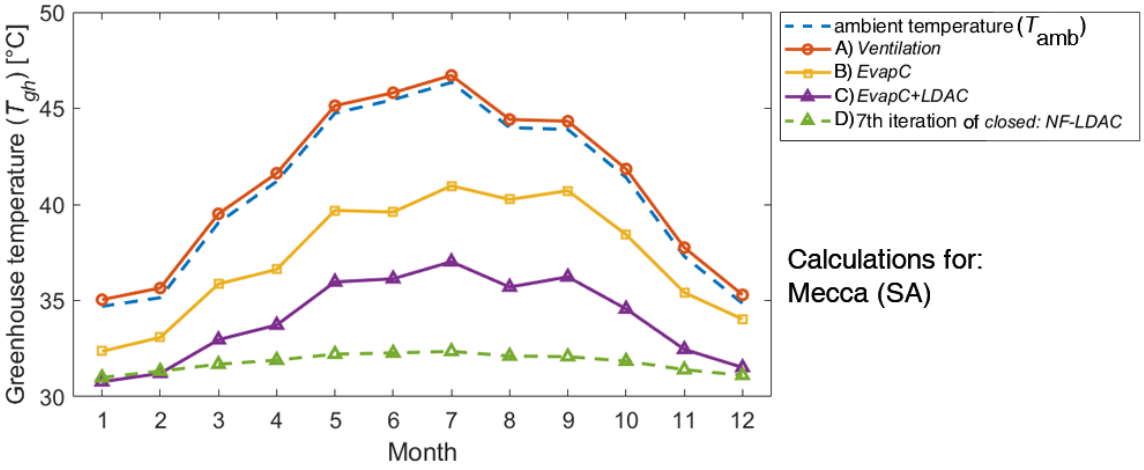

Figure 3-5. Monthly ambient temperature (T_{amb}) and monthly greenhouse temperature (T_{gh}) calculated for four cooling technologies: A) simple fan ventilation (Ventilation), B) conventional evaporative cooling (EvapC), C) evaporative cooling coupled with conventional LDAC (EvapC+LDAC), and D) the proposed closed recirculated LDAC using a multi-stage nanofiltration regenerator (closed: NF-LDAC). Cases A, B, and C are illustrated in a previous paper [9]. Case D) shows the results for the seventh (last and convergent) model iteration. Case D) is illustrated in Figure 3-1. These results are regarding hot and humid climates (such as Mecca, Saudi Arabia).

Regarding the *COP* of *closed: NF-LDAC*, this remains between 11.9 and 13, with an average of 12.4 during the year (Figure 3-6). The *COP* depends on the power requirement of the 9-stage NF regenerator, which requires at maximum 6.2 kW_{el} (Figure 3-6). The *COP* is calculated using maximum solar radiations which represent the worst conditions for the greenhouse, but the best for the PV collectors which can generate more power.

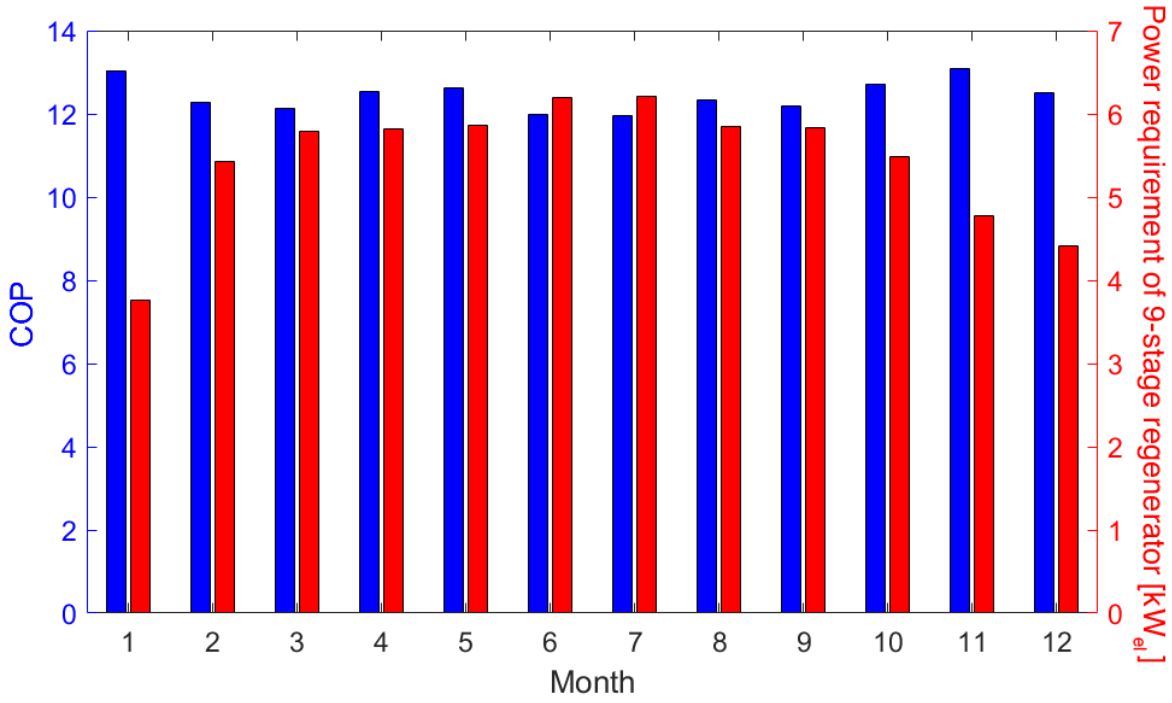

Figure 3-6. Monthly coefficient of performance (COP) for closed: NF-LDAC using a 9-stage nanofiltration regenerator (values on the left y-axis) and monthly power requirement of the 9-stage NF regenerator (values on the right y-axis). The results are regarding hot and humid climates (such as Mecca, Saudi Arabia) for a 250 m^2 greenhouse.

The results of Figures 3-5 and 3-6 are for the main case using $CaCl_2$ with a mass flow of 20 kg/s, concentration of 15 wt.% (165 g/L), and temperature of 30 °C. The LD temperature is an important parameter that can affect the greenhouse conditions. Therefore, three LD temperatures of 25, 30, and 35 °C have been considered and the results for the monthly T_{gh}, RH_{gh}, and ω_{gh} are shown in Figure 3-7.

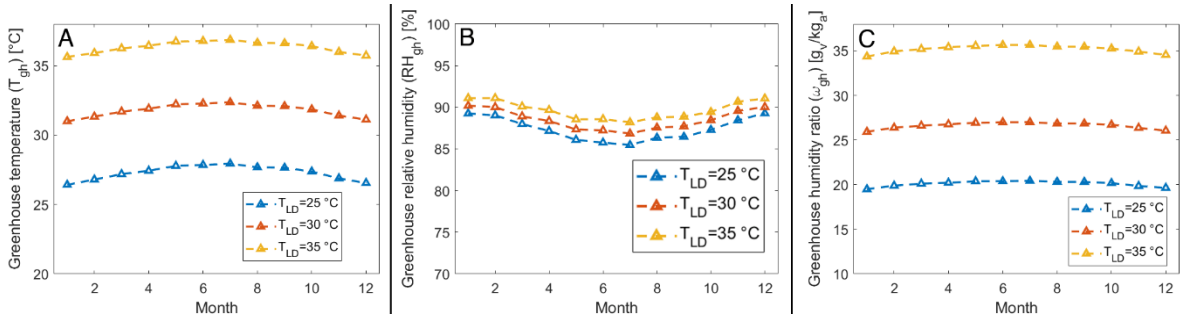

Figure 3-7. A) Monthly greenhouse temperature (T_{gh}), B) monthly greenhouse relative humidity (RH_{gh}), and C) monthly greenhouse humidity ratio (ω_{gh}) for LD temperatures (T_{LD}) of 25, 30, and 35 °C. These results are regarding hot and humid climates (such as Mecca, Saudi Arabia) for closed: NF-LDAC.

Other parameters with a significant effect are the LD mass flow, the sink temperature, and the fraction of plan area covered by PV collectors (β). Regarding the LD mass flow, the monthly T_{gh}, RH_{gh}, and ω_{gh} are shown in Figure 3-8 for LD mass flows of 10, 20, and 30 kg/s.

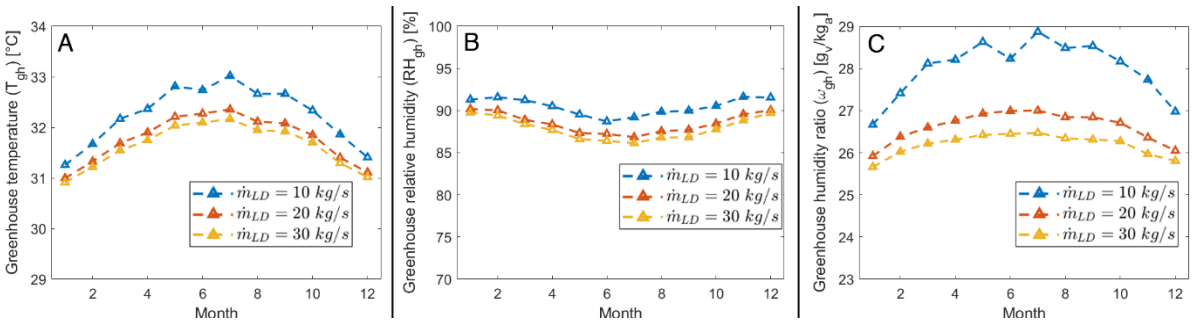

Figure 3-8. A) Monthly greenhouse temperature (T_{gh}), B) monthly greenhouse relative humidity (RH_{gh}), and C) monthly greenhouse humidity ratio (ω_{gh}) for LD mass flows ($\dot{m}_{LD}$) of 10, 20, and 30 kg/s. These results are regarding hot and humid climates (such as Mecca, Saudi Arabia) for closed: NF-LDAC.

Lower T_{gh} and RH_{gh} can be achieved with higher LD mass flows, but T_{gh} and RH_{gh} change marginally between LD mass flows of 20 and 30 kg/s. Since a LD mass flow of 30 kg/s would be hard to achieve at the dehumidifier, the LD mass flow of the main case was set to 20 kg/s. The $Power_{\mathrm{reg}}$ and SEC_{el} of the 9-stage NF regenerator for the three investigated LD mass flows are shown in Table 3-3.

Table 3-3. Electric specific energy consumption (SEC_{el}) and electric power requirement ($Power_{reg}$) of the 9-stage NF regenerator for LD mass flows ($\dot{m}_{LD}$) of 10, 20, and 30 kg/s.

$\dot{m}_{\mathrm{LD}}$ [kg/s]	$Power_{\mathrm{reg}}$ [$\mathrm{kW_{el}}$]	SEC_{el} [$\mathrm{kWh/m^3}$]
10	7.1	105
20	6.2	86
30	5.3	78

Regarding the sink temperature, this study considers a main case value of 30 °C. The sink temperature is important as lower sink temperatures allows lower T_{gh}. Figure 3-9 shows the results for the monthly T_{gh}, RH_{gh}, and ω_{gh} having sink temperatures of 30 and 26 °C. The sink temperature of 26 °C was arbitrarily selected as a temperature below 30 °C to compare with the sink temperature of 30 °C.

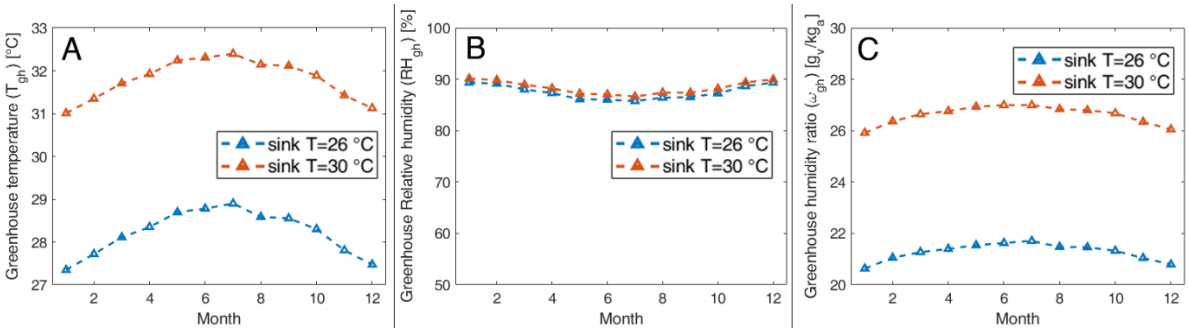

Figure 3-9. A) Monthly greenhouse temperature (T_{gh}), B) monthly greenhouse relative humidity (RH_{gh}), and C) monthly greenhouse humidity ratio (ω_{gh}) for sink temperatures (sink T) of 26 and 30 °C. These results are regarding hot and humid climates (such as Mecca, Saudi Arabia) for closed: NF-LDAC.

Regarding β, a value of 0.5 was used. The minimum β for single-band gap PV collectors is 0.15 [93], but β of 0.15 is too low. The T_{gh} increases by 3 °C by decreasing β from 0.5 to 0.15 (Figure 3-10). Since β of 0.5 maintains the T_{gh} below 32 °C (maximum allowable), β of 0.5 was selected as the main case value.

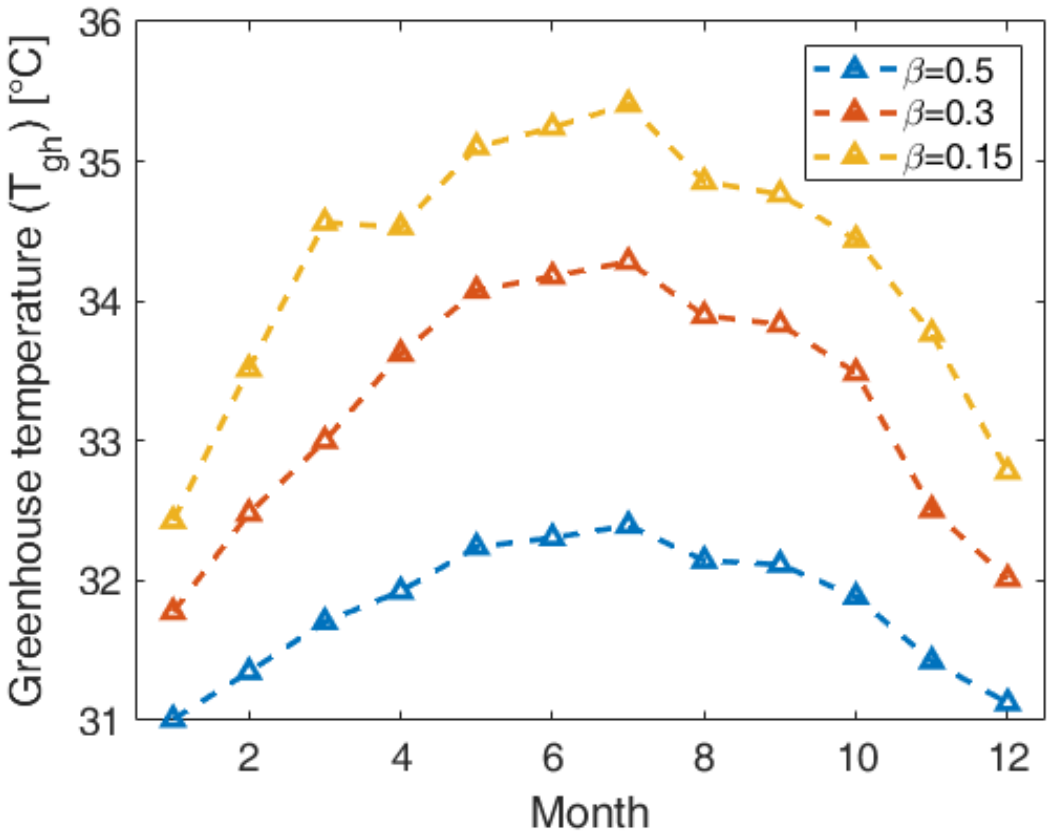

Figure 3-10. Monthly greenhouse temperature (T_{gh}) calculated for PV collectors covering fractions of 0.5, 0.3, and 0.15 of the greenhouse plan area (β). These results are regarding hot and humid climates (such as Mecca, Saudi Arabia) for closed: NF-LDAC.

Finally, climate is also investigated. The main case climate is *hot and humid* (like Mecca, Saudi Arabia), but the same greenhouse model was evaluated for *hot and arid* (like Timbuktu, Mali) and *semi-hot and semi-arid* climates (like Cairo, Egypt). Figure 3-11 shows the monthly T_{gh} for these other two climates.

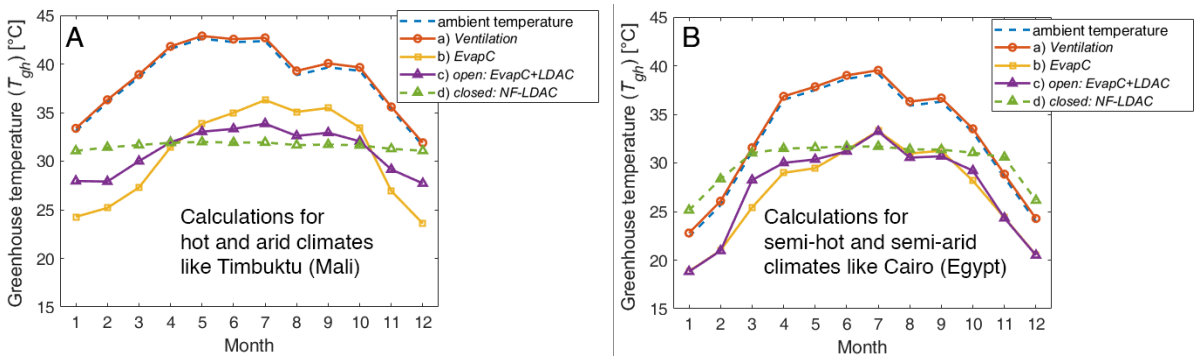

Figure 3-11. Monthly ambient temperatures and monthly greenhouse temperature (T_{gh}) calculated for four cooling technologies, as labelled in Figure 3-5, considering weather conditions of A) hot and arid climate (like Timbuktu, Mali) and B) semi-hot and semi-arid climate (like Cairo, Egypt).

3.4 Discussion

In *hot and humid* climates, such as Mecca, the technology using only a fan (*Ventilation*) does not provide any cooling; thus T_{gh} is equal to the ambient temperature. The addition of evaporative cooling (*EvapC*) achieves a temperature drop of 5.8 °C compared to *Ventilation* during summer; while the addition of both evaporative cooling and LDAC (*EvapC+LDAC*) achieves a temperature drop of 8.9 °C compared to *Ventilation* during summer (Figure 3-5). The proposed *closed: NF-LDAC* system, operating in closed recirculation using LDAC and a dehumidifier, achieves even lower temperatures, having T_{gh} of 4 °C lower than *EvapC+LDAC* during summer.

The *closed: NF-LDAC* system was evaluated by varying different parameters, including LD temperature, sink temperature, and fraction of greenhouse plan area covered by PV collectors (β). Regarding the LD temperature, lower LD temperatures are preferred because lower T_{gh} and RH_{gh} can be achieved (Figure 3-7). The LD mass flow was also investigated, with higher LD mass flows achieving lower T_{gh} and lower RH_{gh} (Figure 3-8). If the rejections of the membranes were held constant, higher LD mass flow would result in higher power requirement for the multi-stage NF regenerator because the power of the pumps is

proportional to the mass flow. However, higher LD mass produces more permeate. To maintain the permeate flowrate constant, the recovery must decrease by increasing the rejection of the membranes (see opposite trend of recovery and rejection in Figure 3-4), which decreases the flows across the multi-stage system, and thus decreases the power requirement of each pump. Consequently, higher LD mass flow decreases the electric power requirement and the SEC_{el} of the NF regenerator (Table 3-3).

Regarding the efficiency of *closed: NF-LDAC* for the main case ($CaCl_2$ with a mass flux of 20 kg/s, a temperature of 30 °C and a concentration of 15 wt.% or 165 g/L), an average *COP* of 12.4 (Figure 3-6) was achieved with T_{gh} below $32°C$ and RH_{gh} below 90% throughout the year. This *COP* approaches the maximum of 14.3 based on the ideal equation taken from Lefers et al. [5] for $CaCl_2$ with a concentration of 15 wt.% (165 g/L). A *COP* of 12.4 is significantly higher than the experimentally obtained with open evaporative solar regenerators, where values of only 0.3–0.5 were reported [57]. Moreover, commercial chillers using vapour compression have *COP* values of 2.5–4.3 [282-284]. This means that *closed: NF-LDAC* achieves *COP* values three times higher than commercially available technologies.

Although a 9-stage NF regenerator may be complex and expensive, there is potential to reduce the number of stages with improved NF membranes. The 9-stage system, using an applied pressure (ΔP) of 40 bar for the NF stages, requires at most 6.2 kW_{el} to reconcentrate $CaCl_2$ with a concentration of 15 wt.% (165 g/L) and achieves a SEC_{el} of 86 kWh_{el}/m^3. By using NF stages withstanding pressures of 55 bar, the 4-stage regenerator requires at most 6.2 kW_{el}, achieves a SEC_{el} of 87 kWh_{el}/m^3, and maintains the same *COP* as the 9-stage regenerator. This means that the NF stages require a burst pressure above 55 bar, which is reasonable since commercial RO membranes have burst pressures of 83 bar [107, 108]. Thus, research regarding the fabrication of NF membranes with higher burst pressures would

decrease the number of stages, the cost, and the size of the regenerator. The 4-stage and 9-stage regenerators have almost the same SEC_{el} for two reasons. On the one hand, the SEC_{el} is proportional to the power requirement of the pumps which in turn are proportional to ΔP. If the flow is fixed, a ΔP of 55 bar increases the power requirement by 38% compared to a ΔP of 40 bar. On the other hand, a 4-stage regenerator has fewer pumps and lower recirculating flows compared to the 9-stage regenerator. These two effects nearly cancel each other for this specific case, resulting in similar SEC_{el} values for both the 4-stage and 9-stage regenerators.

Regarding the effect of the sink temperature, lower sink temperature results in lower T_{gh} (Figure 3-9). Specifically, a sink temperature of 26 °C obtains a T_{gh} of 3.6 °C lower than the sink temperature of 30 °C.

Regarding β, the model used a β of 0.5 with a PV efficiency of 18%. The PV collectors produce from 15.7 to 23.6 kW_{el} considering monthly maximum solar radiations. Since the maximum power of the multi-stage NF regenerator is only 6.2 kW_{el} (Figure 3-6), the PV collectors produce more than twice the energy requirement of the multi-stage regenerator. However, lower β results in T_{gh} above the allowed maximum of 32 °C because of less shading (Figure 3-10), so these oversized PV collectors are preferred. Excess electricity may be possible to be exported to the grid if there is a scheme allowing the consumer to do so. If not, the excess electricity could be stored in batteries for local utilisation. For example, it may be helpful in maintaining system operation under transient conditions such as passing clouds. However, batteries have a high cost and their utilisation will depend on the payback time of the system. Another option is to employ a lower PV collector area together with passive shading to achieve 50% of overall shading and thus maintain the greenhouse temperature below 32 °C.

Theoretically, a β of 0.15 is the minimum for single-band gap PV collectors [93]. Although β of this study is higher than the ideal, future improvements in PV technology, such as higher PV efficiencies (η_{PV}) or selective PV cells, could lower β to values close to this ideal. On the one hand, higher η_{PV} would capture the same solar energy with a smaller PV area. Commercial PV cells have η_{PV} of ~20% [285], however, newer PV types such as thermophotovoltaics would require half the area of commercial PV cells because they can reach η_{PV} of ~40% [286]. On the other hand, selective PV cells capable of rejecting the infrared radiation would decrease T_{gh}. The infrared radiation makes up half of the total incoming radiation but, since infrared radiation is rejected by the crops [23], it only increases T_{gh}. Therefore, selective PV cells would be a major improvement for greenhouse applications, albeit their high expected cost.

Based on the second law of thermodynamics, a regeneration system driven by a generic solar thermal collector could provide cooling with a β of 0.37 [93]. However, experimental studies regarding open-type solar LD regenerators found that a β of 4 (i.e., four times the greenhouse plan area) is required depending on the climate [22]. Closed-type solar LD regenerators have also been investigated for LD regeneration and are expected to be more energy efficient than open-type regenerators [287]. For example, Yang and Wang [288] investigated a closed-type solar collector coupled with an evaporator to reconcentrate a LiCl solution. Although their study did not calculate β (as they did not investigate greenhouses), a comparison can be made based on the evaporated water which was 2.7 times higher than the open-type solar LD regenerator mentioned earlier [22]. Thus, closed-type solar LD regenerators may require a β of 1.5 (but would also require water for the evaporator) which is still much higher than β of 0.5 used for *closed: NF-LDAC*. Therefore, the results shows that a

multi-stage NF regenerator makes the system more compact, as the required β is several times lower compared to conventional open-type and closed-type solar collectors.

The effect of climatic conditions is mitigated by the greenhouse closed air recirculation. Thus, *closed: NF-LDAC* maintains T_{gh} below 32 °C independently of the climate (Figure 3-11). During winter, in a *semi-hot and semi-arid* climate (such as Cairo), *EvapC* and *EvapC+LDAC* achieve lower T_{gh} than *closed: NF-LDAC*. This is because the T_{amb} is lower than the sink temperature (assumed equal to 30 °C). Therefore, *closed: NF-LDAC* is advantageous when T_{amb} is above the sink temperature. During summer for *semi-hot and semi-arid* climates and during winter for *hot and arid* climates (such as Timbuktu), *EvapC* and *EvapC+LDAC* achieve lower temperatures than *closed: NF-LDAC*. This is because *EvapC* achieves low T_{gh} when operated with low RH_{amb}. Nonetheless, *EvapC* has high water demands. Based on energy balance equations, 10.36 L of water evaporates daily during winter for every m^2 of greenhouse plan area [L/(m^2 day)] (considering an inlet water temperature of 30 °C and an evaporative cooling pad effectiveness of 0.8). During summer, the evaporated water increases to 20.72 L/(m^2 day). Since the water supply must be higher than the rate of evaporation, *EvapC* would require at least 12 L/(m^2 day) of water during winter, and 24 L/(m^2 day) during summer. Therefore, *closed: NF-LDAC* could include *EvapC* to achieve lower monthly T_{gh} for *semi-hot and semi-arid* and *hot and arid* climates, but the water demand would be an issue for such water-scarce locations.

A conventional greenhouse requires water for the evaporative cooling pads and for irrigation. *closed: NF-LDAC* eliminates the need of evaporative pads because the LD is cooled using seawater (for example, using a liquid-to-liquid heat exchanger). Regarding the requirement for irrigation in conventional greenhouses, this is typically close to the crop transpiration rate. This water requirement is eliminated by *closed: NF-LDAC* because the

evaporated moisture from the crops is absorbed by the LD, collected as the permeate of the multi-stage NF regenerator, and reused for irrigation. Consequently, *closed: NF-LDAC* saves at least 16.8 L/(m^2 day) of water during winter, and 30.6 L/(m^2 day) during summer.

3.5 Conclusions

A novel LD regeneration system using a multi-stage NF regenerator for a closed recirculated greenhouse (*closed: NF-LDAC*) was modelled. The novelty is the utilisation of NF membranes to remove the absorbed moisture from the LD. This moisture can be recovered as the permeate of the multi-stage NF regenerator and reused for irrigation. In contrast, conventional regenerators waste the moisture by rejecting it to the environment. The main findings of Chapter 3 are:

• Lower LD temperature, higher LD mass flow, lower sink temperature, and higher β are better at maintaining the greenhouse in the acceptable temperature range (27–29 °C [9]) and relative humidity range (70–90% [23]) for crop cultivation.

• The proposed *closed: NF-LDAC* system is particularly advantageous in a *hot and humid* climate where the ambient temperature is above the sink temperature. In this climate, *closed: NF-LDAC* achieves temperatures of 4 °C lower than conventional cooling combining evaporative pads and open ventilated LDAC (*EvapC+LDAC*). Compared with technologies using evaporative cooling (*EvapC*), *closed: NF-LDAC* saves 16.8 L/(m^2 day) of water during winter, and 30.6 L/(m^2 day) during summer.

• For *hot and arid* and *semi-hot and semi-arid* climates, *closed: NF-LDAC* performs worse than the conventional technologies using *EvapC*. Nevertheless, it maintains the greenhouse temperature below 32 °C regardless of climate. *EvapC* is not combined with *closed: NF-*

LDAC to eliminate the water supply for irrigation. This is because *EvapC* has the disadvantage that it can only operate in water-abundant locations.

• For the main case – which considers a 250 m^2 greenhouse using $CaCl_2$ as the LD with a mass flow of 20 kg/s, a temperature of 30 °C, and a concentration of 15 wt.% (165 g/L) – the greenhouse temperature and relative humidity are maintained between optimal ranges for cultivation. This main case requires a 9-stage NF regenerator which has a maximum electric power requirement of 6.2 kW, a SEC_{el} of 86 kWh_{el}/m^3, and an annual average *COP* of 12.4. The electric power requirement of the 9-stage regenerator can be fully provided by PV collectors covering half the plan area of the greenhouse, while generating excess electricity for other purposes besides regenerating the LD.

• A 9-stage regenerator is required because commercial NF membranes have a burst pressure of around 40 bar [124-126, 128]. However, NF membranes withstanding pressures of 55 bar would give the same results using only 4 stages, thereby decreasing the complexity, size, and cost of the multi-stage regenerator. Therefore, the fabrication of improved NF membranes with rejections of 10–40% and high operating pressures is an important topic for future research.

Chapter 4: Experimental and theoretical investigation of nanofiltration membranes for liquid desiccant regeneration in greenhouse climatisation

Title of published paper: Experimental and theoretical investigation of nanofiltration membranes for liquid desiccant regeneration in air conditioning applications

Paper information: Applied Thermal Engineering, 2022. 221: p.119644.

Author contributions and affiliations:

- P. Pasqualin: conceptualisation, original draft, writing, review, editing, modelling, data curation, investigation and visualisation

- P.A. Davies: review and editing

School of Engineering, University of Birmingham, Edgbaston, Birmingham B15 2TT, UK.

4.1 Introduction

Since NF membranes have not yet been experimentally investigated for LD regeneration, there is a lack of knowledge about how their properties, such as rejection and permeate flux, change when operated with concentrated LDs. Therefore, the aim of Chapter 4 is to define experimental and theoretical methods to predict the rejection and permeate flux of NF membranes, according to the applied pressure and LD concentration.

A study regarding the influence of the operating conditions on NF membranes has already been done by Hilal et al. [133] who found that higher feed concentrations increase the reflection factor (σ), increase the solute permeability (P_s), decrease the permeate flux (J_v), and the observed rejection. These authors investigated NaCl weight concentrations of 0.5–2.5 wt.% (equivalent to 5–25 g/L), which are too low for LDAC applications. Moreover, NaCl is an ineffective LD [25]. To gain more practical insights into NF regeneration of typical LD concentrations, this Chapter investigates highly concentrated LDs such as LiCl, LiBr, and $MgCl_2$ that are typically used in LDAC systems [10, 18, 25, 35, 37-39, 44, 289-294].

The LD concentration can be correlated to the *ERH* of the LD [25]. Conde [47] and Zaytsev et al. [295] measured the *ERH* of LiCl, LiBr, and $MgCl_2$ for different weight concentrations (Figure 4-1). The concentration of the LD in a LDAC system depends on the required indoor relative humidity. For example, greenhouses require LD concentrations of 15–25 wt.% (165–290 g/L) [47, 295] because typical crops require relative humidities of 70–90% [23]. Residential buildings require higher LD concentrations, in the range of 30–40 wt.% (350–500 g/L) [47, 295], because human comfort requires relative humidities of 50% [50]. There are also niche applications which require relative humidities below 50%, such as in the pharmaceutical industry where injections must be prepared with relative humidities of 45% [296].

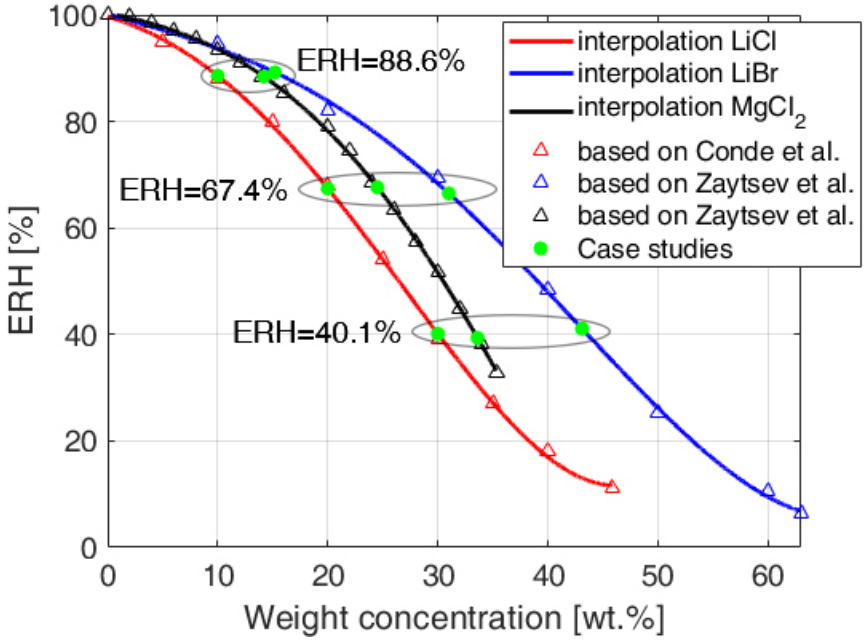

Figure 4-1. Equilibrium relative humidity (ERH) of the investigated case studies using LiCl, LiBr, and $MgCl_2$. The case studies were selected based on the ERH; three weight concentrations are shown for each liquid desiccant, having ERH values of 88.6, 67.4, and 40.1%. The case studies are shown in green dots, the triangles are based on Conde [47] and Zaytsev et al. [295] studies, and the lines are polynomial fittings of these two studies.

The investigated LD concentrations (indicated in Figure 4-1 as "case studies") were selected to have *ERH* being in the range of 40–90% to cover greenhouse, residential, and niche applications. LiCl concentrations of 10, 20, and 30 wt.% (105, 220, 355 g/L) were first selected which have *ERH* values of 88.6, 67.4, and 40.1%, respectively. Then, the concentrations of LiBr and $MgCl_2$ were chosen to have the same *ERH* values. Specifically, LiBr concentrations of 15.2, 31, and 43.1 wt.% (170, 400, 620 g/L) and $MgCl_2$ concentrations of 14.2, 24.5, and 33.6 wt.% (155, 285, 415 g/L) were selected. Since the *ERH* is the driving force of dehumidification, equivalent *ERH* allows a fair comparison among different LDs. The highest investigated concentrations of LiCl, LiBr, and $MgCl_2$ of 355, 620, and 415 g/L, respectively, are at least 14 times higher than in the study of Hilal et al. [133].

Since permeate flux is proportional to the difference between applied pressure (ΔP) and effective osmotic pressure ($\Delta \Pi_e$), higher ΔP is required at higher feed concentrations. Different equations have been proposed for desalination applications to calculate $\Delta \Pi_e$ [297]; however, these equations utilise the van 't Hoff approximation which is valid for dilute solutions like seawater, but not for highly concentrated solutions like LDs. For more accurate calculations, an iterative method to calculate $\Delta \Pi_e$ is proposed in this Chapter (later in Section 3.2.1).

The structure of Chapter 4 is as follows. First, the theory is presented. Then, the experimental set-up and procedure are explained. Subsequently, the results are presented for the observed rejections and permeate fluxes, and the reflection factor for the investigated case studies. Then, polynomial equations are proposed for the rejections and permeate fluxes. A new model (using accurate osmotic pressure and including variable rejection based on concentration and pressure) is introduced, providing improved calculations against idealised models (using constant rejection). Finally, the *COP* of the multi-stage NF regenerator is calculated, showing that the *COP* of a multi-stage NF regenerator using improved NF membranes can be several times higher than conventional solar regenerators.

4.2 Theory

4.2.1 Irreversible thermodynamics equations

The thermodynamic equations of NF are taken from Ahmad et al. [298] who used the same stirred cell used here. The experimental stirred cell has only a permeate, meaning that it is a dead-end filtration process. Information is also provided for which parameters can be fixed, measured, or calculated.

The permeate flux (J_v) [L/(m^2 h)] is proportional to the pure water permeability (L_p) [L/(m^2 h bar)] and the difference between ΔP [bar] and the product of $\Delta \Pi_e$ and reflection factor (σ).

$$J_v = L_p(\Delta P - \sigma \Delta \Pi_e) \quad (3\text{-}1)$$

The solute flux (J_s) [g/(m^2 h)] is calculated as the product of the solute permeability (P_s) [L/(m^2 h bar)] and the concentration difference between feed and permeate (ΔC) [g/L] plus a term that depends on the feed concentration (C_f) [g/L], σ, and J_v.

$$J_s = P_s \Delta C + (1 - \sigma) C_f J_v \quad (3\text{-}2)$$

where ΔC is calculated as

$$\Delta C = C_f - C_p \quad (3\text{-}3)$$

where C_p [g/L] is the permeate concentration, calculated as:

$$C_p = \frac{J_s}{J_v} \quad (3\text{-}4)$$

The observed rejection (R_{os}) is calculated through the feed and permeate concentrations:

$$R_{os} = 1 - \frac{C_p}{C_f} \quad (3\text{-}5)$$

but, due to the concentration polarisation (CP) effect, the true rejection (R_s) is calculated as:

$$R_s = 1 - \frac{C_p}{C_m} \quad (3\text{-}6)$$

where C_m [g/L] is the concentration at the wall on the feed side. R_s can also be calculated as:

$$R_s = \frac{\sigma(1 - F)}{1 - \sigma F} \quad (3\text{-}7)$$

where the flow parameter (F) is given from:

$$F = \exp\left(\frac{\sigma - 1}{P_{\mathrm{s}}} J_{\mathrm{v}}\right) \tag{3-8}$$

The parameters C_f, C_m, and C_p are correlated by:

$$\frac{C_{\mathrm{m}} - C_{\mathrm{p}}}{C_{\mathrm{f}} - C_{\mathrm{p}}} = \exp\left(\frac{J_{\mathrm{v}}}{3.6 \times 10^6 \, k_{\mathrm{s}}}\right) \tag{3-9}$$

where the mass transfer coefficient (k_{s}) [m/s] can be estimated from:

$$k_{\mathrm{s}} = \frac{Sh \, D_{\mathrm{w}}}{R_{\mathrm{sc}}} \tag{3-10}$$

where R_{sc} is the radius of the stirred cell (equal to 0.0255 m). The diffusion coefficient (D_{w}) [m^2/s] is estimated from:

$$D_{\mathrm{w}} = 2.7 \frac{10^{-4}}{MM^{0.71}} \tag{3-11}$$

where MM is the relative molecular mass [g/mol] of the LD, equal to 42.38, 86.84, and 95.211 g/mol for LiCl, LiBr, and $MgCl_2$, respectively.

The Sherwood number (Sh) is given by:

$$Sh = \gamma Re^{\lambda} Sc^{\theta} \tag{3-12}$$

According to Koutsou et al. [299], who performed experiments using the same stirred cell used here, the Sherwood number can be approximated as:

$$Sh = 0.49 Re^{0.55} Sc^{0.33} \tag{3-13}$$

while Reynold (Re) and Schmidt (Sc) numbers are calculated from:

$$Re = \frac{\rho v L}{\mu} \tag{3-14}$$

$$Sc = \frac{\mu}{\rho D_{\mathrm{w}}} \tag{3-15}$$

where ρ [kg/m^3] is the density of the solution, v [m/s] is the velocity of the fluid, L [m] is the characteristic length of the system, and μ [Pa s] is the viscosity of the solution. Here, Re number is calculated by using the rotational equation, given by:

$$Re = \frac{\rho\, rpm\, {R_{\mathrm{sc}}}^2}{\mu} \tag{3-16}$$

where rpm is the stirring rate equal to 700 rpm.

The osmotic pressure difference in desalination applications is calculated using the van 't Hoff approximation equation ($\Delta\Pi_{\mathrm{Hoff}}$) [297]:

$$\Delta\Pi_{\mathrm{Hoff}} = 0.0832 i T_K \frac{\Delta C}{M} \tag{3-17}$$

where i is the van 't Hoff dissociation parameter which for LiCl, LiBr, and $MgCl_2$ is approximately equal to 2, 2, and 3, respectively, and T_{K} is the temperature [K]. However, this expression is valid only for diluted solutions like seawater. Since the effective osmotic pressure difference ($\Delta\Pi_{\mathrm{e}}$) is much higher for concentrated LDs, $\Delta\Pi_{\mathrm{e}}$ is calculated more accurately through an iterative method to estimate σ. Removing the $\Delta\Pi_{\mathrm{Hoff}}$ equation results in an implicit equation for σ. Starting from an initial estimate of σ, iterative application of this equation provides convergingly accurate values.

The values of C_{f}, ΔP, J_{v}, C_{p}, and L_{p} allow all the parameters to be determined, except P_{s}, σ, $\Delta\Pi_{\mathrm{e}}$ which remain unknown. The unknown parameters can be calculated by combining equations 3-1, 3-2, 3-3, 3-6, and 3-7 which leads to the following implicit equation for σ (refer to Appendix 3 for a detailed explanation of how the equation is derived):

$$\sigma = \ln\left[\frac{\sigma - R_s}{\sigma(1 - R_s)}\right]\left(\frac{\sigma}{R_{os}} - 1\right) + 1 \quad (3\text{-}18)$$

Typical values of σ for NF membranes are in the range of 0.8-1.0 [133]. An initial σ estimate of 0.8 is used which, substituted in Eq. 3-18, provides a new value of σ. The iteration is repeated until the difference between the old and new σ is below 0.0001. Once σ is calculated, $\Delta\Pi_e$ is calculated from Eq. 3-1 and P_s from Eq. 3-2. Eq. 3-18 does not always have a singular solution; therefore, this method finds the lowest σ that solves the system of equations. If a σ is calculated with $\Delta\Pi_e > \Delta P$ (corresponding to negative permeate flux, J_v), the calculation is repeated with an incrementally higher initial σ until $\Delta\Pi_e$ is below ΔP. This ensures that all the equations are satisfied while giving a positive permeate flux as in practical NF systems.

The calculation of J_v (Eq. 3-1) depends on σ and $\Delta\Pi_e$ which are not given by the membrane manufacturers since these two parameters depend on the operating conditions. A more appropriate equation for J_v is:

$$J_v = L_p \Delta P \exp(-q\, wt_f) \quad (3\text{-}19)$$

where wt_f is the weight concentration of the feed [wt.%]. The parameters wt_f, L_p, and ΔP are known while the permeate flux coefficient (q) [wt.%$^{-1}$] can be calculated as:

$$q = \frac{-\ln\left(1 - \frac{\sigma\Delta\Pi_e}{\Delta P}\right)}{wt_f} \quad (3\text{-}20)$$

Since q depends on the LD and the membrane and is mostly independent of the other parameters, J_v can be calculated easily using Eq. 3-19.

To represent the decrease of R_{os} with increasing wt_f, the following equation can be used:

$$R_{\mathrm{os}} = \frac{\zeta}{wt_{\mathrm{f}} + \frac{10^2 \zeta}{R_{std}}} \tag{3-21}$$

where R_{std} is the specified rejection (by the manufacturer) of the membrane while ζ can be calculated, as:

$$\zeta = \frac{wt_{\mathrm{f}}\, \Delta C}{\frac{C_{\mathrm{f}}}{10^2} - \frac{10^2 \Delta C}{R_{std}}} \tag{3-22}$$

For a given LD concentration and membrane, ζ can be approximated by a linear function of ΔP:

$$\zeta = a\Delta P - b \tag{3-23}$$

The values of q, a, and b depend on the membrane type and LD (and are provided later in Subsection 3.4.5).

4.2.2 Properties of liquid desiccants

The properties ρ, μ, and ERH depend on the LD and the weight concentration. For all the LDs, ρ is calculated as:

$$\rho = \frac{1 + \frac{x}{1-x}}{10^{-3} + \frac{x}{(1-x)\rho_{LD}}} \tag{3-24}$$

where ρ is the density of the LD [kg/m^3], ρ_{LD} is the density of desiccant in solid form [kg/m^3], and x is the LD mass fraction (mass of solute per mass of solution), calculated as:

$$x = \frac{wt}{10^2} \tag{3-25}$$

where *wt* is the LD weight concentration (percentage of solute per solution) [wt.%].

Regarding the viscosity of LiCl, the following correlation is based on the experiments of Abdulagatov et al. [300]:

$$\mu_{\mathrm{LiCl}} = 10^{-3}[0.8834\exp(0.03733wt) + 0.00118\exp(0.2145wt)] \quad (3\text{-}26)$$

where μ_{LiCl} is the viscosity of LiCl [Pa s].

For LiBr, the equation for μ was taken from [301]:

$$\ln(10^3\mu_{\mathrm{LiBr}}) = A_0 + A_1x^2 + \frac{B_0}{T} + \frac{B_1x^2}{T} + \frac{C_0}{T^2} + \frac{C_1x^2}{T^2} \quad (3\text{-}27)$$

where μ_{LiBr} is the viscosity of LiBr [Pa s], T is the temperature [K], A_0 = -2.321, B_0 = -609.449, C_0 = 372994.855, A_1 = 3.190, B_1 = 963.163, C_1 = -35211.996. Regarding the viscosity of $MgCl_2$, a fitting equation was created based on the experiments of Phang and Stokes [302]:

$$\mu_{\mathrm{MgCl2}} = 10^{-6}\ 889.1[0.9656\exp(0.04636wt) + 0.006045\exp(0.2043wt)] \quad (3\text{-}28)$$

where μ_{MgCl2} is the viscosity of $MgCl_2$ [Pa s] and *wt* is the $MgCl_2$ weight concentration [wt.%].

The ERH can be calculated using polynomial fitting equations based on Conde [47] and Zaytsev et al. [295] studies, as follows:

$$ERH_{\mathrm{LiCl}} = 26.43x^4 - 9.353x^3 - 4.061x^2 - 0.6398x + 1 \quad (3\text{-}29)$$

$$ERH_{\mathrm{LiBr}} = 12.01x^4 - 10.87x^3 + 0.7164x^2 - 0.6225x + 1 \quad (3\text{-}30)$$

$$ERH_{\mathrm{MgCl2}} = 16.5x^4 - 14.4x^3 - 1.116x^2 - 0.4418x + 1 \quad (3\text{-}31)$$

where ERH_{LiCl}, ERH_{LiBr}, and ERH_{MgCl2} are the ERH of LiCl, LiBr, and $MgCl_2$, respectively. The ERH equations are used to calculate the weight concentration of the LD. The curves of ERH_{LiCl}, ERH_{LiBr}, and ERH_{MgCl2} can be seen in Figure 4-1.

4.2.3 Determination of membrane permeability

The pure water permeability L_{p} of the membranes was determined by performing experiments with deionised water as the feed. Based on these measurements, J_{v} and L_{p} were calculated as:

$$J_{\mathrm{v}} = \frac{\Delta V}{\Delta t\, A} \quad (3\text{-}32)$$

$$L_{\mathrm{p}} = \frac{J_{\mathrm{v}}}{\Delta P} \quad (3\text{-}33)$$

where ΔV is the permeate volume collected [L], Δt the time difference [h], and A is the membrane area [m^2]. The precision balance measured the weight difference (Δg) of the permeate, the weights were converted to litres using:

$$\Delta V = \Delta g / \rho \quad (3\text{-}34)$$

The effective diameter (excluding the area covered by the seal) of each membrane sample was 43.1 mm giving an area of 0.00146 m^2. Figure 4-2 shows the experimental results for J_{v} at different ΔP with deionised water as the feed. These results were used to create

interpolating lines for each membrane; the slope of each line represents the L_p of each membrane.

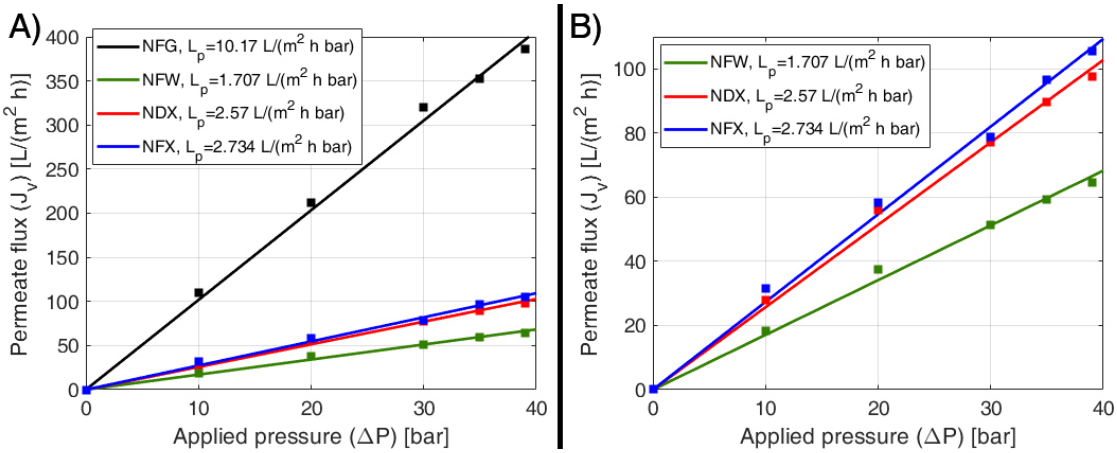

Figure 4-2. Measured permeate flux (J_v) using deionised water at applied pressures (ΔP) of 10, 20, 30, 35, and 39 bar. The experimental data are represented by squares with distinct colours for the four nanofiltration membranes. The experimental data is used to create interpolating lines; with the slope of each line being the pure water permeability (L_p) [L/(m² h bar)] of each membrane. Names and L_p of membranes are shown in the legends.

4.3 Method

This section first presents the materials used in the experimental set-up and then the experimental procedure.

4.3.1 Set-up

The experimental set-up is shown in Figure 4-3. A stainless-steel stirred cell (model HP4750 from Sterlitech, USA) was used together with four flat sheet NF membranes (NFG, NFW, NDX, and NFX types from Synder filtration, USA). These membranes have different rejections, within the range of 10–40%. Different rejection is achieved by having different molecular weight cut-off (*MWCO*) values. Specifically, NFG, NFW, NDX, and NFX have *MWCO* [Da] in the range of 600-800Da, 300-500Da, 500-700Da, and 150-300Da, respectively.

For the LDs, LiCl, LiBr, and $MgCl_2$ salts were purchased (Fisher Scientific, UK) with a purity of 99%. A magnetic stirring disc (diameter of 25 mm) and a magnetic stirring plate

mixed the LD to mitigate fouling and crystallisation that might happen due to the high desiccant concentrations. ΔP was measured by using a digital pressure gauge (model DG-10-S from WIKA Instruments Ltd, UK) with an accuracy of ±0.6 bar and measuring range of 0–50 bar. The permeate was directed through a tube into a collection vessel. The permeate flowrate was measured using a precision balance with an error of ±0.1 g (model SKX421 from Fisher Scientific, UK). Based on the errors or accuracies of the instruments, J_{v} and L_{p} have maximum uncertainties of ±6% and ±1%, respectively. Uncertainties were calculated as [303]:

$$\text{if } z = \frac{x}{y}, \text{ then } \frac{dz}{z} = \sqrt{\left(\frac{dx}{x}\right)^2 + \left(\frac{dy}{y}\right)^2} \tag{3-35}$$

where x and y are measured parameters, dx and dy are the uncertainties of x and y, respectively, and dz is the uncertainty of z. For example, if $J_{\mathrm{v}} = z$, then:

$x = \Delta V$
dx = ±0.1 g
$y = \Delta t$
dy =±1 sec

The solution that remains inside the stirred cell is the concentrated LD. This type of filtration is known as dead-end. The weight concentrations of feed, permeate, and concentrated LD were measured using an automatic refractometer (model J357 from Rudolph Research Analytical, USA) with an accuracy of ±0.00002 (method explained in Appendix 4). This extremely accurate measurement eliminates the uncertainty in wt and R_{os}.

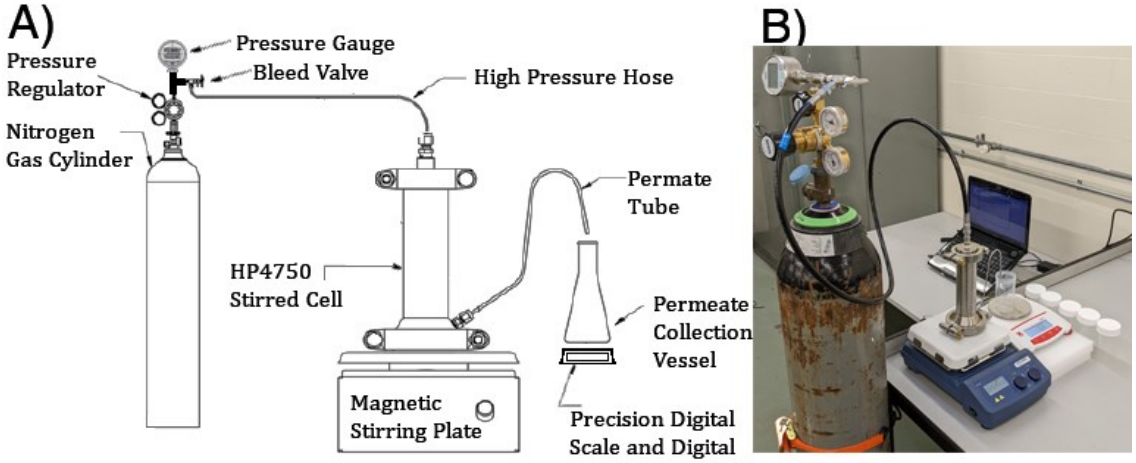

Figure 4-3. Experimental set-up: A) Schematic representation (adapted from [304]). B) Photograph.

4.3.2 Procedure

Four NF membrane samples, namely NFG, NFW, NDX, and NFX were tested. The samples were stored in deionised water before and after each experiment. Three solutions having different weight concentrations were prepared for each LD by mixing the desiccant salt with deionised water, up to a total volume of 0.2 L (see Appendix 5). An initial sample of each feed solution was taken to measure the weight concentration using a refractometer (see Appendix 4). At the beginning of the first experiment, the membrane sample was placed at the bottom of the stirred cell, the LD solution was poured into the cell, and the cell was sealed to avoid leakage of LD and pressure losses. Subsequently, the regulator valve was opened until the desired pressure was reached. Three ΔP of 30, 35, and 39 bar were investigated in a range approaching the burst pressure of 41 bar, because membranes perform better at high pressures [133]. A time delay (membrane dependent) occurred in the first experiment before the first permeate drop was observed[7]. The digital scale then started recording the weight every second. The experiment continued for 30 minutes for all sets of combinations (ΔP, membrane sample,

[7] Usually, the first permeate drop was observed after 5 minutes, however, 23 experiments did not produce any permeate even after 20 minutes. The experiments with zero permeate fluxes were terminated after 20 minutes.

and LD concentration), except for the NFG membrane at low weight concentration (corresponding *ERH* of 88.6%). For these NFG experiments, the permeate flux was higher than the other membranes and it was not possible to run experiments for 30 minutes. Thus, the NFG experiments lasted until 15 g of permeate was collected. At the end of each experiment, the permeate collection vessel was replaced and a new experiment was started by zeroing the scale and restarting the time and data recordings. For each combination of ΔP, membrane sample, and LD concentration, four experiments were performed. However, the first experiment was discarded as the membranes were not preconditioned. The other three experiments were replicates to improve the repeatability of the measurements. A better repeatability does not guarantee a higher accuracy. However, since the three replicate experiments give similar results, this shows that the experiments were conducted without random errors. In turn, low random errors can imply a higher accuracy. Therefore, each reported J_v is an average of three experiments. Uncertainty bars (based on the uncertainties calculated using Eq. 3-35) for J_v are noticeable only for low LD concentrations. At low concentrations, J_v±15 L/(m^2 h) lies within a probabilistic coverage of 100%. While at medium-high LD concentrations, the probabilistic coverage of 100% lies in a lower variance of J_v±1 L/(m^2 h). Nevertheless, maximum J_v uncertainty is ±6% for all LD concentrations. Similarly for L_p, probabilistic coverage of 100% lies in L_p±0.2 L/(m^2 h bar) for all LD concentrations with a maximum uncertainty of ±1%.

At the end of the four experiments, the gas cylinder valve was closed, the pressure in the stirred cell was released through the bleed valve, and the stirred cell was opened. The membrane sample was cleaned with deionised water and stored at room temperature (25 °C) in sealed vessels filled with deionised water. The concentrated LD, which remained in the stirred cell, was poured in a collection vessel. The weight concentrations of feed, concentrated

LD, and three permeate samples were measured using the refractometer. Since the temperature can affect the measurement of weight concentration, all measurements were performed at 25 °C (automatically adjusted by the refractometer) because 25 °C is the nominal temperature at which NF membranes are assessed.

The observed rejection was then calculated through the feed and permeate concentrations. The reported permeate fluxes and observed rejections are the average values of the three triplicate experiments. Having calculated the permeate flux and observed rejection for a certain combination of ΔP, membrane sample, and LD concentration, the next set of experiments was conducted. This gave 27 results (3 concentrations for each LD×3 applied pressures×3 triplicates) for each membrane, giving 108 results (27×4 NF membranes) in total for all membranes. Since there were 3 LDs, altogether there were 324 results.

4.4 Results

This section starts by showing the results of the four investigated NF membranes, namely NFG, NFW, NDX, and NFX, tested at standard temperature, ΔP, and NaCl concentration as defined by the manufacturer. The section continues by showing Tables with the measured R_{os} and J_v of the experiments conducted with LiCl, LiBr, and $MgCl_2$ and ΔP of 30, 35, and 39 bar. The Tables also contain σ and $\Delta\Pi_e$ calculated with the iterative method, and $\Delta\Pi_{Hoff}$ calculated with the van 't Hoff theory. Eq. 3-21 is fitted to the experimental results and used to predict the rejection of the NF membranes at ΔP of 80 bar.

4.4.1 Results at standard conditions

The NF membranes were evaluated at standard conditions of 25 °C, ΔP of 7.6 bar, and feed concentration of 0.2 wt.% (2 g/L) of NaCl [53, 57, 271, 272]. The specified rejections (by the

manufacturer) and the measured rejections under the standard conditions are compared in Table 4-1. The difference is small, suggesting normal functioning of the membranes.

Table 4-1. Specified (by the manufacturer) and measured rejections of the NFG, NFW, NDX, and NFX nanofiltration membranes under standard conditions using NaCl with a concentration of 0.2 wt.% (equivalent to 2 g/L).

	Rejection [%]		
Membrane	Specified	Measured	Deviation [%]
NFG	10	8.1	19
NFW	20	18.1	9.5
NDX	30	29.3	2.5
NFX	40	38.6	3.5

4.4.2 Results for LiCl

This Section shows the experimental (J_v and R_{os}) and the theoretical (σ, $\Delta\Pi_e$, and $\Delta\Pi_{Hoff}$) results regarding LiCl with weight concentrations of 10, 20, and 30 wt.% (105, 220, 355 g/L) and ΔP of 30, 35, and 39 bar (Tables 4-2 to 4-5). Figures 4-4 and 4-5 show the experimental (ΔP of 30, 35, and 39 bar) and expected (ΔP of 80 bar, theoretical value investigated) results for J_v and R_{os}, respectively.

Table 4-2. NFG membrane results using LiCl for the observed rejection (R_{os}) and permeate flux (J_v) and the calculated reflection factor (σ), effective osmotic pressure difference ($\Delta\Pi_e$, using the iterative method), and van 't Hoff osmotic pressure difference ($\Delta\Pi_{Hoff}$). The results are shown for feed concentrations (wt_f) of 10, 20, and 30 wt.% and applied pressures (ΔP) of 30, 35, and 39 bar.

wt_f [wt.%]:	10			20			30		
ΔP [bar]:	30	35	39	30	35	39	30	35	39
R_{os} [%]	1.99	2.97	3.95	0.83	1.32	1.82	0.59	0.93	1.2
J_v [L/(m^2 h)]	127.35	142.36	155.62	27.42	35.08	37.77	26.65	30.46	32.72
σ [%]	96.81	97.71	98.19	95.19	96.59	97.39	93.74	95.48	96.29
$\Delta\Pi_e$ [bar]	18.05	21.5	24.14	28.68	32.66	36.23	29.21	33.52	37.16
$\Delta\Pi_{Hoff}$ [bar]	2.46	3.67	4.88	2.17	3.45	4.75	2.45	3.86	4.98

Table 4-3. NFW membrane results using LiCl for the observed rejection (R_{os}) and permeate flux (J_v) and the calculated reflection factor (σ), effective osmotic pressure difference ($\Delta\Pi_e$, using the iterative method), and van 't Hoff osmotic pressure difference ($\Delta\Pi_{Hoff}$). The results are shown for feed concentrations (wt_f) of 10, 20, and 30 wt.% and applied pressures (ΔP) of 30, 35, and 39 bar.

wt_f [wt. %]:	10			20			30		
ΔP [bar]:	30	35	39	30	35	39	30	35	39
R_{os} [%]	2.46	3.69	5.02	1.63	2.68	3.57	1.45	2.38	3.25
J_v [L/(m^2 h)]	20.61	24.41	26.39	7.51	9.09	10.51	2.66	2.99	3.34
σ [%]	98.15	98.71	99.04	97.44	98.35	98.73	97.22	98.2	98.65
$\Delta\Pi_e$ [bar]	18.27	20.97	23.77	26.27	30.17	33.27	29.25	33.86	37.55
$\Delta\Pi_{Hoff}$ [bar]	3.04	4.55	6.2	4.25	6.99	9.32	6.02	9.88	13.5

Table 4-4. NDX membrane results using LiCl for the observed rejection (R_{os}) and permeate flux (J_v) and the calculated reflection factor (σ), effective osmotic pressure difference ($\Delta\Pi_e$, using the iterative method), and van 't Hoff osmotic pressure difference ($\Delta\Pi_{Hoff}$). The results are shown for feed concentrations (wt_f) of 10, 20, and 30 wt.% and applied pressures (ΔP) of 30, 35, and 39 bar.

wt_f [wt. %]:	10			20			30		
ΔP [bar]:	30	35	39	30	35	39	30	35	39
R_{os} [%]	5.77	7.43	8.58	3.99	4.8	5.87	3.61	4.25	4.36
J_v [L/(m^2 h)]	30.92	34.17	37.62	8.07	9.31	10.36	4.31	4.9	5.48
σ [%]	99.15	99.34	99.42	98.87	99.05	99.22	98.77	98.95	98.97
$\Delta\Pi_e$ [bar]	18.13	21.85	24.5	27.17	31.68	35.24	28.68	33.45	37.25
$\Delta\Pi_{Hoff}$ [bar]	7.12	9.17	10.59	10.41	12.53	15.32	14.99	17.65	18.11

Table 4-5. NFX membrane results using LiCl for the observed rejection (R_{os}) and permeate flux (J_v) and the calculated reflection factor (σ), effective osmotic pressure difference ($\Delta\Pi_e$, using the iterative method), and van 't Hoff osmotic pressure difference ($\Delta\Pi_{Hoff}$). The results are shown for feed concentrations (wt_f) of 10, 20, and 30 wt.% and applied pressures (ΔP) of 30, 35, and 39 bar.

wt_f [wt. %]:	10			20			30		
ΔP [bar]:	30	35	39	30	35	39	30	35	39
R_{os} [%]	7.67	8.88	10.15	5.1	6.22	6.76	4.63	5.89	6.05
J_v [L/(m^2 h)]	16.67	19.45	21.67	4.48	5.73	6.93	0.68	0.8	0.89
σ [%]	99.4	99.48	99.54	99.12	99.28	99.33	99.19	99.34	99.36
$\Delta\Pi_e$ [bar]	24.05	28.03	31.22	28.61	33.14	36.71	29.99	34.94	38.93
$\Delta\Pi_{Hoff}$ [bar]	9.47	10.96	12.53	13.31	16.23	17.64	19.22	24.46	25.13

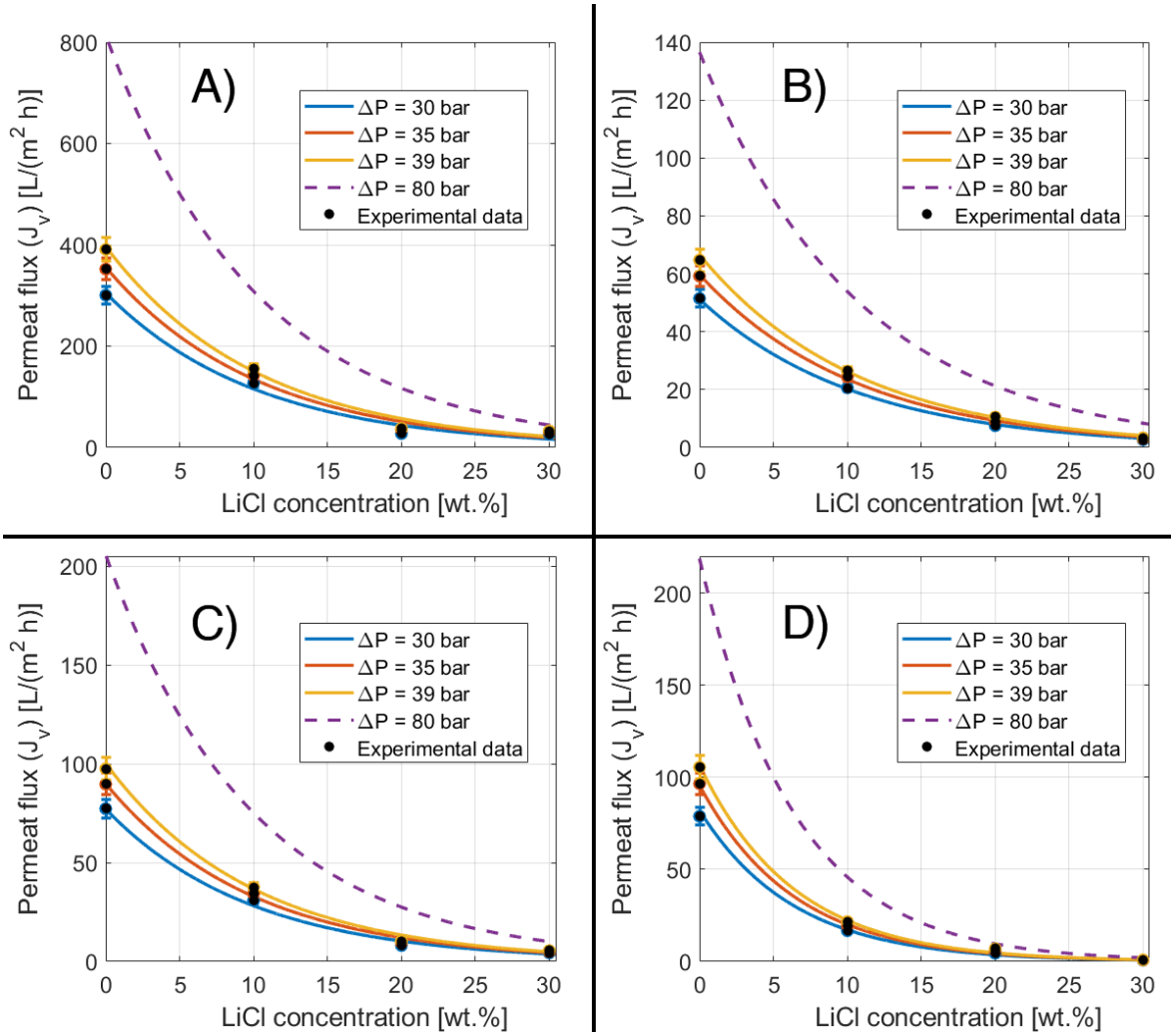

Figure 4-4. Permeate flux (J_v) against LiCl weight concentration for: A) NFG membrane, B) NFW membrane, C) NDX membrane, and D) NFX membrane. The dots represent the experimental data, the lines represent polynomial equations for J_v at different applied pressures (ΔP) based on the experimental results, and the dashed line predicts J_v at an applied pressure of 80 bar. Note that the investigated membranes have a maximum applied pressure of 41 bar. Points at zero concentration are taken from Figure 4-2.

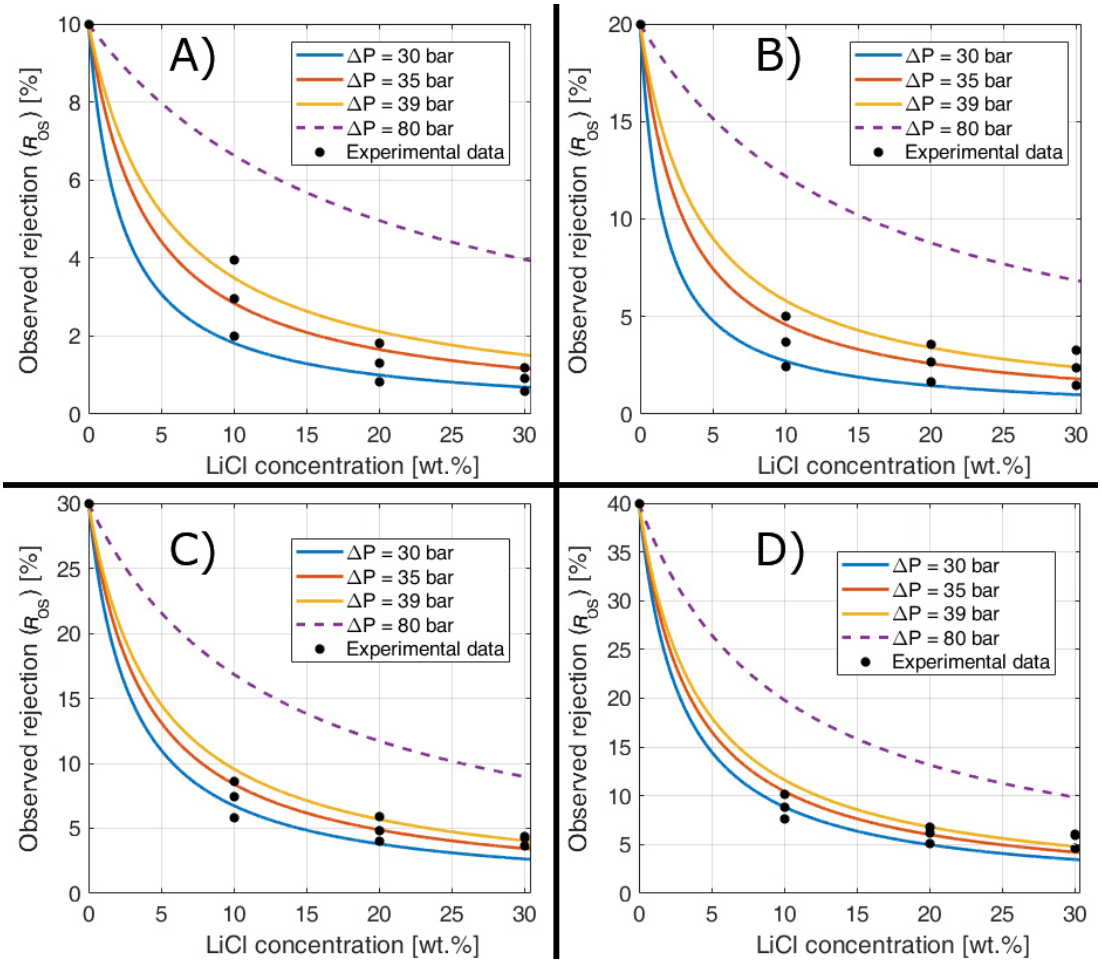

Figure 4-5. Observed rejection (R_{os}) against LiCl weight concentration for: A) NFG membrane, B) NFW membrane, C) NDX membrane, and D) NFX membrane. The dots represent the experimental data, the lines represent polynomial equations for R_{os} at different applied pressures (ΔP) based on the experimental results, and the dashed line predicts R_{os} at an applied pressure of 80 bar. Note that the investigated membranes have a maximum applied pressure of 41 bar. Points at zero concentration are taken from the datasheets of the membranes.

4.4.3 Results for LiBr

This section shows the experimental (J_v and R_{os}) and the theoretical (σ, $\Delta\Pi_e$, and $\Delta\Pi_{Hoff}$) results regarding LiBr with weight concentrations of 15.2, 31, and 43.1 wt.% (170, 400, 620 g/L) and ΔP of 30, 35, and 39 bar (Tables 4-8 and 4-9). Figures 4-6 and 4-7 show the experimental (ΔP of 30, 35, and 39 bar) and expected (ΔP of 80 bar, theoretical value investigated) results for J_v and R_{os}, respectively.

Table 4-6. NFG membrane results using LiBr for the observed rejection (R_{os}) and permeate flux (J_v) and the calculated reflection factor (σ), effective osmotic pressure difference ($\Delta\Pi_e$, using the iterative method), and van 't Hoff osmotic pressure difference ($\Delta\Pi_{Hoff}$). The results are shown for feed concentrations (wt_f) of 15.2, 31, and 43.1 wt.% and applied pressures (ΔP) of 30, 35, and 39 bar.

wt_f [wt. %]:	15.2			31			43.1		
ΔP [bar]:	30	35	39	30	35	39	30	35	39
R_{os} [%]	4.65	5.26	5.99	3.43	3.87	4.5	2.42	2.89	3.22
J_v [L/(m^2 h)]	209.66	228.59	247.86	123.72	146.09	168	68.76	76.63	81
σ [%]	97.91	98.04	98.19	97.82	97.9	98.04	97.51	97.82	97.99
$\Delta\Pi_e$ [bar]	9.59	12.77	14.9	18.23	21.08	22.93	23.83	28.08	31.67
$\Delta\Pi_{Hoff}$ [bar]	4.53	5.12	5.83	7.79	8.79	10.22	8.59	10.26	11.43

Table 4-7. NFW membrane results using LiBr for the observed rejection (R_{os}) and permeate flux (J_v) and the calculated reflection factor (σ), effective osmotic pressure difference ($\Delta\Pi_e$, using the iterative method), and van 't Hoff osmotic pressure difference ($\Delta\Pi_{Hoff}$). The results are shown for feed concentrations (wt_f) of 15.2, 31, and 43.1 wt.% and applied pressures (ΔP) of 30, 35, and 39 bar.

wt_f [wt. %]:	15.2			31			43.1		
ΔP [bar]:	30	35	39	30	35	39	30	35	39
R_{os} [%]	3.28	4.62	5.25	1.29	1.78	2.33	0.84	1.23	1.87
J_v [L/(m^2 h)]	20.93	23.15	24.96	8.03	9.29	9.92	2.29	2.52	2.62
σ [%]	98.55	98.95	99.07	96.85	97.59	98.1	95.69	96.81	97.76
$\Delta\Pi_e$ [bar]	18	21.67	24.61	26.12	30.29	33.83	29.95	34.63	38.32
$\Delta\Pi_{Hoff}$ [bar]	3.19	4.5	5.11	2.93	4.04	5.29	2.98	4.37	6.64

Table 4-8. NDX membrane results using LiBr for the observed rejection (R_{os}) and permeate flux (J_v) and the calculated reflection factor (σ), effective osmotic pressure difference ($\Delta\Pi_e$, using the iterative method), and van 't Hoff osmotic pressure difference ($\Delta\Pi_{Hoff}$). The results are shown for feed concentrations (wt_f) of 15.2, 31, and 43.1 wt.% and applied pressures (ΔP) of 30, 35, and 39 bar.

wt_f [wt. %]:	15.2			31			43.1		
ΔP [bar]:	30	35	39	30	35	39	30	35	39
R_{os} [%]	5.67	6.62	7.18	2.1	2.8	3.16	0.99	1.53	1.78
J_v [L/(m^2 h)]	22.45	25.4	28.51	10.08	11.75	13.86	3.23	3.86	4.21
σ [%]	99.14	99.26	99.31	97.91	98.38	98.54	96.18	97.32	97.64
$\Delta\Pi_e$ [bar]	21.45	25.31	28.1	26.64	30.93	34.11	29.88	34.42	38.26
$\Delta\Pi_{Hoff}$ [bar]	5.52	6.44	6.99	4.77	6.36	7.18	3.51	5.43	6.32

Table 4-9. NFX membrane results using LiBr for the observed rejection (R_{os}) and permeate flux (J_v) and the calculated reflection factor (σ), effective osmotic pressure difference ($\Delta\Pi_e$, using the iterative method), and van 't Hoff osmotic pressure difference ($\Delta\Pi_{Hoff}$). The results are shown for feed concentrations (wt_f) of 15.2, 31, and 43.1 wt.% and applied pressures (ΔP) of 30, 35, and 39 bar.

wt_f [wt. %]:	15.2			31			43.1		
ΔP [bar]:	30	35	39	30	35	39	30	35	39
R_{os} [%]	8.03	9.45	10.9	3.23	3.89	5.04			
J_v [L/(m^2 h)]	13.75	16.44	19.2	2.32	2.85	3.16	0.00	0.00	0.00
σ [%]	99.42	99.51	99.57	98.64	98.86	99.11			
$\Delta\Pi_e$ [bar]	25.11	29.13	32.12	29.55	34.35	38.18	>30	>35	>39
$\Delta\Pi_{Hoff}$ [bar]	7.81	9.2	10.61	7.34	8.84	11.45			

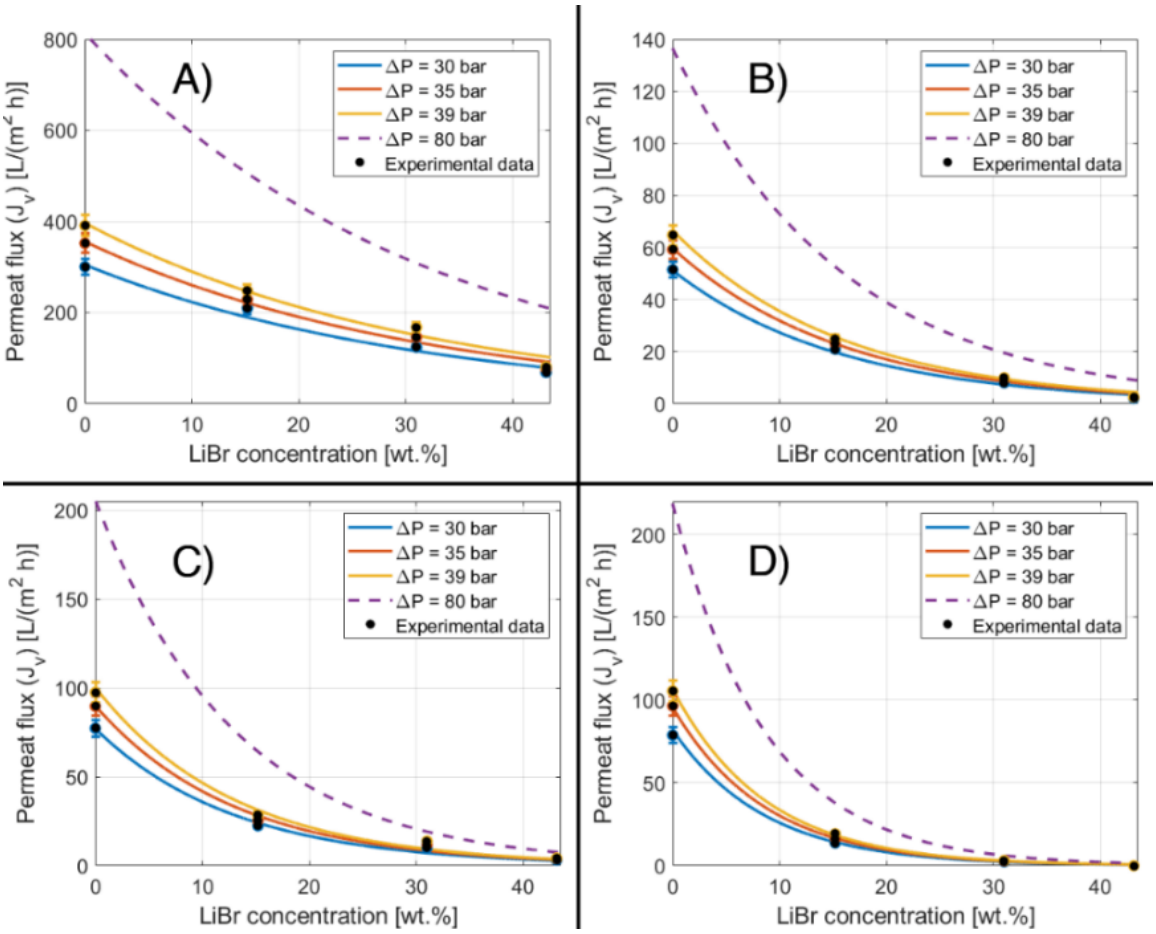

Figure 4-6. Permeate flux (J_v) against LiBr weight concentration for: A) NFG membrane, B) NFW membrane, C) NDX membrane, and D) NFX membrane. The dots represent the experimental data, the lines represent polynomial equations for J_v at different applied pressures (ΔP) based on the experimental results, and the dashed line predicts J_v at an applied pressure of 80 bar. Note that the investigated membranes have a maximum applied pressure of 41 bar. Points at zero concentration are taken from Figure 4-2.

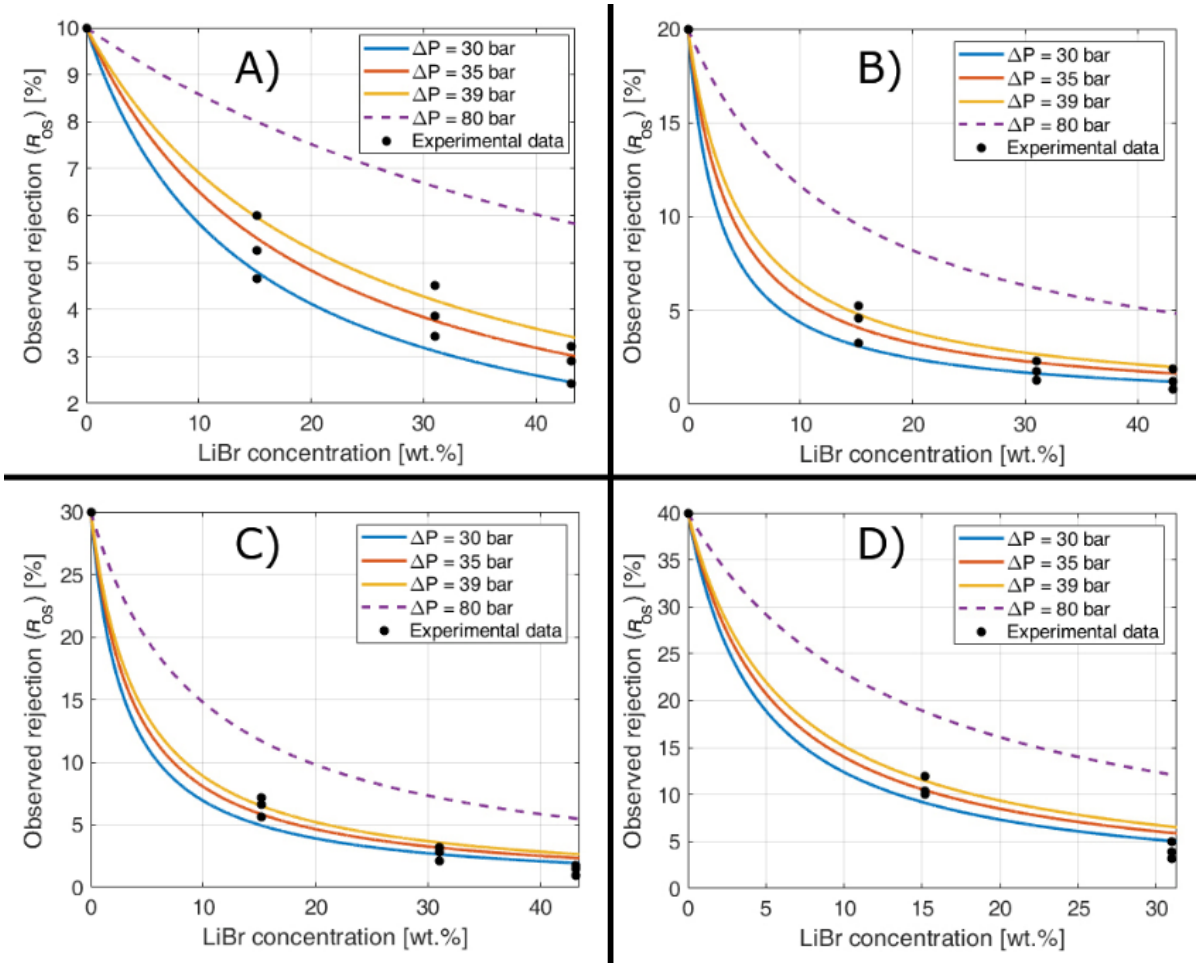

Figure 4-7. Observed rejection (R_{os}) against LiBr weight concentration for: A) NFG membrane, B) NFW membrane, C) NDX membrane, and D) NFX membrane. The dots represent the experimental data, the lines represent polynomial equations for R_{os} at different applied pressures (ΔP) based on the experimental results, and the dashed line predicts R_{os} at an applied pressure of 80 bar. Note that the investigated membranes have a maximum applied pressure of 41 bar. Points at zero concentration are taken from the datasheets of the membranes.

The case studies regarding LiBr weight concentrations of 31 and 43.1 wt.% had zero J_v when operated with the NFX membrane. The operating conditions which result in zero J_v should be avoided because they damage the membrane (see Figure 4-8).

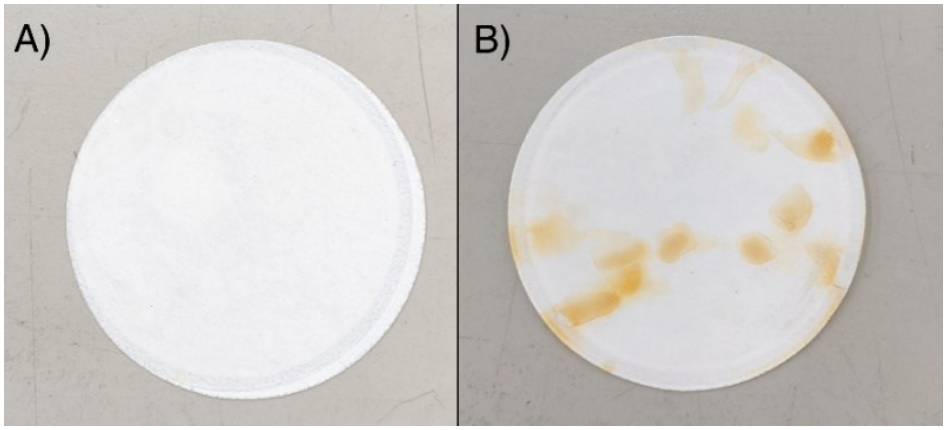

Figure 4-8. Effect of zero permeate flux on the NFX membrane. A) shows the membrane after operating with LiBr feeds of 15.2 and 31 wt.% and applied pressures of 30, 35, and 39 bar. Thus, six experiments were carried out without noticing any marks on the membrane. B) shows the membrane of A) after operating with LiBr feed of 43.1 wt.% and applied pressures of 30, 35, and 39 bar. Three experiments were carried out, each for 20 minutes, with none of them producing any permeate. These experiments damaged the membranes by leaving marks.

4.4.4 Results for $MgCl_2$

This Section shows the experimental (J_v and R_{os}) and the theoretical (σ, $\Delta\Pi_e$, and $\Delta\Pi_{Hoff}$) results regarding $MgCl_2$ with weight concentrations of 14.2, 24.5, and 33.6 wt.% (170, 400, 620 g/L) and ΔP of 30, 35, and 39 bar (Tables 4-12 and 4-13). Figures 4-9 and 4-10 show the experimental (ΔP of 30, 35, and 39 bar) and expected (ΔP of 80 bar, theoretical value investigated) results for J_v and R_{os}, respectively.

Table 4-10. NFG membrane results using $MgCl_2$ for the observed rejection (R_{os}) and permeate flux (J_v) and the calculated reflection factor (σ), effective osmotic pressure difference ($\Delta\Pi_e$, using the iterative method), and van 't Hoff osmotic pressure difference ($\Delta\Pi_{Hoff}$). The results are shown for feed concentrations (wt_f) of 14.2, 24.5, and 33.6 wt.% and applied pressures (ΔP) of 30, 35, and 39 bar.

wt_f [wt.%]:	14.2			24.5			33.6		
ΔP [bar]:	30	35	39	30	35	39	30	35	39
R_{os} [%]	2.95	3.59	4.02	2.09	3.11	3.78	1.25	2.77	3.49
J_v [L/(m^2 h)]	85.01	97.21	109.89	18.51	21.99	27.91	1.01	1.2	1.28
σ [%]	97.76	98.04	98.14	97.75	98.4	98.63	99.67	99.7	99.72
$\Delta\Pi_e$ [bar]	22.14	25.95	28.73	28.83	33.37	36.76	29.99	34.99	38.96
$\Delta\Pi_{Hoff}$ [bar]	3.56	4.33	4.85	4.65	6.92	8.41	4.06	8.99	11.33

Table 4-11. NFW membrane results using $MgCl_2$ for the observed rejection (R_{os}) and permeate flux (J_v) and the calculated reflection factor (σ), effective osmotic pressure difference ($\Delta\Pi_e$, using the iterative method), and van 't Hoff osmotic pressure difference ($\Delta\Pi_{Hoff}$). The results are shown for feed concentrations (wt_f) of 14.2, 24.5, and 33.6 wt.% and applied pressures (ΔP) of 30, 35, and 39 bar.

wt_f [wt. %]:	14.2			24.5			33.6		
ΔP [bar]:	30	35	39	30	35	39	30	35	39
R_{os} [%]	4.46	5.87	6.32						
J_v [L/(m^2 h)]	2.1	2.36	2.63	0.00	0.00	0.00	0.00	0.00	0.00
σ [%]	99	99.24	99.29						
$\Delta\Pi_e$ [bar]	29.06	33.88	37.73	>30	>35	>39	>30	>35	>39
$\Delta\Pi_{Hoff}$ [bar]	5.39	7.09	7.63						

Table 4-12. NDX membrane results using $MgCl_2$ for the observed rejection (R_{os}) and permeate flux (J_v) and the calculated reflection factor (σ), effective osmotic pressure difference ($\Delta\Pi_e$, using the iterative method), and van 't Hoff osmotic pressure difference ($\Delta\Pi_{Hoff}$). The results are shown for feed concentrations (wt_f) of 14.2, 24.5, and 33.6 wt.% and applied pressures (ΔP) of 30, 35, and 39 bar.

wt_f [wt. %]:	14.2			24.5			33.6		
ΔP [bar]:	30	35	39	30	35	39	30	35	39
R_{os} [%]	4.33	6.3	8.51						
J_v [L/(m^2 h)]	5.69	6.9	7.41	0.00	0.00	0.00	0.00	0.00	0.00
σ [%]	98.96	99.28	99.47						
$\Delta\Pi_e$ [bar]	26.95	31.18	34.85	>30	>35	>39	>30	>35	>39
$\Delta\Pi_{Hoff}$ [bar]	5.23	7.61	10.28						

Table 4-13. NFX membrane results using $MgCl_2$ for the observed rejection (R_{os}) and permeate flux (J_v) and the calculated reflection factor (σ), effective osmotic pressure difference ($\Delta\Pi_e$, using the iterative method), and van 't Hoff osmotic pressure difference ($\Delta\Pi_{Hoff}$). The results are shown for feed concentrations (wt_f) of 14.2, 24.5, and 33.6 wt.% and applied pressures (ΔP) of 30, 35, and 39 bar.

wt_f [wt. %]:	14.2			24.5			33.6		
ΔP [bar]:	30	35	39	30	35	39	30	35	39
R_{os} [%]			12.12						
J_v [L/(m^2 h)]	0.00	0.00	0.98	0.00	0.00	0.00	0.00	0.00	0.00
σ [%]			99.65						
$\Delta\Pi_e$ [bar]	>30	>35	38.78	>30	>35	>39	>30	>35	>39
$\Delta\Pi_{Hoff}$ [bar]			14.63						

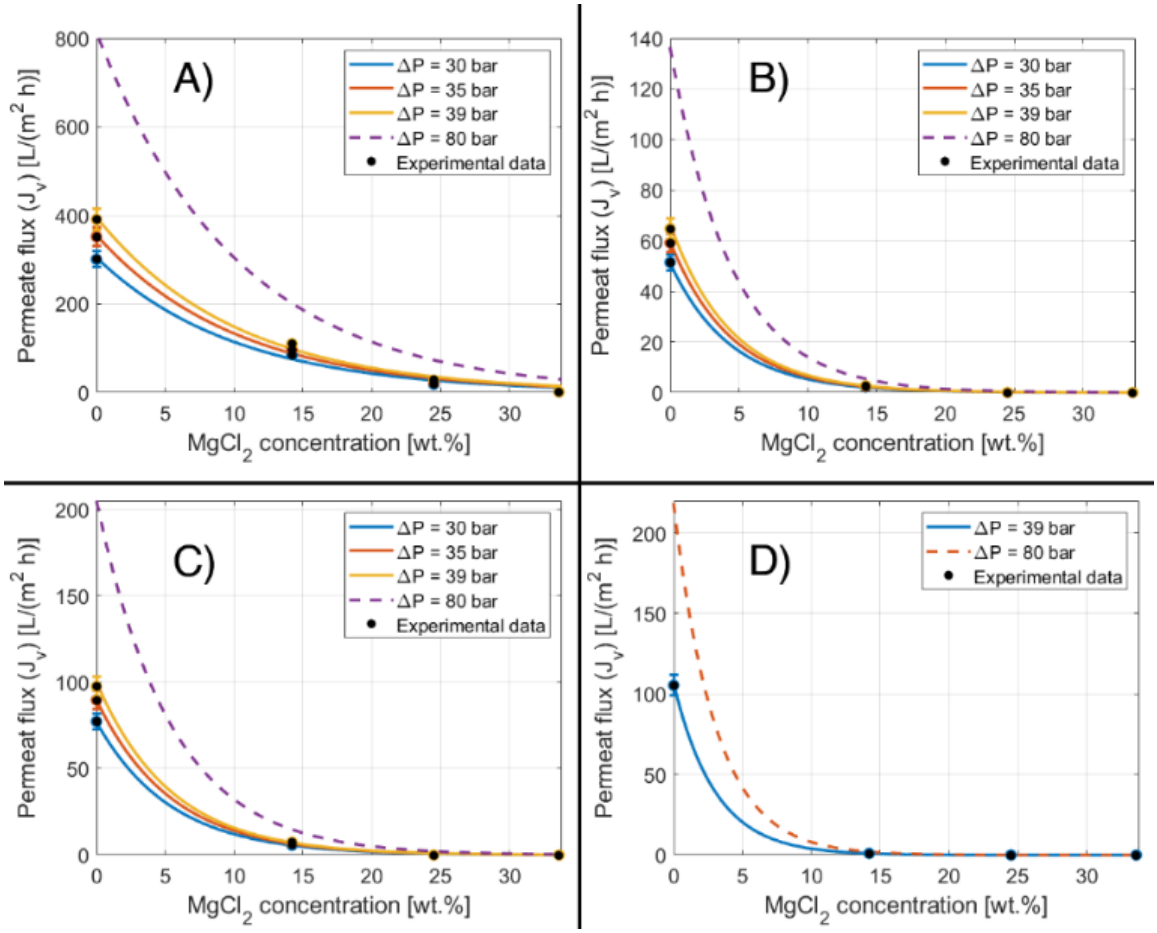

Figure 4-9. Permeate flux (J_v) against $MgCl_2$ weight concentration for: A) NFG membrane, B) NFW membrane, C) NDX membrane, and D) NFX membrane. The dots represent the experimental data, the lines represent polynomial equations for J_v at different applied pressures (ΔP) based on the experimental results, and the dashed line predicts J_v at an applied pressure of 80 bar. Note that the investigated membranes have a maximum applied pressure of 41 bar. Points at zero concentration are taken from Figure 4-2.

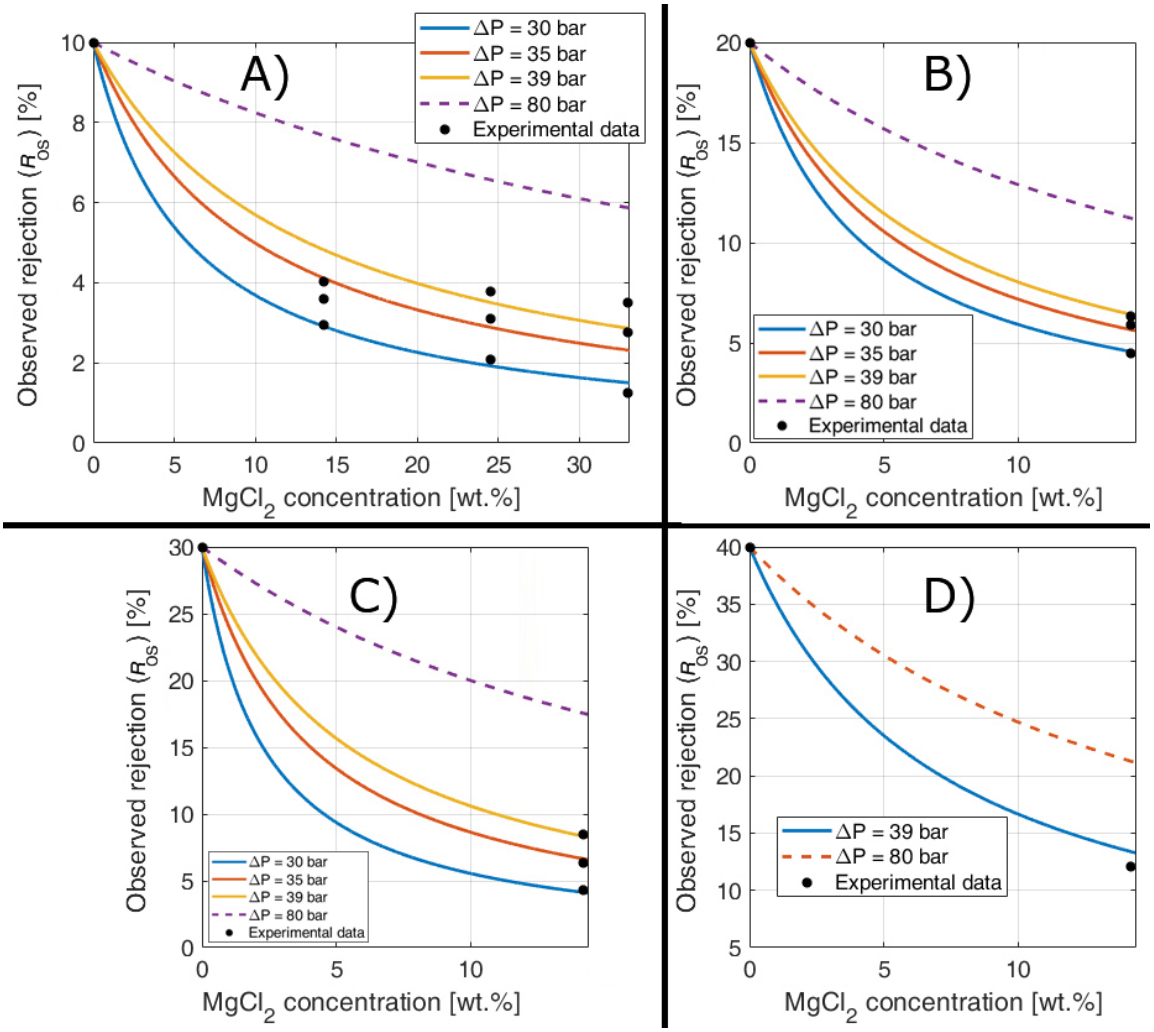

Figure 4-10. Observed rejection (R_{os}) against $MgCl_2$ weight concentration for: A) NFG membrane, B) NFW membrane, C) NDX membrane, and D) NFX membrane. The dots represent the experimental data, the lines represent polynomial equations for R_{os} at different applied pressures (ΔP) based on the experimental results, and the dashed line predicts R_{os} at an applied pressure of 80 bar. Note that the investigated membranes have a maximum applied pressure of 41 bar. Points at zero concentration are taken from the datasheets of the membranes.

When the LD concentration exceeds its saturation concentration, the LD starts to precipitate which contributes to the crystallisation process, a known risk of concentrated LDs [305, 306]. This phenomenon decreases the LD regeneration effectiveness over time by increasing the moisture transfer resistance [305, 306]. Although the maximum concentration $MgCl_2$ of 33.6 wt.% (415 g/L) was close to the crystallisation concentration of 35.3 wt.%

(440 g/L) [295], no crystallisation visible to the naked eye was observed on the membrane. The stirring at 700 rpm was sufficiently rigorous to prevent crystallisation. Nevertheless, as this study did not utilise any special techniques (such as microscopy) or equipment to detect crystallisation, its occurrence cannot be discounted.

4.4.5 Parameters used in the polynomial equations

The permeate fluxes and observed rejections of LiCl (Figures 4-4 and 4-5), LiBr (Figures 4-6 and 4-7) and $MgCl_2$ (Figures 4-9 and 4-10) were plotted[8] using equations 3-19 and 3-21 which depend on the parameters q, a, and b which were adjusted to fit the experimental data (adjusted R^2 above 0.986). Table 4-14 summarises the values of q for each membrane operating with LiCl, LiBr and $MgCl_2$.

Table 4-14. Values of q used for Eq. 3-19. The q values are shown for four nanofiltration membranes, namely NGF, NFW, NDX, and NFX (having different specified rejections) and for three liquid desiccants (LD), i.e., LiCl, LiBr, and $MgCl_2$.

q	Nanofiltration membrane			
LD	NFG	NFW	NDX	NFX
LiCl	0.097	0.093	0.1006	0.1562
LiBr	0.0313	0.0628	0.0766	0.1154
$MgCl_2$	0.0982	0.2277	0.1854	0.3304

Table 4-15 summarises the values of a and b for the four investigated membranes operating with LiCl, LiBr, and $MgCl_2$, and regarding three weight concentrations for each LD.

[8] a and b used to plot Figures 4-5, 4-7 and 4-10 are average values of a and b for each LD. For example, Figure 4-5A was plotted with a =3.27 and b =78.36.

Table 4-15. Values of a and b used for Eq. 3-21. The values are shown for four nanofiltration membranes, namely NGF, NFW, NDX, and NFX, for three liquid desiccants (LD), i.e., LiCl, LiBr, and $MgCl_2$, and for three weight concentrations (wt.%) for each LD. Null values are the case studies which had zero permeate fluxes.

	Nanofiltration membrane							
	NFG		NFW		NDX		NFX	
LD (wt.%)	*a*	*b*	*a*	*b*	*a*	*b*	*a*	*b*
LiCl (10)	4.45	110.2	4.29	102.1	5.42	90.97	4.54	42.34
LiCl (20)	2.91	70	5.7	136	5.93	88.06	5.13	35.48
LiCl (30)	2.45	54.87	7.69	185	3.4	23.79	6.46	31.21
LiBr (15.2)	10.42	185.2	5.44	102	4.15	17.64	8.28	97.68
LiBr (31)	10.06	145	4.3	87.47	4.42	61.46	7.64	124.6
LiBr (43.1)	7.46	86.02	5.6	133.1	4.2	80.42		
$MgCl_2$ (14.2)	4.01	60.71	5.59	83.71	10.66	251.5		
$MgCl_2$ (24.5)	9.34	215.8						
$MgCl_2$ (33.6)	14.74	392.1						

4.4.6 Comparison of idealised and improved models

The polynomial equations based on the results from the above dead-end filtration experiments can be integrated into the multi-stage NF models to improve the earlier models. The earlier models proposed by Altaee and Sharif [132] and Wang et al. [73] neglected the effects of high concentrations in the osmotic pressure and in the membrane behaviour. To improve the existing idealised models at high concentrations, the first modification introduced here is to calculate the osmotic pressure using Eq. 2-4 rather than the van ‘t Hoff approximation. Eq. 2-4 gives osmotic pressures that can be several times higher than by using the van ’t Hoff formula as in the earlier models (see Appendix 6). Eq. 2-4 must be used for the osmotic pressure because the estimate based on the iterative method requires knowing the values of the outlet parameters. The second modification is to include Eq. 3-21 for the rejection of the NF membrane.

By including these two modifications and assuming a nominal LiCl feed flow of 1000 L/h, ΔP of 41 bar (burst pressure of commercial NF membranes), T_{K} of 298.15 K, r_{std} between 0

and 40% (with increment of 0.1%), and feed concentration of 7 wt.% (70 g/L), the outlet flowrates and concentrations of a 1-stage NF regenerator differ significantly from the results of the idealised model (using fixed rejection and van 't Hoff linear approximation), as seen from Figure 4-11. The improved and idealised model results diverge further when using the same input parameters but with a feed concentration of 14 wt.% (150 g/L), as seen from Figure 4-12.

Figures 4-11 and 4-12 show the outlet flowrates and concentrations based on variable R_{std}. With zero rejection (R_{std} =0), all the feed flowrate leaves the membrane as permeate (both improved and idealised models give permeate flowrate starting from 1000 L/h). R_{std} equal to zero results in a permeate concentration equal to the feed concentration. Since the concentrated LD flowrates are zero for both models, the initial concentration of the concentrated LD represents the concentration difference between permeate and concentrated LD that can be achieved with ΔP of 41 bar. This concentration difference is always equal to 1.5 wt.% (15 g/L) due to the constant applied pressure (for both Figures 4-11 and 4-12).

As R_{std} increases, the concentrated LD flowrate increases and the permeate flowrate decreases. For the idealised model, a maximum rejection (R^*) exists where the permeate flowrate becomes zero. With zero permeate, all the feed flowrate leaves the membrane as concentrated LD (i.e., 1000 L/h) and thus, the concentration of the concentrated LD is equal to the feed concentration. By including Eq. 3-21, permeate can be produced also with $R_{std} > R^*$. The results of the improved model in Figures 4-11 and 4-12 are plotted with the polynomial equations of the NFG, NFW, NDX, and NFX membranes for $R_{std} \leq 10\%$, $10\% < R_{std} \leq 20\%$, $20\% < R_{std} \leq 30\%$, and $30\% < R_{std} \leq 40\%$, respectively.

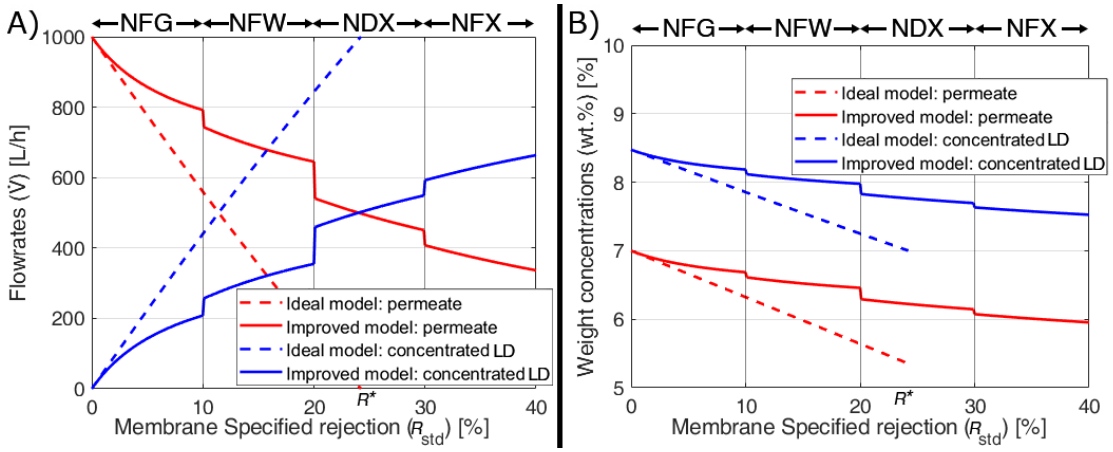

Figure 4-11. A) Flowrates and B) weight concentrations of the permeate and concentrated LD at the output of the 1-stage regenerator. The results are plotted for different membrane specified rejections (R_{std}), LiCl feed with flux of 1000 L/h, and concentration of 7 wt.% (70 g/L). The dashed lines are based on constant R_{std} and van 't Hoff approximation (idealised model), while the continuous lines (improved model) include the modification for the observed rejection (Eq. 3-21) and accurate osmotic pressure (Eq. 2-4). The weight concentrations of the idealised model were calculated for $R_{std}<R^*$. R^* is the rejection where the permeate flux (calculated with the idealised model) becomes zero.

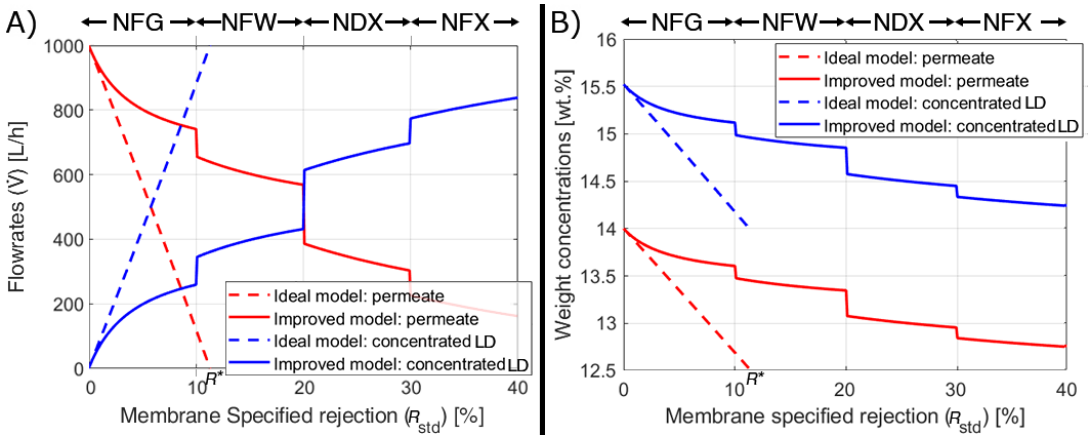

Figure 4-12. A) Flowrates and B) weight concentrations of the permeate and concentrated LD at the output of the 1-stage regenerator. The results are plotted for different membrane specified rejections (R_{std}), LiCl feed with flowrate of 1000 L/h, and concentration of 14 wt.% (150 g/L). The dashed lines are based on constant R_{std} and van 't Hoff approximation (idealised model), while the continuous lines (improved model) include the modification for the observed rejection (Eq. 3-21) and accurate osmotic pressure (Eq. 2-4). The weight concentrations of the idealised model were calculated for $R_{std}<R^*$. R^* is the rejection where the permeate flux (calculated with the idealised model) becomes zero.

The idealised model assumes constant rejection of the membranes equal to the specified by the manufacturer (i.e., R_{std}). However, such assumption is incorrect when using NF membranes with concentrated LDs, as seen from the measured rejection being several times

lower than R_{std}. For example, the results using the NFG membrane with an applied pressure of 39 bar and $MgCl_2$ show that the calculation error for the rejection using the idealised model is above 148% (Table 4-16). This error is below 20% when using the improved model that considers variable rejection based on applied pressure, LD concentration, LD used, and membrane used (Table 4-16).

Table 4-16. Calculation errors for the rejection of the NFG membrane when operated with an applied pressure of 39 bar and $MgCl_2$ as the liquid desiccant. The $MgCl_2$ concentrations and measured rejections are taken from Table 4-10.

$MgCl_2$ concentration [wt.%]	Rejection of idealised model [%]	Rejection of improved model [%]	Measured rejection [%]	Error idealised model [%]	Error improved model [%]
14.2	10	4.825	4.02	148.76	20
24.5	10	3.508	3.78	164.55	7.2
33.6	10	2.827	3.49	186.53	19

4.4.7 Comparison of multi-stage and conventional solar regeneration

The performance of the multi-stage NF regenerator was compared against the results of Bouzenada et al. [57]. The authors measured the *COP* of a LDAC system using LiCl and driven by solar collectors evacuated-tube, flat-plate collectors, or a combination of the two technologies. These authors validated their model against experimental results (error below 12%) and calculated a maximum *COP* of 0.65 assuming the weather data from Kolkata (India). Based on their model, the boiler (which provided the energy to the system) required 44.8 kW and could remove 29.1 kW. Thus, the LD absorbed 40.4 L/h of moisture and consequently, the regenerator had to remove 40.4 L/h of water from the LD (having a feed flowrate of 420 L/h). To achieve this dehumidification and regeneration, the LDAC system needed to operate with a concentration of 12 wt.% (130 g/L) of LiCl.

To achieve the same output using the multi-stage NF regenerator, such concentration needs a 15-stage regenerator which requires 8.66 kW and has *COP* of 3.37 (calculated with Eq. 2-27). If NF membranes withstood 80 bar, a 6-stage regenerator would provide the same dehumidification and regeneration with a power requirement of 3.81 kW, resulting in a *COP* of 15.

4.5 Discussion

The experimental results show that higher feed concentrations (C_f) increase the reflection factor (σ) and the effective osmotic pressure difference ($\Delta\Pi_e$) and decrease the permeate flux (J_v) and the observed rejection (R_{os}) of the membranes. These results agree with the findings of Hilal et al. [133] in that $\Delta\Pi_e$, J_v, and R_{os} increased or decreased similarly with higher C_f.

The proposed iterative method (Eq. 3-18), which avoids the linear approximation of the van 't Hoff equation, gives accurate predictions at high concentrations. Firstly, the model calculates $\Delta\Pi_e > \Delta\Pi_{Hoff}$ for all the investigated cases. Secondly, the calculated $\Delta\Pi_e$ is a good indicator to predict cases with zero J_v. For example, using the NFX membrane and LiBr C_f of 31 wt.% (400 g/L), $\Delta\Pi_e$ is equal to 29.56, 34.36, and 38.19 bar. These $\Delta\Pi_e$ values are slightly less than the applied pressures of 30, 35, and 39 bar. Since higher $\Delta\Pi_e$ are expected at higher LD concentrations, the case with LiBr feed concentration of 43.1 wt.% (620 g/L) was expected to have $\Delta\Pi_e > \Delta P$ and thus zero J_v (Table 4-9).

Regarding the fluxes, LiBr gives permeate fluxes of 2.5 and 6 times higher than LiCl and $MgCl_2$, respectively, when operating with the NFG membrane. For the other membranes, LiBr and LiCl give higher fluxes than $MgCl_2$. When operating with the NFX membrane, LiCl has permeate flux of 1.2–2.2 times higher than LiBr and 22.1 times higher than $MgCl_2$. These results can be explained by the molecular sizes of the investigated LDs. Since LiCl and LiBr

are monovalent ions, their hydrated molecular sizes are smaller than $MgCl_2$, which allows LiCl and LiBr to pass through the pores more easily. Whereas the lower fluxes at higher C_f can be attributed to a lower difference between ΔP and $\Delta \Pi_e$ which is the driving force of J_v.

Regarding the rejections, LiCl has slightly lower rejections than the other LDs but produces J_v for all the investigated LiCl cases. The lower rejections at higher C_f can be correlated to $\Delta \Pi_e$. Since $\Delta \Pi_e$ increases to values close to ΔP at high C_f, the membrane struggles more to produce permeate which results in a decreased rejection. From the investigated LDs, LiBr is better for applications requiring high humidities because the rejections and permeate fluxes are higher than the other LDs. For applications requiring medium to high humidities, LiCl is the only LD with permeate fluxes above zero for all the investigated case studies. Overall, LiCl is the best LD having lower rejections than LiBr and $MgCl_2$ but higher permeate fluxes than LiBr and $MgCl_2$. However, for greenhouse applications where toxic solutions should be avoided, $MgCl_2$ represents the best option since possible leaks would work as fertiliser for a variety of crops [307].

Higher rejections were observed as C_f decreased. As the LD gets diluted from stage to stage, the rejection of the NF stages gradually increases, which is desired. Moreover, lower rejections at the first NF stage of the regenerator are desired to obtain a highly concentrated LD (see Figures 4-11 and 4-12 where higher outlet LD concentrations are achieved with lower R_{std}). In practice, however, too low rejections make the multi-stage NF regenerator less efficient. This occurs because the permeate concentration of each NF stage calculated with the improved model is higher than the one calculated with the idealised model. Since the required number of stages depends on how fast the permeate is diluted from stage to stage, more NF stages are required in practice compared to the idealised model.

The first stage of the multi-stage NF regenerator has an optimal rejection between 10 and 30%. Improvements such as higher operating pressures would increase the rejection of LiCl at high C_f from 6 to 10%, bringing the rejection in the desired range of 10–30%. Other research approaches could also be investigated, such as membranes with larger pores at low C_f which would have the required pore size at higher C_f. Another approach is the fabrication of membranes with specified rejections in the range of 60–80% which would likely achieve the desired 10–30% at high C_f.

Two more disadvantages can be deducted from the experiments. First, as the discrepancy of R_{os} and R_{std} increases, higher permeate flowrates are calculated, meaning that in practice, the pumps must operate with higher flowrates. Second, since low R_{std} results in a more concentrated LD (see Figure 4-11B) with low flowrate (see 4-11A), a compromise exists between a high flowrate and a high LD concentration.

The difference between the idealised model (constant rejection and van 't Hoff linear approximation) and the improved model (with the additions of Eq. 3-21 and accurate $\Delta\Pi$ calculation) becomes higher as R_{std} increases because R_{os} diverges more from R_{std}. The error of assuming a constant rejection is high when using the idealised model and decreased by seven times when employing the improved model (Table 4-16).

The efficiency of the multi-stage regenerator using commercial NF and RO membranes was found to be better than conventional solar collector regenerators. Although a *COP* of 3.37 (6.6 times higher than conventional solar regenerators) may be achieved, it should be noted that the two methods required different types of energy. The multi-stage regenerator requires electric rather than thermal energy; thus, a fair comparison should include an energy conversion factor which would decrease the *COP* difference between the two regeneration methods. Moreover, a 15-stage regenerator is required to achieve the same dehumidification

as the conventional solar regenerators, but a 15-stage regenerator is more expensive and complex than the conventional thermal regenerator. A *COP* of 3.37 is estimated based on current NF burst pressure of 41 bar. However, multi-stage regeneration has potential if used with NF burst pressures of 80 bar. Although most RO membranes have bust pressures of around 80 bar, some RO membranes can withstand 160 bar [103], making it feasible for future NF membranes with low rejections to withstand 80 bar. With such improved NF membranes, a *COP* of 15 (30 times higher than conventional solar regenerators) may be achieved. Thus, the *COP* difference between the two methods would be high even by using an energy conversion factor. Specifically, a *COP* of 15 is much higher even compared with commercial chillers using vapour compression with *COP* values of 2.5−4.3 [282-284]. Moreover, the benefit of higher NF burst pressure agrees with the findings in Chapter 3, where it was found that increasing the applied pressure from 40 to 55 bar decreased the required stages from 9 to 4, making the multi-stage regenerator more compact.

Since the same dehumidification and regeneration is achieved with 6 rather than 15 stages, a significant advantage of higher NF burst pressure is the decreased cost, size, and complexity of the multi-stage regenerator. To decrease the system to 1-stage, a RO membrane withstanding 222 bar is needed. Without accounting for pressure losses, one-stage RO requires 1.47 kW for the previously mentioned case (calculation based on Wang et al. [308]). A one-stage RO could achieve a *COP* of 39 which represents the maximum achievable when regenerating the LD using a single stage.

4.6 Conclusions

The possibility of LD regeneration via NF membranes was experimentally proven in this Chapter. The main conclusions are:

• Although multi-stage NF models have already been theoretically proposed, these models do not account for variation of the properties of NF membranes. Thus, the modelling was improved by integrating accurate osmotic pressure and experimental data. Rejection and permeate flux of commercial NF membranes were investigated with various combinations of applied pressure and feed concentration using LiCl, LiBr, and $MgCl_2$ solutions. Based on the experimental results, polynomial equations were developed to estimate the rejection and permeate flux, while an iterative method was developed for the prediction of the reflection factor (σ) of the membrane.

• The observed rejection of commercial NF membranes decreases as the feed concentration increases, with maximum rejections below 12%. For instance, the NFX membrane with a specified rejection of 40% has an observed rejection of 6% when treating 30 wt.% (355 g/L) LiCl. Decreased rejections at high concentrations are desired for the first stage in a multi-stage NF regenerator due to high feed osmotic pressure. However, low rejections are not desired for the remaining NF stages because they increase the required number of stages and the capacity of the pumps. A trade-off is achieved with rejections in the range of 10–30%. The proposed equation predicts that an 80 bar burst pressure could increase the rejection from 6 to 10% (regarding the NFX membrane with LiCl at 30 wt.%), reaching the desired rejection range of 10–30%.

• The proposed method for calculating σ estimates osmotic pressure more accurately at high LD concentrations than the linear van ‘t Hoff approximation. It also predicts LD concentrations that result in zero permeate flux, which in turn damages the membrane. If the estimated osmotic pressure for a certain concentration approaches the applied pressure, then higher concentrations will result in zero permeate production.

Chapter 5: Multi-stage nanofiltration for brine concentration: experimental and modelling study

Title of published paper: Multi-stage nanofiltration for brine concentration: experimental and modelling study

Paper information: Desalination, 2023. 566: p.116928.

Author contributions and affiliations:

- P. Pasqualin: conceptualisation, original draft, writing, review, editing, modelling, data curation, investigation and visualisation

- P.A. Davies: review and editing

School of Engineering, University of Birmingham, Edgbaston, Birmingham B15 2TT, UK.

5.1 Introduction

Multi-stage NF systems have potential to operate with brine concentrations exceeding those possible in conventional membrane desalination (see Chapter 4). These systems hold promise for various applications, including LDAC for greenhouses (as explained in Chapter 3) and zero liquid discharge (ZLD) [73].

In LDAC, the aim is to remove water from, and thus concentrate, the LD that is used to dehumidify air. To achieve low air humidity, very concentrated LDs are required. For further details, information about LDAC can be found in Chapter 1.

In ZLD, the aim is to recover water from effluents and thus avoid or reduce harmful discharges to the environment. ZLD is used globally in many industries [55]. For example, in the USA and China most ZLD plants are related to the power industry, whereas in India they are more related to the textile, brewing, and distilling industries [55]. As wastewater regulations are becoming stricter worldwide, the use of ZLD is expected to increase and attract an estimated investment of $100−200 million per year [55], accumulating a total of $9 billion by the end of 2029 [309].

Typically, the ZLD process comprises three technologies in series: a RO stage, a brine concentrator, and a crystalliser [55, 310]. The RO stage removes dissolved salts and other contaminants while minimising the volume of wastewater entering the brine concentrator thus reducing its energy consumption [55]. However, the brine concentrator still consumes more than 70% of the ZLD process [311]. To decrease the energy requirement of the ZLD process, it has been suggested to replace the thermal-based brine concentrator with a pressure-based multi-stage NF system [73].

Depending on the composition of the feed, ZLD operates with different recoveries. A survey of ZLD in the USA [312] mentions plants using brackish water (5 g/L) or rejected RO brines (60 g/L) as their feed, resulting in recoveries of 98% or 85%, respectively. Most of these ZLD plants are associated with the power industry [312]. In the USA, as well as many countries in Europe and Asia, the power industry is related to coal mining since many power plants are fuelled by coal [313, 314]. In coal mining ZLD applications, where the feed is seawater with concentrations of 20−35 g/L [315-318], the recovery is around 90%. Thus, treatment of brackish water, seawater, and rejected RO brines are important examples of ZLD applications with recoveries of 75−98%. For more information about ZLD, a comprehensive review article by Yaqub and Lee [319] is available.

Both conventional LDAC and ZLD employ thermal processes that are energy intensive and require a brine concentrator with a high outlet brine concentration, which cannot be achieved by conventional RO because of excessive osmotic pressures. Multi-stage NF is less energy intensive than the thermal processes and achieves brine concentrations exceeding RO by taking advantage of low salt rejection.

Many configurations combining NF and RO [320-325] or multiple NF like NF-NF [132, 311], have been presented in the past. However, the difference between these studies and the multi-stage NF concept (Figure 3-2) lies in the role of the NF stages. In previous studies, NF stages were either used as pretreatment or for energy recovery, whereas here multi-stage NF is a way of overcoming the high feed osmotic pressure. LDAC has not yet been investigated with NF and RO. In contrast, ZLD configurations include NF and RO [311, 324]. Some ZLD configurations also include electrodialysis stages, such as NF-ED-RO [315, 326], 2NF-RO-ED [317, 318] and 2NF-RO-2ED [316]. Since electrodialysis has a low effectiveness in LDAC applications (see Chapter 2) and a low current efficiency in hypersaline desalination

applications (making it energy-intensive) [327], the current study focuses on configurations without electrodialysis.

A theoretical investigation of multi-stage NF for greenhouse LDAC was carried out in Chapter 3 where an 8NF-RO system (i.e., eight NF, then RO, Figure 5-1A shows the concept for *n*NF-RO) was modelled as a LD regenerator. The 8NF-RO system was assumed with pure water as its permeate and able to concentrate $CaCl_2$ to 165 g/L with a SEC_{el} of 86 kWh_{el}/m^3 (Table 3-3 in Chapter 3). It was found that the 8NF-RO system used fewer stages (i.e., 3NF-RO) when the NF allowable applied pressure increased from 40 to 55 bar, but this improvement did not decrease the SEC_{el}. Even though a SEC_{el} of 86 kWh_{el}/m^3 is high in the field of membrane desalination, it is much lower than that of conventional solar regenerators which have a thermal *SEC* of 1110 kWh_{th}/m^3 (based on the comparison in Chapter 4 where LDAC solar collectors required 44.8 kW and produced 40.4 L/h of permeate). Although electrical and thermal *SEC* are not directly comparable, assuming a thermal-to-electric conversion factor of 35% (as in [328]), this thermal *SEC* nonetheless equates to a very high electrical SEC_{el} of 390–400 kWh_{el}/m^3. Another alternative for LD regeneration is through vapour compression refrigeration (VCR), but its SEC_{el} remains relatively high at 120–145 kWh_{el}/m^3 (calculated based on [329]).

Regarding multi-stage NF for ZLD, Wang et al. [73] investigated theoretically a RO-2NF (e.g., first RO, then two NF) and a RO-3NF system (e.g., first RO, then three NF, Figure 5-1B shows the concept for RO-*n*NF). These systems concentrated RO brines from 60 g/L to 233 g/L for NaCl crystallisation in ZLD applications. The authors reported SEC_{el} of 15.7 and 8 kWh_{el}/m^3 for RO-2NF and RO-3NF, respectively, using an ERD. These SEC_{el} are based on the idealised assumptions of zero pressure losses, 100% efficiencies, and production of pure water as the permeate. Compared against its thermal alternatives like multi-stage flash

distillation (MSF), multi-effect distillation (MED), and mechanical vapour compressor (MVC), multi-stage NF achieves lower SEC_{el} [101]. Among the three alternatives, MVC has the lowest SEC_{el} [330]. To concentrate seawater from 60 to 233 g/L, as in the case of RO-3NF, MVC has a SEC_{el} of 23 kWh_{el}/m^3 (calculated based on [101]). Based on the theoretical prediction that RO-3NF consumes 8 kWh_{el}/m^3, RO-*n*NF has potential to replace MVC.

In *n*NF-RO (i.e., the multi-stage concept for LDAC), the permeate flowing from stage to stage is gradually diluted which allows the NF rejections to increase gradually without exceeding the burst pressure of the membranes. Once the concentration has decreased sufficiently and the osmotic pressure difference becomes lower than the RO burst pressure, a final RO stage with nearly 100% rejection is used. Brine recirculation is necessary from each stage, except the first, to avoid loss of solution to the environment.

In RO-*n*NF (i.e., the multi-stage concept for ZLD), the brine from each stage feeds the next stage. As the brine becomes more concentrated from one stage to the next, NF rejections must decrease to avoid exceeding the burst pressure at each stage. Permeate recirculation is necessary to avoid loss of solution to the environment, except in the case of the initial RO stage.

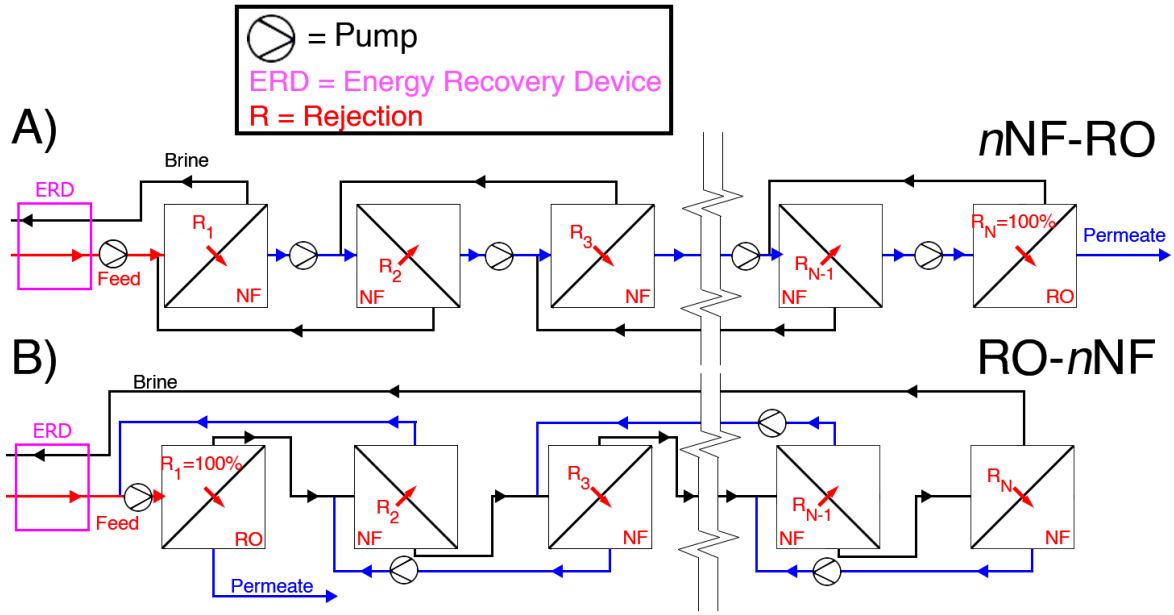

Figure 5-1. Two multi-stage NF concepts. A) nNF-RO concept proposed in Chapter 3 for greenhouse LDAC applications. This system utilises an energy recovery device (ERD) and comprises several NF stages followed by a last RO stage. B) RO-nNF concept proposed by Wang et al. [73] for ZLD applications. This system utilises an ERD and comprises a first RO stage followed by several NF stages. R_i is the rejection of the "i-th" stage. Stages having R =100% are indicated as RO. The feed of the first stage is shown as a red line, permeates as blue lines, and brines as black lines.

The above-mentioned *n*NF-RO and RO-*n*NF concepts showed promising predictions, but they assumed zero pressure losses which are expected to reduce the actual performance of the systems. Additionally, these concepts lacked experimental validation. It is essential to develop *n*NF-RO and RO-*n*NF models that provide more accurate results. Thus, the primary objective of Chapter 5 is to conduct an accurate evaluation of *n*NF-RO and RO-*n*NF in comparison to their conventional thermal alternatives.

Experiments were conducted using a 2-stage laboratory system for two configurations: NF-RO representing the *n*NF-RO concept for greenhouses and RO-NF representing the RO-*n*NF concept for ZLD applications. The experimental 2-stage system utilises a NF membrane and a RO membrane, both operating in cross-flow filtration. The system can be configured either as RO-NF or NF-RO, simply by operating one or both pumps and rerouting feed tank

connections (Figure 5-2). The experimental results validate models which include energy and pressure losses, thus enabling a more realistic assessment of how multi-stage NF compares to conventional brine concentration technologies.

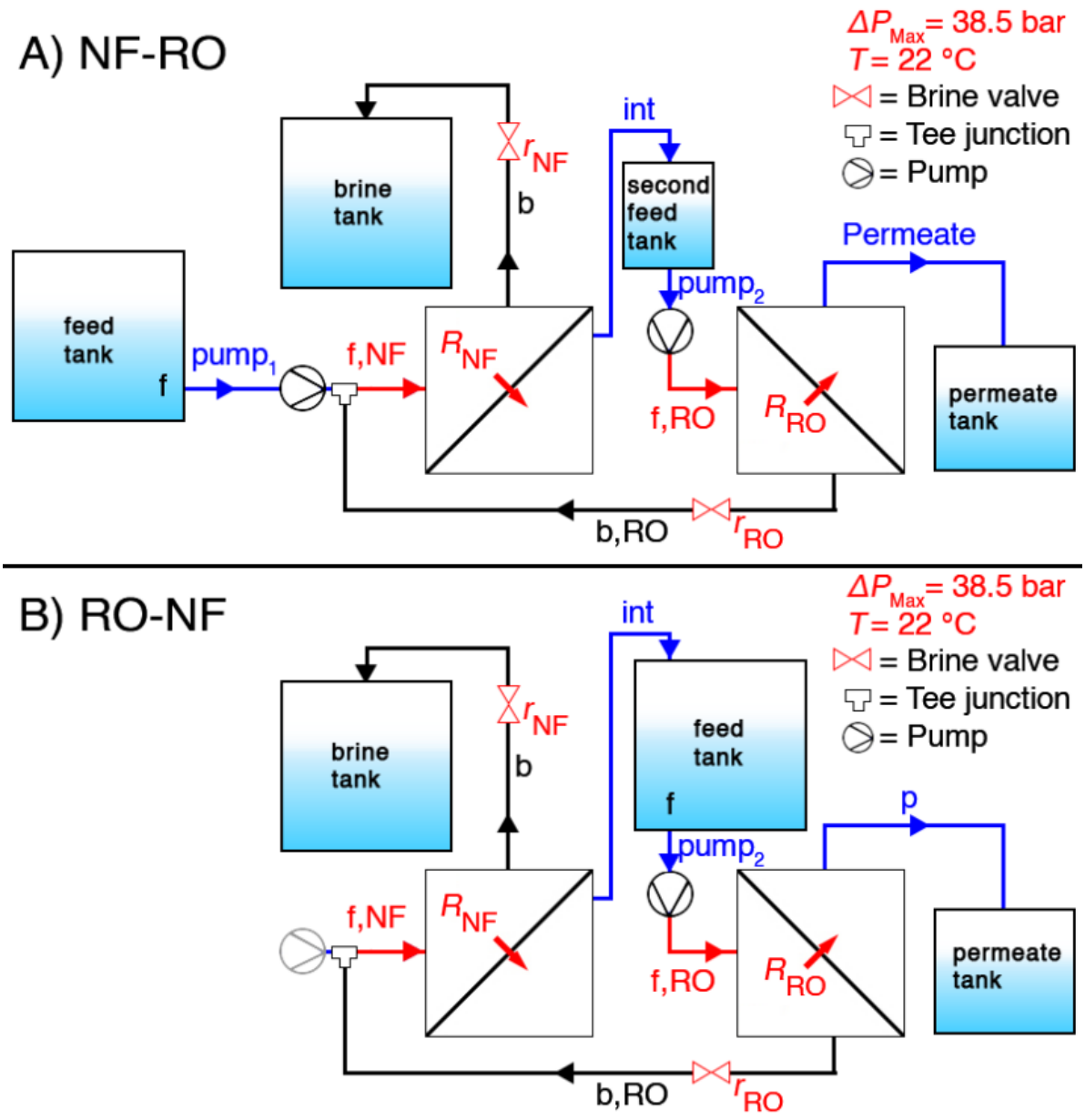

Figure 5-2. Schematics of laboratory systems: A) NF-RO and B) RO-NF (pump 1 is greyed out to indicate that it is not used). Feeds are drawn as red lines, permeates as blue lines, and brines as black lines. "f" stands for "feed", "b" for brine, "p" for permeate, "R" for rejection, "r" for recovery, "NF" for nanofiltration, and "RO" for reverse osmosis. "f" in the feed tank indicates feed concentration.

For NF-RO, several LDs can be used as the feed, such as LiCl, LiBr, $CaCl_2$, and $MgCl_2$. However, LiCl and LiBr are toxic [264, 265] whereas the properties of $CaCl_2$ change with operating conditions (see Section 1.2). In contrast, $MgCl_2$ does not have these limitations. Moreover, $MgCl_2$ has been used for LD regeneration in greenhouses using vacuum membrane distillation [34]. In greenhouse applications, $MgCl_2$ can be beneficial in case of leaks since magnesium is a fertiliser that enhances quality and yield of crops [307, 331, 332]. There are also other applications involving magnesium. For example, $MgCl_2$ recovery has been investigated in metallurgy and chemical applications [333, 334], and magnesium recovery from brines of desalination plants [335, 336]. Thus, experiments with $MgCl_2$ are representative of a range of LDAC and mineral recovery applications.

For RO-NF, it is more difficult to choose a specific feed composition because of the range of ZLD applications. For example, the ZLD survey of Mickley [312] reports high SO_4^{2-} concentrations in brackish water, with Na^+ and Cl^- being 30% of the total dissolved solids (*TDS*). Whereas in ZLD for seawater, Na^+ and Cl^- represent more than 90% of the total *TDS* [311, 316, 318, 324]. Thus, a $MgCl_2$ solution is used for both NF-RO and RO-NF to compare the two configurations consistently. Moreover, an additional validation of the RO-NF model using NaCl was conducted using data from Laskowska et al. [324] who modelled RO-NF with seawater (95% of which was Na^+ and Cl^-).

After verifying the 2-stage models, the models were applied to the 4-stage systems as investigated in previous idealised configurations. Thus, a 3NF-RO system was modelled for a baseline greenhouse LDAC application based on Chapter 3, and a RO-3NF system for a baseline ZLD application based on Wang et al. [73]. Finally, a sensitivity analysis was performed for the 4-stage systems by varying feed concentration, ERD efficiency, and feed temperature.

The structure of Chapter 5 is as follows. First, the theoretical modelling of the multi-stage NF systems is presented. Then, the equipment and experimental procedure are described. Subsequently, experimental results for NF-RO and RO-NF are shown followed by their model validation. Finally, the model results of the 4-stage systems are compared to those reported in previous theoretical studies and their conventional thermal alternatives.

5.2 Theory

The interpolation equations and the iterative method to calculate σ, developed in Chapter 4, did not match the experimental results of this Chapter. Specifically, the rejection interpolation using the NFX membrane and $MgCl_2$ concentrations of 33–52 g/L (as for the experiments conducted in this Chapter) calculates values of 27–23%, but rejections above 70% were measured during the experiments using the same membrane type and feed. This discrepancy can be attributed to the different types of filtration. In Chapter 4, the stirred cell used membrane samples and operated in dead-end filtration having no brine outlet and recovery of 100%. In this Chapter, the 2-stage system uses spiral wound membranes and operates in cross-flow filtration having a brine outlet and low recovery (below 20%). Consequently, a new model was developed for the 2-stage system.

The model of each membrane stage has six input and six output parameters (Figure 5-3). The input parameters for the NF membrane are NF feed mass flow[9] ($\dot{m}_{f,NF}$) [kg/min], NF feed concentration ($C_{f,NF}$) [g/L], NF membrane rejection (R_{NF}), feed temperature (T_f) [°C], NF recovery (r_{NF}), and maximum allowable pressure (ΔP_{max}) [bar]. The output parameters are intermediate mass flow ($\dot{m}_{int}$) [kg/min], intermediate concentration (C_{int}) [g/L], brine mass

[9] In Chapter 5, the mass flows are presented in [kg/min] instead of [kg/s] (as in other Chapters) to provide a clearer visualisation of the experimental flows, which are relatively low. For instance, the experimental flow of 1 kg/min that will be discussed later is equivalent to 0.0166 kg/s.

flow ($\dot{m}_b$) [kg/min], brine concentration (C_b) [g/L], NF membrane permeability ($L_{p,NF}$) [L/(m^2 h bar)], and the applied pressure to the NF membrane (ΔP_{NF}) [bar]. The output parameters $\dot{m}_{int}$, $\dot{m}_b$, and C_b are calculated based on mass conservation equations:

$$\dot{m}_{int} = \dot{m}_{f,NF}\, r_{NF} \tag{4-1}$$

$$\dot{m}_b = \dot{m}_{f,NF} - \dot{m}_{int} \tag{4-2}$$

$$wt_b = \frac{\dot{m}_{f,NF}\, wt_{f,NF} - \dot{m}_{int}\, wt_{int}}{\dot{m}_b} \tag{4-3}$$

where *wt* is the weight concentration (weight percentage of solute per solution) [wt.%]. The results are presented using concentrations *C* [g/L] based on conversion equations from *C* to *wt* found in appendix 7. The use of [g/L] enables the following standard definition of rejection to be used:

$$C_{int} = C_{f,NF}(1 - R_{NF}) \tag{4-4}$$

For an ideal membrane, the applied pressure ΔP_{NF} has elsewhere been assumed equal to the transmembrane osmotic pressure which is calculated as $\Delta P_{NF} = \Delta \Pi_{b,NF}$ [308]. This assumption does not, however, account for any pressure losses. Here, ΔP_{NF} is calculated more realistically as the sum of transmembrane osmotic pressure, membrane pore resistance loss, and cross-flow pressure drop:

$$\Delta P_{NF} = CP\, \Delta \Pi_{b,NF} + \frac{J_{v,NF}}{L_{p,NF}} + \frac{\Delta P_m}{2} \tag{4-5}$$

where $\Delta \Pi_{b,NF}$ [bar] is calculated as:

$$\Delta \Pi_{b,NF} = R_{NF}\, \Pi_b \tag{4-6}$$

where Π_b [bar] is the osmotic pressure of the brine (calculated with Eq. 2-4 based on T_f). Concentration polarisation (*CP*) is included as a multiplier of $\Delta \Pi_{b,NF}$, calculated as in [337].

Like the NF membrane stage model, the RO membrane stage model also utilises the above equations but with the rejection (R_{RO}) set equal to one. The subscript 'RO' is used in place of 'NF' and 'p' in place of 'int' to distinguish this case, as shown in Figure 5-3B.

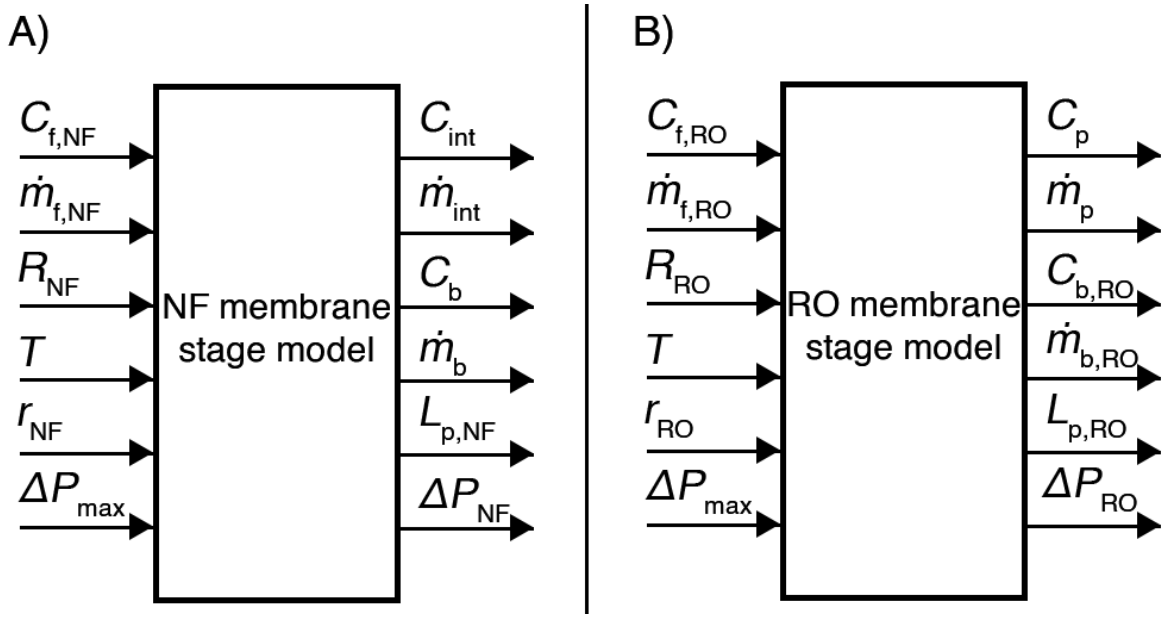

Figure 5-3. A) NF membrane stage model with input and output parameters. B) RO membrane stage model with input and output parameters. "C" stands for concentration, "ṁ" stands for flow, "R" stands for rejection, "T" for feed temperature, "r" for recovery, "ΔP" for applied pressure, and "L_p" for permeability. Subscripts match the nomenclature of Figure 5-2. Note that the red coloured parameters in Figure 5-2 are inputs of the membrane stage models.

Mixing occurs at the tee junction (see Figure 5-2) where mass flow conservation equations are applied. Thus, the sum of pump 1 inlet flow ($\dot{m}_{pump1}$) [kg/min] and brine RO flow ($\dot{m}_{b,RO}$) [kg/min] equals the feed flow into the NF membrane ($\dot{m}_{f,NF}$) [kg/min]:

$$\dot{m}_{pump1} + \dot{m}_{b,RO} = \dot{m}_{f,NF} \tag{4-7}$$

Similarly, the sum of the two inlet flows multiplied by their respective concentrations (wt_{pump1} and $wt_{b,RO}$) [g/L] equals $\dot{m}_{f,NF}$ multiplied by its concentration ($wt_{f,NF}$) [g/L]. For RO-NF, pump 1 does not operate and therefore $\dot{m}_{pump1}$ and C_{pump1} are both zero.

$$\dot{m}_{\text{pump1}}\, wt_{\text{pump1}} + \dot{m}_{\text{b,RO}}\, wt_{\text{b,RO}} = \dot{m}_{\text{f,NF}}\, wt_{\text{f,NF}} \tag{4-8}$$

An ERD was not part of the experimental system but was included in the model. The power $Power_{ERD}$ [kW_{el}] recovered by the ERD from the brine is calculated as:

$$Power_{\text{ERD}} = \frac{(\Delta P_{NF} - \Delta P_m)\dot{m}_{\text{b}}\, \eta_{\text{ERD}}}{60\rho_b} \tag{4-9}$$

where ρ_b [kg/m^3] is the density of the brine and η_{ERD} is the efficiency of the ERD assumed equal to 70%. To calculate the net power required when using an ERD, $Power_{ERD}$ is subtracted from the total power required by the two motors. The power required by the motors was modelled using a linear interpolation based on experiments (see Appendix 7, Figure A7-1).

The above equations define the steady-state model of the 2-stage system. However, to match the model to the experiments, the tanks also need to be modelled. The tanks are not steady-state since their weight (m) [kg] change according to the difference between the inlet flow ($\dot{m}_{\text{in}}$) minus the outlet flow ($\dot{m}_{\text{out}}$) [kg/min], i.e.

$$\frac{dm}{dt} = \dot{m}_{\text{in}} - \dot{m}_{\text{out}} \tag{4-10}$$

For NF-RO, the first feed tank has $\dot{m}_{\text{in}}$ equal to zero and $\dot{m}_{\text{out}}$ equal to $\dot{m}_{\text{pump1}}$. The second feed tank has $\dot{m}_{\text{in}}$ equal to the NF permeate flow ($\dot{m}_{\text{int}}$) and $\dot{m}_{\text{out}}$ equal to $\dot{m}_{\text{pump2}}$. For RO-NF, which has only one feed tank, $\dot{m}_{\text{in}}$ is equal to $\dot{m}_{\text{int}}$ and $\dot{m}_{\text{out}}$ is equal to $\dot{m}_{\text{pump2}}$. In RO-NF, both the concentration and weight of the feed tank vary. The following equation assumes ideal mixing ($wt_{\text{out}} = wt$):

$$\frac{d(m\, wt)}{dt} = \dot{m}_{\text{in}}\, wt_{\text{in}} - \dot{m}_{out}\, wt \tag{4-11}$$

The four sub-models: membrane stage, tee junction, tank weights, and tank concentration constitute a model for each membrane stage. The first stage of *n*NF-RO and the last stage of RO-*n*NF also include the ERD sub-model. A multi-stage system is modelled by connecting multiple membrane stage models in series. Thus, NF-RO and RO-NF each contain two membrane models, one for NF and one for RO. NF-RO and RO-NF were modelled using Matlab-Simulink® (release 2022a, Natick, Massachusetts: The MathWorks Inc) where models are easily linked (Figures A7-2 and A7-3 in Appendix 7). The systems were simulated over 100 minutes with a timestep of 1 minute. The 4-stage systems (3NF-RO and RO-3NF) were also modelled using Matlab-Simulink® (Figures A7-4 and A7-5 in Appendix 7), using the same approach as for the 2-stage systems.

5.3 Method

5.3.1 Description of equipment

This subsection provides information about the pumps and motors, membranes and their vessels, and details of pipework, tanks, and instrumentation used in the experimental set-up (Figures 5-4 and 5-5).

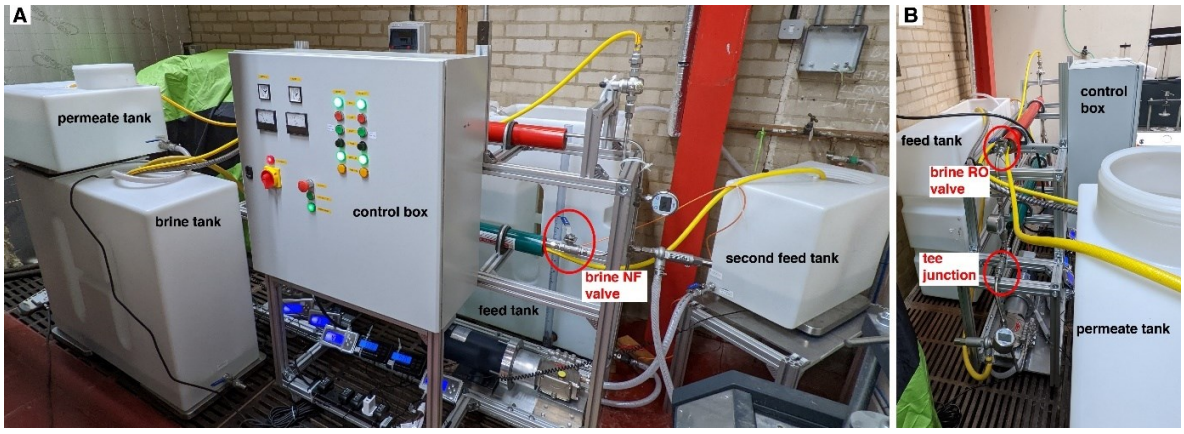

Figure 5-4. Photographs of the 2-stage system: A) front view B) left view.

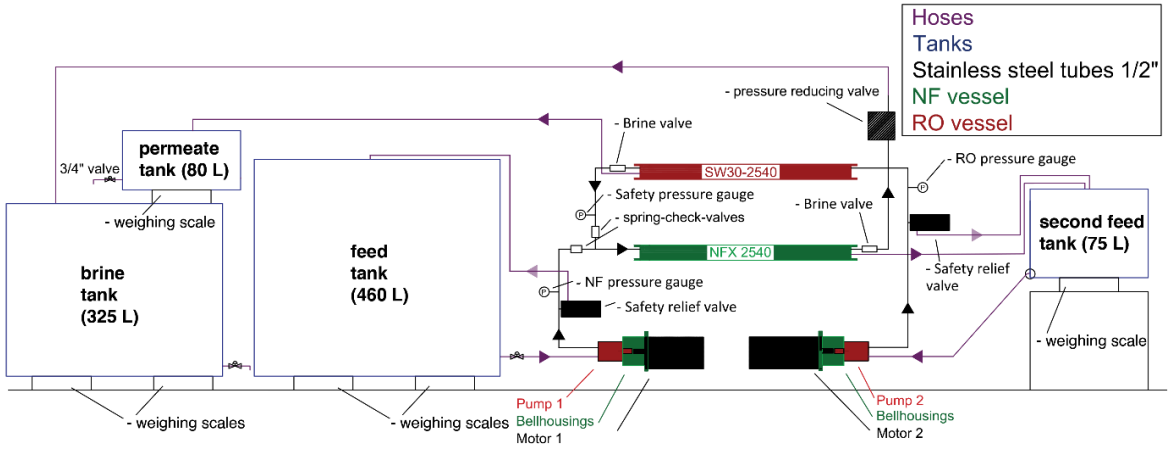

Figure 5-5. Schematic of the 2-stage system operated as NF-RO (control box and structure not shown). Arrows show the direction of flow. Semi-transparent arrows indicate that these flows exist only when the safety relief valves are activated.

Two stainless-steel 53SS series pumps were purchased from Interpump group (Italy). Pump 1 is the SS1B503 model while pump 2 is the SS1B505 model. To drive the pumps, two low voltage DC permanent magnet motors were purchased from Leeson electric corporation (USA). Motors 1 and 2 have rated powers of 0.75 kW and 1.5 kW, respectively, at 1800 RPM.

A type NFX membrane module – diameter of 0.0635 m (2.5”), length of 1.016 m (40”), and area of 2.6 m^2 – was purchased from Synder filtration (USA). According to the Synder datasheet, the membrane has a maximum operating pressure of 41 bar, average $MgSO_4$ rejection of 95%, average NaCl rejection of 40%, and pure water permeability of 2.734 L/(m^2 h bar) [126]. A type SW30 RO membrane module (of the same dimensions and area as the NF module) was purchased from Dupont (USA). According to the Dupont datasheet, the RO membrane has a maximum operating pressure of 69 bar, NaCl rejection above 99.4%, and pure water permeability of 1.401 L/(m^2 h bar) [338]. By using tap water, pure water permeabilities of 2.669±0.16 and 1.451±0.09 L/(m^2 h bar) were experimentally measured, respectively, thus showing an error of less than 4% compared to datasheets. Two pressure

vessels were purchased from PHOENIX Vessel Technology Ltd (UK) with maximum operating pressure of 69 and 83 bar for the NF and RO membranes, respectively. For both membranes, their longitudinal pressure drop (ΔP_m) was measured experimentally in the range of 0.6–1 bar. ΔP_m increased with flow but did not increase after conducting the experiments, implying that fouling did not take place. However, fouling may not have been noticed because the total experimental time was less than 20 hours.

The NF membrane has a maximum operating pressure of 41 bar and experiments were carried out at 38.5 bar for safety. The RO membrane has a maximum operating pressure of 69 bar, but pressures above 41 bar were not possible because the RO brine was an inlet of the tee junction preceding the NF membrane (see Figure 5-2). The applied pressure at the NF membrane (ΔP_{NF}) and applied pressure at the RO membrane (ΔP_{RO}) were inlets of the tee junction and their values were affected when using both pump 1 and pump 2 at different applied pressures; therefore both ΔP_{NF} and ΔP_{RO} must be equal to 38.5 bar.

The 2-stage system includes two CF8M stainless-steel ball-valves (called brine valves in Figure 5-5), two 316 stainless-steel spring check valves, one CF8M stainless-steel pressure reducing valve (type 481-SP), two CF8M stainless-steel safety relief valves, three 316 stainless-steel pressure gauges (model DG-10 digital), one 316 stainless-steel tee junction, and 3.2 m of 316 stainless-steel tubes (outer diameter of 0.0127 m and the wall thickness of 0.0012 m). Based on datasheets, the NF pressure gauge has an accuracy of ±0.25% and measuring range of 0–50 bar based on its datasheet, whereas the RO and safety pressure gauges have an accuracy of ±0.5% and measuring range of 0–100 bar based on its datasheet. The NF and RO pressure gauges measure ΔP_{NF} and ΔP_{RO}, respectively. Whereas the safety pressure gauge was used to check that the RO brine did not increase ΔP_{NF} above 38.5 bar.

At high flows, mixing at the tee junction affected ΔP_{NF} and ΔP_{RO}. For example, while testing with tap water, ΔP_{NF} was equal to 14 bar when using only pump 1 at 3.6 kg/min. Whereas using only pump 2 at 4.45 kg/min, ΔP_{RO} was equal to 17.8 bar. But when operating pump 1 at 3.6 kg/min and pump 2 at 4.45 kg/min together, the two streams affected each other and their pressure increased[10] to 32.2 bar. To avoid this issue, it was necessary to operate NF-RO with a pump 2 flow below 0.5 kg/min when the pump 1 flow was above 3 kg/min. This almost nullified the ΔP disturbance in the tee junction. This ΔP disturbance did not occur in the RO-NF system which only utilises one pump.

Four tanks made of medium density polyethylene (volumes shown in Figure 5-5) were purchased from Kingspan Water & Energy Ltd (UK). To weigh the feed in the feed tank, two weighing scales were purchased from Oypla (UK) having an accuracy of ±0.1 kg and measuring range of 0–300 kg. For the brine, permeate, and intermediate solutions, four weighing scales were purchased from T-Mech (UK) having an accuracy of ±0.1 kg and measuring range of 0–200 kg. Due to space limitations, the permeate tank was placed on top of the brine tank. Thus, two scales placed under the brine tank measured the weight of the brine in the brine tank and the permeate in the permeate tank. One scale placed under the permeate tank measured the weight of the permeate in the permeate tank, and one scale placed under the second feed tank measured the weight of the intermediate solution in the second feed tank. The weight of the tanks and the weight of the scale on top of the brine tank were set to zero by using the tare feature. The weight of the brine was calculated as the combined weight of brine and permeate (measured by two scales) minus the weight of the permeate (measured by another scale).

[10] To calculate the equilibrium ΔP, first the single ΔP must be divided by their flows ($\Delta P_{NF}/3.6 = \Delta P_{RO}/4.45 = 4$). Then, the equilibrium ΔP is given by multiplying $\Delta P_{NF}/3.6$ with the outlet flow, equal to 8.05 kg/min. Thus, the equilibrium ΔP is 8.05×4 =32.2 bar.

5.3.2 Solution preparation and experimental procedure

This section first describes how the $MgCl_2$ solutions were prepared. Subsequently, the experimental procedure and pressure control are presented, followed by information regarding data recording, sample collection, and uncertainties of parameters.

Three solutions (concentrations of 33.6, 40.9, and 51.5 g/L) were prepared by mixing tap water with $MgCl_2$ powder (purity of 99% purchased by Fisher Scientific, UK). Initially, the solution with concentration of 33.6 g/L was prepared by mixing 398 kg of tap water with 13.58 kg of $MgCl_2$. Sodium metabisulphite (0.6 g) was also added to mitigate membrane oxidation. After performing six experiments, three for NF-RO and three for RO-NF, the solution concentration was increased to 40.9 g/L by adding another 2.87 kg of $MgCl_2$ to the feed solution. After repeating the six experiments with 40.9 g/L, the solution concentration was further increased to 51.5 g/L by adding 4.5 kg of $MgCl_2$ to the feed solution. The concentration of 51.5 g/L was chosen because its osmotic pressure is 2 bar higher than ΔP equal to 38.5 bar. The concentration was not increased above 51.5 g/L because the permeate flux of the NF membrane was extremely low and took 50–70 minutes (depending on flow) to produce 4 kg which was the minimum required in the second feed tank to activate pump 2 without damaging it. Even though concentrations of 33.6 and 40.9 g/L produced 4 kg faster, pump 2 was also activated after 50–70 minutes. This was done for consistency, which allows a fair comparison among different concentrations. The concentrations of 33.6 and 40.9 g/L were chosen as lower concentrations, but still close to the maximum of 51.5 g/L to evaluate system operation with high feed concentrations.

Before each experiment, the solution in the feed tank was homogenised for 15 minutes using a mixing pump. Then the mixing pump was placed in the brine tank and used to recirculate the brine from the brine tank to the feed tank. Brine recirculation was used for NF-

RO and RO-NF systems and activated when the brine tank reached 70 kg for low pump mass flows, and 170 kg for medium and high flows. The brine recirculation lasted 5 minutes for experiments with low flows and 10 minutes with medium-high flows. Recirculation of brine was only used to increase the duration of experiments but was not an investigated parameter. Manual stirring of the feed tank was performed every 5 minutes to ensure uniform concentration.

Experiments were carried out at room temperature of 22±1 °C. During experiments, the speeds of the pumps were controlled manually to keep ΔP_{NF} and ΔP_{RO} at 38.5 bar. This maximised the flux while remaining below the 41 bar pressure limit of the NF membrane. Thus, the speed of pump 1 was slightly increased whenever ΔP_{NF} started to decrease below 38.5 bar. In contrast, the speed of pump 1 was slightly decreased whenever ΔP_{NF} started to increase above 38.5 bar. As a result of these adjustments, pump 1 flow for NF-RO was 1±0.12 kg/min (for low flow experiments), 2.8±0.15 kg/min (medium flow experiments), and 3.6±0.15 kg/min (high flow experiments). The system was operated to find the opening of the NF brine valve that resulted in ΔP_{NF} of 38.5 bar using these three pump 1 flows. Only the NF brine was regulated while the RO brine valve was completely opened for all experiments. This is because the brine of the RO membrane was constantly under pressure due to the tee junction.

For RO-NF, the investigated pump 2 flows were 1.13±0.2 kg/min (low flow), 3±0.19 kg/min (medium flow), and 4.45±0.25 kg/min (high flow). These pump 2 flows were selected according to the NF brine valve settings which were the same as in NF-RO. Thus, the flows of pump 2 were selected to provide a ΔP_{RO} of 38.5 bar.

The set of experiments started with NF-RO first using low pump 1 flow, then medium pump 1 flow, and finally high pump 1 flow. After finishing the NF-RO experiments, RO-NF

was investigated in the same order, e.g., low, medium, and finally high flows at pump 2. After finishing an experiment, the solutions in the brine, permeate, and second feed tanks were recirculated to the feed tank. To change from NF-RO to RO-NF, the hoses connecting feed tank to pump 1 and second feed tank to pump 2 were disconnected, and then the hose of the feed tank was connected to pump 2. For both systems, low pump flow experiments lasted 95 minutes, medium pump flow lasted 90 minutes, and high pump flow lasted 80 minutes.

The operating parameters covered three feed $MgCl_2$ concentrations combined with three mass flows for each pump, resulting in nine experiments with NF-RO and nine with RO-NF. Recovery of NF (i.e., brine valve setting) was not fixed but was adjusted for each pump flow to provide ΔP_{NF} and ΔP_{RO} of 38.5 bar.

The weights of feed, second feed, permeate, and brine tanks were measured by the weighing scales, applied pressures by pressure gauges, currents of the motors through ammeters, and voltages of the motors through voltmeters. The values of the instruments were recorded by taking photos after 1 minute of operation, after 5 minutes of operation, and then every 5 minutes. The time was measured by using a precision stopwatch with an accuracy of ±1 second. Weighing scales and pressure gauges were digital, while ammeters and voltmeters were analogue. The software GetData Graph Digitizer was used to digitalise the analogue pointers of the ammeters and voltmeters.

For the concentration of feed, intermediate, permeate, and brine (as indicated in Figure 5-2), samples were taken every 15 minutes for the low pump flow experiments, every 10 minutes for medium and high pump flow experiments, and whenever the brine recirculation was activated or deactivated. The measured refractive indexes were almost constant throughout the experiment, confirming steady-state operation (as also seen from the constant osmotic pressures during the experiment in Figure 5-6); therefore, samples did not need to be

taken more often. The refractive indexes were measured by using an automatic refractometer (model J357 from Rudolph Research Analytical, USA) with an accuracy of ±0.00002, resulting in an accuracy of ±0.8 g/L for the C concentrations. The concentrations at times between sampling were calculated by linear interpolation.

For parameters x and y having uncertainties $\pm dx$ and $\pm dy$, respectively, the uncertainty dz of parameter z, where $z = x/y$ or $z = xy$, is given by Eq. 3-35. The uncertainties for the investigated parameters are shown in Table 5-1.

Table 5-1. Accuracies of investigated parameters with information regarding their calculation based on Eq. 3-35.

Parameter	Accuracy and unit	Calculated based on
Tank weight (m)	±0.1 kg	Manufacturer datasheet
NF pressure gauge (ΔP_{NF})	±0.25% bar	Manufacturer datasheet
RO pressure gauge (ΔP_{RO})	±0.5% bar	Manufacturer datasheet
Timestep (Δt)	±1 second	Accuracy of stopwatch
Concertation (C)	±0.8 g/L	Accuracy of refractometer
Electric power	±9% kW_{el}	Accuracies of ammeters and voltmeters
Osmotic pressure ($\Delta\Pi$)	±0.391 bar	Accuracy of C
Mass flow ($\dot{m}$)	±0.01 kg/min	Accuracies of m and Δt
Recovery (r)	±2%	Accuracy of m
SEC	±12.7% kWh_{el}/m^3	Accuracies of electric power and $\dot{m}$
Permeability (L_p)	±5.6% $L/(m^2\ h\ bar)$	Accuracies of ΔP_{RO} and $\dot{m}$
Rejection (R)	±1.5%	Accuracy of Ref_{ind}

5.4 Results

This section presents results of the steady-state operation for NF-RO, for RO-NF, and comparisons between them.

5.4.1 Experimental

Steady values for ΔP and $\Delta\Pi$ (and consequently C) were observed after 5 minutes, as shown in Figure 5-6.

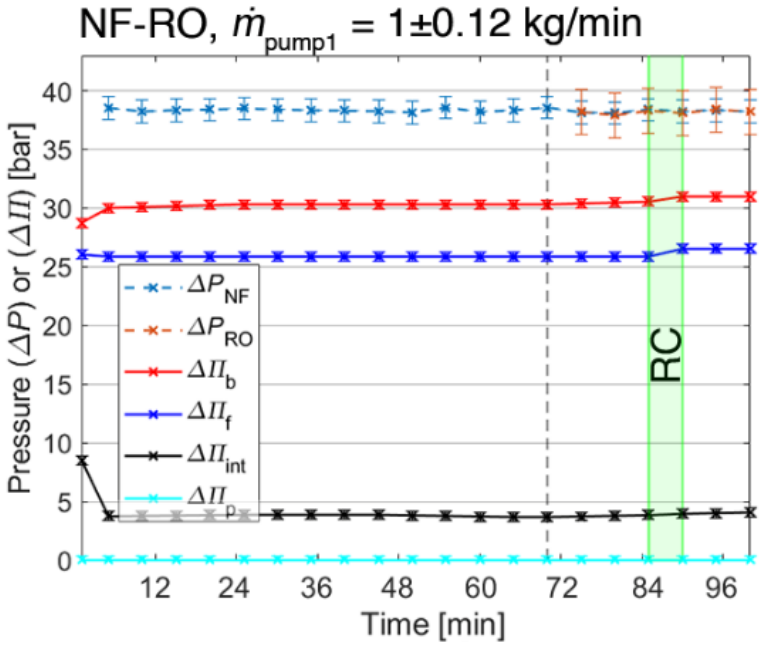

Figure 5-6. Applied pressures and osmotic pressures for NF-RO operating with feed concentration of 33.6 g/L and pump 1 flow of 1±0.12 kg/min. The vertical dashed line indicates when pump 2 was activated, while the lightly shaded green area indicates the duration during which the brine recirculation (RC) was active.

A longer period of 25 minutes was needed for r_{NF} to become constant (Figure 5-7). Figure 5-7 also shows that lower pump 1 flow achieves higher r_{NF} which decreased as C_f increased. The decrease in r_{NF} as C_f increased can be attributed to the reduced permeate driving force. At C_f of 33.6, 40.9, and 51.5 g/L, the corresponding feed osmotic pressures (Π_f) are 26.4, 32.2, and 40.7 bar, respectively. The permeate flux is directly proportional to the difference between ΔP and Π_f. Since ΔP was maintained constant at 38.5 bar during the experiments, the decreased driving force of permeate flux at higher C_f results in lower r_{NF}. Decrease in r_{NF} as C_f increased agrees with the experiments in Chapter 4 where the permeate flux (J_v, proportional to r) decreased as C_f increased. Additionally, the observed decrease in r_{NF} with increasing flow can be attributed to higher pressure losses. As the flow increases, so does J_v which is directly proportional to pore resistance loss. The cross-flow pressure drop also increases with feed flow [339], but its contribution is relatively low compared to pore resistance loss.

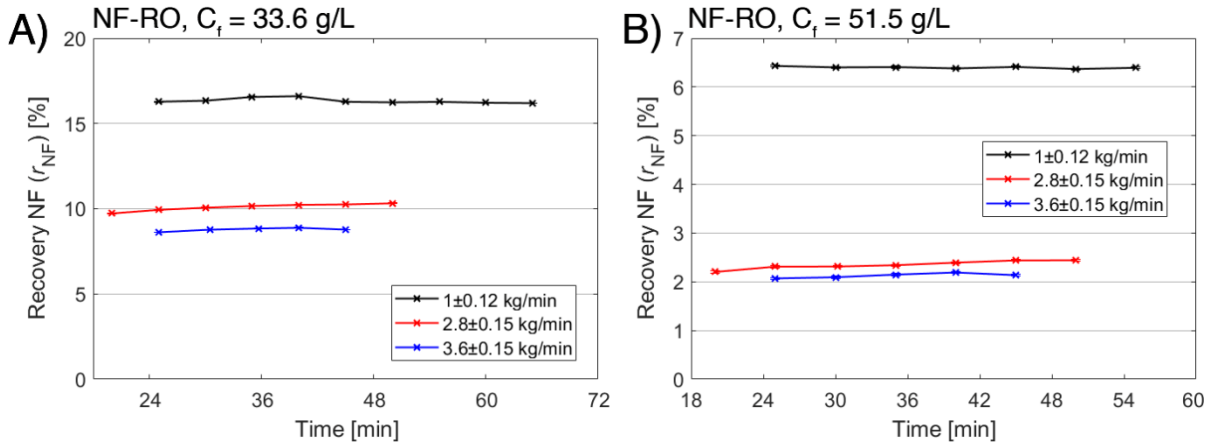

Figure 5-7. A) NF recovery (r_{NF}) measured during NF-RO operating with feed concentration (C_f) of 33.6 g/L and pump 1 flows of 1±0.12, 2.8±0.15, and 3.6±0.15 kg/min. B) Similar to A) but operating with C_f of 51.5 g/L. r_{NF} is plotted after stabilisation and until brine recirculation was deactivated.

Tables 5-2 to 5-4 summarise the steady-state results for C_b, r_{NF}, SEC_{hyd}, SEC_{el}, R_{NF}, and R_{RO} at different values of C_f. The lowest flow at pump 1 required less power than the other flows and gave the lowest SEC_{hyd}, and in turn the lowest SEC_{el}. Due to also having higher C_b, the lowest pump 1 flow was the preferred option.

Lower R_{NF} was measured when C_f increased (see Tables 5-2 to 5-4), with experimental R_{NF} values between 70% and 90%. This agrees with the findings of previous studies [133, 340]. Mitko et al. [340] conducted experiments using the same NF membrane, namely NFX, as in the experimental system, and attributed the lower R_{NF} at higher C_f to a higher diffusivity across the membrane, induced by the presence of more ions. In contrast, Hilal et al. [133] suggested that low R_{NF} at high C_f means that the membranes operate under unsuitable conditions. Both explanations may apply here since the NFX is a sanitary membrane designed for low C_f applications, such as dye concentration and coffee extraction [126], but experiments were conducted at high C_f.

At fixed C_f, R_{NF} decreased as the pump flow decreased (see Table 5-2). At higher flows, the concentration polarisation effect is reduced [341], leading to a lower concentration at the

membrane surface and, in turn, resulting in a higher R_{NF}. Another possible explanation is that the decrease in R_{NF} was accompanied by an increase in r_{NF}. At higher r_{NF}, more permeate is produced, which explains why low flow gives a higher C_b. Thus, the membrane works harder at low flow which leads to a decrease in R_{NF}. Lower R_{NF} at higher r_{NF} is consistent with the interpolation equation (Eq. 3-21) developed in Chapter 4 to predict R_{NF}. Eq. 3-21 is based on dead-end filtration experiments, meaning r_{NF} of 100%. Therefore, the calculated R_{NF} of 27–23% using Eq. 3-21 (mentioned earlier in Section 4.2) represents the value that would be measured if the NFX membrane of the 2-stage system was operated with r_{NF} of 100% (i.e., fully closed NF brine valve). Similar findings were also observed by Hilal et al. [133] who investigated three NF membranes (NF90, NF270, and N30F) and found lower R_{NF} at lower flows.

The flow of pump 1 and C_f did not have a significant effect on R_{RO} which remained above 98% in all experiments. SEC_{hyd} increased as C_f increased for all flows, as shown from Table 5-2 to Table 5-4, meaning that the system struggles to produce permeate at higher C_f. SEC_{el} rises less than SEC_{hyd} because of improved pump efficiency at higher flow.

Table 5-2. Summary of NF-RO results with feed concentration of 33.6 g/L at steady-state conditions. SEC values are measured from when pump 2 was activated (causing permeate production to begin) until the end of the experiment.

NF-RO experiment	Pump 1 flow [kg/min]	C_b [g/L]	r_{NF} [%]	SEC_{hyd} [kWh/m^3]	SEC_{el} [kWh$_{el}$/m^3]	R_{NF} [%]	R_{RO} [%]
1	1±0.12	40.04	17.2	2.97	8.25	84.41±0.83	99.18±0.76
2	2.8±0.15	39.64	10.32	6.92	19.65	90.65±0.83	99.17±0.76
3	3.6±0.15	39.03	8.78	8.78	18.01	90.84±0.83	99.12±0.76

Table 5-3. Summary of NF-RO results with feed concentration of 40.9 g/L at steady-state conditions. SEC values are measured from when pump 2 was activated (causing permeate production to begin) until the end of the experiment.

NF-RO experiment	Pump 1 flow [kg/min]	C_b [g/L]	r_{NF} [%]	SEC_{hyd} [kWh/m^3]	SEC_{el} [kWh$_{el}$/m^3]	R_{NF} [%]	R_{RO} [%]
4	1±0.12	45.43	11.4	9.43	26.19	82.3±0.77	99.19±0.76
5	2.8±0.15	44.24	5.75	13.68	30.69	88.95±0.77	99.15±0.76
6	3.6±0.15	43.92	4.79	18.42	40.01	90.9±0.77	99.14±0.76

Table 5-4. Summary of NF-RO results with feed concentration of 51.5 g/L at steady-state conditions. SEC values are measured from when pump 2 was activated (causing permeate production to begin) until the end of the experiment.

NF-RO experiment	Pump 1 flow [kg/min]	C_b [g/L]	r_{NF} [%]	SEC_{hyd} [kWh/m^3]	SEC_{el} [kWh$_{el}$/m^3]	R_{NF} [%]	R_{RO} [%]
7	1±0.12	54.56	6.39	20.81	46.24	71.6±0.53	99.19±0.74
8	2.8±0.15	53.77	2.44	30.29	64.81	77.15±0.53	99.13±0.74
9	3.6±0.15	53.44	2.14	53.22	108.25	78.8±0.53	99.04±0.74

The RO-NF system required 25-45 minutes to reach steady-state operation, where system recovery (r) became constant (Figure 5-8). Similarly for NF-RO, lower flow and lower C_f resulted in higher r.

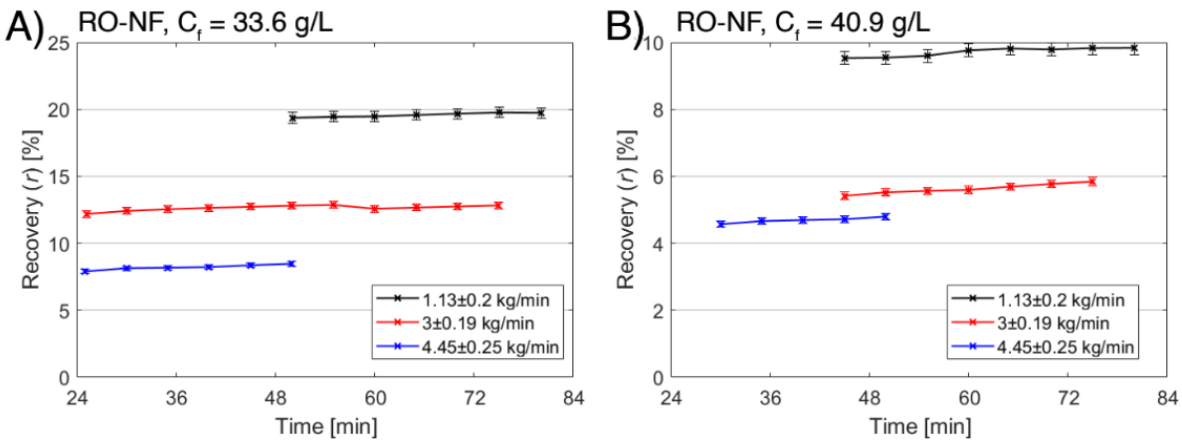

Figure 5-8. Total system recovery (r) measured during RO-NF operating with feed concentration (C_f) of 33.6 g/L and pump 2 flows of 1.13±0.2, 3±0.19, and 4.45±0.25 kg/min. B) Similar to A) but operating with C_f of 40.9 g/L. r is plotted after stabilisation and until brine recirculation was deactivated.

Steady-state results for C_b, r, SEC_{hyd}, SEC_{el}, and R_{RO} are summarised in Tables 5-5 and 5-6 for C_f of 33.6 and 40.9 g/L, respectively, for various pump 2 mass flows. SEC_{hyd} and SEC_{el} increase with flow. The lowest pump 2 flow gave the highest C_b and the lowest SEC_{el}, making it the preferred option. R_{RO} was not affected by the flow of pump 2 or C_f and remained above 98% in all experiments. Increasing C_f results in higher SEC_{hyd}.

Table 5-5. Summary of RO-NF with feed concentration of 33.6 g/L at steady-state conditions.

RO-NF experiment	Pump 2 flow [kg/min]	C_b [g/L]	r [%]	SEC_{hyd} [kWh/m^3]	SEC_{el} [kWh$_{el}$/m^3]	R_{RO} [%]
1	1.13±0.2	46.82	19.74	5.62	11.82	99.18±0.76
2	3±0.19	43.3	12.83	9.86	15.64	99.17±0.76
3	4.45±0.25	40.78	8.48	14.22	20.44	99.16±0.76

Table 5-6. Summary of RO-NF with feed concentration of 40.9 g/L at steady-state conditions.

RO-NF experiment	Pump 2 flow [kg/min]	C_b [g/L]	r [%]	SEC_{hyd} [kWh/m^3]	SEC_{el} [kWh$_{el}$/m^3]	R_{RO} [%]
4	1.13±0.2	48.22	9.84	10.69	22.5	99.18±0.76
5	3±0.19	46.49	5.84	19.48	29.52	99.16±0.76
6	4.45±0.25	45.27	4.8	23.89	35.63	99.15±0.76

For $C_f \leq$40.9 g/L, RO-NF had $L_{p,RO}$ of 70–180% higher than NF-RO (Figure 5-9), whereas the difference for C_b was 6–17% (Tables 5-7 and 5-8). However, at C_f of 51.5 g/L, RO-NF was not able to produce permeate (L_p is zero in Figure 5-9).

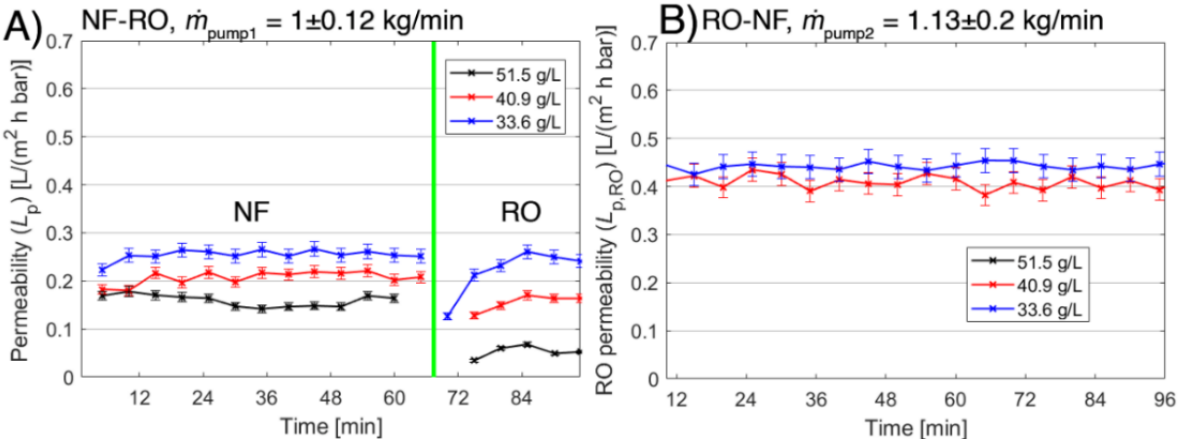

Figure 5-9. A) Permeability (L_p) measured during NF-RO operating with pump 1 flow of 1±0.12 kg/min and feed concentrations (C_f) of 33.6, 40.9, and 51.5 g/L. The vertical green line separates the nanofiltration ($L_{p,NF}$) from the reverse osmosis ($L_{p,RO}$). B) $L_{p,RO}$ measured during RO-NF operating with pump 2 flow of 1.13±0.2 kg/min and C_f of 33.6, 40.9, and 51.5 g/L. For C_f of 51.5 g/L, $L_{p,RO}$ was zero meaning that the system did not produce permeate.

The concept of *n*NF-RO was proven since the NF-RO system produced permeate with ΔP of 38.5 bar being lower than Π_f of 40.7 bar (i.e., C_f of 51.5 g/L). This was possible because R_{NF} was in the range of 70–90% which resulted in a reduced osmotic pressure difference across the NF membrane ($\Delta\Pi_f$) of 28.5–36.6 bar.

The calculated L_p values, obtained using the iterative method (see Appendix 7), are below their pure water permeability. The iterative method decreases L_p until the system of equations is solved. Consequently, pore resistance loss increases as it is inversely proportional to L_p. Some studies suggest that increasing the pure water permeability may not significantly improve the performance. For example, Werber et al. [342] found that increasing the pure water permeability from 2 to 100 L/(m^2 h bar) would decrease the energy requirement by only 4.7%. However, increasing the pure water permeability could lead to higher L_p values and, in turn, lower pore resistance losses. For example, aquaporin-based biological membranes have high L_p [343], which decreases pore resistance. Optimising the shape of aquaporins, such as using conical entrances, can further increase L_p [344].

Additionally, pore resistance loss across spiral wound RO and NF membranes can be reduced by employing lower feed flowrates or bigger membrane modules [345]. Fouling is also a significant factor affecting pore resistance. In fact, pore resistance loss increases with the concentration of organic matter [345]. Therefore, limiting fouling is crucial to minimise pore resistance.

Results for max C_f, max C_b, and brine-feed concentration differences are summarised in Tables 5-7 and 5-8. The brine-feed concentration difference for NF-RO was low, confirming the theory that *n*NF-RO can work for applications requiring little concentration increase starting from a high Π_f. RO-NF achieved higher brine-feed concentration differences than NF-RO which confirms the theory that RO-*n*NF is preferred for applications requiring high concentration differences but starting from a low Π_f.

Table 5-7. Summary of feed concentration (C_f), maximum brine concentration (C_b), and their difference for all NF-RO experiments.

NF-RO experiment	C_f [g/L]	Max C_b [g/L]	Concentration difference [g/L]
1	33.6	40.04	6.44
2	33.6	39.64	6.04
3	33.6	39.03	5.43
4	40.9	45.43	4.53
5	40.9	44.24	3.34
6	40.9	43.92	3.02
7	51.9	54.56	2.66
8	51.9	53.77	1.87
9	51.9	53.44	1.54

Table 5-8. Summary of feed concentration (C_f), maximum brine concentration (C_b), and their difference for all RO-NF experiments. Results in parenthesis did not produce permeate.

RO-NF experiment	C_f [g/L]	Max C_b [g/L]	Concentration difference [g/L]
1	33.6	46.82	13.22
2	33.6	43.3	9.7
3	33.6	40.78	7.18
4	40.9	48.22	7.32
5	40.9	46.49	5.59
6	40.9	45.27	4.37
7	(51.9)	(54.52)	(2.62)
8	(51.9)	(53.48)	(1.59)
9	(51.9)	(53.15)	(1.25)

5.4.2 Model validation and predictions

This section starts with the 2-stage model validation, continues with the 4-stage baseline cases for greenhouse LDAC and for ZLD, and concludes with a sensitivity analysis for the 4-stage systems.

The 2-stage system modelling results agreed well with the experimental values. Predictions and experiments regarding C and ΔP agreed with errors below 2% and 7% respectively for NF-RO (Figures 5-10A and 5-11A), and 3% and 2% for RO-NF (Figures 5-10B and 5-11B). For NF-RO, $\dot{m}$ and L_p agreed with errors below 8% and 10% respectively (Figures A8-2A and A8-3A), whereas for RO-NF the same parameters had errors below 8% and 7% (Figures A8-2B and A8-3B). These model errors are comparable to the experimental accuracies of SEC_{el}, $\dot{m}$, C, ΔP, and L_p equal to ±12.7 kWh_{el}/m^3, ±0.01 kg/min, ±0.8 g/L, ±0.5% bar, and ±5.6% $L/(m^2\ h\ bar)$, respectively (see Table 5-1). The accuracy of SEC_{el} was the worst because of the low accuracy of ±9% kW_{el} to calculate the electric power, related to the low accuracies of the ammeters and voltmeters.

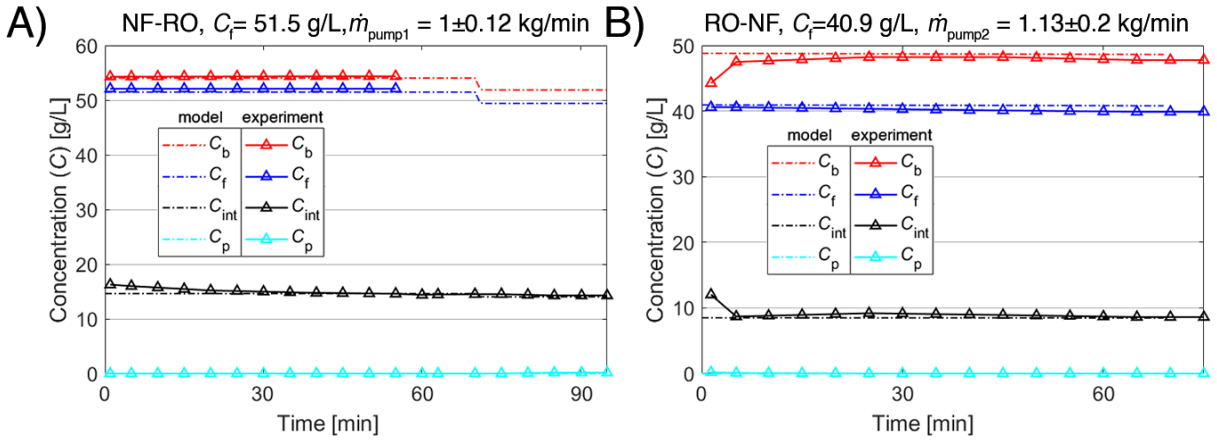

Figure 5-10. A) Concentrations against time. Subscripts as in Figure 5-2. Results in triangles are experimental during NF-RO operating with pump 1 flow of 1±0.12 kg/min and feed concentration (C_f) of 51.5 g/L. Experimental C_f and C_b results are shown until brine recirculation was deactivated (model does not include brine recirculation). Model results are shown by dashed lines. B) Similar to A) but for RO-NF with C_f of 40.9 g/L and pump 2 flow of 1.13±0.2 kg/min.

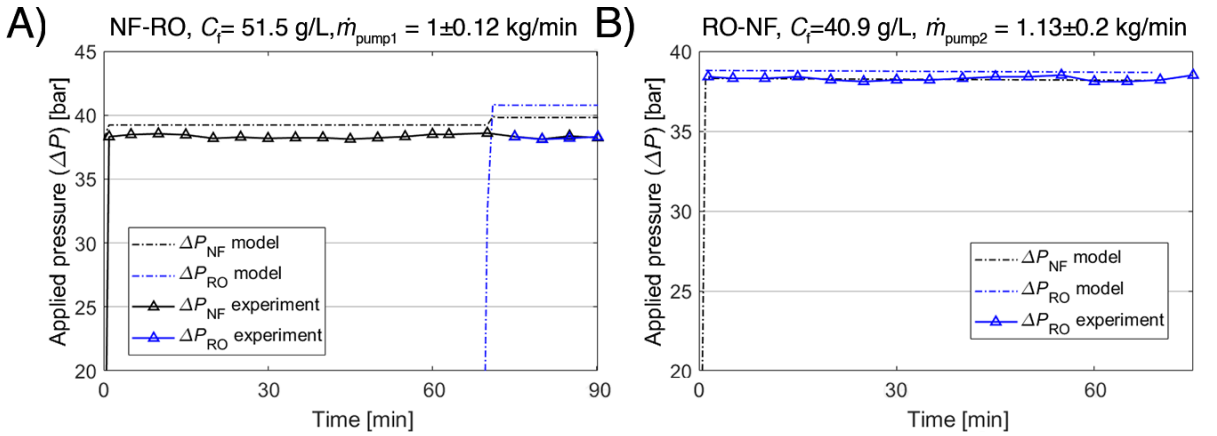

Figure 5-11. A) Applied pressures against time. Results in triangles are experimental during NF-RO operating with pump 1 flow of 1±0.12 kg/min and feed concentration (C_f) of 51.5 g/L. Model results are shown with dashed lines. B) Similar to A) but for RO-NF with C_f of 40.9 g/L and pump 2 flow of 1.13±0.2 kg/min.

The lowest and highest errors were both for NF-RO, equal to 2% for C (Figure 5-10A) and 11% for the SEC_{el}. The NF-RO model for its baseline case calculates a SEC_{el} of 41.14 kWh_{el}/m^3 while the experimental was 46.24 kWh_{el}/m^3. For the RO-NF baseline case, model and experiment have SEC_{el} values of 23.15 and 22.5 kWh_{el}/m^3, respectively, corresponding to an error of only 3%. The NF-RO model was less accurate than the RO-NF because it

produced less permeate. Since the permeate production is the denominator of the SEC_{el}, a small error in calculating the permeate production results in a high error for the SEC_{el}. The SEC_{el} error can decrease by increasing the permeate production, which can be achieved by matching the flow of pump 2 with the NF permeate so that permeate is produced throughout the experiment, or by extending the duration of the experiments.

The second highest error was for L_p. Often, L_p is modelled as a constant regardless of ΔP or C_f [346], but several experimental studies reported significant variation in L_p due to membrane compaction. For example, Persson et al. [347] found that high ΔP compressed the membranes and decreased their thickness which in turn decreased L_p. This also agrees with Davenport et al. [348] who measured a L_p reduction of 22% when ΔP increased from 80 to 150 bar using 35 g/L of NaCl. Davenport et al. [348] also found that L_p decreased with C_f. Specifically, L_p decreased by 50% when C_f increased from 5 to 35 g/L at a constant ΔP of 80 bar. Decreased L_p at higher C_f was similarly observed during experiments (Figure 5-9) and this effect was represented in the model by the iterative method. The iterative method is required because L_p and ΔP are interdependent (see Appendix 7). Nonetheless, there was a residual error of 7–10% in L_p which may be reduced by future model improvements.

The third highest error of 8% for $\dot{m}$ can be correlated to the ΔP control. Without adjusting $\dot{m}$, ΔP varied during experiments. Therefore, $\dot{m}$ had to be decreased or increased to maintain ΔP at 38.5 bar. In fact, the highest $\dot{m}$ were measured when these manual adjustments took place. An automatic controller could maintain ΔP at a constant value with slight $\dot{m}$ variations, which would decrease the error in $\dot{m}$.

The fourth highest error of 7% was for ΔP. Since ΔP and L_p are interdependent, decreasing the latter also decreases the former. The error of ΔP could be zero if ΔP was an input parameter of the membrane model (which would also reduce to zero the error of L_p), as done

for the idealised model in Chapter 3 for greenhouse LDAC applications and the idealised model of Wang et al. [73] for ZLD applications. This approach simplifies the model but compromises its accuracy as it fails to account for real phenomena like membrane compaction or decreased L_p at high C_f. More information about the 2-stage model validation can be found in Appendix 8.

Since RO-3NF is later modelled using NaCl, an additional validation of the RO-NF model using NaCl was performed based on the findings of Laskowska et al. [324]. The authors experimentally investigated NF membrane samples using a stirred cell (the same as in Chapter 4) and used their experimental findings to theoretically investigate the same RO-NF configuration as in the current work. The model of Laskowska et al. [324] includes many ions, but here for the comparison, only Na^+ and Cl^- were considered. They reported 12 combinations of r and ΔP for which SEC_{el} varied between 2.9–3.3 kWh_{el}/m^3 (see Table 5-9).

When modelling RO-NF with NaCl properties instead of $MgCl_2$, the SEC_{el} was in the range of 3.3–3.5 kWh_{el}/m^3. The discrepancy between the two models can be attributed to the low efficiency pumps used in the 2-stage model. Another possible reason is that the Laskowska et al. [324] model is based on membrane samples, while the current model is based on spiral wound membranes, which can lead to significant differences as seen from the results of Chapters 3 and 4 (see Section 4.2). Nevertheless, the discrepancy is below 18%.

Table 5-9. SEC_{el} comparison between the RO-NF model using NaCl and results from Laskowska et al. [324]. Combinations of inputs and C_b = 87 g/L are taken from Laskowska et al. [324].

C_f = 29 g/L				C_b = 87 g/L	
RO recovery (r_{RO}) [%]	RO applied pressure (ΔP_{RO}) [bar]	NF recovery (r_{NF}) [%]	NF applied pressure (ΔP_{NF}) [bar]	SEC_{el} [kWh_{el}/m^3] of Laskowska et al. [324]	SEC_{el} [kWh_{el}/m^3] of RO-NF model using NaCl
35	55.79	45	54.33	3.1	3.5
35	55.66	50	55.81	3.3	3.5
40	58.24	40	56.55	2.9	3.3
40	57.91	45	57.89	3.1	3.4
40	57.87	50	58.59	3.3	3.4
45	60.7	40	60.43	2.9	3.3
45	60.43	45	62.1	3.1	3.4
45	60.48	50	63.07	3.3	3.4
50	64.08	35	62.1	2.8	3.3
50	63.64	40	65.07	3	3.4
50	63.44	45	67.14	3.1	3.4
50	63.61	50	68.43	3.3	3.5

5.4.3 Predictions for 4-stage system in baseline cases

The verified NF-RO and RO-NF models were applied to 3NF-RO and RO-3NF systems, respectively, for two baseline cases. Their constant parameters are summarised in Table 5-10. Different combinations of rejections R_i and recoveries r_i were investigated while maintaining C_f and C_b as in the previous theoretical studies. For 3NF-RO, the values in Table 5-10 were chosen to give the lowest SEC_{el}. For RO-3NF, the optimal combination of R_i and r_i were taken from Wang et al. study [73].

The 4-stage model used mostly the same parameters as the 2-stage experimental system but with some differences. Since the experimental flow of 1 kg/min gave the best results, the feed flow ($\dot{m}_f$) of the models was also set to 1 kg/min. Other membrane parameters, such as

membrane area A_m, pure water permeability, and pressure drop ΔP_m, were the same as the experimental ones. The temperature of the solution was 22 °C as in the experiments.

Regarding the differences, the 4-stage models assumed NF membranes with ΔP_{max} of 80 and 100 bar for LDAC and ZLD, respectively, which are higher than the experimental value of 41 bar. These values were selected as the lowest required to operate the 4-stage systems with the same C_f and C_b as in previous theoretical studies. The models also assumed pump-motor efficiency of $\eta_{m\text{-}p}$ of 70% (experimental was below 60%), and ERD efficiency η_{ERD} of 70% which is the efficiency of a Pelton wheel [279] (experimental was 0%, i.e., no ERD).

Table 5-10. Input parameters for the baseline 3NF-RO (for greenhouse LDAC) and baseline RO-3NF (for ZLD) cases. Parameters below the intermediate line are the same for both cases.

Parameter	3NF-RO	RO-3NF
C_f [g/L]	165	60
C_b [g/L]	191	233
ΔP_{max} [bar]	80	100
R_1 [%]	25	100
R_2 [%]	35	46
R_3 [%]	65	51
R_4 [%]	100	65
r_1 [%]	49	36
r_2 [%]	40	51
r_3 [%]	40	51
r_4 [%]	60	65
$\dot{m}_f$ [kg/min]	1	
$\eta_{m\text{-}p}$ [%]	70	
η_{ERD} [%]	70	
T [°C]	22	
A_m [m^2]	2.6	
ΔP_m [bar]	1	

Figure 5-12 shows the inputs and outputs of the baseline 3NF-RO case. Although the baseline 3NF-RO has the same C_f and C_b as in Chapter 3, a fair comparison could not be made because, in Chapter 3, a high $\dot{m}_f$ of 1200 kg/min was used and because the model

considered $CaCl_2$ instead of $MgCl_2$. Therefore, an idealised 3NF-RO model was created using $MgCl_2$ which assumed that ΔP is equal to the transmembrane osmotic pressure, while also setting $\eta_{m\text{-}p}$ and η_{ERD} equal to 100%. These simplifications decreased the calculated ΔP. As a result, the verified and idealised models of the baseline 3NF-RO case have SEC_{el} values of 49.4 and 22.3 kWh_{el}/m^3, respectively.

The first NF stage has a relatively high r and receives the highest C (see Figure 5-12). Since the risk of fouling increases with r and C [340], the first NF stage is the most critical in terms of fouling. Therefore, NF membranes (several membranes may be required on each stage depending on the feed flow and the maximum recommended flow of each membrane) with low fouling propensity must be placed at the first stage. A possible candidate is the experimental NFX used in the experiments. In fact, Mitko et al. [340] investigated three types of membranes, e.g., NF270, NFX, NFDL, and found that NFX had the lowest risk of scaling. Another requirement of the first stage is to have a R of 50%. Although a R of 70% was measured at 50 g/L, NFX could have a R of 50% at 165 g/L since the R decreases with C_f. For the second and third stages, other types of NF membranes with higher R than NFX should be used. It should also be noted that the feed of 3NF-RO is a LD which does not incorporate many types of ions as the feed of typical desalination applications. Therefore, the risk of scaling can be minimised by selecting an appropriate LD. Since monovalent ions are less prone to fouling, LiCl and LiBr could be used, which are considered the best LDs but have the disadvantage of being toxic.

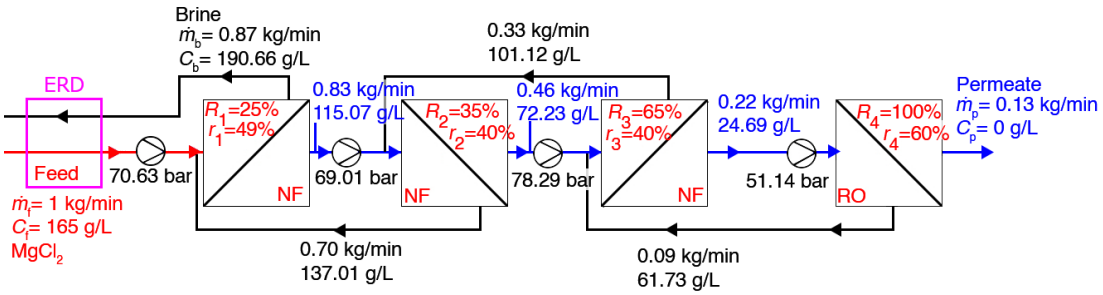

Figure 5-12. Verified model results of 3NF-RO for the baseline greenhouse LDAC case. Results are shown for feed flow of 1 kg/min and feed concentration (C_f) of 165 g/L of $MgCl_2$. Each line has mass flow in [kg/min] and concentration in [g/L]. The applied pressure is shown under each pump. Stages contain their rejections (R) and recoveries (r). Colours as in Figure 5-2.

The inputs and outputs of the baseline RO-3NF case are visualised in Figure 5-13. Wang et al. [73] investigated C_f of 5, 35, and 60 g/L; and 60 g/L was selected as the C_f for the baseline RO-3NF. This is because the ZLD process comprises a RO stage, followed by a brine concentrator (RO-3NF), and concluding with a crystalliser [310]. The 60 g/L is approximately representative of the RO brine and was therefore used as the feed of the baseline RO-3NF case. The verified and idealised RO-3NF models both used NaCl (instead of $MgCl_2$ as for 3NF-RO, see Appendix 7 for NaCl properties), but differ in calculating ΔP and the energy requirement.

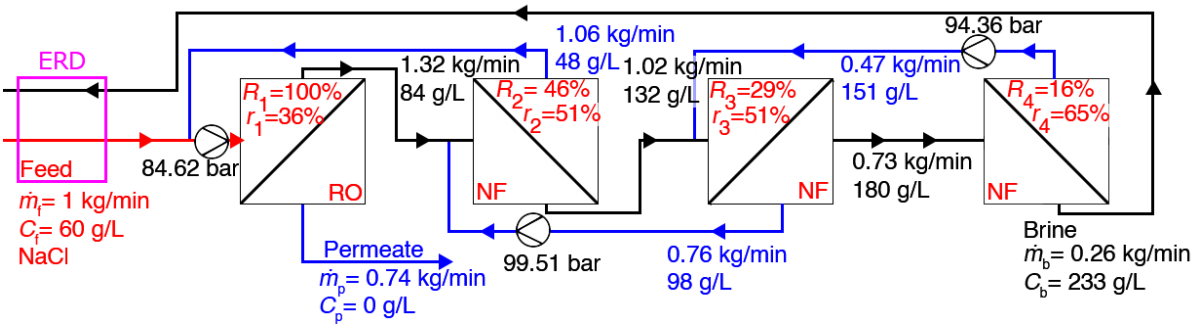

Figure 5-13. Verified model results of RO-3NF for the baseline ZLD case. Results are shown for feed flow of 1 kg/min and feed concentration (C_f) of 60 g/L of NaCl. Each line has mass flow in [kg/min] and concentration in [g/L]. The applied pressure is shown close to each pump. Stages contain their rejections (R) and recoveries (r). Colours as in Figure 5-2.

For RO-3NF, the most critical fouling condition occurs at the last NF stage, especially due to the high r of 65%. Moreover, the model assumes only Na^+ and Cl^- which are the most abundant ions in seawater, but in practice Mg^{2+}, Ca^{2+}, SO_4^{2-}, and HCO_3^- are also present [311, 316, 318, 324]. Among them, Ca^{2+} and SO_4^{2-} are especially critical because they form gypsum [315]. For this reason, ZLD processes typically include a pretreatment [349, 350], which can also be a preliminary NF stage [311, 316, 318, 324]. Thus, the absence of a pretreatment or NF stage at the beginning of the RO-3NF may lead to fouling or scaling. Without modifying the system, possible options to mitigate fouling include physical cleaning, surface modifications, pH adjustment, or antiscalants [340]. The choice depends on the specific application as these have pros and cons. Physical cleaning using deionised water can remove gypsum but requires additional maintenance and is not as effective as antiscalants in preventing scale formation [351]. Surface modification can decrease the risk of fouling but requires complex and expensive modifications [352]. pH adjustment inhibits carbonate scaling [353] but requires additional equipment and pH monitoring. Lastly, antiscalants enable operation at the highest possible r, decrease the risk of premature replacement, and reduce the need for chemicals and acids, but enhance membrane biofouling [354]. Alternatively, a NF stage can be used as pretreatment with the downside of needing frequent replacement.

For both the baseline cases of 3NF-RO and RO-3NF, verified and idealised model had same C and $\dot{m}$, but differ in that the verified models had higher ΔP (see Table 5-11).

Table 5-11. Applied pressures in [bar] calculated using the verified and idealised models for the 3NF-RO and RO-3NF baseline cases. The RO-3NF model does not utilise a pump for the last stage because the pressure is provided by the brine of the previous stage.

No. of stage	Verified 3NF-RO	Idealised 3NF-RO	Verified RO-3NF	Idealised RO-3NF
1	70.63	60.86	84.62	70.84
2	69.01	47.92	99.51	51.09
3	78.29	54.54	94.36	51.35
4	51.14	47.76		

5.4.4 Sensitivity analysis for 4-stage systems

In both 3NF-RO and RO-3NF, C_b is fixed while C_f can vary. For example, C_f of 3NF-RO in greenhouse LDAC decreases when more moisture is produced by the crops. Whereas in a ZLD, C_f of RO-3NF depends on the upstream RO stage. Figure 5-14 shows the verified 3NF-RO and RO-3NF models with C_f of 135–185 g/L ($MgCl_2$) and 5–115 g/L (NaCl), respectively, while adjusting the recovery of the first stage r_1 to keep C_b fixed. NaCl concentrations of 5, 35, and 60 g/L represent ZLD feeds (brackish water, seawater, and rejected RO brines, respectively). A NaCl concentration of 60–115 g/L can be associated with the chemical industry which has wastewaters with up to 200 g/L [355]. Thus, C_f above 60 g/L represents a chemical industry that achieves ZLD using a 3NF-RO and a crystalliser.

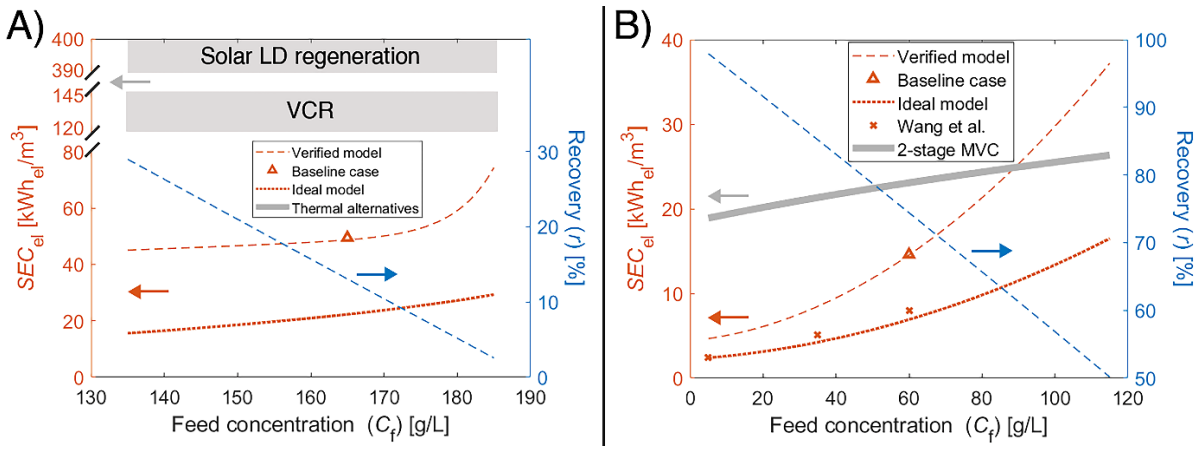

Figure 5-14. A) Electric specific energy consumption (SEC_{el}) and recovery (r) of 3NF-RO against feed concentration (for LDAC). B) SEC_{el} and r of RO-3NF against feed concentration (for ZLD). SEC_{el} of the verified and idealised models are shown on the left vertical axis and r (same for verified and idealised models) on the right vertical axis. The grey boxes or continuous line show the SEC_{el} of the conventional thermal alternatives. The legend includes the names of the models or technologies regarding their SEC_{el}.

The SEC_{el} of 3NF-RO (for LDAC) and RO-3NF (for ZLD) is defined as the required electric energy [kWh_{el}] per m^3 of permeate. This is appropriate because in LDAC the permeate represents the energy (in the form of Gibbs energy or heat of evaporation) that needs to be provided to the LD regenerator to concentrate the LD. In the field of LDAC, this energy is linked to the *COP* of the system, which generally improves as the SEC_{el} decreases. Whereas in ZLD, the permeate represents the reduction in brine volume which reduces the burden on the downstream crystalliser.

For 3NF-RO, SEC_{el} decreases as C_f decreases, meaning that lower C_f is preferred. However, low C_f has high r which makes the membranes more prone to fouling [356]. In LDAC, fouling is enhanced by the high C_b required for efficient dehumidification performance [18, 46]. Since C_b remains constant for all investigated C_f values, operating the systems with lower r at higher C_f reduces the risk of fouling. To establish a continuous loop where permeate is recycled for irrigation, the permeate flow must match the irrigation demand (which is constant). Although r decreases as C_f increases, all the water absorbed by the LD

can be recovered as the permeate of 3NF-RO (otherwise C_b would be lower). If the permeate flow is less than the irrigation demand, the permeate flow can increase by scaling up the system. Nevertheless, changing the size of 3NF-RO does not affect its SEC_{el} or r.

For RO-3NF, SEC_{el} decreases as C_f decreases, indicating that RO-3NF achieves higher efficiency when preceded by a RO stage with a low brine concentration. Since RO-3NF reaches C_b of 233 g/L even with C_f of 5 g/L, new ZLD designs do not need to include a RO stage, thus having only RO-3NF and a crystalliser to decrease the SEC_{el} of the ZLD process.

The SEC_{el} of 3NF-RO is higher than that of RO-3NF, but the first has additional advantages than a desalination system. It also provides dehumidification and water recycling for the greenhouse. Although 3NF-RO operates with r below 30% (see Figure 5-14A), all the irrigation water is collected and recycled when considering the whole greenhouse LDAC system. This enables the system to operate without the need for continuous water supply.

3NF-RO and RO-3NF models were investigated with three ERD efficiencies (η_{ERD}) of 0 (no ERD), 70% (Pelton wheel [279]), and 95% (isobaric pressure exchanger [279]). Figure 5-15 shows the SEC_{el} of 3NF-RO at C_f of 135, 165, and 185 g/L, and for RO-3NF at C_f of 5, 60, 115 g/L. The selected C_f are the lowest, medium, and highest considered for the sensitivity analysis. When applied to 3NF-RO, the use of an ERD results in lower energy requirement as C_f increases, with a maximum energy reduction of 64% at C_f of 185 g/L. In contrast, the benefit of an ERD for RO-3NF is limited. Even by considering the most efficient ERD with η_{ERD} of 95%, the SEC_{el} reduction remains below 7% for all C_f (Figure 5-15), suggesting that an ERD may not be advantageous for industrial applications due to its high cost.

The verified models were also investigated with different feed temperatures (T_f) for the same C_f values as for the η_{ERD} investigation. Both 3NF-RO and RO-3NF are efficient

regardless of T_f, with SEC_{el} variations below 5% for all investigated T_f (Figure 5-16). T_f is an important parameter for both greenhouses and ZLD applications. The LD temperature in greenhouses is expected to vary based on climate conditions, while the T_f in ZLD depends on the temperature of the water source.

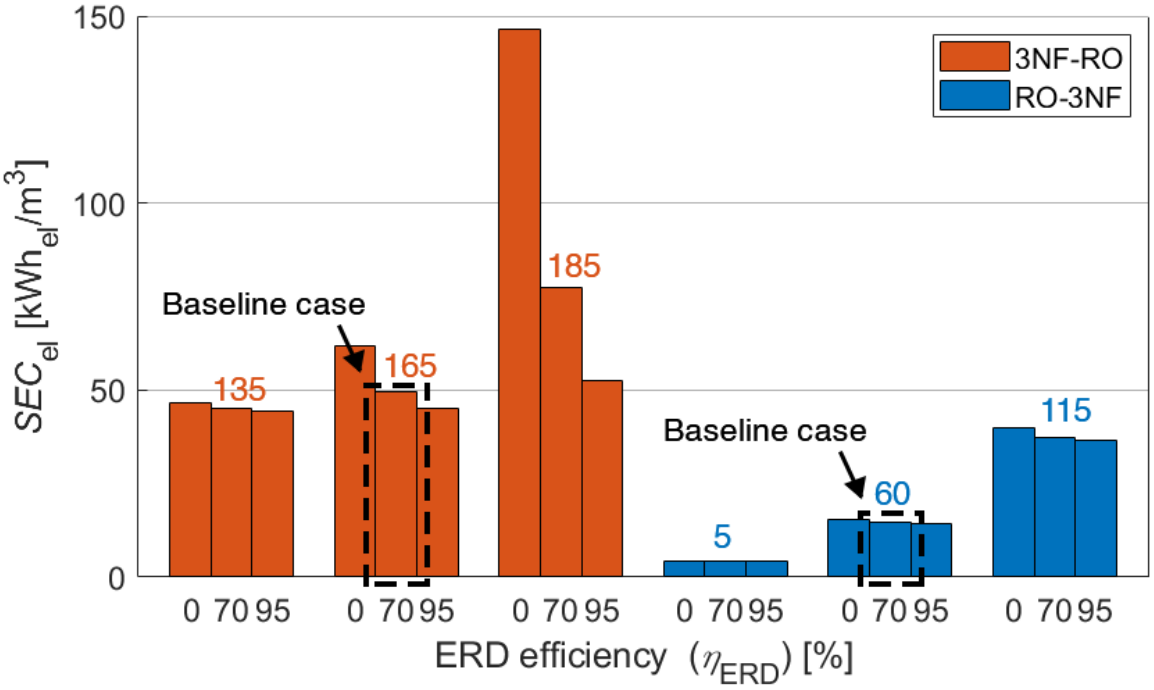

Figure 5-15. Electric specific energy consumption (SEC_{el}) against efficiency of energy recovery device (η_{ERD}). Results in orange are regarding 3NF-RO and in blue regarding RO-3NF. Grouped bars are regarding a feed concentration (C_f) [g/L]. Numbers above the groups indicate C_f.

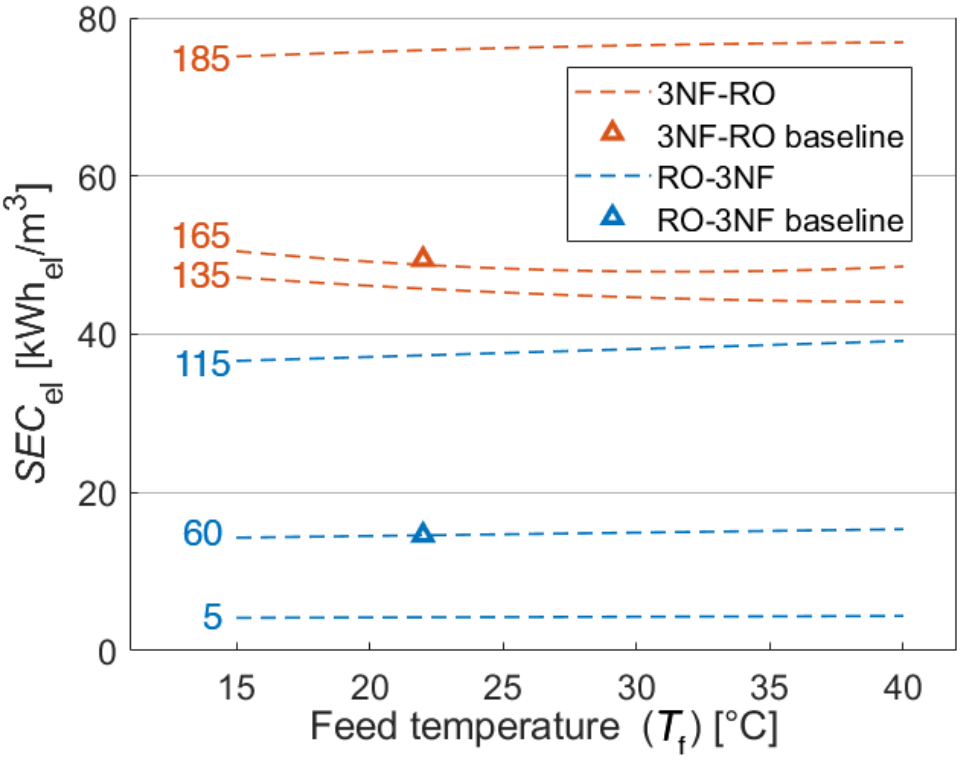

Figure 5-16. Electric specific energy consumption (SEC_{el}) against feed temperature (T_f). Results in orange are regarding 3NF-RO, and in blue regarding RO-3NF. Each line corresponds to a feed concentration (C_f) [g/L].

5.5 Discussion

For the greenhouse LDAC baseline case, the verified 3NF-RO model predicts SEC_{el} more than twice that of the idealised 3NF-RO model (49.4 compared to 22.3 kWh_{el}/m^3). The SEC_{el} difference occurs for two reasons. First, the verified model requires more energy because it assumes pump and ERD efficiencies of 70%, whereas the idealised model assumes 100% for both. Second, a maximum allowable pressure (ΔP_{max}) of 78 bar is required for the verified model (see third stage of Figure 5-12); whereas the idealised model requires only 55 bar because it does not account for pressure losses caused by pore resistance. Operating continuously 3NF-RO at ΔP_{max} of 78 bar could damage a commercial membrane with typical burst pressures of 80 bar. A burst pressure of 20–30% higher would be needed in this case, highlighting the need of a NF membrane with a burst pressure of 100 bar.

For the ZLD case, the verified RO-3NF model predicts SEC_{el} values nearly twice those reported by Wang et al. [73] using their idealised model. For C_f of 5, 35, and 60 g/L (representative of brackish water, seawater, and rejected RO brines, respectively) the verified model predicts SEC_{el} of 4.21, 9.25, and 14.6 kWh_{el}/m^3, respectively, whereas Wang et al. reported SEC_{el} of 2.39, 5.14, and 7.98 kWh_{el}/m^3. These SEC_{el} differences arise for the same two reasons as in the LDAC case. The verified and idealised RO-3NF models require a ΔP_{max} of 100 and 70 bar, respectively. This ΔP_{max} difference occurs because Wang et al. assumed that ΔP was equal to only the transmembrane osmotic pressure while neglecting pore resistance. Thus, practical RO-3NF requires stages operating at 100 bar which is higher than the typical operating pressures of commercial membranes. Therefore, significant advances in membrane fabrication are required with NF having rejections of 10–70% and burst pressures of 120 bar to enable continuous operation.

The idealised RO-3NF model developed here agrees with a SEC_{el} difference below 1 kWh_{el}/m^3 compared to the idealised model of Wang et al. [73]. This small difference might be related to the different approach for modelling the osmotic pressure, i.e., the current model uses the Gibbs energy whereas Wang et al. used only the van ’t Hoff approximation.

The verified models predict higher SEC_{el} than the idealised models, but the SEC_{el} remains lower than that of conventional technologies in most cases. In a greenhouse LDAC application, 3NF-RO is the LD regenerator. Thus, 3NF-RO is compared to a conventional LD regenerator powered by solar collectors based on Bouzenada et al. [57] and a VCR based on Mansuriya et al. [329].

Based on the data of Bouzenada et al. [57], solar LD regeneration has a SEC_{el} of 390–400 kWh_{el}/m^3 (see “solar LD regeneration” in Figure 5-14A). For the sensitivity analysis against C_f, the SEC_{el} values of 45–75 kWh_{el}/m^3 for 3NF-RO with ERD are 5.3–8.9 times lower than

the SEC_{el} of solar LD regeneration. The improvement factor of 8.9 achieved at C_f of 135 g/L increases only marginally to 9 when η_{ERD} increases from 70% to 95%. In contrast, the SEC_{el} difference of 5.3 achieved at C_f of 185 g/L increases significantly to 8.3 when η_{ERD} increases from 70% to 95%, thus showing the importance of including an ERD for LDAC applications with high C_f. Based on the data of Mansuriya et al. [329], VCR has a SEC_{el} of 120–145 kWh_{el}/m^3 (see "VCR" in Figure 5-14A). Thus, 3NF-RO with η_{ERD} of 70% requires 1.6–2.65 times less energy than the VCR. Whereas this improvement factor increases to 2.35–2.7 for η_{ERD} of 95%. 3NF-RO without an ERD has a SEC_{el} of 140 kWh_{el}/m^3, which is higher than the SEC_{el} of VCR. Therefore, 3NF-RO is more efficient than VCR when incorporating an ERD. When considering also environmental aspects, 3NF-RO does not use refrigerants that are used in VCR, making 3NF-RO less harmful to the environment. The disadvantages of conventional solar regeneration are the low *COP* (see Subsection 3.4.7) and the requirement of a huge solar collector area – up to four times the plan area of the conditioned space [22].

For ZLD applications, RO-3NF is compared to MVC which is the most efficient conventional brine concentrator used in ZLD processes [73]. Based on the equation taken from Davenport et al. [101] for sea salt, a 2-stage MVC has a SEC_{el} of 20–25 kWh_{el}/m^3 over the investigated C_f range (see "2-stage MVC" in Figure 5-14B). At the baseline C_f of 60 g/L, MVC requires 35% more energy than RO-3NF. However, RO-3NF is not better than MVC for all the investigated C_f values. At C_f of 90 g/L, the SEC_{el} of RO-3NF and MVC are both equal to 23 kWh_{el}/m^3. Whereas for C_f above 90 g/L, the SEC_{el} of RO-3NF increases more rapidly than MVC, showing that MVC is more energy-efficient than RO-3NF when C_f is above 90 g/L. Since brackish water, seawater, and rejected RO brines have C_f below 90 g/L, RO-3NF is preferred against MVC for these feeds. In the case of wastewaters from chemical industries, which typically have C_f above 90 g/L, MVC becomes preferable. The advantage of

RO-3NF against MVC improves as C_f decreases; by employing RO-3NF with a C_f of 5 g/L (i.e., brackish water), RO-3NF requires 75% less energy than 2-stage MVC.

Regarding the limitations of the 4-stage systems, these are more complex than their conventional thermal alternatives and may require careful control to adjust and balance the flows according to feed concentration. Another limitation is that most NF membranes with low rejections, including the experimentally investigated, withstand pressures of only 40 bar, whereas the 4-stage systems require applied pressures of 80–100 bar. Since the burst pressure must be higher than the applied pressure, burst pressure of 100–120 bar may be needed for continuous operation. Additionally, an important limiting factor of multi-stage systems is the risk of fouling, but this is also an issue in VCR and MVC [55]. In fact, VCR and MVC utilise titanium or stainless steel to mitigate fouling, which contributes to their high capital cost [55].

The results indicate future research topics for membrane development, experiments, and modelling. For the multi-stage systems to be practical, they require NF membranes capable of operating at 80–100 bar with R_{NF} of 10–70%, thus membranes should be developed accordingly. Improving other membrane properties such as pure water permeability may also lead to better performance as it could decrease the pore resistance losses. But it should be noted that the reported results relate to specific membranes, and future studies could investigate membranes with different properties. Moreover, future idealised studies not accounting for pressure losses should consider applied pressures of 40–50 bar below the burst pressure of the membranes to enable practical experiments subsequently.

Experimental investigations should also be conducted on 3-stage or 4-stage systems. For *n*NF-RO systems, an ERD should be incorporated to achieve low SEC_{el}. For RO-*n*NF systems, investigations focusing on fouling should be carried out as RO-*n*NF operates under conditions that are favourable for fouling. By optimising the design of the multi-stage

systems, it may be possible to operate to a target r that has a low risk of fouling or a minimised SEC_{el}.

Furthermore, the use of variable motor speeds based on tank weights/volumes and more efficient pumps/ motors would also decrease the SEC_{el}. Theoretical investigations can also be conducted to determine the optimal number of stages based on variable C_f and C_b.

5.6 Conclusions

The NF-RO and RO-NF systems were successfully operated, demonstrating their practicality. These systems were accurately modelled and applied to 4-stage systems. The verified 4-stage systems were investigated over a wide range of feed concentrations, ERD efficiencies, and feed temperatures. The main findings are:

• The verified model predictions and the experiments agree with error below 11% for NF-RO, and below 8% for RO-NF. The models accurately predict the measured parameters for NF-RO and RO-NF for both dynamic and steady-state operations. This is relevant for greenhouse LDAC systems which are typically dynamic according to varying weather conditions; whereas ZLD systems are typically steady-state, operating continuously for long periods of time.

• The permeabilities (L_p) decrease as C_f increases; with measured values lower than those given in the datasheets. This effect was included in the verified models using an iterative method to calculate L_p, which is used to calculate the membrane resistance. For the investigated cases, membrane resistance was equal to 5–25 bar and 15–50 bar for 3NF-RO (for LDAC) and RO-3NF (for ZLD), respectively.

• 3NF-RO is expected to be less prone to fouling due to its operation at lower r than RO-3NF. RO-3NF may require antifouling or an additional NF stage as a pretreatment.

• Lower C_f is preferred for both 3NF-RO and RO-3NF to achieve lower SEC_{el}. For RO-3NF. Lower C_f can be achieved by designing a ZLD process comprising a RO-3NF followed by a crystalliser.

• Regarding the ERD, 3NF-RO requires an ERD to outperform the thermal alternatives whereas the moderate energy reduction below 7% for RO-3NF regardless of C_f suggests that ERD should be avoided due to its high cost.

• The SEC_{el} variation with feed temperatures of 15–40 °C is below 5%, suggesting that 3NF-RO and RO-3NF can work efficiently even under fluctuating ambient temperatures.

• The SEC_{el} of 3NF-RO is higher than RO-3NF, but 3NF-RO also concentrates the LD which dehumidifies the greenhouse, while also completely recycling the irrigation water. Thus, 3NF-RO makes the whole system self-sustaining in terms of water.

• The idealised multi-stage NF models do not predict accurately the experimental results of the real cross-flow filtration systems and were therefore improved here by including pressure and energy losses. These losses increase the SEC_{el} by 2–3 times. Although most of the SEC_{el} results remain lower than the thermal alternative technologies, multi-stage systems in ZLD applications outperform MVC only at C_f below 90 g/L. In LDAC applications, however, multi-stage NF incorporating an ERD outperform the thermal alternatives throughout the entire C_f range that was investigated.

Chapter 6: Dynamic simulation of a novel liquid desiccant air-conditioning system for greenhouse cooling and water recovery

Title of paper: Dynamic simulation of a novel liquid desiccant air-conditioning system for greenhouse cooling and water recovery

Was submitted to: Energy Journal

Author contributions and affiliations:

- P. Pasqualin: conceptualisation, original draft, writing, review, editing, modelling, data curation, investigation and visualisation

- P.A. Davies: review and editing

School of Engineering, University of Birmingham, Edgbaston, Birmingham B15 2TT, UK.

6.1 Introduction

In Chapter 3, an idealised model of the *closed: NF-LDAC* concept was studied (this will be referred to as "idealised model") and found to achieve lower temperatures than other types of cooling technologies. Specifically, *closed: NF-LDAC* achieved a greenhouse temperature of 18.7 °C lower than simple fan ventilation (*Ventilation*), 14.7 °C lower than evaporative cooling (*EvapC*), and 4 °C lower than *EvapC* coupled with conventional LDAC (*EvapC+LDAC*). However, the idealised model employed a monthly time step and was not based on experimental data or datasheets. To provide more accurate results, a dynamic model with a 1-hour time step was developed in this Chapter which incorporates experimentally validated components and datasheets.

Conventionally, greenhouses regulate internal conditions through *Ventilation* or *EvapC*. The desired conditions involve maintaining T of 25–33 °C [9] and RH of 70–90% [23]. On the one hand, *Ventilation* does not regulate either T or RH, and is therefore incapable of maintaining the desired conditions in hot regions. On the other hand, *EvapC* is typically regulated based on RH, activating when RH falls below 70% and deactivating when it exceeds 90%. However, regulating solely based on RH may result in undesired conditions. Moreover, *EvapC* requires significant amounts of water, which is often scarce in hot regions [5, 6].

Conventional air-conditioning (*AC*) can regulate both T and RH, but it is not commonly used in greenhouses due to their high energy demands caused by the need for 20–40 times higher air change rates compared to residential buildings. As an alternative to *AC*, greenhouses may utilise NF-LDAC.

In Chapter 3, *closed: NF-LDAC* was compared against *Ventilation* and *EvapC*. In this Chapter, *semi-closed NF-LDAC* (Figure 6-1) is used instead of *closed: NF-LDAC*. S*emi-closed NF-LDAC* requires less energy while providing the same cooling and dehumidification

as *closed: NF-LDAC* (explained later in Section 5.2.1). Moreover, *AC* is also considered for the comparison, unlike in Chapter 3.

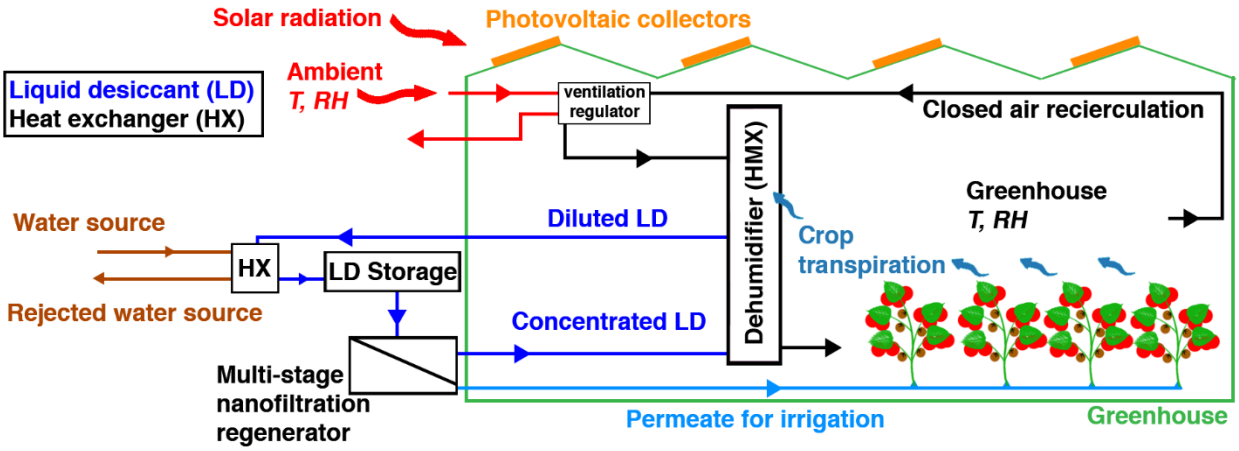

Figure 6-1. Schematic of a greenhouse operating with semi-closed: NF-LDAC. The greenhouse absorbs heat from the air entering the dehumidifier and rejects this heat to a water source (such as seawater, lake, or river) through a liquid-to-liquid heat exchanger (HX). Colours of diluted liquid desiccant (LD), concentrated LD, and permeate for irrigation as in Figure 1-1A and Figure 3-2.

Although in Chapter 3 the technologies were compared solely based on *T*, here the comparison is based on the vapour pressure deficit (*VPD*) that combines *T* and *RH* [357]. *VPD* provides a better indication of crop performance than only *T* [357]. Moreover, using *T* and *RH* regulation has two drawbacks. Firstly, conventional *T* and *RH* ranges (blue box in Figure 6-2) can result in undesired crop conditions, such as *RH* =70% and *T* =32 °C. Secondly, many *T* and *RH* combinations for optimal cultivation are excluded when operating within conventional ranges. The use of *VPD* also simplifies the regulation process since a single parameter is used instead of two.

VPD	Relative humidity [%]													
Temperature [°C]	35	40	45	50	55	60	65	70	75	80	85	90	95	100
15	1.11	1.02	0.94	0.85	0.77	0.68	0.60	0.51	0.43	0.34	0.26	0.17	0.09	0.00
16	1.18	1.09	1.00	0.91	0.82	0.73	0.64	0.55	0.45	0.36	0.27	0.18	0.09	0.00
17	1.26	1.16	1.07	0.97	0.87	0.78	0.68	0.58	0.48	0.39	0.29	0.19	0.10	0.00
18	1.34	1.24	1.14	1.03	0.93	0.83	0.72	0.62	0.52	0.41	0.31	0.21	0.10	0.00
19	1.43	1.32	1.21	1.10	0.99	0.88	0.77	0.66	0.55	0.44	0.33	0.22	0.11	0.00
20	1.52	1.40	1.29	1.17	1.05	0.94	0.82	0.70	0.59	0.47	0.35	0.23	0.12	0.00
21	1.62	1.49	1.37	1.24	1.12	1.00	0.87	0.75	0.62	0.50	0.37	0.25	0.12	0.00
22	1.72	1.59	1.46	1.32	1.19	1.06	0.93	0.79	0.66	0.53	0.40	0.26	0.13	0.00
23	1.83	1.69	1.55	1.41	1.27	1.12	0.98	0.84	0.70	0.56	0.42	0.28	0.14	0.00
24	1.94	1.79	1.64	1.49	1.34	1.19	1.05	0.90	0.75	0.60	0.45	0.30	0.15	0.00
25	2.06	1.90	1.74	1.59	1.43	1.27	1.11	0.95	0.79	0.63	0.48	0.32	0.16	0.00
26	2.19	2.02	1.85	1.68	1.51	1.35	1.18	1.01	0.84	0.67	0.50	0.34	0.17	0.00
27	2.32	2.14	1.96	1.78	1.61	1.43	1.25	1.07	0.89	0.71	0.54	0.36	0.18	0.00
28	2.46	2.27	2.08	1.89	1.70	1.51	1.32	1.13	0.95	0.76	0.57	0.38	0.19	0.00
29	2.61	2.40	2.20	2.00	1.80	1.60	1.40	1.20	1.00	0.80	0.60	0.40	0.20	0.00
30	2.76	2.55	2.34	2.12	1.91	1.70	1.49	1.27	1.06	0.85	0.64	0.42	0.21	0.00
31	2.92	2.70	2.47	2.25	2.02	1.80	1.57	1.35	1.12	0.90	0.67	0.45	0.22	0.00
32	3.09	2.85	2.62	2.38	2.14	1.90	1.67	1.43	1.19	0.95	0.71	0.48	0.24	0.00
33	3.27	3.02	2.77	2.52	2.26	2.01	1.76	1.51	1.26	1.01	0.75	0.50	0.25	0.00
34	3.46	3.19	2.93	2.66	2.39	2.13	1.86	1.60	1.33	1.06	0.80	0.53	0.27	0.00
35	3.66	3.37	3.09	2.81	2.53	2.25	1.97	1.69	1.41	1.12	0.84	0.56	0.28	0.00
36	3.86	3.57	3.27	2.97	2.67	2.38	2.08	1.78	1.49	1.19	0.89	0.59	0.30	0.00
37	4.08	3.77	3.45	3.14	2.82	2.51	2.20	1.88	1.57	1.26	0.94	0.63	0.31	0.00
38	4.31	3.98	3.64	3.31	2.98	2.65	2.32	1.99	1.66	1.33	0.99	0.66	0.33	0.00
39	4.55	4.20	3.85	3.50	3.15	2.80	2.45	2.10	1.75	1.40	1.05	0.70	0.35	0.00
40	4.79	4.43	4.06	3.69	3.32	2.95	2.58	2.21	1.84	1.48	1.11	0.74	0.37	0.00

Figure 6-2. Vapour pressure deficit (VPD) in [kPa] according to temperature and relative humidity for tomatoes based on Shamshiri et al. [358]. Optimal values for cultivation are shown in green, undesired conditions are shown in red, and acceptable conditions in yellow. Blue box represents temperature and humidity ranges used in conventionally-regulated greenhouses during the day. During the night, the temperature range decreases by around 10 °C.

Unlike in Chapter 3 where only three locations were considered, this Chapter investigates 17 locations[11] (Figure 6-3). The 17 locations are among the warmest cities close to a water source (such as sea, lake, or river) required as a sink temperature for NF-LDAC. Although not all the 17 locations are known for agriculture (some might not even be involved in agriculture), suburban areas around these locations may be more involved in agriculture.

Because locations close to each other have similar ambient conditions, similar results are expected between the 17 locations and their suburban areas. Additionally, if a location not

[11] Although Las Palmas (Gran Canaria) is not geographically located in the Mediterranean region, its climate and model results resemble those of Casablanca, which is characterised by a hot Mediterranean climate. Thus, both Las Palmas and Casablanca are categorised as having a hot Mediterranean climate for the purpose of this study.

included in the 17 has similar ambient conditions with a location within the 17, it is expected that these two locations will have similar results.

Many studies have investigated greenhouses for LDAC (see Section 1.3), and NF-LDAC achieved better results for crop cultivation than conventional cooling technologies (see Section 2.4).

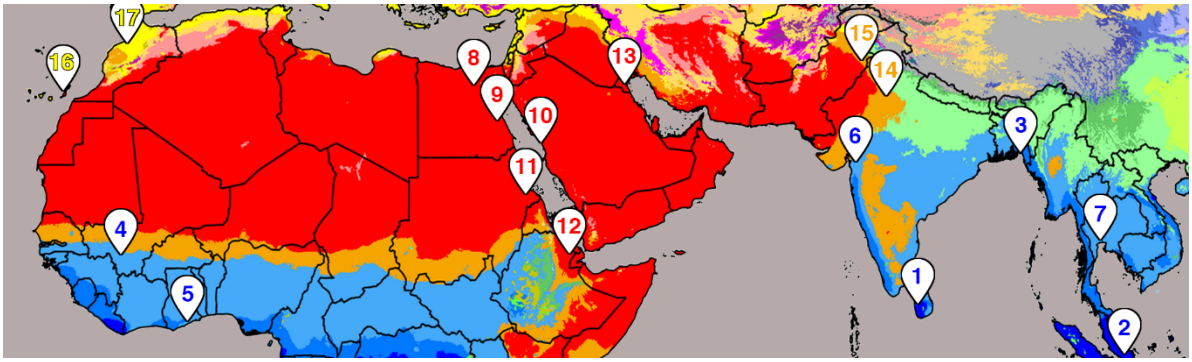

Figure 6-3. The 17 investigated locations (map taken from Beck et al. [359]). The locations are divided into four groups based on the Köppen-Geiger climate classification. Locations 1–7 are tropical, 8–13 are hot deserts, 14 and 15 are hot semi-arid, 16 and 17 are hot Mediterranean. The locations 1–17 are: 1 Colombo, 2 Singapore City, 3 Chittagong, 4 Bamako, 5 Accra, 6 Mumbai, 7 Bangkok, 8 Cairo, 9 Hurghada, 10 Mecca, 11 Port Sudan, 12 Djibouti city, 13 Kuwait City, 14 New Delhi, 15 Lahore, 16 Las Palmas (Gran Canaria), and 17 Casablanca (Morocco).

The structure of Chapter 6 is as follows: first, the model is described, including schematics of the four investigated technologies and the software used to create their models. Then, results are presented for the percentage of time that conditions remain within the acceptable *VPD* range. Annual results are then presented for the energy produced by the PV collectors, energy requirements and *COP* of *AC* and *semi-closed: NF-LDAC*, and water savings using *semi-closed: NF-LDAC*. The *COP* of *semi-closed: NF-LDAC* is based on commercially available NF membranes; results with improved NF membranes are also presented.

6.2 Theory

The model was created using three software packages: TRNSYS®, SketchUp®, and Matlab-Simulink® (see Figure 6-4). TRNSYS® is a dynamic simulator and was selected because many studies have shown that it can accurately simulate greenhouses. For instance, Hamdi et al. [360] measured the moisture removal rate of a greenhouse solar dryer and found good agreement compared to their TRNSYS model. Asa'd et al. [361] measured the temperature of a solar greenhouse, attached to a building, for three months and found almost identical trends with their TRNSYS results. TRNSYS® has also been validated for desiccant systems by Jani et al. [362] who modelled components used for heating and cooling with good agreement with their experimental results.

TRNSYS® includes around 250 standard components, among which 9 were used in the models (see TRNSYS components in Figure 6-4). One of them is the greenhouse and its geometry was created using SketchUp® Pro 2021. The components "weather data" and "plotter" are automatically set by TRNSYS. TRNSYS includes typical meteorological years for Bamako, Cairo, Mecca, Port Sudan, Djibouti, Kuwait, New Delhi, and Lahore. The weather data of the other locations were taken from EnergyPlus [363].

The component "differential controller" represents an on/off regulation based on two user-defined limits. The component "equation" can be used for constant values or to perform unit conversions. The remaining components, i.e., "PV collectors", "Evaporative cooling pad", "LD storage", and "HX" have user-defined parameters whose values can be found in Appendix 9. The PV collectors' parameters were set based on the "BLD350-72M" datasheet (commercially available PV collector) [285].

The four models also require components for the multi-stage regenerator, the HMX, the crop transpiration, AC with variable COP, the temperature of the water source, and the

ventilation regulator. Since these six components do not exist in TRNSYS, they were created using Matlab-Simulink introduced into the model using a component of TRNSYS that interconnects the two software environments.

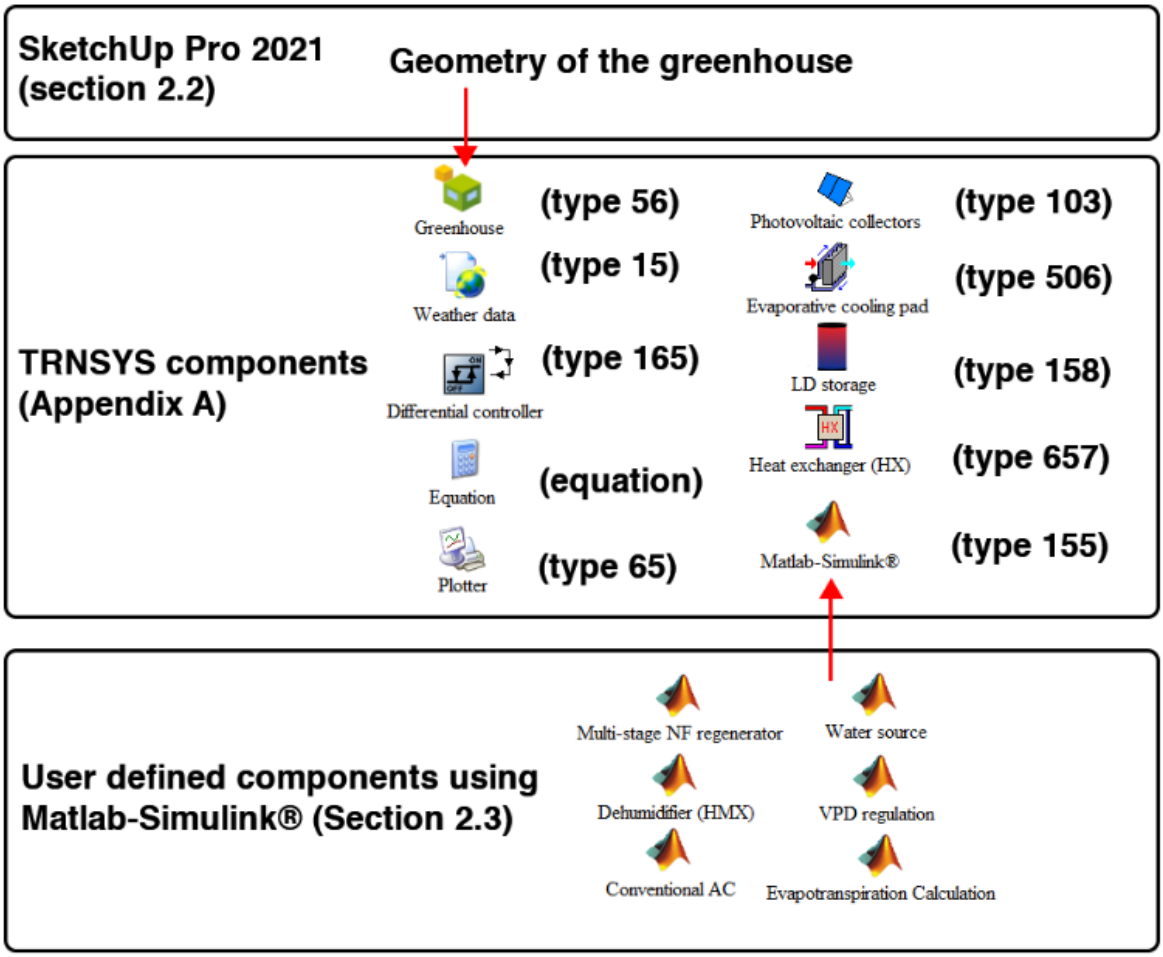

Figure 6-4. Schematic of the three software used to create the TRNSYS model. Arrows show how SketchUp® Pro 2021 and Matlab-Simulink® were introduced into the TRNSYS model. Parenthesis next to the components show the TRNSYS type number.

The four models which will be referred to as "TRNSYS models". Thus, a TRNSYS model was created for each of the four cooling technologies; for example, Figure 6-5 shows the model of *semi-closed: NF-LDAC*. Each model was used to run a dynamic annual calculation with a timestep of 1-hour giving a total of 8760 time values.

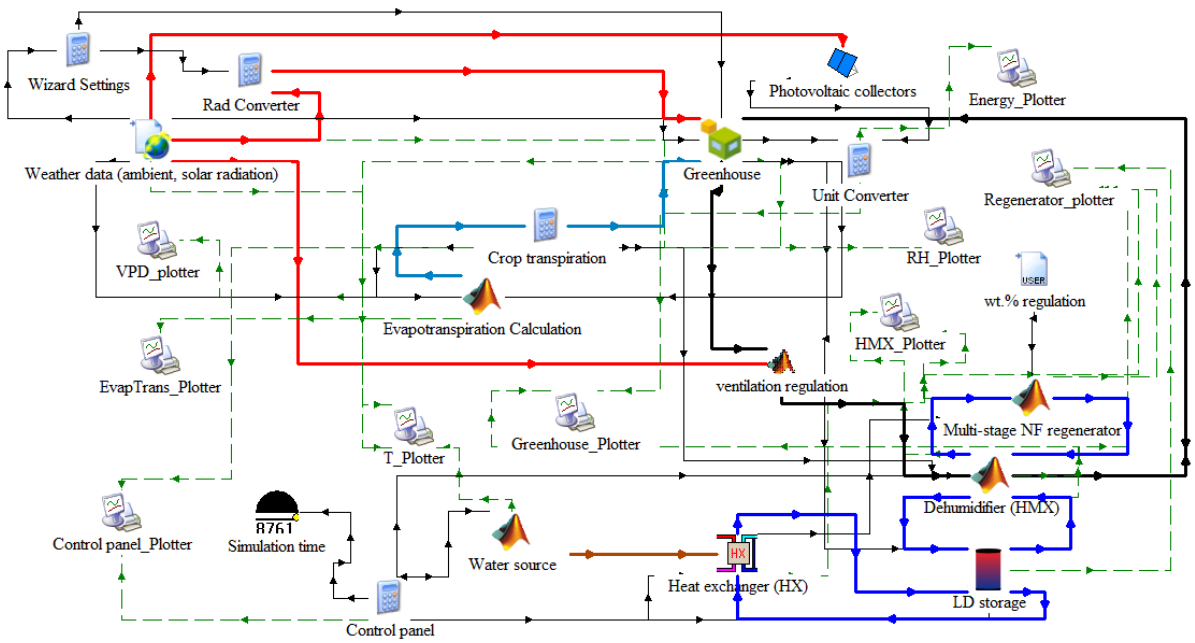

Figure 6-5. The TRNSYS model for semi-closed: NF-LDAC. Colours of lines as in Figure 6-1. Thin black lines are connections between the components (not shown in Figure 6-1). Dashed lines are used for the plotters. Models of Ventilation, EvapC, and conventional AC are a simplified version of semi-closed: NF-LDAC which do not include the multi-stage regenerator, LD storage, ventilation regulator, HMX, and HX.

The following subsections present the schematics of the four technologies, the geometry of the greenhouse, and the user-defined components.

6.2.1 The cooling technologies

The four cooling technologies were modelled individually for the same greenhouse. These technologies differ regarding their operation. The simplest technology is *Ventilation* which only includes fans to circulate the ambient air. *EvapC* also includes an evaporative cooling pad which was modelled with an effectiveness of 0.8 (based on [9]). *EvapC* is activated when the ambient *RH* (RH_{amb}) falls below 70% and deactivated when RH_{amb} goes above 90%. *AC* is like *Ventilation* with the addition of air-conditioning that activates when the greenhouse *T* (T_{gh}) falls below 25 °C and deactivates when T_{gh} goes above 33 °C. *AC* also regulates

humidity by humidifying the air when the greenhouse *RH* (RH_{gh}) falls below 70% and by dehumidifying the air when RH_{gh} goes above 90%.

The *semi-closed: NF-LDAC* technology is called such due to the "ventilation regulator" which operates as follows to increase the *COP*. When the ambient *VPD* (VPD_{amb}) is not within the acceptable range, the greenhouse operates in closed recirculation and the regenerator is active. When the ambient *VPD* (VPD_{amb}) is within the acceptable range, the greenhouse operates in open ventilation and the regenerator is deactivated, but the drawback is that some moisture is lost to the external environment, leading to lower water savings. Thus, the "ventilation regulator" makes the greenhouse operate in a semi-closed ventilation.

Compared to closed recirculation, semi-closed ventilation achieves higher cost-effectiveness while maintaining desired CO_2 concentrations [24]. Additionally, closed recirculation is prone to fungus growth due to the high *RH*. NF-LDAC could constantly operate in open ventilation, but this would lead to even higher water losses. When compared to open ventilation, semi-closed ventilation achieves higher yield [24].

The *semi-closed: NF-LDAC* technology is the most complex. It includes a regulator that activates the multi-stage regenerator when the LD concentration (wt_{LD}) falls below 17.2 wt.%. Using Eq. 3-31, a monthly wt_{LD} of 17.2 wt.% (191 g/L) achieves an *ERH* of 83% (i.e., RH_{gh} of 83%) and was found to maintain the *VPD* in the acceptable range for more than 60% of the year for most locations. For locations where wt_{LD} of 17.2 wt.% (191 g/L) did not achieve the monthly *VPD* target of 60%, wt_{LD} was increased, but some locations were still unable to reach 60%. A target value of 60% for the monthly *VPD* percentage was selected because undesired *VPD* values are accepted if they occur for short periods of time [357]. The monthly wt_{LD} values used for all the locations can be found in Appendix 9.

6.2.2 Greenhouse geometry and other parameters

Figure 6-6 shows the dimensions of the greenhouse. Based on [364-367], greenhouses can have floor areas above 500 m^2. Thus, the plan area and volume of the greenhouse model are equal to 512 m^2 and 3328 m^3. The greenhouse materials are based on [368, 369]. The greenhouse is mainly made of 4 mm windows with thermal transmittance (U) of 5.75 W/(m^2 K). The structure of the greenhouse is made of expanded polystyrene sandwich panels with the external sheets made of aluminium. The total thickness of the panels is 40 mm with U of 2.2 W/(m^2K). External shadings were used to represent the PV collectors on top of the greenhouse. To model the greenhouse geometry, SketchUp® Pro 2021 software was used which allows the 3D model to be imported into TRNSYS®.

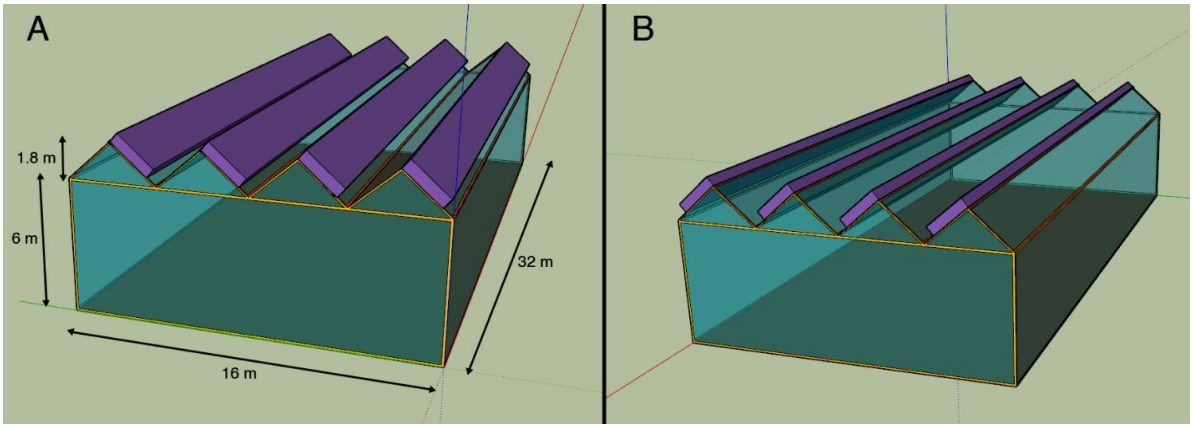

Figure 6-6. Greenhouse geometry created using SketchUp® Pro 2021 software. A) and B) show two sides of the greenhouse. The purple blocks are external shadings which represent the photovoltaic (PV) collectors. The orientation of the greenhouse is such that the PV collectors face south.

Other constant parameters used for the greenhouse TRNSYS model are the air changes of 42.6 and 21.4 1/h during the day and night, respectively based on [370]. These air changes are equivalent to 51 and 25.5 kg/s during the day and night, respectively.

6.2.3 User-defined components

The multi-stage regenerator component is based on the verified model presented in Chapter 5, where a 4-stage regenerator was used to produce a concentrated LD with a concentration of 191 g/L. Here, a 16-stage regenerator is required to achieve the same outlet LD concentration for two reasons. First, the 4-stage regenerator in Chapter 5 assumed NF membranes able to operate at 80 bar, while here they are assumed to resist 40 bar, like commercially available NF membranes. Second, the feed mass flow here is almost 900 times higher than in Chapter 5. Specifically, the 16-stage regenerator is modelled with a LD feed flow of 3.5 times lower than the air flow (LD feed flow is 14.5 kg/s during the day and 7.3 kg/s during the night). The factor of 3.5 was selected because the HMX component is based on the model in Appendix 1 which requires a factor <4 for its outputs to converge. Ideally, this factor must be as low as possible, meaning higher LD flow and low air flow. A high LD flow can cool and dehumidify the air more efficiently, while a low air flow is easier to cool and dehumidify. The model uses an air flow of 51 kg/s. However, a LD flow of 51 kg/s would be impossible to achieve in practice. Even the 20 kg/s used in Chapter 3 is practically challenging to achieve. Thus, a practical LD flow of 14.5 kg/s was selected, giving a factor of 3.5 that is below but close to 4.

The HMX component is described in Appendix 1 where it was validated with experiments. For crop transpiration, Eq. 2-25 by Stanghellini [274] is used as it is considered the most accurate for greenhouses [275, 276]. Tomatoes are assumed as the crops; to provide accurate predictions, hourly crop coefficient (k_c) and leaf area index (LAI) [m^2/m^2] values were extrapolated based on data from Acquah et al. [371]. The hourly k_c and LAI are shown in Figure 6-7. k_c and LAI follow curves that are repeated twice per year to account for a harvest during the year.

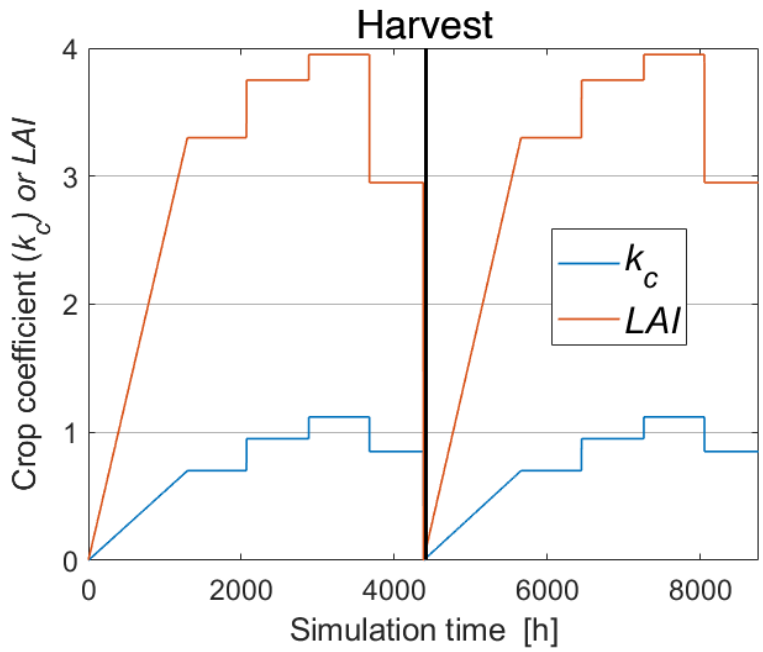

Figure 6-7. Crop coefficient (k_c) and LAI [m^2/m^2] of tomatoes against time (extrapolated from Acquah et al. [371]). Vertical line shows when the harvest takes place.

The *COP* was calculated as the thermal power provided by the system divided by its electric power requirement. The required thermal or cooling power is calculated by TRNSYS while the Daikin datasheet of the "UATYQ100ABAY1" air-conditioning unit is used to convert these thermal requirements into electric requirements. The unit has different datasheets for cooling and heating. The curve fitter app of Matlab® software was used to develop interpolating *COP* equations based on the datasheets (Figure 6-8 shows cooling and heating *COP* results for Mecca). For cooling, the *COP* is calculated as:

$$COP = 8.171 - 0.1646T - 0.0799h + 0.00132T^2 + 0.000116Th + 0.0009h^2 \quad (5\text{-}1)$$

where T and h are temperature and enthalpy of air on the supply coil, respectively. For heating, the *COP* is calculated as:

$$COP = \frac{74.84 - 0.1943T + 1.424h - 0.001743T^2 - 0.00654Th + 0.0124h^2}{19.93 + 0.369T + 0.183h + 0.00563T^2 + 0.0006Th - 0.00029h^2} \quad (5\text{-}2)$$

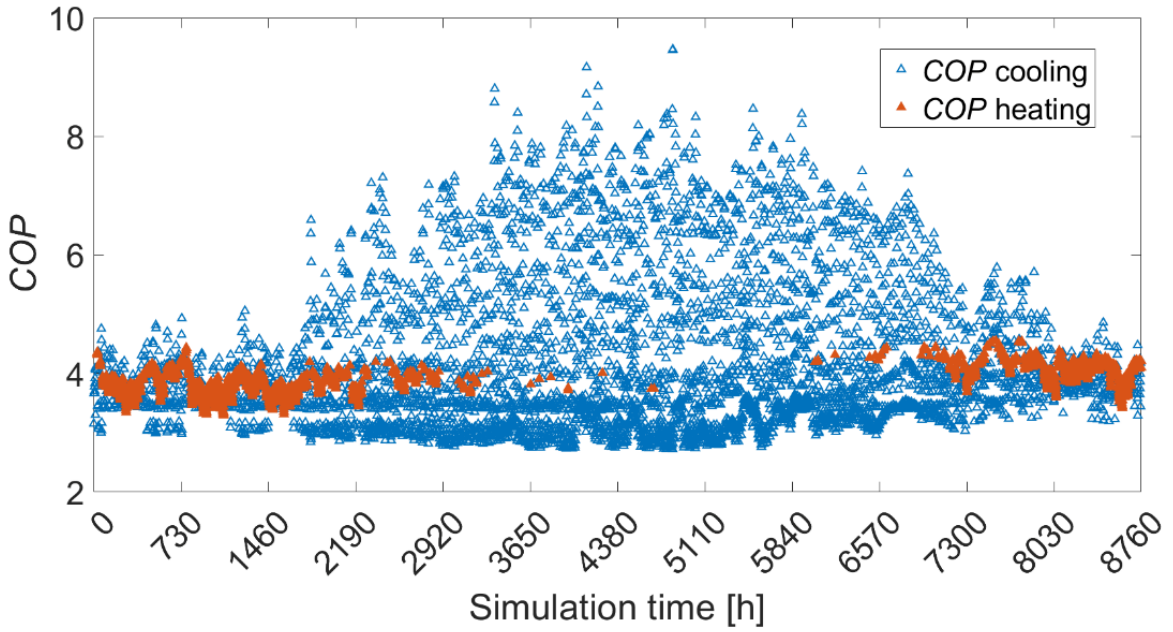

Figure 6-8. Coefficient of performance (COP) of conventional air-conditioning (AC) at Mecca. Blue values are for cooling and orange for heating. During winter, both heating and cooling are required throughout the day.

For the seawater source temperature (T_{ws}) [°C], monthly T_{ws} were taken from a seawater temperature database [372]. For other water sources like lakes and rivers, their monthly T_{ws} were assumed equal to the Red Sea which represents the worst sink temperature because it has the highest monthly values among the selected locations. The monthly values were converted to hourly using an interpolation:

$$T_{ws} = p_1 t^3 + p_2 t^2 + p_3 t + p_4 \quad (5\text{-}3)$$

where p_1, p_2, p_3, and p_4 depend on the location (see Appendix 9) and t is the simulation time [h]. The model considers a water source flow that is two times lower than the LD flow; thus, water source flow is 7.3 kg/s during the day and 3.6 kg/s during the night.

For the ventilation regulator, the greenhouse operates in open ventilation when VPD_{amb} is within 0.41–1. 37 kPa. VPD_{amb} is calculated as:

$$VPD_{\mathrm{amb}} = 4042.9 \exp\left(23.57712 - \frac{4042.9}{T_{\mathrm{amb}} + 237.57}\right)\left(1 - \frac{RH_{\mathrm{amb}}}{100}\right) \quad (5\text{-}4)$$

Although TRNSYS® allows to co-simulate using several software, Matlab-Simulink® was selected for these six user-defined components because this co-simulation is convenient as it allows the model to be reproduced easily.

6.3 Results

The TRNSYS models of *AC* and *semi-closed: NF-LDAC* were developed by maximising the monthly percentage of time during which the *VPD* remained within the acceptable range for cultivation. *AC* was optimised by including vapour regulation whereas *semi-closed: NF-LDAC* by including both *VPD* and wt_{LD} regulations. *Ventilation* and *EvapC* were also modelled but their *VPD* could not be optimised as *Ventilation* has no regulation, and *EvapC* is regulated solely based on *RH*. A target percentage of 60% per month within the acceptable *VPD* range is assumed as the minimum requirement. Therefore, a month reaching acceptable conditions means that the *VPD* remained within the acceptable range for at least 60% of the month (based on calendar year). For each technology, Figures 6-9 to 6-12 show the percentage of each month during which *VPD* was kept in the acceptable range (>70% in green, 60–70% in orange, <60% in red.

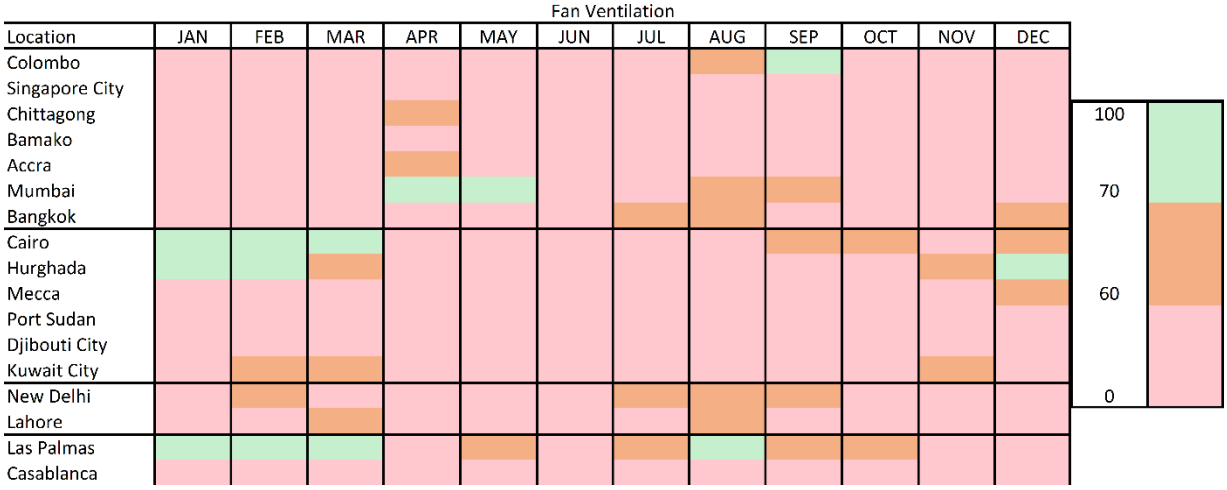

Figure 6-9. Monthly VPD percentages for the four technologies at the 17 locations using fan ventilation. Months in red represent a percentage of time below 60%, orange between 60% and 70%, and green above 70%. Lines separate the locations into four climates. From top to bottom, the climates are tropical, hot desert, hot semi-arid, and hot Mediterranean.

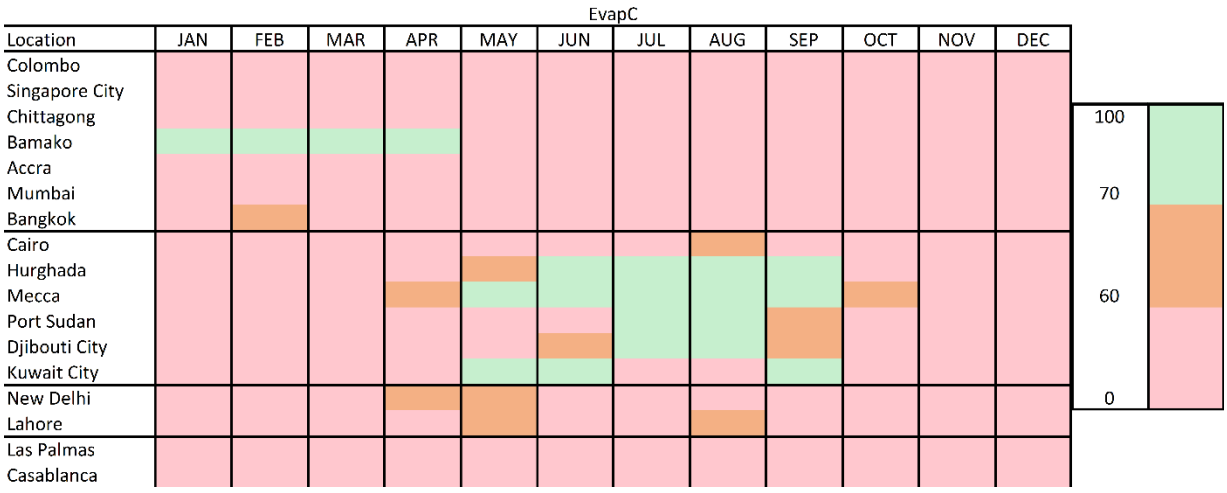

Figure 6-10. Monthly VPD percentages for the four technologies at the 17 locations using evaporative cooling. Months in red represent a percentage of time below 60%, orange between 60% and 70%, and green above 70%. Lines separate the locations into four climates. From top to bottom, the climates are tropical, hot desert, hot semi-arid, and hot Mediterranean.

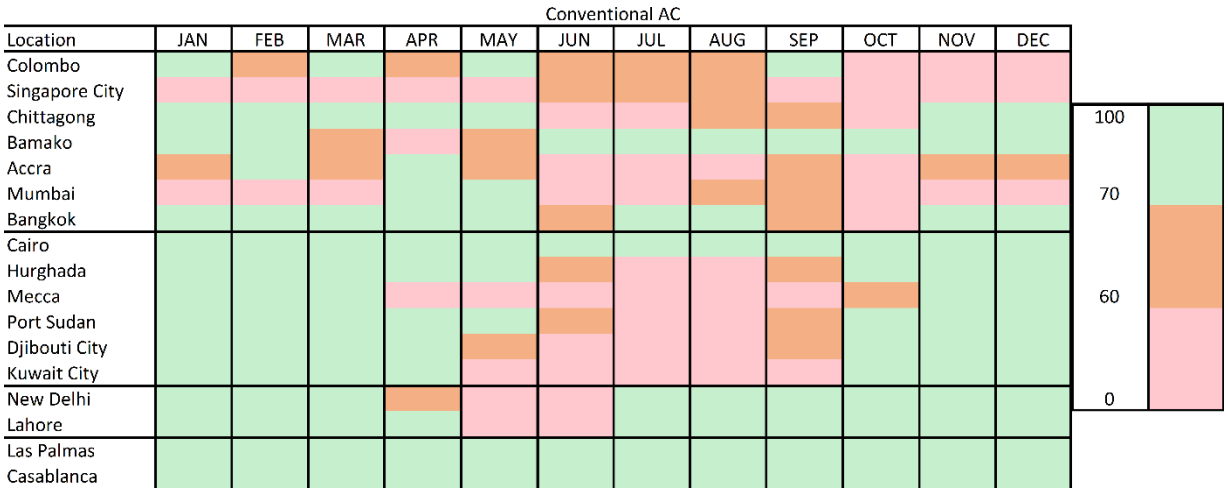

Figure 6-11. Monthly VPD percentages for the four technologies at the 17 locations using conventional air-conditioning. Months in red represent a percentage of time below 60%, orange between 60% and 70%, and green above 70%. Lines separate the locations into four climates. From top to bottom, the climates are tropical, hot desert, hot semi-arid, and hot Mediterranean.

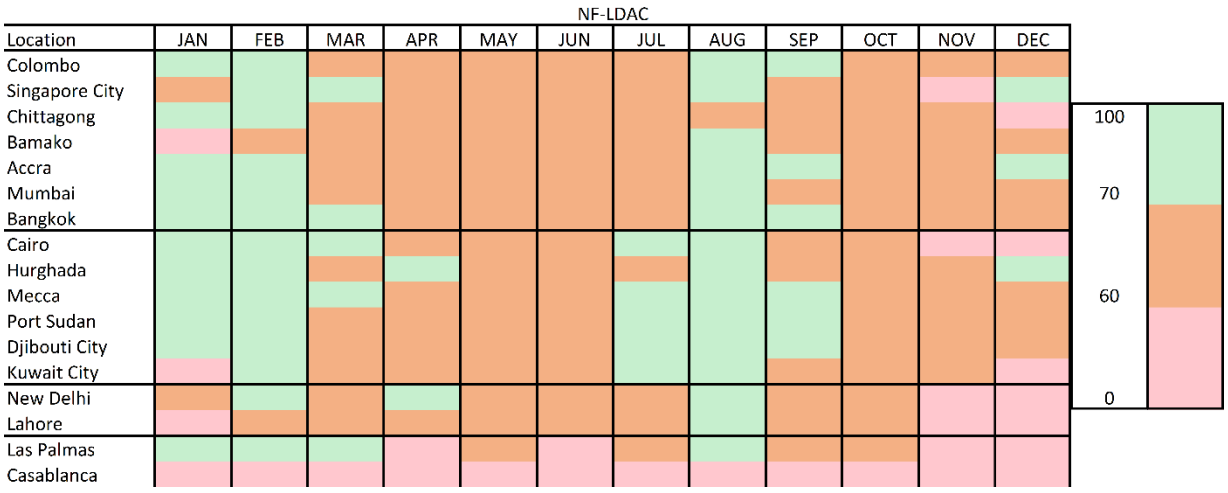

Figure 6-12. Monthly VPD percentages for the four technologies at the 17 locations using NF-LDAC. Months in red represent a percentage of time below 60%, orange between 60% and 70%, and green above 70%. Lines separate the locations into four climates. From top to bottom, the climates are tropical, hot desert, hot semi-arid, and hot Mediterranean.

Ventilation and *EvapC* reach the *VPD* target for 2 months per year. *Ventilation* is suboptimal for all climates, except for Las Palmas where the *VPD* target is met for 8 months. *EvapC* performs better in hot desert climates, reaching the *VPD* target for 4.5 months, instead of the average 2 months reached in other climates. Improved *EvapC* performance in hot desert

climates aligns with the literature [373, 374], but the literature does not specify the duration of crop production. It can be assumed that *EvapC* enables crop production for more than 4.5 months; otherwise, it would not be utilised. This suggests that a target *VPD* percentage below 60% can also be accepted for cultivation, albeit with reduced crop quality.

AC achieves the *VPD* target throughout the year at Cairo, Las Palmas, and Casablanca. *AC* performs slightly less efficiently in Hurghada, New Delhi, and Lahore where it achieves the *VPD* target for 10 months only. These results indicate that *AC* is preferable in climates with low T_{amb} (see Figure 6-13). In hot desert and hot semi-arid climates, *AC* achieves the target *VPD* percentage during winter, but not during summer. Since *EvapC* achieves the target *VPD* percentage during the summer, *AC* and *EvapC* can be coupled to achieve the target *VPD* percentage year-round.

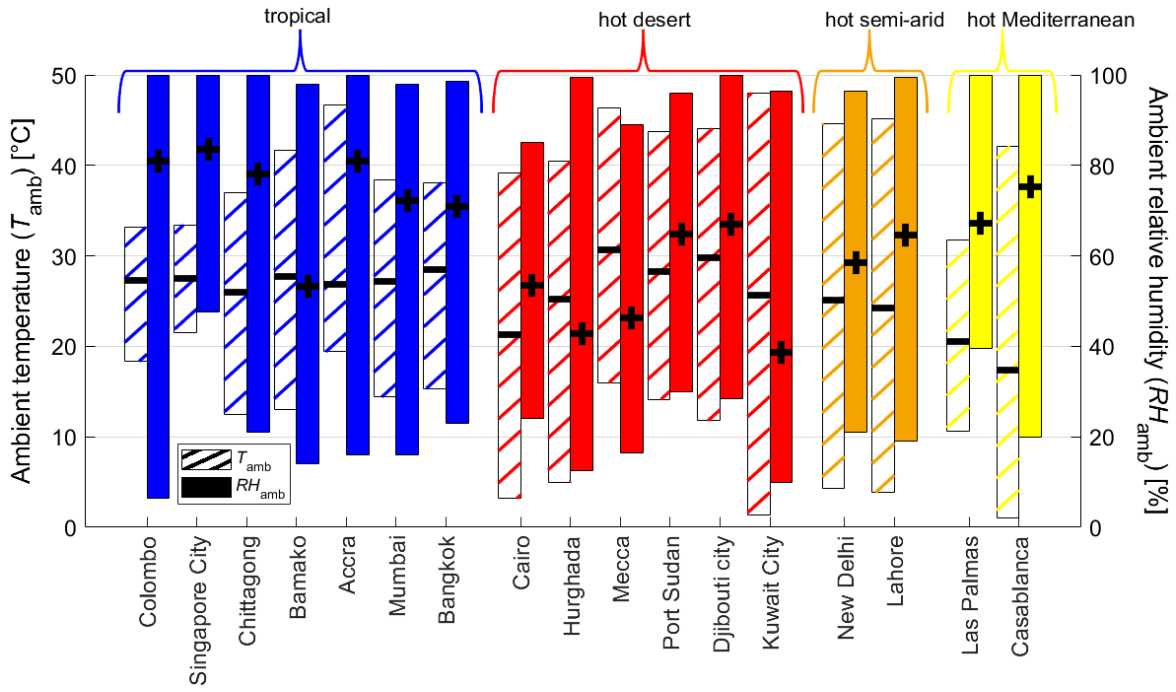

Figure 6-13. Ambient temperature (T_{amb}) and ambient relative humidity (RH_{amb}) ranges at the 17 locations. The "-" and "+" indicate the average T_{amb} and RH_{amb}, respectively, of each location.

In contrast to *AC*, *semi-closed: NF-LDAC* achieves the target *VPD* percentage in hotter climates, enabling year-round cultivation in 4 out of 7 tropical locations and 4 out of 6 hot desert locations. However, *semi-closed: NF-LDAC* cannot achieve the target *VPD* percentage in colder climates due to the absence of heating. To achieve the target *VPD* percentage year-round in all climates, *semi-closed: NF-LDAC* needs heating during cold months. However, heating increases the cost of the system and could make *semi-closed: NF-LDAC* less environmentally friendly.

The annual electric energy requirements per greenhouse plan area [kWh_{el}/m^2] of *AC* and *semi-closed: NF-LDAC* are shown in Figure 6-14. The results include an additional 50 kWh_{el}/m^2 to account for the energy consumption of the fans (present in all technologies) based on commercial data [375]. On average, air ventilations accounts for 96% of the total electric energy requirement, while solar radiation contributes to the remaining 4%. Due to heating, *AC* requires 65% more electric energy than *semi-closed: NF-LDAC*.

The electric energy requirement of *semi-closed: NF-LDAC* is calculated using a 16-stage regenerator made of commercially available NF membranes capable of withstanding 40 bar [124-127], and commercial RO membranes withstanding 80 bar at the last stage [63]. With improved NF membranes capable of withstanding 80 bar, an 8-stage regenerator in Mecca would achieve the same regeneration performance and require 30% less energy than the 16-stage regenerator (Figure 6-15).

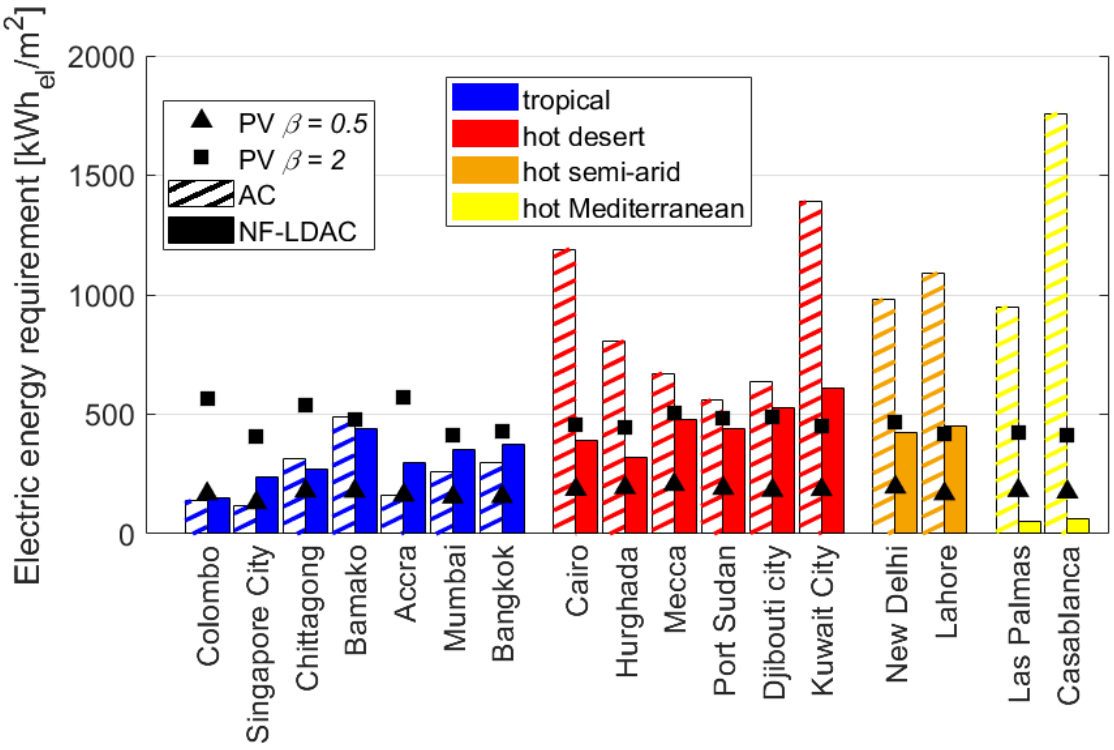

Figure 6-14. Annual electric energy per greenhouse plan area. The triangles show the electric energy produced by the photovoltaic (PV) collectors with β of 0.5, while rectangles show PV results with β of 2. Hatched bars for AC and full bars for semi-closed: NF-LDAC show their energy requirements.

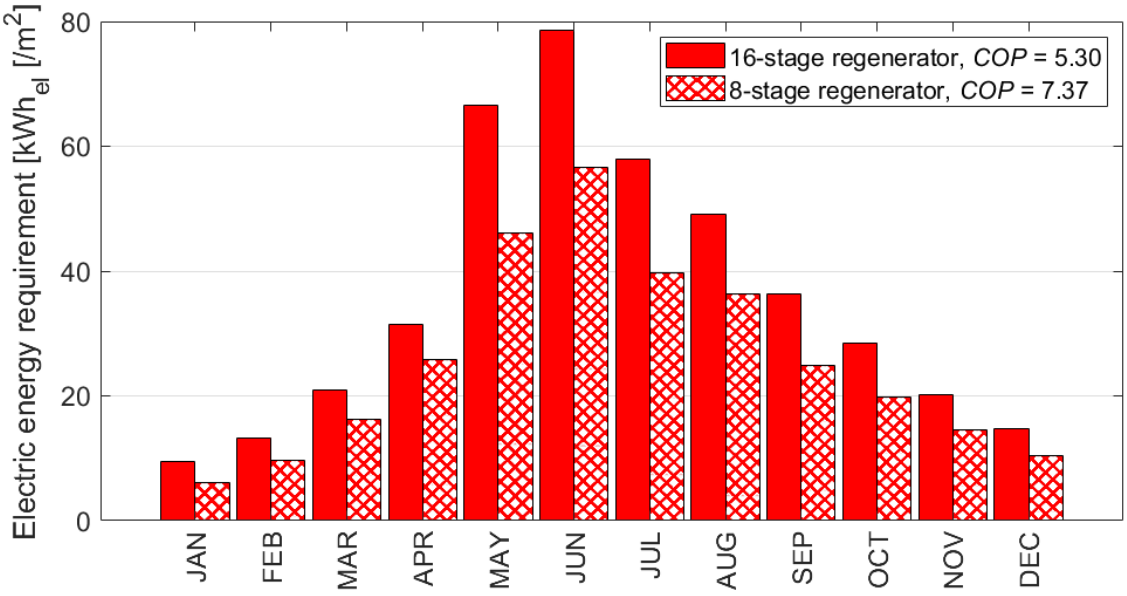

Figure 6-15. Monthly electric energy requirements of the 16-stage (full bars) and 8-stage (cross bars) regenerators at Mecca (hot desert climate). Legend reports the annual COP of semi-closed: NF-LDAC using these two multi-stage regenerators.

The PV collectors' area was assumed equal to half the plan area of the greenhouse, i.e., β of 0.5. To compare the energy requirements with the generated PV energy, the electric PV energy is also calculated per greenhouse plan area (indicated as "PV" in Figure 6-14). The results show that the PV collectors can fully provide the required energy for *AC* at Colombo, Singapore City, and Accra. However, *semi-closed: NF-LDAC* achieves self-sustainability only at Colombo. Complete coverage of the greenhouse by also covering the walls, i.e., β of 2 (indicated with transparent triangles in Figure 6-14) is required for *semi-closed: NF-LDAC* to achieve self-sustainability, except at Djibouti, Kuwait, and Lahore where even higher β are required. In contrast, β =2 still does not provide enough electricity for AC in all hot desert, hot semi-arid, and hot Mediterranean climates. Despite the four-fold increase in β, the PV energy only increases by a factor of 2.7 due to suboptimal wall orientation for PV energy production.

The annual electric energy requirements of *AC* and *semi-closed: NF-LDAC* can be converted into average annual *COP* values (Figure 6-16). *AC* achieves *COP* values of 3–4.4 which are consistent with the *COP* values of other commercially available vapour compression technologies [282-284]. On average, *semi-closed: NF-LDAC* exhibits higher annual *COP* values than *AC*, and 9 times higher than conventional solar regenerators with *COP* of only 0.3–0.5 [57]. By utilising improved NF membranes, the *COP* of *semi-closed: NF-LDAC* can further increase to values of 3.5–12.1 (as indicated by the dashed bars in Figure 6-16).

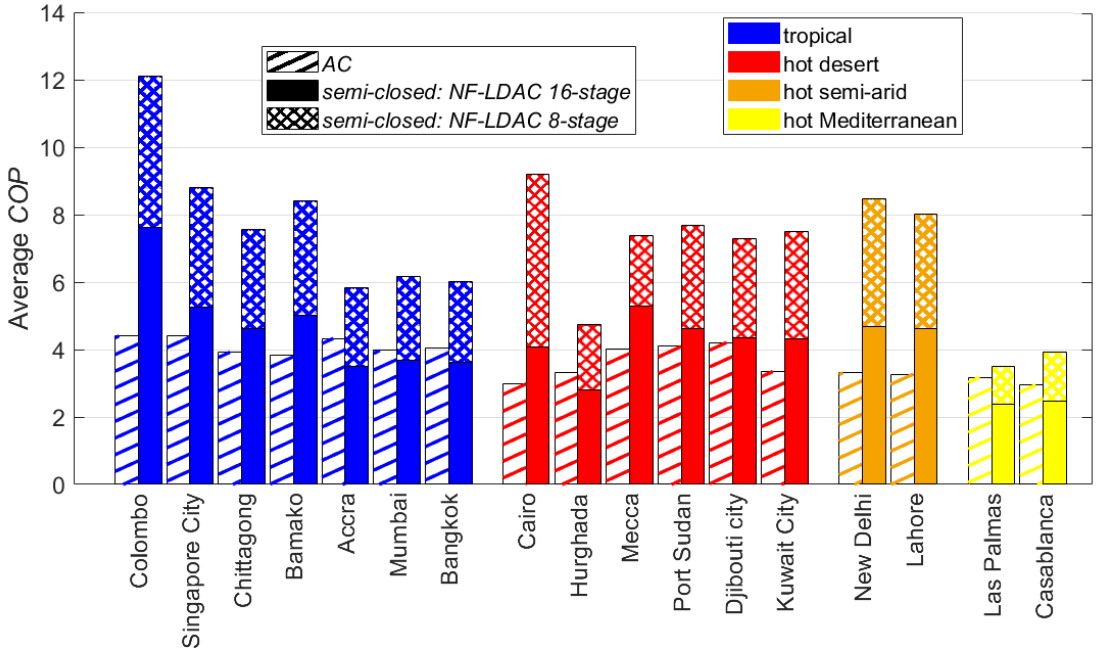

Figure 6-16. Annual average COP at the 17 locations. Hatched bars are for AC, orange bars for semi-closed: NF-LDAC using the 16-stage regenerator, and cross bars for semi-closed: NF-LDAC using the 8-stage regenerator.

Based on climate, *semi-closed: NF-LDAC* achieves annual average *COP* values of 4.8, 4.6, 4.7, and 2.4 in tropical, hot desert, hot semi-arid, and hot Mediterranean climates, respectively. When utilising the 8-stage regenerator, these annual average *COP* values increase to 7.8, 7.3, 8.2, and 3.7. The highest *COP* value for *semi-closed: NF-LDAC*, 7.6 with the 16-stage regenerator or 11.2 with the 8-stage regenerator, is achieved at Colombo. The *COP* of Colombo is 1.3–3.5 times higher in other locations which could be attributed to the low external temperature variance (see Figure 6-13), aiding in maintaining the T_{gh} within the desired range. This assumption is supported by the results of Singapore City which also has both low external temperature variance and high *COP*. However, the *COP* of 12.1 at Colombo is half of the theoretical maximum of 21.2, calculated for $MgCl_2$ with a concentration of 17.2 wt.% (191 g/L) based on the ideal equation of Lefers et al. [5].

The *semi-closed: NF-LDAC* technology also recovers water as the permeate of the multi-stage regenerator, which can be used for irrigation, thereby reducing the water demand of the greenhouse. Figure 6-17 shows the maximum recoverable amount of water when the greenhouse operates with *closed: NF-LDAC* and the recovered amount when it operates with *closed: NF-LDAC*. On average, water savings of 30% are calculated in tropical, 50% in hot desert and hot semi-arid, and only 5% in hot Mediterranean climates. The low water saving calculated in hot Mediterranean climate indicates that *semi-closed: NF-LDAC* is mostly deactivated throughout the year in this climate, as also seen from their low electric energy requirements in Figure 6-14.

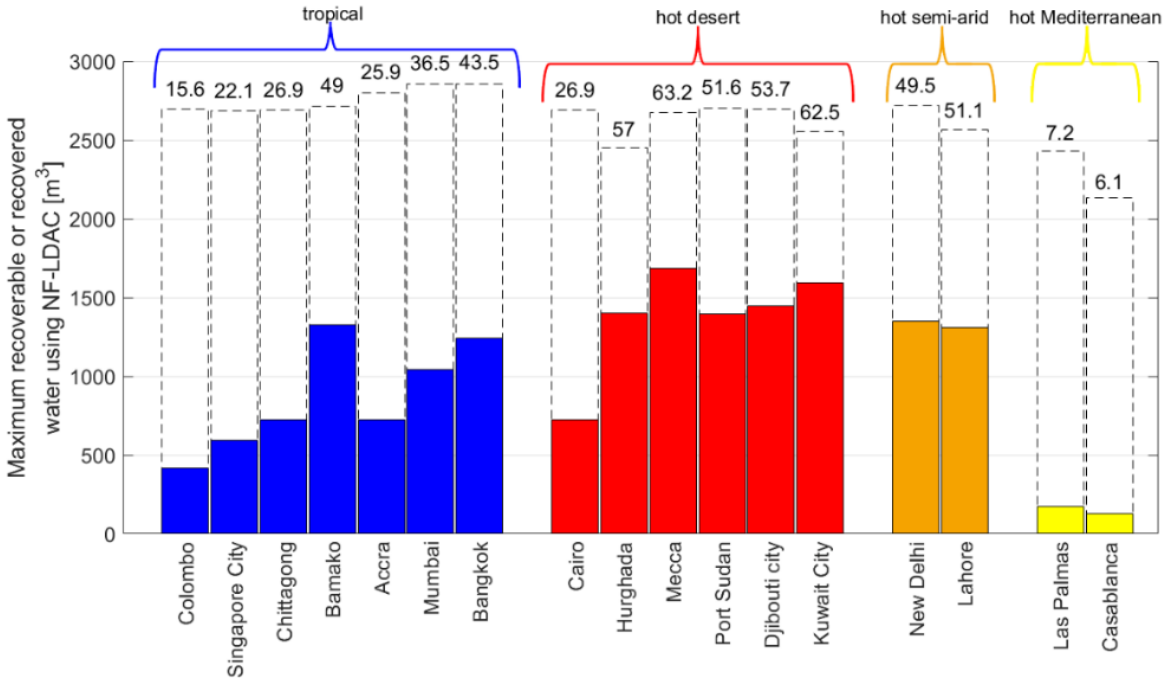

Figure 6-17. Maximum recoverable water when operating with closed: NF-LDAC (empty bars) or recovered water when operating with semi-closed: NF-LDAC (full bars). Numbers on top of the bars indicate the percentage of recovered water compared to the maximum.

6.4 Discussion

The aim of Chapter 6 is to provide more accurate results compared to previous theoretical greenhouse LDAC studies. Earlier studies in this field include Davies [9] and Lychnos and

Davies [22] who calculated greenhouse temperatures of 5–7.5 °C lower than *EvapC* when including conventional LDAC. In Chapter 3, it was found that the idealised model of *closed: NF-LDAC* achieves greenhouse temperatures of 14.7 °C compared to *EvapC*, therefore showing that *closed: NF-LDAC* is preferred against conventional LDAC. In common, the previous studies [9, 22] and Chapter 3 found that year-round cultivation could be achieved. However, the previous studies [9, 22] and Chapter 3 were limited for two reasons. First, they compared the results based solely on temperature and did not consider humidity. Second, they considered only one time-step per month. To provide more accurate results, this Chapter investigated the *VPD* which is a better indication of crop performance, which however does not allow a comparison to be made with the temperature results of the previously mentioned studies and Chapter 3. About year-round cultivation, the current study also found that most locations achieved that, but acceptable cultivation was maintained on average for 60% of the month. Thus, the results show the importance of considering more time steps than just one per month.

Since NF-LDAC achieves better results than other cooling technologies, Chapter 6 compares the results of the TRNSYS model with those of the idealised model developed in Chapter 3. Table 6-1 highlights the main differences between the two models.

Although the two models consider the same PV area per greenhouse plan area (β) of 0.5, their *COP* results differ for several reasons. The TRNSYS model, which accounts for the 3D geometry of the greenhouse and the sun direction throughout the day, indicates that most locations cannot be self-sustained. In contrast, In Chapter 3 it was concluded that the PV collectors can produce twice the required energy of NF-LDAC regardless of climate. This self-sustainability difference can be attributed to the TRNSYS model accounting for geometries and solar directions.

Table 6-1. Comparison of dynamic TRNSYS model (Chapter 6) against the simplified steady-stage model (Chapter 3). Arrows towards up means that higher COP is achieved when the parameter is increased. Parameters above the intermediate line are the same for both models.

Parameters	TRNSYS model (dynamic)	Idealised model of Chapter 3 (steady-state)	Higher *COP* with
β	0.5		↑
η_{pump}	0.85		↑
η_{ERD}	0.9 (isobaric pressure exchanger [279] with 5% friction losses)		↑
LD flowrate [kg/s]	14.5	20	↑
time values per year	8760	12	↓
Floor area [m^2]	512	250	↓
plan area [m^2]	590	450	↓
Air flowrate [kg/s]	51	20	↓
Stages of regenerator	16	9	↓
Stages of improved regenerator	8	4	↓
Maximum k_c	1.12	0.45	↓
Maximum *LAI* [m^2/m^2]	3.95	0.8	↓

To achieve self-sustainability, a complete greenhouse coverage, i.e., β=2, is required. However, a β=2 prevents photosynthesis when using conventional PV collectors. Innovative PV collectors capable of generating electric energy from the blue light spectrum while utilising red light for cultivation [376], or those capable of rejecting infrared radiation (as mentioned in Section 2.4), may enable simultaneous β=2 and photosynthesis. It should be noted that innovative PV collectors generate less energy compared to conventional ones, as part of the radiation passes through them. This implies that self-sustainability with innovative PV collectors can be achieved in locations where self-sustainability is possible with β<1 when operating with conventional PV collectors. However, implementing complete greenhouse coverage would lead to an increase in the cost of the system.

Self-sustainability at a lower cost can be achieved through improvements in NF membranes. The main investigation utilises a 16-stage regenerator made of commercially available NF membranes withstanding 40 bar. By modelling the membranes with an applied

pressure of 80 bar, the regenerator can be simplified to 8 stages which would reduce its cost and complexity. It would also decrease the energy requirement by 30%, double the *COP*, and enable *semi-closed: NF-LDAC* to sustain the greenhouse with an average β of 0.6. Similar results were also found in Chapters 2 and 3, with improved NF membranes decreasing the energy requirement and size of the regenerator.

The TRNSYS model of NF-LDAC calculates a *COP* that is half of the idealised model. Specifically at Mecca, the models calculate *COP* values of 5.3 and 12.4. This difference is because TRNSYS calculates a higher electric power requirement for the multi-stage regenerator ($Power_{reg}$). Despite both models considering the same η_{pump} and η_{ERD}, TRNSYS has a higher $Power_{reg}$ because it utilises a lower LD flow. As the LD flow decreases while the permeate flow must remain constant, the regenerator needs to work more to convert a higher fraction of the LD into permeate. This agrees with the results of Chapter 3 where $Power_{reg}$ of 7 and 6.2 were calculated for LD flows of 10 and 20 kg/s, respectively (see Table 3-3). The TRNSYS model utilises a LD flow of 14.5 kg/s instead of 20 kg/s as in the idealised model because 20 kg/s is challenging to achieve in practice with a wetted pad HMX (similar construction to an evaporative cooling pad). Evaporative pads typically have a small LD entrance area which restricts the flow of LD, such that a flow of 51 kg/s would be impractically large leading to LD spilling out of the pad with lower cooling efficiency, and danger of droplet carry over. Another difference is that the idealised model assumes an air flow of 20 kg/s, whereas real greenhouses require air flows of 51 kg/s (based on [370]). The combination of higher air flow and lower LD flow in the TRNSYS model intensifies the workload for the regenerator as it needs to cool and dehumidify the air more intensively, thereby increasing $Power_{reg}$.

Additionally, the difference in *COP* can also be attributed to the assumption that was made in the idealised model that the applied pressure is equal to only the transmembrane osmotic pressure, while the TRNSYS model includes membrane pore resistance loss and cross-flow pressure drop (based on the multi-stage model developed in Chapter 5), which increases $Power_{reg}$ by 30%. The idealised assumption enabled the use of a 9-stage instead of a 16-stage regenerator. Moreover, the idealised model considered only 12 time steps per year, whereas the TRNSYS model considers 8760 values per year. Hourly *COP* and annual *COP* differ significantly. For example, *AC* achieves maximum hourly *COP* and average annual *COP* of 10 (Figure 6-8) and 4.3 (Figure 6-16), respectively. Thus, modelling the components based on experimental data, datasheets, and 1-hour time steps introduces energy and pressure losses that were not accounted for in the idealised model.

In terms of water savings, *semi-closed: NF-LDAC* reduces the water demand by 50% in hot desert and hot semi-arid climates, 30% in tropical climates, and 5% in hot Mediterranean climates. Mecca has the highest water saving of 63%, followed by Kuwait City with 62%. These savings were calculated by optimising the *COP* of *semi-closed: NF-LDAC*. While *closed: NF-LDAC* allows for 100% water savings, it also has higher energy requirements as the regenerator remains always active. This disagrees with the findings in Chapter 3, where *closed: NF-LDAC* was energy-efficient regardless of the climate. This difference can be due to the low constant values of k_c and *LAI* used by the idealised model to calculate the crop transpiration, whereas the TRNSYS model utilises more accurate hourly values. The TRNSYS model has maximum k_c and *LAI* values of 1.12 and 3.95, respectively, which are 2 and 5 times higher than those employed in the idealised model (refer to Table 6-1).

Another difference between the TRNSYS model and Chapter 3 are the number of investigated locations (refer to Table 6-1). The idealised study included only Mecca, Cairo,

and Timbuktu. The current study also included Mecca and Cairo. In terms of acceptable conditions for cultivation based on location, Chapter 3 found that NF-LDAC performed worse than *EvapC* at Cairo while the TRNSYS model found that NF-LDAC is notably better than *EvapC* (10.5 months against 2 months). This is a significant difference since the idealised study underestimated the performance of NF-LDAC in hot desert and hot semi-arid climates. When comparing locations with the same climate, such as Mecca and Cairo, the TRNSYS model provides different results, highlighting that the climate classification alone is not a reliable performance indicator. Thus, for different locations than the 17 investigated, the current study allows to make more accurate assumptions than the idealised study by covering a wider range of locations.

6.5 Conclusions

A 512 m^2 greenhouse was studied dynamically using TRNSYS software by incorporating experimental data, datasheets, realistic operating conditions, energy and pressure losses. The model was applied across 17 locations using individually four cooling technologies, i.e., simple ventilation (*Ventilation*), evaporative cooling (*EvapC*), conventional air-conditioning (*AC*), and *semi-closed: NF-LDAC*. The main findings are:

• *Ventilation* is suboptimal in all climates when assessed based on the monthly *VPD* target of 60%. In hot desert and hot semi-arid climates, *EvapC* achieves the *VPD* target during summer, while *AC* during winter. This suggests that a combination of *EvapC* and *AC* can be used in such climates to achieve the *VPD* target throughout the year. On average, *semi-closed: NF-LDAC* achieves the *VPD* target for 10.5 months per year. Monthly percentages below the *VPD* target occur during cold winter months, indicating that year-round cultivation could be accomplished in such climates by including heating.

• Innovative PV collectors could make the greenhouse self-sustained by completely covering the greenhouse, but this will increase the cost of the system. Alternatively, self-sustainability can be achieved by developing improved NF membranes with low rejections able to resist 80 bar. With such membranes, the regenerator is simplified to 8 stages, making it more compact, less complex, less expensive, and 30% more energy efficient. Consequently, *semi-closed: NF-LDAC* becomes self-sustainable with a PV collectors' area equal to 60% of the greenhouse plan area.

• *Semi-closed: NF-LDAC* achieves annual average *COP* values of 4.8, 4.6, 4.7 and 2.4 in tropical, hot desert, hot semi-arid, and hot Mediterranean climates, respectively. On average, the *COP* of *semi-closed: NF-LDAC* is slightly higher than *AC*, but the *COP* of *semi-closed: NF-LDAC* can be twice that of *AC* by developing improved NF membranes.

• The idealised model of NF-LDAC developed in Chapter 3 represents the highest achievable performance. While the TRNSYS model provides more realistic results and a *COP* that is two times lower than the idealised model, the difference between the two models shows the potential for improvement by highlighting the main contributors for the reduced *COP*. It is mainly attributed to pressure losses in the multi-stage regenerator, which were not accounted for in the idealised model.

• *Semi-closed: NF-LDAC* achieves significant water savings, with irrigation decreasing by 50% in hot desert and hot semi-arid climates, and 30% in tropical climates. In hot Mediterranean climates, the water savings is only 5%, indicating that *semi-closed: NF-LDAC* remains mostly deactivated throughout the year. When considering both *VPD* and *COP*, *semi-closed: NF-LDAC* outperforms conventional cooling technologies in tropical, hot desert, and hot semi-arid climates.

• *Semi-closed: NF-LDAC* shows promising results as a sustainable and efficient approach for greenhouse cooling, dehumidification, and water conservation. Its ability to achieve the target *VPD* percentage throughout the year with a relatively high annual *COP* makes it a compelling option. Further advancements in NF membranes have the potential to enhance the energy performance of *semi-closed: NF-LDAC* even further.

Chapter 7: General Discussion and Conclusions

This PhD project investigated the potential of a multi-stage nanofiltration (NF) regenerator combined with liquid desiccant air-conditioning, namely NF-LDAC, as an approach to address water scarcity and food insecurity in hot regions where horticultural greenhouses are used. Among six membrane-based desalination technologies that could be employed as liquid desiccant regenerators, NF-LDAC was identified as the most promising and practical option (Section 1.4). Consequently, an idealised model was developed to demonstrate the advantages of NF-LDAC over conventional greenhouse cooling technologies and thermal regenerators (Section 2.4). Subsequently, dead-end filtration experiments were conducted using a 1-stage regenerator (Chapter 4), followed by cross-flow filtration experiments with a 2-stage regenerator (Chapter 5), demonstrating the feasibility of liquid desiccant regeneration through NF membranes. The developed 2-stage regenerator model, accounting for energy and mass balance equations as well as energy and pressure losses, yielded results with errors below 11% compared to the experimental data (Section 4.4.2). Finally, this verified model was applied to a dynamic simulation of a greenhouse, showing the potential of NF-LDAC at hot desert and hot semi-arid climates where it achieves year-round cultivation, average annual coefficient of performance (*COP*) of 4.7, and water savings of 50% (Section 5.5).

In this concluding Chapter, the limitations of the research are discussed followed by future research directions that may overcome these limitations, before concluding with a summary of the main conclusions.

7.1 Limitations

The proposed multi-stage NF regenerator is limited by three factors. First, commercially available NF membranes with rejections of 10–70% have a low burst pressure of

approximately 40 bar (Section 3.3.2), which significantly limits the system. Since LDAC requires concentrated liquid desiccant (LD) solutions for efficient dehumidification, such solutions have high osmotic pressures. For instance, the osmotic pressure of $MgCl_2$ for greenhouse applications is around 250 bar. To produce permeate, the pressure applied by the multi-stage regenerator must be higher than the osmotic pressure plus the pressure losses. Consequently, a low burst pressure makes NF-LDAC more complex by increasing the required number of stages.

Second, the performance of NF-LDAC is limited by the pressure losses of the multi-stage regenerator. Without considering pressure losses (Chapter 3), the regenerator requires 9 stages which increases to 16 stages when considering pressure losses (Chapter 6). These multi-stage regenerators are expected to be complex, with complexity increasing as more stages are added. As the stages increase, the cost of the regenerator also increases because more material and a better control system are required. Moreover, without considering pressure losses, NF-LDAC achieves a *COP* of 12 (Section 2.4). However, when considering pressure losses, NF-LDAC achieves a *COP* of 4.7 (Section 5.4). The lower *COP* is also a result of incorporating more realistic operating conditions and applying a more accurate modelling approach, validated by experiments. Nonetheless, the required applied pressures increase by 5–25 bar at each stage of the regenerator solely due to pressure losses (Section 4.6). Pressure losses decrease the net pressure applied at each stage, which in turn increases the required number of stages.

Third, membranes can be affected by fouling. Fouling was not directly investigated in this work but it was considered by indirect means, such as based on recovery and concentration. The first stage of the regenerator is the most at risk due to both high recovery and feed concentration (Subsection 4.4.3). Therefore, the first stage must utilise NF membranes which

are less prone to fouling, such as the NFX type used for the experiments in Chapters 3 and 4. Since Ca^{2+} and SO_4^{2-} can form gypsum, which can damage the membranes, the use of $MgCl_2$ as the LD is expected to avoid this risk. Except recovery and concentration, other parameters were also considered for fouling, such as the longitudinal pressure which remained constant, thus suggesting that fouling did not occur (Subsection 4.3.1). However, the duration of the experiments was limited and fouling may have affected the experiments if operated for longer periods. Thus, experiments focusing on fouling are needed to verify that multi-stage NF regenerators using $MgCl_2$ are less prone to fouling.

7.2 Future research

To make NF-LDAC a practical choice for greenhouse applications, future research should focus on overcoming the above-mentioned limitations. This includes developing improved NF membranes with rejections of 10–70% and operating pressures of 80 bar (Section 4.5). An operating pressure of 80 bar is reasonable since some reverse osmosis membranes have burst pressures 160 bar (Section 3.5). With commercial NF membranes, the *COP* is low and the multi-stage NF regenerator requires many stages. By doubling the operating pressure of commercial NF membranes from 40 to 80 bar, the *COP* doubles and the number of stages decreases by half, making the multi-stage NF regenerator less complex and expensive (Section 5.4).

Moreover, optimising the design and operation of the multi-stage NF regenerator could further increase the *COP* or decrease the risk of fouling (Section 4.5). Therefore, additional experiments and simulations regarding multi-stage NF regenerators are required to achieve improved results. Regarding pressure losses limiting the regenerators, pore resistance loss is the main contributor, which decreases the performance of the regenerators and should always

be considered in future models. Previous studies investigated aquaporin-based biological membranes to decrease pore resistance loss and found that optimised shapes can increase water permeability, thereby reducing pore resistance loss (Subsection 4.4.1). Future aquaporin-based studies could be conducted regarding LD regeneration. Another approach to decrease pore resistance loss is by employing lower feed flows or bigger membranes (Subsection 4.4.1), suggesting that future investigations could explore 8" membrane modules (rather than 2.5" as in Chapter 5) with low feed flowrates.

7.3 Conclusions

The main findings of this PhD project are:

• Among six desalination technologies that can be used for greenhouse LDAC applications, the most promising are thermoresponsive (TR) solutions, membrane distillation (MD), and multi-stage NF. TR solutions have potential due to the rapid change of their equilibrium relative humidity, but investigations so far have only considered low concentrations. MD can operate with concentrated solutions but is energy-intensive due to phase transition. High-temperature MD operating at 100 °C could improve its energy efficiency. However, commercial MD membranes have a limit of 80 °C. Theoretical studies on multi-stage NF show potential for high concentration applications. Since NF membranes are commercially available, multi-stage NF was chosen as the preferred option (Section 1.4).

• When modelling NF-LDAC without accounting for pressure losses (idealised model), NF-LDAC operating in closed air recirculation outperforms conventional cooling technologies (Section 2.4). Specifically, it achieves an additional temperature drop of 18.7 °C compared to simple ventilation, 14.7 °C compared to evaporative cooling, and 4 °C compared to evaporative cooling coupled with conventional LDAC. The *COP* of 12.4 attained by NF-

LDAC operating in closed recirculation represents the maximum achievable without considering pressure losses.

• The first NF stage of the multi-stage regenerator should have a low rejection, followed by NF stages with gradually higher rejections and a final reverse osmosis stage with a rejection close to 100%. As the LD flows through the multi-stage regenerator, it gets gradually diluted. Based on dead-end filtration experiments using a 1-stage regenerator, the rejection of a NF membrane increases as the feed concentration decreases (Section 3.4). Thus, the rejections of the NF stages will become higher as the LD flows from stage to stage, which is advantageous for the multi-stage regenerator. However, if the rejections of the NF stages are too low, the dilution of the LD will require too many stages and bigger pumps to accommodate higher capacities (Section 3.5).

• The experiments conducted in Chapter 4 demonstrated that NF membranes can operate with extremely high concentrations, specifically up to 355 g/L of LiCl, 620 g/L of LiBr, and 415 g/L of $MgCl_2$. Among the four NF membrane samples investigated, only one membrane type was able to produce permeate at these highest concentrations. At lower LD concentrations, all the membrane types produced permeate, showing that regeneration of highly concentrated LD solutions can be achieved with several stages by appropriately arranging the NF stages.

• The multi-stage NF regenerator model developed in Chapter 4 is based on dead-end filtration experiments, achieving a recovery of 100%. In contrast, the model developed in Chapter 5 is based on cross-flow filtration, resulting in recoveries below 20%. In desalination applications, higher recoveries are desired, but desalination plants often use cross-flow filtration membranes due to their advantages, including continuous operation and reduced fouling risk. Due to the difference in filtration types, the model from Chapter 4 did not match the experimental results of the 2-stage regenerator investigated in Chapter 5. While the model

of Chapter 4 could be applied to the 2-stage regenerator of Chapter 5 if operated with fully closed brine valves (attaining 100% recovery), it would require extremely low feed flowrates to maintain the applied pressure below 41 bar (maximum recommended by the manufacturer). This would significantly decrease the permeate flowrate and in turn the time required by the multi-stage regenerator to reconcentrate the LD.

• Thus, a new model was developed for the 2-stage regenerator which was verified with errors below 11% compared to the experimental data (Subsection 4.4.2). The verified model was then applied to a 4-stage regenerator, which required 45–75 kWh_{el}/m^3 (per volume of permeate) when incorporating an energy recovery device, calculated for feed concentrations of 135–185 g/L. This energy requirement is lower compared to conventional thermal regenerators. For example, LD regeneration powered by solar collectors requires 390–400 kWh_{el}/m^3, while vapour compression refrigeration requires 120–145 kWh_{el}/m^3. Thus, NF-LDAC requires 1.6–8.8 times less energy than these conventional regeneration technologies (Section 4.5). However, the results were calculated by assuming NF membranes with low rejections and capable of operating at 80 bar, but such NF membranes are not commercially available.

• The verified multi-stage NF regenerator model was applied to a 16-stage regenerator using commercially available membranes (e.g., operation at 40 bar) for a NF-LDAC system operating in semi-closed air recirculation (Section 5.1). The model was dynamically studied at 17 locations. NF-LDAC provided acceptable cultivation conditions year-round in hot desert and tropical climates while recovering 50% and 30% of water, respectively, in these climates (Section 5.3). To enable year-round cultivation in hot semi-arid and hot Mediterranean climates, NF-LDAC requires heating.

• NF-LDAC using a 16-stage regenerator achieves the highest *COP* of 7.6 at Colombo (Sri Lanka), followed by 5.3 at Mecca (Saudi Arabia). With future advantages in NF membrane fabrication, NF-LDAC using an 8-stage regenerator could reach *COP* values of 12.1 at Colombo and 7.4 at Mecca (Section 5.3).

7.4 Research gap and thesis contribution

The research gaps in the field of LDAC for greenhouses are:

• Due to water scarcity in hot climates, agriculture using conventional cooling technologies is neither sustainable nor economical. This is primarily attributed to the low efficiency of conventional thermal regenerators, highlighting the need for a more efficient regeneration method.

• Multi-stage systems that combine several nanofiltration membranes with a reverse osmosis membrane have not been experimentally investigated and their models are based on idealised assumptions, such as 100% efficiencies of pumps and energy recovery devices, no pressure losses, constant membrane properties under variable operating conditions, and osmotic pressures calculated using approximations like the van ‘t Hoff equation. Specifically, nanofiltration membrane samples used with extremely concentrated LDs for LD regeneration have not yet been studied. Moreover, a multi-stage system used as a liquid desiccant regenerator has also never been experimentally investigated. Consequently, multi-stage models are inaccurate since they are not based on real experiments or realistic conditions.

• Although studies that have modelled greenhouses using LDAC systems found that year-round cultivation was possible, these studies considered only one time step per month. This implies that the feasibility of cultivation was assessed based on average monthly conditions, which may occur briefly during the month.

To address these gaps, this thesis:

• Conducted a comparative review of six desalination technologies which found that NF-LDAC is the best alternative to conventional thermal LD regenerators.

• Proposed a conceptual design of NF-LDAC applied to greenhouses. For the first time, NF-LDAC was theoretically compared against three conventional greenhouse cooling technologies.

• Conducted, for the first time, experiments with nanofiltration membrane samples using extremely concentrated LDs. Additionally, it designed, built, and conducted experiments with a 2-stage nanofiltration LD regenerator. Improved models were developed, verified through experiments, and then used to accurately compare the performance of multi-stage systems with their conventional thermal alternatives.

• By integrating the verified models, datasheets, and realistic operating conditions into a dynamic simulation, this thesis is the first to perform an hourly-based simulation of a greenhouse using NF-LDAC, and to use the dynamic model to compare NF-LDAC against three conventional cooling technologies.

Overall, this PhD project found promising results for NF-LDAC from theoretical steady-state (Chapter 3), experimental (Chapters 3 and 4), and theoretical dynamic based on experimental data (Chapter 6) perspectives, highlighting its potential in greenhouse applications as a viable approach to address the pressing issue of water scarcity and food insecurity in hot climates.

References

1. *United Nations, Department of Economic and Social Affairs, Population Division (ST/ESA/SER.A/423), World Population Prospects 2019 Highlights.* 2019.
2. R.M. Lefers, M. Tester, and K.J.J.F.i.P.S. Lauersen, *Emerging Technologies to Enable Sustainable Controlled Environment Agriculture in the Extreme Environments of Middle East-North Africa Coastal Regions.* 2020. **11**.
3. M. Ghoulem, K. El Moueddeb, E. Nehdi, R. Boukhanouf, and J.K. Calautit, *Greenhouse design and cooling technologies for sustainable food cultivation in hot climates: Review of current practice and future status.* Biosystems Engineering, 2019. **183**: p. 121-150.
4. P.M. Cuce and S. Riffat, *A state of the art review of evaporative cooling systems for building applications.* Renewable and Sustainable Energy Reviews, 2016. **54**: p. 1240-1249.
5. R. Lefers, N.M.S. Bettahalli, S.P. Nunes, N. Fedoroff, P.A. Davies, and T. Leiknes, *Liquid desiccant dehumidification and regeneration process to meet cooling and freshwater needs of desert greenhouses.* Desalination and Water Treatment, 2016. **57**(48-49): p. 23430-23442.
6. C. Kittas, T. Bartzanas, and A. Jaffrin, *Greenhouse evaporative cooling: measurement and data analysis.* Transactions of the ASAE, 2001. **44**(3): p. 683.
7. S.K. Abdel-wahab, *Energy and water management in evaporitive cooling systems in Saudi Arabia.* Resources, conservation and recycling, 1994. **12**(3-4): p. 135-146.
8. N.C. Sabeh, *Evaluating and Miniziming Water Use by Greenhouse Evaporative Cooling Systems in a Semi-Arid Climate.* 2007.
9. P. Davies, *A solar cooling system for greenhouse food production in hot climates.* Solar energy, 2005. **79**(6): p. 661-668.
10. M.M. Rafique, P. Gandhidasan, and H.M. Bahaidarah, *Liquid desiccant materials and dehumidifiers–A review.* Renewable and Sustainable Energy Reviews, 2016. **56**: p. 179-195.
11. A.H. Abdel-Salam and C.J. Simonson, *Annual evaluation of energy, environmental and economic performances of a membrane liquid desiccant air conditioning system with/without ERV.* Applied Energy, 2014. **116**: p. 134-148.
12. R. Qi, L. Lu, and Y. Huang, *Parameter analysis and optimization of the energy and economic performance of solar-assisted liquid desiccant cooling system under different climate conditions.* Energy Conversion and Management, 2015. **106**: p. 1387-1395.
13. D. Kim and C.I. Ferreira, *Solar refrigeration options–a state-of-the-art review.* International journal of refrigeration, 2008. **31**(1): p. 3-15.
14. X. Ou, W. Cai, X. He, and D. Zhai, *Experimental investigations on heat and mass transfer performances of a liquid desiccant cooling and dehumidification system.* Applied Energy, 2018. **220**: p. 164-175.
15. H. Ren, Z. Ma, W. Lin, S. Wang, and W. Li, *Optimal design and size of a desiccant cooling system with onsite energy generation and thermal storage using a multilayer perceptron neural network and a genetic algorithm.* Energy Conversion and Management, 2019. **180**: p. 598-608.
16. Y. Yin, J. Qian, and X. Zhang, *Recent advancements in liquid desiccant dehumidification technology.* Renewable and Sustainable Energy Reviews, 2014. **31**: p. 38-52.
17. R. Qi, C. Dong, and L.-Z. Zhang, *A review of liquid desiccant air dehumidification: from system to material manipulations.* Energy and Buildings, 2020: p. 109897.
18. H.C. Duong, A.J. Ansari, L.D. Nghiem, H.T. Cao, T.D. Vu, and T.P. Nguyen, *Membrane Processes for the Regeneration of Liquid Desiccant Solution for Air Conditioning.* Current Pollution Reports, 2019. **5**(4): p. 308-318.

19. C.A. Balaras, G. Grossman, H.-M. Henning, C.A.I. Ferreira, E. Podesser, L. Wang, and E. Wiemken, *Solar air conditioning in Europe—an overview.* Renewable and sustainable energy reviews, 2007. **11**(2): p. 299-314.
20. I. Sarbu, C. Sebarchievici, I. Sarbu, and C. Sebarchievici, *Chapter 7-Solar Thermal-Driven Cooling Systems.* Solar Heating and Cooling Systems, 2017: p. 241-313.
21. F. Bruno, *An indirect evaporative cooler for supplying air near the dew point*. 2010, Australian Solar Energy Society.
22. G. Lychnos and P.A. Davies, *Modelling and experimental verification of a solar-powered liquid desiccant cooling system for greenhouse food production in hot climates.* Energy, 2012. **40**(1): p. 116-130.
23. C. Stanghellini, B. Oosfer, and E. Heuvelink, *Greenhouse horticulture: technology for optimal crop production*. 2019: Wageningen Academic Publishers.
24. M. Teitel, J. Montero, and E. Baeza. *Greenhouse design: Concepts and trends*. in *International Symposium on Advanced Technologies and Management Towards Sustainable Greenhouse Ecosystems: Greensys2011 952*. 2011.
25. P. Davies and P. Knowles, *Seawater bitterns as a source of liquid desiccant for use in solar-cooled greenhouses.* Desalination, 2006. **196**(1-3): p. 266-279.
26. E. Elsarrag, *Dehumidification of air by chemical liquid desiccant in a packed column and its heat and mass transfer effectiveness.* HVAC&R Research, 2006. **12**(1): p. 3-16.
27. R. Qi, C. Dong, and L.-Z. Zhang, *A review of liquid desiccant air dehumidification: From system to material manipulations.* Energy and Buildings, 2020. **215**: p. 109897. Retrieved from https://www.sciencedirect.com/science/article/pii/S0378778819337892
28. I. Koronaki, R. Christodoulaki, V. Papaefthimiou, and E. Rogdakis, *Thermodynamic analysis of a counter flow adiabatic dehumidifier with different liquid desiccant materials.* Applied Thermal Engineering, 2013. **50**(1): p. 361-373.
29. J. Liu, T. Zhang, X. Liu, and J. Jiang, *Experimental analysis of an internally-cooled/heated liquid desiccant dehumidifier/regenerator made of thermally conductive plastic.* Energy and Buildings, 2015. **99**: p. 75-86.
30. X. LIU, X. YI, and Y. JIANG, *Mass transfer performance comparison of two commonly used liquid desiccants [J].* Journal of the Chemical Industry and Engineering Society of China, 2009. **3**.
31. M. Tu, C.-Q. Ren, L.-A. Zhang, and J.-W. Shao, *Simulation and analysis of a novel liquid desiccant air-conditioning system.* Applied Thermal Engineering, 2009. **29**(11-12): p. 2417-2425.
32. Y. Yin, X. Zhang, G. Wang, and L. Luo, *Experimental study on a new internally cooled/heated dehumidifier/regenerator of liquid desiccant systems.* International Journal of Refrigeration, 2008. **31**(5): p. 857-866.
33. G. Lychnos, R. Amdouni, and P.A. Davies, *Concentrated seawater brines for use in solar-powered desiccant cooling cycles.* RSC advances, 2012. **2**(21): p. 7978-7982.
34. R.M. Lefers, N.S. Bettahalli, N.V. Fedoroff, N. Ghaffour, P.A. Davies, S.P. Nunes, and T. Leiknes, *Hollow fibre membrane-based liquid desiccant humidity control for controlled environment agriculture.* Biosystems Engineering, 2019. **183**: p. 47-57.
35. G. Lychnos, J.P. Fletcher, and P.A. Davies, *Properties of seawater bitterns with regard to liquid-desiccant cooling.* Desalination, 2010. **250**(1): p. 172-178.
36. A. Zuber, R. Checoni, R. Mathew, J. Santos, F. Tavares, and M. Castier, *Thermodynamic properties of 1: 1 salt aqueous solutions with the electrolattice equation of state.* Oil & Gas Science and Technology–Revue d'IFP Energies nouvelles, 2013. **68**(2): p. 255-270.

37. X. Chen, S. Riffat, H. Bai, X. Zheng, and D. Reay, *Recent progress in liquid desiccant dehumidification and air-conditioning: A review.* Energy and Built Environment, 2020. **1**(1): p. 106-130.
38. L. Mei and Y. Dai, *A technical review on use of liquid-desiccant dehumidification for air-conditioning application.* Renewable and Sustainable Energy Reviews, 2008. **12**(3): p. 662-689.
39. X. Liu, M. Qu, X. Liu, and L. Wang, *Membrane-based liquid desiccant air dehumidification: A comprehensive review on materials, components, systems and performances.* Renewable and Sustainable Energy Reviews, 2019. **110**: p. 444-466.
40. N. Zhang, X. Chen, Y. Su, H. Zheng, O. Ramadan, X. Zhang, H. Chen, and S. Riffat, *Numerical investigations and performance comparisons of a novel cross-flow hollow fiber integrated liquid desiccant dehumidification system.* Energy, 2019. **182**: p. 1115-1131.
41. G.A. Longo and A. Gasparella, *Experimental measurement of thermophysical properties of H2O/KCOOH (potassium formate) desiccant.* International Journal of Refrigeration, 2016. **62**: p. 106-113.
42. T. Elmer, M. Worall, S. Wu, and S. Riffat, *Experimental evaluation of a liquid desiccant air conditioning system for tri-generation/waste-heat-driven applications.* International Journal of Low-Carbon Technologies, 2017. **12**(2): p. 110-125.
43. A.S. Valarezo, X. Sun, T. Ge, Y. Dai, and R. Wang, *Experimental investigation on performance of a novel composite desiccant coated heat exchanger in summer and winter seasons.* Energy, 2019. **166**: p. 506-518.
44. A. Giampieri, Z. Ma, A. Smallbone, and A.P. Roskilly, *Thermodynamics and economics of liquid desiccants for heating, ventilation and air-conditioning–An overview.* Applied Energy, 2018. **220**: p. 455-479.
45. S. Riffat, S. James, and C. Wong, *Experimental analysis of the absorption and desorption rates of HCOOK/H2O and LiBr/H2O.* International journal of energy research, 1998. **22**(12): p. 1099-1103.
46. S. Bouzenada, L. Frainkin, and A. Léonard, *Experimental investigation on vapor pressure of desiccant for air conditioning application.* Procedia Computer Science, 2017. **109**: p. 817-824.
47. M.R. Conde, *Properties of aqueous solutions of lithium and calcium chlorides: formulations for use in air conditioning equipment design.* International Journal of Thermal Sciences, 2004. **43**(4): p. 367-382.
48. Y. Yao, Y. Yu, and Z.J.S.E. Zhu, *Experimental investigations on surface vapor pressure models for LiCl–CaCl2 desiccant solutions.* 2016. **126**: p. 1-13.
49. P. Gandhidasan, *A simplified model for air dehumidification with liquid desiccant.* Solar energy, 2004. **76**(4): p. 409-416.
50. B. Olesen, *The philosophy behind EN15251. Indoor environmental criteria for design and calculation of energy performance of buildings; De filosofie achter EN15251. Binnenklimaatcriteria voor de energieprestatie van gebouwen.* TVVL Magazine, 2008. **37**.
51. H. Monnier, N. Mhiri, and L. Falk, *Falling liquid film stability in microgas/liquid absorption.* Chemical Engineering and Processing: Process Intensification, 2010. **49**(9): p. 953-957.
52. H. Trivedi, N.P. Jaiswal, and D. Patel, *A Review on Liquid Desiccant Air Cooling Systems.*
53. W. Li, Y. Pan, Y. Yao, and M. Dong, *Modeling and parametric study of the ultrasonic atomization regeneration of desiccant solution.* International Journal of Heat and Mass Transfer, 2018. **127**: p. 687-702.
54. Y. Yao, W. Li, and Y. Hu, *Modeling and performance investigation on the counter-flow ultrasonic atomization liquid desiccant regenerator.* Applied Thermal Engineering, 2020. **165**: p. 114573.

55. T. Tong and M. Elimelech, *The global rise of zero liquid discharge for wastewater management: drivers, technologies, and future directions.* Environmental science & technology, 2016. **50**(13): p. 6846-6855.
56. R.S. Das and S. Jain, *Experimental investigations on a solar assisted liquid desiccant cooling system with indirect contact dehumidifier.* Solar Energy, 2017. **153**: p. 289-300.
57. S. Bouzenada, C. McNevin, S. Harrison, and A. Kaabi, *Performance of a liquid desiccant air-conditioner driven by evacuated-tube, flat-plate, or hybrid solar thermal arrays.* Energy and Buildings, 2016. **117**: p. 53-62.
58. S. Riffat and M. Gillott, *Performance of a novel mechanical ventilation heat recovery heat pump system.* Applied thermal engineering, 2002. **22**(7): p. 839-845.
59. A.H. Abdel-Salam and C.J. Simonson, *Capacity matching in heat-pump membrane liquid desiccant air conditioning systems.* International journal of refrigeration, 2014. **48**: p. 166-177.
60. A.H. Abdel-Salam and C.J. Simonson, *Optimal design, sizing and operation of heat-pump liquid desiccant air conditioning systems.* Science and Technology for the Built Environment, 2020. **26**(2): p. 161-176.
61. K. Harby, *Hydrocarbons and their mixtures as alternatives to environmental unfriendly halogenated refrigerants: An updated overview.* Renewable and Sustainable Energy Reviews, 2017. **73**: p. 1247-1264.
62. R.L. McGinnis, N.T. Hancock, M.S. Nowosielski-Slepowron, and G.D. McGurgan, *Pilot demonstration of the NH3/CO2 forward osmosis desalination process on high salinity brines.* Desalination, 2013. **312**: p. 67-74.
63. C. Fritzmann, J. Löwenberg, T. Wintgens, and T. Melin, *State-of-the-art of reverse osmosis desalination.* Desalination, 2007. **216**(1-3): p. 1-76.
64. Y. Guo, Z. Ma, A. Al-Jubainawi, P. Cooper, and L.D. Nghiem, *Using electrodialysis for regeneration of aqueous lithium chloride solution in liquid desiccant air conditioning systems.* Energy and Buildings, 2016. **116**: p. 285-295.
65. H.G. Zeweldi, A.P. Bendoy, M.J. Park, H.K. Shon, H.-S. Kim, E.M. Johnson, H. Kim, S.-P. Lee, W.-J. Chung, and G.M. Nisola, *Tetrabutylammonium 2, 4, 6-trimethylbenzenesulfonate as an effective and regenerable thermo-responsive ionic liquid drawing agent in forward osmosis for seawater desalination.* Desalination, 2020. **495**: p. 114635.
66. J. Andrés-Mañas, L. Roca, A. Ruiz-Aguirre, F. Acién, J.D. Gil, and G. Zaragoza, *Application of solar energy to seawater desalination in a pilot system based on vacuum multi-effect membrane distillation.* Applied Energy, 2020. **258**: p. 114068.
67. J. Andrés-Mañas, A. Ruiz-Aguirre, F. Acién, and G. Zaragoza, *Assessment of a pilot system for seawater desalination based on vacuum multi-effect membrane distillation with enhanced heat recovery.* Desalination, 2018. **443**: p. 110-121.
68. G. Chen, Y. Lu, X. Yang, R. Wang, and A.G. Fane, *Quantitative study on crystallization-induced scaling in high-concentration direct-contact membrane distillation.* Industrial & Engineering Chemistry Research, 2014. **53**(40): p. 15656-15666.
69. J.-P. Mericq, S. Laborie, and C. Cabassud, *Vacuum membrane distillation of seawater reverse osmosis brines.* Water research, 2010. **44**(18): p. 5260-5273.
70. C.A. Quist-Jensen, A. Ali, S. Mondal, F. Macedonio, and E. Drioli, *A study of membrane distillation and crystallization for lithium recovery from high-concentrated aqueous solutions.* Journal of Membrane Science, 2016. **505**: p. 167-173.
71. C.M. Tun, A.G. Fane, J.T. Matheickal, and R. Sheikholeslami, *Membrane distillation crystallization of concentrated salts—flux and crystal formation.* Journal of Membrane Science, 2005. **257**(1-2): p. 144-155.

72. Y. Yun, R. Ma, W. Zhang, A. Fane, and J. Li, *Direct contact membrane distillation mechanism for high concentration NaCl solutions.* Desalination, 2006. **188**(1-3): p. 251-262.
73. Z. Wang, A. Deshmukh, Y. Du, and M. Elimelech, *Minimal and zero liquid discharge with reverse osmosis using low-salt-rejection membranes.* Water Research, 2020. **170**: p. 115317.
74. S. Burn, M. Hoang, D. Zarzo, F. Olewniak, E. Campos, B. Bolto, and O. Barron, *Desalination techniques—A review of the opportunities for desalination in agriculture.* Desalination, 2015. **364**: p. 2-16.
75. R. Miladi, N. Frikha, A. Kheiri, and S. Gabsi, *Energetic performance analysis of seawater desalination with a solar membrane distillation.* Energy Conversion and Management, 2019. **185**: p. 143-154.
76. E. Curcio and E. Drioli, *Membrane distillation and related operations—a review.* Separation and Purification Reviews, 2005. **34**(1): p. 35-86.
77. V. Alves and I. Coelhoso, *Orange juice concentration by osmotic evaporation and membrane distillation: a comparative study.* Journal of Food Engineering, 2006. **74**(1): p. 125-133.
78. S. Gunko, S. Verbych, M. Bryk, and N. Hilal, *Concentration of apple juice using direct contact membrane distillation.* Desalination, 2006. **190**(1-3): p. 117-124.
79. M. Tomaszewska, M. Gryta, and A. Morawski, *Study on the concentration of acids by membrane distillation.* Journal of Membrane Science, 1995. **102**: p. 113-122.
80. A. Alkhudhiri, N. Darwish, and N. Hilal, *Membrane distillation: A comprehensive review.* Desalination, 2012. **287**: p. 2-18.
81. M. Khayet, *Membranes and theoretical modeling of membrane distillation: a review.* Advances in colloid and interface science, 2011. **164**(1-2): p. 56-88.
82. M.A.E.-R. Abu-Zeid, Y. Zhang, H. Dong, L. Zhang, H.-L. Chen, and L. Hou, *A comprehensive review of vacuum membrane distillation technique.* Desalination, 2015. **356**: p. 1-14.
83. I.M. Mujtaba, S.M. Alsadaie, A. Mudhar, R. Patel, M. Sowgath, D. Manca, S. Sarkar, A.K. SenGupta, A. Altaee, and S.R. Wahadj, *1.1 Model-Based Techniques in Desalination Processes: A Review.*
84. E. Guillén-Burrieza, J. Blanco, G. Zaragoza, D.-C. Alarcón, P. Palenzuela, M. Ibarra, and W. Gernjak, *Experimental analysis of an air gap membrane distillation solar desalination pilot system.* Journal of Membrane Science, 2011. **379**(1-2): p. 386-396.
85. E. Guillén-Burrieza, G. Zaragoza, S. Miralles-Cuevas, and J. Blanco, *Experimental evaluation of two pilot-scale membrane distillation modules used for solar desalination.* Journal of Membrane Science, 2012. **409**: p. 264-275.
86. G. Zaragoza, A. Ruiz-Aguirre, and E. Guillén-Burrieza, *Efficiency in the use of solar thermal energy of small membrane desalination systems for decentralized water production.* Applied Energy, 2014. **130**: p. 491-499.
87. B. Zhao, N. Peng, C. Liang, W.F. Yong, and T.-S. Chung, *Hollow fiber membrane dehumidification device for air conditioning system.* Membranes, 2015. **5**(4): p. 722-738.
88. H.C. Duong, F.I. Hai, A. Al-Jubainawi, Z. Ma, T. He, and L.D. Nghiem, *Liquid desiccant lithium chloride regeneration by membrane distillation for air conditioning.* Separation and Purification Technology, 2017. **177**: p. 121-128.
89. A.S. Rattner, A.K. Nagavarapu, S. Garimella, and T.F. Fuller, *Modeling of a flat plate membrane-distillation system for liquid desiccant regeneration in air-conditioning applications.* International journal of heat and mass transfer, 2011. **54**(15-16): p. 3650-3660.

90. R. Lefers, N.S. Bettahalli, N. Fedoroff, S.P. Nunes, and T. Leiknes, *Vacuum membrane distillation of liquid desiccants utilizing hollow fiber membranes.* Separation and Purification Technology, 2018. **199**: p. 57-63.
91. J. Zhou, X. Zhang, W. Su, and B. Sun, *Performance analysis of vacuum membrane distillation regenerator in liquid desiccant air conditioning system.* International Journal of Refrigeration, 2019. **102**: p. 112-121.
92. J. Zhou, F. Wang, N. Noor, and X. Zhang, *An experimental study on liquid regeneration process of a liquid desiccant air conditioning system (LDACs) based on vacuum membrane distillation.* Energy, 2020. **194**: p. 116891.
93. P.A. Davies and G. Zaragoza, *Ideal performance of a self-cooling greenhouse.* Applied Thermal Engineering, 2019. **149**: p. 502-511.
94. T.V. Bartholomew, L. Mey, J.T. Arena, N.S. Siefert, and M.S. Mauter, *Osmotically assisted reverse osmosis for high salinity brine treatment.* Desalination, 2017. **421**: p. 3-11.
95. R. Semiat, *Present and future.* Water International, 2000. **25**(1): p. 54-65.
96. L.F. Greenlee, D.F. Lawler, B.D. Freeman, B. Marrot, and P. Moulin, *Reverse osmosis desalination: water sources, technology, and today's challenges.* Water research, 2009. **43**(9): p. 2317-2348.
97. K.B. Gregory, R.D. Vidic, and D.A. Dzombak, *Water management challenges associated with the production of shale gas by hydraulic fracturing.* Elements, 2011. **7**(3): p. 181-186.
98. J.A. Slutz, J.A. Anderson, R. Broderick, and P.H. Horner. *Key shale gas water management strategies: an economic assessment*. in *International Conference on Health, Safety and Environment in Oil and Gas Exploration and Production*. 2012. Society of Petroleum Engineers.
99. R. Rautenbach and T. Linn, *High-pressure reverse osmosis and nanofiltration, a "zero discharge" process combination for the treatment of waste water with severe fouling/scaling potential.* Desalination, 1996. **105**(1-2): p. 63-70.
100. R. Rautenbach, T. Linn, and L. Eilers, *Treatment of severely contaminated waste water by a combination of RO, high-pressure RO and NF—potential and limits of the process.* Journal of Membrane Science, 2000. **174**(2): p. 231-241.
101. D.M. Davenport, A. Deshmukh, J.R. Werber, and M. Elimelech, *High-pressure reverse osmosis for energy-efficient hypersaline brine desalination: current status, design considerations, and research needs.* Environmental Science & Technology Letters, 2018. **5**(8): p. 467-475.
102. *DuPont™, XUS180808 Reverse Osmosis Element Product Data Sheet.* 2020. Retrieved from https://www.dupont.com/content/dam/dupont/amer/us/en/water-solutions/public/documents/en/45-D01736-en.pdf
103. *Pall corporation, Disc Tube™ Module System, Accessed: 01-01-2023.* Retrieved from https://www.google.com/url?sa=t&rct=j&q=&esrc=s&source=web&cd=&ved=2ahUKEwjT3vmf6sPsAhVDqHEKHdATBbwQFjAAegQIAxAC&url=https%3A%2F%2Fwww.pall.com%2Fcontent%2Fdam%2Fpall%2Foil-gas%2Fliterature-library%2Fnon-gated%2FWPDTLLEN.pdf&usg=AOvVaw3jAHzSmg_3kBexLeTbwH2b
104. B.D. Coday, D.M. Heil, P. Xu, and T.Y. Cath, *Effects of transmembrane hydraulic pressure on performance of forward osmosis membranes.* Environmental science & technology, 2013. **47**(5): p. 2386-2393.
105. K.L. Hickenbottom, J. Vanneste, M. Elimelech, and T.Y. Cath, *Assessing the current state of commercially available membranes and spacers for energy production with pressure retarded osmosis.* Desalination, 2016. **389**: p. 108-118.

106. A.P. Straub, C.O. Osuji, T.Y. Cath, and M. Elimelech, *Selectivity and mass transfer limitations in pressure-retarded osmosis at high concentrations and increased operating pressures.* Environmental science & technology, 2015. **49**(20): p. 12551-12559.
107. *Hydranautics Nitto Group Company, SWC4 MAX. Accessed: 08-01-2022.* 2019. Retrieved from https://membranes.com/wp-content/uploads/Documents/Element-Specification-Sheets/RO/SWC/SWC4-MAX.pdf
108. *Toray Innovation by Chemistry, Standard SWRO TM800M, 2019. Accessed: 01-01-2023.* Retrieved from https://www.toraywater.com/products/ro/pdf/TM800M.pdf
109. M. Wilf. *Fundamentals of RO–NF technology*. in *International conference on desalination costing, Limassol*. 2004.
110. M. Islam, A. Sultana, A. Saadat, M. Shammi, and M. Uddin, *Desalination technologies for developing countries: A review.* Journal of Scientific Research, 2018. **10**(1): p. 77-97.
111. M. Elimelech and W.A. Phillip, *The future of seawater desalination: energy, technology, and the environment.* science, 2011. **333**(6043): p. 712-717.
112. C. Cabassud and D. Wirth, *Membrane distillation for water desalination: how to chose an appropriate membrane?* Desalination, 2003. **157**(1-3): p. 307-314.
113. P. Datt, *Latent Heat of Vaporization/Condensation*, in *Encyclopedia of Snow, Ice and Glaciers*, V.P. Singh, P. Singh, and U.K. Haritashya, Editors. 2011, Springer Netherlands: Dordrecht. p. 703-703.
114. X. Chen and N.Y. Yip, *Unlocking high-salinity desalination with cascading osmotically mediated reverse osmosis: Energy and operating pressure analysis.* Environmental science & technology, 2018. **52**(4): p. 2242-2250.
115. M. Arjmandi, M. Peyravi, A. Altaee, A. Arjmandi, M.P. Chenar, M. Jahanshahi, and E.J.D. Binaeian, *A state-of-the-art protocol to minimize the internal concentration polarization in forward osmosis membranes.* 2020. **480**: p. 114355.
116. K. Nakagawa, K. Uchida, J.L.C. Wu, T. Shintani, T. Yoshioka, Y. Sasaki, L.-F. Fang, E. Kamio, H.K. Shon, H.J.S. Matsuyama, and P. Technology, *Fabrication of porous polyketone forward osmosis membranes modified with aromatic compounds: Improved pressure resistance and low structural parameter.* 2020. **251**: p. 117400.
117. A. Shakeri, S.M.M. Babaheydari, H. Salehi, and S.R.J.L. Razavi, *Reduction of the Structure Parameter of Forward Osmosis Membranes by Using Sodium Bicarbonate as Pore-Forming Agent.* 2021.
118. K. Park and D.R. Yang, *Cost-based feasibility study and sensitivity analysis of a new draw solution assisted reverse osmosis (DSARO) process for seawater desalination.* Desalination, 2017. **422**: p. 182-193.
119. D. Zhao, L.Y. Lee, S.L. Ong, P. Chowdhury, K.B. Siah, and H.Y. Ng, *Electrodialysis reversal for industrial reverse osmosis brine treatment.* Separation and Purification Technology, 2019. **213**: p. 339-347.
120. T. Mezher, H. Fath, Z. Abbas, and A. Khaled, *Techno-economic assessment and environmental impacts of desalination technologies.* Desalination, 2011. **266**(1-3): p. 263-273.
121. F.A. Al-Sulaiman, P. Gandhidasan, and S.M. Zubair, *Liquid desiccant based two-stage evaporative cooling system using reverse osmosis (RO) process for regeneration.* Applied thermal engineering, 2007. **27**(14-15): p. 2449-2454.
122. D. Zhou, L. Zhu, Y. Fu, M. Zhu, and L. Xue, *Development of lower cost seawater desalination processes using nanofiltration technologies—A review.* Desalination, 2015. **376**: p. 109-116.

123. N. Hilal, H. Al-Zoubi, N. Darwish, A. Mohamma, and M.A. Arabi, *A comprehensive review of nanofiltration membranes: Treatment, pretreatment, modelling, and atomic force microscopy.* Desalination, 2004. **170**(3): p. 281-308.
124. *Synder Filtration, NFG (TFC 600-800Da) Sanitary NF Membrane Specsheet. Accessed: 08-01-2022.* Retrieved from https://synderfiltration.com/2014/wp-content/uploads/2018/11/NFG-TFC-600-800Da-Sanitary-Specsheet.pdf
125. *Synder Filtration, NFW (TFC 300-500Da) Sanitary NF Membrane Specsheet. Accessed: 08-01-2022.* Retrieved from https://synderfiltration.com/2014/wp-content/uploads/2018/11/NFW-TFC-300-500Da-Sanitary-Specsheet.pdf
126. *Synder Filtration, NFX (TFC 150-300Da) Sanitary NF Membrane Specsheet. Accessed: 01-01-2023.* Retrieved from https://synderfiltration.com/2014/wp-content/uploads/2018/11/NFX-TFC-150-300Da-Sanitary-Specsheet.pdf
127. *Synder Filtration, Industrial Nanofiltration Membranes - NDX, Membrane Specsheet. Accessed: 08-01-2022.* Retrieved from https://www.lenntech.com/Data-sheets/Synder-Industrial-NDX-TFC-500-700Da-L.pdf
128. *Synder Filtration, NFS (TFC 100-250Da) Sanitary NF Membrane Specsheet. Accessed: 08-01-2022.* Retrieved from https://synderfiltration.com/2014/wp-content/uploads/2018/11/NFS-TFC-100-250Da-Sanitary-Specsheet.pdf
129. *Toray, CSM® NANOFILTRATION MEMBRANE, product datasheetnanofiltration membranes. Accessed: 08-01-2022.* Retrieved from https://www.wqpmag.com/sites/wqp/files/2019-02/CSM%20NF.pdf
130. A.W. Mohammad, Y. Teow, W. Ang, Y. Chung, D. Oatley-Radcliffe, and N. Hilal, *Nanofiltration membranes review: Recent advances and future prospects.* Desalination, 2015. **356**: p. 226-254.
131. S. Subramanian and R. Seeram, *New directions in nanofiltration applications—are nanofibers the right materials as membranes in desalination?* Desalination, 2013. **308**: p. 198-208.
132. A. AlTaee and A.O. Sharif, *Alternative design to dual stage NF seawater desalination using high rejection brackish water membranes.* Desalination, 2011. **273**(2-3): p. 391-397.
133. N. Hilal, H. Al-Zoubi, A. Mohammad, and N. Darwish, *Nanofiltration of highly concentrated salt solutions up to seawater salinity.* Desalination, 2005. **184**(1): p. 315-326.
134. P. Eriksson, M. Kyburz, and W. Pergande, *NF membrane characteristics and evaluation for sea water processing applications.* Desalination, 2005. **184**(1-3): p. 281-294.
135. K. Lutchmiah, D.J. Harmsen, B.A. Wols, L.C. Rietveld, J. Qin, and E.R. Cornelissen, *Continuous and discontinuous pressure assisted osmosis (PAO).* Journal of Membrane Science, 2015. **476**: p. 182-193.
136. H. Luo, Q. Wang, T.C. Zhang, T. Tao, A. Zhou, L. Chen, and X. Bie, *A review on the recovery methods of draw solutes in forward osmosis.* Journal of Water Process Engineering, 2014. **4**: p. 212-223.
137. M. Qasim, N.A. Darwish, S. Sarp, and N. Hilal, *Water desalination by forward (direct) osmosis phenomenon: A comprehensive review.* Desalination, 2015. **374**: p. 47-69.
138. J.R. McCutcheon and M. Elimelech, *Influence of concentrative and dilutive internal concentration polarization on flux behavior in forward osmosis.* Journal of membrane science, 2006. **284**(1-2): p. 237-247.
139. H.C. Duong, A.J. Ansari, L.D. Nghiem, T.M. Pham, and T.D. Pham, *Low carbon desalination by innovative membrane materials and processes.* Current Pollution Reports, 2018. **4**(4): p. 251-264.

140. L. Chekli, S. Phuntsho, J.E. Kim, J. Kim, J.Y. Choi, J.-S. Choi, S. Kim, J.H. Kim, S. Hong, and J. Sohn, *A comprehensive review of hybrid forward osmosis systems: Performance, applications and future prospects.* Journal of Membrane Science, 2016. **497**: p. 430-449.
141. A. Achilli, T.Y. Cath, and A.E. Childress, *Selection of inorganic-based draw solutions for forward osmosis applications.* Journal of membrane science, 2010. **364**(1-2): p. 233-241.
142. Y. Hartanto, S. Yun, B. Jin, and S. Dai, *Functionalized thermo-responsive microgels for high performance forward osmosis desalination.* Water research, 2015. **70**: p. 385-393.
143. J.E. Kim, S. Phuntsho, F. Lotfi, and H.K. Shon, *Investigation of pilot-scale 8040 FO membrane module under different operating conditions for brackish water desalination.* Desalination and Water Treatment, 2015. **53**(10): p. 2782-2791. Retrieved from https://doi.org/10.1080/19443994.2014.931528
144. T.Y. Cath, A.E. Childress, and M. Elimelech, *Forward osmosis: principles, applications, and recent developments.* Journal of membrane science, 2006. **281**(1-2): p. 70-87.
145. K.B. Petrotos and H.N. Lazarides, *Osmotic concentration of liquid foods.* Journal of Food Engineering, 2001. **49**(2-3): p. 201-206.
146. A. Achilli, T.Y. Cath, E.A. Marchand, and A.E. Childress, *The forward osmosis membrane bioreactor: a low fouling alternative to MBR processes.* Desalination, 2009. **239**(1-3): p. 10-21.
147. R.W. Holloway, A.E. Childress, K.E. Dennett, and T.Y. Cath, *Forward osmosis for concentration of anaerobic digester centrate.* Water research, 2007. **41**(17): p. 4005-4014.
148. S. Phuntsho, H.K. Shon, S. Hong, S. Lee, and S. Vigneswaran, *A novel low energy fertilizer driven forward osmosis desalination for direct fertigation: evaluating the performance of fertilizer draw solutions.* Journal of Membrane Science, 2011. **375**(1-2): p. 172-181.
149. S. Phuntsho, H.K. Shon, T. Majeed, I. El Saliby, S. Vigneswaran, J. Kandasamy, S. Hong, and S. Lee, *Blended fertilizers as draw solutions for fertilizer-drawn forward osmosis desalination.* Environmental science & technology, 2012. **46**(8): p. 4567-4575.
150. K. Lee, R. Baker, and H. Lonsdale, *Membranes for power generation by pressure-retarded osmosis.* Journal of membrane science, 1981. **8**(2): p. 141-171.
151. A. Achilli, T.Y. Cath, and A.E. Childress, *Power generation with pressure retarded osmosis: An experimental and theoretical investigation.* Journal of membrane science, 2009. **343**(1-2): p. 42-52.
152. C. Klaysom, T.Y. Cath, T. Depuydt, and I.F. Vankelecom, *Forward and pressure retarded osmosis: potential solutions for global challenges in energy and water supply.* Chemical society reviews, 2013. **42**(16): p. 6959-6989.
153. S. Zhao, L. Zou, C.Y. Tang, and D. Mulcahy, *Recent developments in forward osmosis: opportunities and challenges.* Journal of membrane science, 2012. **396**: p. 1-21.
154. G. Blandin, A.R. Verliefde, C.Y. Tang, A.E. Childress, and P. Le-Clech, *Validation of assisted forward osmosis (AFO) process: Impact of hydraulic pressure.* Journal of membrane science, 2013. **447**: p. 1-11.
155. Y. Oh, S. Lee, M. Elimelech, S. Lee, and S. Hong, *Effect of hydraulic pressure and membrane orientation on water flux and reverse solute flux in pressure assisted osmosis.* Journal of membrane science, 2014. **465**: p. 159-166.
156. S. Sahebi, S. Phuntsho, J.E. Kim, S. Hong, and H.K. Shon, *Pressure assisted fertiliser drawn osmosis process to enhance final dilution of the fertiliser draw solution beyond osmotic equilibrium.* Journal of Membrane Science, 2015. **481**: p. 63-72.
157. C.Y. Tang, Q. She, W.C. Lay, R. Wang, and A.G. Fane, *Coupled effects of internal concentration polarization and fouling on flux behavior of forward osmosis membranes during humic acid filtration.* Journal of membrane science, 2010. **354**(1-2): p. 123-133.

158. B. Lian, G. Blandin, G. Leslie, and P. Le-Clech, *Impact of module design in forward osmosis and pressure assisted osmosis: An experimental and numerical study.* Desalination, 2018. **426**: p. 108-117.
159. Q. She, X. Jin, and C.Y. Tang, *Osmotic power production from salinity gradient resource by pressure retarded osmosis: Effects of operating conditions and reverse solute diffusion.* Journal of Membrane Science, 2012. **401**: p. 262-273.
160. J.R. McCutcheon, R.L. McGinnis, and M. Elimelech, *A novel ammonia—carbon dioxide forward (direct) osmosis desalination process.* Desalination, 2005. **174**(1): p. 1-11.
161. R.W. Field and J.J. Wu, *Mass transfer limitations in forward osmosis: are some potential applications overhyped?* Desalination, 2013. **318**: p. 118-124.
162. W.A. Phillip, J.S. Yong, and M. Elimelech, *Reverse draw solute permeation in forward osmosis: modeling and experiments.* Environmental science & technology, 2010. **44**(13): p. 5170-5176.
163. Q. She, X. Jin, Q. Li, and C.Y. Tang, *Relating reverse and forward solute diffusion to membrane fouling in osmotically driven membrane processes.* Water research, 2012. **46**(7): p. 2478-2486.
164. C. Suh and S. Lee, *Modeling reverse draw solute flux in forward osmosis with external concentration polarization in both sides of the draw and feed solution.* Journal of membrane science, 2013. **427**: p. 365-374.
165. G. Blandin, A. Verliefde, and P. Le-Clech, *Pressure-assisted osmosis (PAO)–RO hybrid: impact of hydraulic pressure on fouling and economics.* Desalination and Water Treatment, 2015. **55**(11): p. 3160-3161.
166. G. Blandin, A.R. Verliefde, J. Comas, I. Rodriguez-Roda, and P. Le-Clech, *Efficiently combining water reuse and desalination through forward osmosis—reverse osmosis (FO-RO) hybrids: a critical review.* Membranes, 2016. **6**(3): p. 37.
167. J. Lee, S. Kook, C. Lee, and I.S. Kim, *Effect of intermittent pressure-assisted forward osmosis (I-PAFO) on organic fouling.* Desalination, 2017. **419**: p. 60-69.
168. M. Xie, J. Lee, L.D. Nghiem, and M. Elimelech, *Role of pressure in organic fouling in forward osmosis and reverse osmosis.* Journal of Membrane Science, 2015. **493**: p. 748-754.
169. Y. Kim, M. Elimelech, H.K. Shon, and S. Hong, *Combined organic and colloidal fouling in forward osmosis: Fouling reversibility and the role of applied pressure.* Journal of Membrane Science, 2014. **460**: p. 206-212.
170. S. Lee, C. Boo, M. Elimelech, and S. Hong, *Comparison of fouling behavior in forward osmosis (FO) and reverse osmosis (RO).* Journal of membrane science, 2010. **365**(1-2): p. 34-39.
171. B. Mi and M. Elimelech, *Organic fouling of forward osmosis membranes: Fouling reversibility and cleaning without chemical reagents.* Journal of membrane science, 2010. **348**(1-2): p. 337-345.
172. C.Y. Tang, T. Chong, and A.G. Fane, *Colloidal interactions and fouling of NF and RO membranes: a review.* Advances in colloid and interface science, 2011. **164**(1-2): p. 126-143.
173. T. Yun, Y.-J. Kim, S. Lee, S. Hong, and G.I. Kim, *Flux behavior and membrane fouling in pressure-assisted forward osmosis.* Desalination and Water Treatment, 2014. **52**(4-6): p. 564-569.
174. Y. Hartanto, M. Zargar, X. Cui, Y. Shen, B. Jin, and S. Dai, *Thermoresponsive cationic copolymer microgels as high performance draw agents in forward osmosis desalination.* Journal of Membrane Science, 2016. **518**: p. 273-281.
175. K. Lutchmiah, L. Lauber, K. Roest, D.J. Harmsen, J.W. Post, L.C. Rietveld, J.B. van Lier, and E.R. Cornelissen, *Zwitterions as alternative draw solutions in forward osmosis for*

application in wastewater reclamation. Journal of Membrane Science, 2014. **460**: p. 82-90.

176. Q. Ge and T.-S. Chung, *Hydroacid complexes: a new class of draw solutes to promote forward osmosis (FO) processes.* Chemical communications, 2013. **49**(76): p. 8471-8473.
177. J. Niskanen and H. Tenhu, *How to manipulate the upper critical solution temperature (UCST)?* Polymer Chemistry, 2017. **8**(1): p. 220-232.
178. D. Zhao, P. Wang, Q. Zhao, N. Chen, and X. Lu, *Thermoresponsive copolymer-based draw solution for seawater desalination in a combined process of forward osmosis and membrane distillation.* Desalination, 2014. **348**: p. 26-32.
179. M. Lemanowicz, A. Gierczycki, W. Kuźnik, R. Sancewicz, and P. Imiela, *Determination of lower critical solution temperature of thermosensitive flocculants.* Minerals Engineering, 2014. **69**: p. 170-176.
180. A. Inada, K. Yumiya, T. Takahashi, K. Kumagai, Y. Hashizume, and H. Matsuyama, *Development of thermoresponsive star oligomers with a glycerol backbone as the draw solute in forward osmosis process.* Journal of Membrane Science, 2019. **574**: p. 147-153.
181. H. Kim, S. Lee, M. Noh, S.H. Lee, Y. Mok, G.-w. Jin, J.-H. Seo, and Y. Lee, *Thermosensitivity control of polyethlyenimine by simple acylation.* Polymer, 2011. **52**(6): p. 1367-1374.
182. X. Zhou, D.B. Gingerich, and M.S. Mauter, *Water treatment capacity of forward-osmosis systems utilizing power-plant waste heat.* Industrial & Engineering Chemistry Research, 2015. **54**(24): p. 6378-6389.
183. L. Chekli, S. Phuntsho, H.K. Shon, S. Vigneswaran, J. Kandasamy, and A. Chanan, *A review of draw solutes in forward osmosis process and their use in modern applications.* Desalination and Water Treatment, 2012. **43**(1-3): p. 167-184.
184. Q. Ge, M. Ling, and T.-S. Chung, *Draw solutions for forward osmosis processes: developments, challenges, and prospects for the future.* Journal of membrane science, 2013. **442**: p. 225-237.
185. Y. Hartanto, M. Zargar, H. Wang, B. Jin, and S. Dai, *Thermoresponsive acidic microgels as functional draw agents for forward osmosis desalination.* Environmental Science & Technology, 2016. **50**(8): p. 4221-4228.
186. A. Inada, K. Kumagai, and H. Matsuyama, *Effect of the molecular weights of thermoresponsive polyalkylene glycol draw solutes on forward osmosis performance.* Separation and Purification Technology, 2020. **252**: p. 117462.
187. Y. Cai, *A critical review on draw solutes development for forward osmosis.* Desalination, 2016. **391**: p. 16-29.
188. C.D. Peters and N.P. Hankins, *The synergy between osmotically assisted reverse osmosis (OARO) and the use of thermo-responsive draw solutions for energy efficient, zero-liquid discharge desalination.* Desalination, 2020. **493**: p. 114630.
189. S. Dutta and K. Nath, *Prospect of ionic liquids and deep eutectic solvents as new generation draw solution in forward osmosis process.* Journal of Water Process Engineering, 2018. **21**: p. 163-176.
190. Y. Zhong, X. Feng, W. Chen, X. Wang, K.-W. Huang, Y. Gnanou, and Z. Lai, *Using UCST ionic liquid as a draw solute in forward osmosis to treat high-salinity water.* Environmental science & technology, 2016. **50**(2): p. 1039-1045.
191. X. Fan, H. Liu, Y. Gao, Z. Zou, V.S. Craig, G. Zhang, and G. Liu, *Forward‐Osmosis Desalination with Poly (Ionic Liquid) Hydrogels as Smart Draw Agents.* Advanced Materials, 2016. **28**(21): p. 4156-4161.
192. Y. Mino, D. Ogawa, and H. Matsuyama, *Functional magnetic particles providing osmotic pressure as reusable draw solutes in forward osmosis membrane process.* Advanced Powder Technology, 2016. **27**(5): p. 2136-2144.

193. S.Y. Park, H.-W. Ahn, J.W. Chung, and S.-Y. Kwak, *Magnetic core-hydrophilic shell nanosphere as stability-enhanced draw solute for forward osmosis (FO) application.* Desalination, 2016. **397**: p. 22-29.
194. Q. Zhao, N. Chen, D. Zhao, and X. Lu, *Thermoresponsive magnetic nanoparticles for seawater desalination.* ACS applied materials & interfaces, 2013. **5**(21): p. 11453-11461.
195. J.-j. Kim, H. Kang, Y.-S. Choi, Y.A. Yu, and J.-C. Lee, *Thermo-responsive oligomeric poly (tetrabutylphosphonium styrenesulfonate) s as draw solutes for forward osmosis (FO) applications.* Desalination, 2016. **381**: p. 84-94.
196. D. Nakayama, Y. Mok, M. Noh, J. Park, S. Kang, and Y. Lee, *Lower critical solution temperature (LCST) phase separation of glycol ethers for forward osmotic control.* Physical Chemistry Chemical Physics, 2014. **16**(11): p. 5319-5325.
197. Q. Ge, J. Su, G.L. Amy, and T.-S. Chung, *Exploration of polyelectrolytes as draw solutes in forward osmosis processes.* Water research, 2012. **46**(4): p. 1318-1326.
198. E. Tian, C. Hu, Y. Qin, Y. Ren, X. Wang, X. Wang, P. Xiao, and X. Yang, *A study of poly (sodium 4-styrenesulfonate) as draw solute in forward osmosis.* Desalination, 2015. **360**: p. 130-137.
199. Y. Yang, M. Chen, S. Zou, X. Yang, T.E. Long, and Z. He, *Efficient recovery of polyelectrolyte draw solutes in forward osmosis towards sustainable water treatment.* Desalination, 2017. **422**: p. 134-141.
200. P. Zhao, B. Gao, S. Xu, J. Kong, D. Ma, H.K. Shon, Q. Yue, and P. Liu, *Polyelectrolyte-promoted forward osmosis process for dye wastewater treatment–exploring the feasibility of using polyacrylamide as draw solute.* Chemical Engineering Journal, 2015. **264**: p. 32-38.
201. M. Cho, S.H. Lee, D. Lee, D.P. Chen, I.-C. Kim, and M.S. Diallo, *Osmotically driven membrane processes: Exploring the potential of branched polyethyleneimine as draw solute using porous FO membranes with NF separation layers.* Journal of Membrane Science, 2016. **511**: p. 278-288.
202. M.S. Diallo, S. Christie, P. Swaminathan, J.H. Johnson, and W.A. Goddard, *Dendrimer enhanced ultrafiltration. 1. Recovery of Cu (II) from aqueous solutions using PAMAM dendrimers with ethylene diamine core and terminal NH2 groups.* Environmental science & technology, 2005. **39**(5): p. 1366-1377.
203. H.G. Zeweldi, L.A. Limjuco, A.P. Bendoy, H.-S. Kim, M.J. Park, H.K. Shon, E.M. Johnson, H. Lee, W.-J. Chung, and G.M. Nisola, *The potential of monocationic imidazolium-, phosphonium-, and ammonium-based hydrophilic ionic liquids as draw solutes for forward osmosis.* Desalination, 2018. **444**: p. 94-106.
204. S.K. Yen, M. Su, K.Y. Wang, and T.-S. Chung, *Study of draw solutes using 2-methylimidazole-based compounds in forward osmosis.* Journal of Membrane Science, 2010. **364**(1-2): p. 242-252.
205. Y. Cai, W. Shen, J. Wei, T.H. Chong, R. Wang, W.B. Krantz, A.G. Fane, and X. Hu, *Energy-efficient desalination by forward osmosis using responsive ionic liquid draw solutes.* Environmental Science: Water Research & Technology, 2015. **1**(3): p. 341-347.
206. Y. Cai, W. Shen, S.L. Loo, W.B. Krantz, R. Wang, A.G. Fane, and X. Hu, *Towards temperature driven forward osmosis desalination using Semi-IPN hydrogels as reversible draw agents.* Water research, 2013. **47**(11): p. 3773-3781.
207. D. Li, X. Zhang, J. Yao, G.P. Simon, and H. Wang, *Stimuli-responsive polymer hydrogels as a new class of draw agent for forward osmosis desalination.* Chemical Communications, 2011. **47**(6): p. 1710-1712.

208. D. Li, X. Zhang, G.P. Simon, and H. Wang, *Forward osmosis desalination using polymer hydrogels as a draw agent: Influence of draw agent, feed solution and membrane on process performance.* Water research, 2013. **47**(1): p. 209-215.
209. Z. Shen, A. Mellati, J. Bi, H. Zhang, and S. Dai, *A thermally responsive cationic nanogel-based platform for three-dimensional cell culture and recovery.* RSC Advances, 2014. **4**(55): p. 29146-29156.
210. R. Ou, H. Zhang, G.P. Simon, and H. Wang, *Microfiber-polymer hydrogel monolith as forward osmosis draw agent.* Journal of Membrane Science, 2016. **510**: p. 426-436.
211. A. Razmjou, G.P. Simon, and H. Wang, *Effect of particle size on the performance of forward osmosis desalination by stimuli-responsive polymer hydrogels as a draw agent.* Chemical engineering journal, 2013. **215**: p. 913-920.
212. X.-Z. Zhang, Y.-Y. Yang, and T.-S. Chung, *The influence of cold treatment on properties of temperature-sensitive poly (N-isopropylacrylamide) hydrogels.* Journal of colloid and interface science, 2002. **246**(1): p. 105-111.
213. A. Razmjou, M.R. Barati, G.P. Simon, K. Suzuki, and H. Wang, *Fast deswelling of nanocomposite polymer hydrogels via magnetic field-induced heating for emerging FO desalination.* Environmental science & technology, 2013. **47**(12): p. 6297-6305.
214. Y. Zeng, L. Qiu, K. Wang, J. Yao, D. Li, G.P. Simon, R. Wang, and H. Wang, *Significantly enhanced water flux in forward osmosis desalination with polymer-graphene composite hydrogels as a draw agent.* Rsc Advances, 2013. **3**(3): p. 887-894.
215. H. Rabiee, B. Jin, S. Yun, and S. Dai, *Gas-responsive cationic microgels for forward osmosis desalination.* Chemical Engineering Journal, 2018. **347**: p. 424-431.
216. H. Bai, Z. Liu, and D.D. Sun, *Highly water soluble and recovered dextran coated Fe3O4 magnetic nanoparticles for brackish water desalination.* Separation and purification technology, 2011. **81**(3): p. 392-399.
217. Q. Ge, J. Su, T.-S. Chung, and G. Amy, *Hydrophilic superparamagnetic nanoparticles: synthesis, characterization, and performance in forward osmosis processes.* Industrial & Engineering Chemistry Research, 2011. **50**(1): p. 382-388.
218. Y. Kim, S. Han, and S. Hong, *A feasibility study of magnetic separation of magnetic nanoparticle for forward osmosis.* Water Science and Technology, 2011. **64**(2): p. 469-476.
219. M.M. Ling and T.-S. Chung, *Novel dual-stage FO system for sustainable protein enrichment using nanoparticles as intermediate draw solutes.* Journal of Membrane Science, 2011. **372**(1-2): p. 201-209.
220. M.M. Ling, K.Y. Wang, and T.-S. Chung, *Highly water-soluble magnetic nanoparticles as novel draw solutes in forward osmosis for water reuse.* Industrial & Engineering Chemistry Research, 2010. **49**(12): p. 5869-5876.
221. M. MingáLing, *Facile synthesis of thermosensitive magnetic nanoparticles as "smart" draw solutes in forward osmosis.* Chemical communications, 2011. **47**(38): p. 10788-10790.
222. G. Sun, T.-S. Chung, N. Chen, X. Lu, and Q. Zhao, *Highly permeable aquaporin-embedded biomimetic membranes featuring a magnetic-aided approach.* RSC advances, 2013. **3**(24): p. 9178-9184.
223. H. Han, J.Y. Lee, and X. Lu, *Thermoresponsive nanoparticles+ plasmonic nanoparticles= photoresponsive heterodimers: Facile synthesis and sunlight-induced reversible clustering.* Chemical Communications, 2013. **49**(55): p. 6122-6124.
224. M. Noh, Y. Mok, S. Lee, H. Kim, S.H. Lee, G.-w. Jin, J.-H. Seo, H. Koo, T.H. Park, and Y. Lee, *Novel lower critical solution temperature phase transition materials effectively control osmosis by mild temperature changes.* Chemical Communications, 2012. **48**(32): p. 3845-3847.

225. M.M. Ling and T.-S. Chung, *Surface-dissociated nanoparticle draw solutions in forward osmosis and the regeneration in an integrated electric field and nanofiltration system.* Industrial & engineering chemistry research, 2012. **51**(47): p. 15463-15471.
226. M. Ahmed, R. Kumar, B. Garudachari, and J.P. Thomas, *Performance evaluation of a thermoresponsive polyelectrolyte draw solution in a pilot scale forward osmosis seawater desalination system.* Desalination, 2019. **452**: p. 132-140.
227. A. Inada, T. Takahashi, K. Kumagai, and H. Matsuyama, *Morpholine Derivatives as Thermoresponsive Draw Solutes for Forward Osmosis Desalination.* Industrial & Engineering Chemistry Research, 2019. **58**(27): p. 12253-12260.
228. W. Bingming, W. Huagen, L. Jianfeng, and X. Ziwen, *Experimental investigation on the performance of NH3/CO2 cascade refrigeration system with twin-screw compressor.* International Journal of Refrigeration, 2009. **32**(6): p. 1358-1365.
229. D. Jankovich and K. Osman, *A feasibility analysis of replacing the standard ammonia refrigeration device with the cascade NH3/CO2 refrigeration device in the food industry.* Thermal Science, 2015. **19**(5): p. 1821-1833.
230. V. Patel, D. Panchal, A. Prajapati, A. Mudgal, and P. Davies, *An efficient optimization and comparative analysis of cascade refrigeration system using NH3/CO2 and C3H8/CO2 refrigerant pairs.* International Journal of Refrigeration, 2019. **102**: p. 62-76.
231. S. Sawalha, J. Rogstam, and P.-O. Nilsson. *Laboratory tests of NH3/CO2 Cascade system for Supermarket Refrigeration*. in *IIR International Conferences, Commercial Refrigeration, Aug*. 2005.
232. G. Van Riessen, *NH3/CO2 supermarket refrigeration system with CO2 in the cooling and freezing section. Technical, energetic and economical issues*. 2004.
233. B. Wang, Z. Xing, and H. Wu, *Experimental study on the performance of a twin-screw CO2 compressor in NH3/CO2 cascade refrigeration system.* Proceedings of the Institution of Mechanical Engineers, Part A: Journal of Power and Energy, 2010. **224**(8): p. 1141-1146.
234. H. Strathmann, *Electrodialysis, a mature technology with a multitude of new applications.* Desalination, 2010. **264**(3): p. 268-288.
235. S. Al-Amshawee, M.Y.B.M. Yunus, A.A.M. Azoddein, D.G. Hassell, I.H. Dakhil, and H.A. Hasan, *Electrodialysis desalination for water and wastewater: A review.* Chemical Engineering Journal, 2020. **380**: p. 122231.
236. A. von Gottberg, *In Proceedings, American Water Works Assoc. Annual Conf.* Dallas TX (1998).
237. A. Campione, L. Gurreri, M. Ciofalo, G. Micale, A. Tamburini, and A. Cipollina, *Electrodialysis for water desalination: A critical assessment of recent developments on process fundamentals, models and applications.* Desalination, 2018. **434**: p. 121-160.
238. H. Strathmann, *Ion-exchange membrane separation processes*. 2004: Elsevier.
239. N. Kabay, M. Arda, I. Kurucaovali, E. Ersoz, H. Kahveci, M. Can, S. Dal, S. Kopuzlu, M. Haner, and M. Demircioglu, *Effect of feed characteristics on the separation performances of monovalent and divalent salts by electrodialysis.* Desalination, 2003. **158**(1-3): p. 95-100.
240. S. Mehdipour, V. Vatanpour, and H.-R. Kariminia, *Influence of ion interaction on lead removal by a polyamide nanofiltration membrane.* Desalination, 2015. **362**: p. 84-92.
241. D. Desai, E.S. Beh, S. Sahu, V. Vedharathinam, Q. van Overmeere, C.F. de Lannoy, A.P. Jose, A.R. Völkel, and J.B. Rivest, *Electrochemical desalination of seawater and hypersaline brines with coupled electricity storage.* ACS Energy Letters, 2018. **3**(2): p. 375-379.
242. W. Tian, X. Wang, C. Fan, and Z. Cui, *Optimal treatment of hypersaline industrial wastewater via bipolar membrane electrodialysis.* ACS Sustainable Chemistry & Engineering, 2019. **7**(14): p. 12358-12368.

243. F. Ilhan, H.A. Kabuk, U. Kurt, Y. Avsar, and M.T. Gonullu, *Recovery of mixed acid and base from wastewater with bipolar membrane electrodialysis—a case study.* Desalination and Water Treatment, 2016. **57**(11): p. 5165-5173.
244. J. Lin, W. Ye, J. Huang, B. Ricard, M.-C. Baltaru, B. Greydanus, S. Balta, J. Shen, M. Vlad, and A. Sotto, *Toward resource recovery from textile wastewater: dye extraction, water and base/acid regeneration using a hybrid NF-BMED process.* ACS Sustainable Chemistry & Engineering, 2015. **3**(9): p. 1993-2001.
245. B. Kim, R. Kwak, H.J. Kwon, M. Kim, B. Al-Anzi, G. Lim, and J. Han, *Purification of high salinity brine by multi-stage ion concentration polarization desalination.* Scientific reports, 2016. **6**: p. 31850.
246. B. Kim, H. Kwon, S.H. Ko, G. Lim, and J. Han, *Partial desalination of hypersaline brine by lab-scale ion concentration polarization device.* Desalination, 2017. **412**: p. 20-31.
247. R.K. McGovern, A.M. Weiner, L. Sun, C.G. Chambers, and S.M. Zubair, *On the cost of electrodialysis for the desalination of high salinity feeds.* Applied Energy, 2014. **136**: p. 649-661.
248. R.A. Tufa, Y. Noviello, G. Di Profio, F. Macedonio, A. Ali, E. Drioli, E. Fontananova, K. Bouzek, and E. Curcio, *Integrated membrane distillation-reverse electrodialysis system for energy-efficient seawater desalination.* Applied Energy, 2019. **253**: p. 113551.
249. R.K. McGovern and S.M. Zubair, *The cost effectiveness of electrodialysis for diverse salinity applications.* Desalination, 2014. **348**: p. 57-65.
250. V. Silva, E. Poiesz, and P. van der Heijden, *Industrial wastewater desalination using electrodialysis: evaluation and plant design.* Journal of applied electrochemistry, 2013. **43**(11): p. 1057-1067.
251. Q. Cheng and W. Pei, *Performance comparison on different liquid desiccants in the liquid desiccant air-conditioning using electrodialysis regeneration: LiCl and LiBr aqueous solutions.* International Journal of Refrigeration, 2019. **107**: p. 1-10.
252. J. Patek and J. Klomfar, *A computationally effective formulation of the thermodynamic properties of LiBr–H2O solutions from 273 to 500 K over full composition range.* International journal of refrigeration, 2006. **29**(4): p. 566-578.
253. W. Pei, Q. Cheng, S. Jiao, and L. Liu, *Performance evaluation of the electrodialysis regenerator for the lithium bromide solution with high concentration in the liquid desiccant air-conditioning system.* Energy, 2019. **187**: p. 115928.
254. B. Sun and X. Zhang, *Experimental study on liquid desiccant regeneration by photovoltaic electrodialysis.* Energy Procedia, 2019. **158**: p. 959-964.
255. A. Al-Jubainawi, Z. Ma, Y. Guo, L.D. Nghiem, P. Cooper, and W. Li, *Factors governing mass transfer during membrane electrodialysis regeneration of LiCl solution for liquid desiccant dehumidification systems.* Sustainable cities and society, 2017. **28**: p. 30-41.
256. G. Sposito and S.V. Mattigod, *On the chemical foundation of the sodium adsorption ratio.* Soil Science Society of America Journal, 1977. **41**(2): p. 323-329.
257. D.L. Suarez, J.D. Wood, and S.M. Lesch, *Effect of SAR on water infiltration under a sequential rain–irrigation management system.* agricultural water management, 2006. **86**(1-2): p. 150-164.
258. R.S. Ayers and D.W. Westcot, *Water quality for agriculture*. Vol. 29. 1985: Food and Agriculture Organization of the United Nations Rome.
259. D. Misra and S. Ghosh, *Evaporative cooling technologies for greenhouses: a comprehensive review.* Agricultural Engineering International: CIGR Journal, 2018. **20**(1): p. 1-15.
260. A. Gurubalan, M. Maiya, and P.J. Geoghegan, *A comprehensive review of liquid desiccant air conditioning system.* Applied Energy, 2019. **254**: p. 113673.

261. M.D. Afonso and M.N. de Pinho, *Transport of MgSO4, MgCl2, and Na2SO4 across an amphoteric nanofiltration membrane.* Journal of membrane science, 2000. **179**(1-2): p. 137-154.
262. Z. Murthy and L.B. Chaudhari, *Rejection behavior of nickel ions from synthetic wastewater containing Na2SO4, NiSO4, MgCl2 and CaCl2 salts by nanofiltration and characterization of the membrane.* Desalination, 2009. **247**(1-3): p. 610-622.
263. W. Li, C. Shi, A. Zhou, X. He, Y. Sun, and J. Zhang, *A positively charged composite nanofiltration membrane modified by EDTA for LiCl/MgCl2 separation.* Separation and Purification Technology, 2017. **186**: p. 233-242.
264. *ThermoFisher SCIENTIFIC, SAFETY DATA SHEET, Product Description: Lithium chloride, anhydrous. Accessed: 29-04-2022.* Retrieved from https://www.fishersci.co.uk/store/msds?partNumber=12367083&productDescription=1KG+Lithium+chloride%2C+99%25%2C+extra+pure&countryCode=GB&language=en
265. *ThermoFisher SCIENTIFIC, SAFETY DATA SHEET, Product Description: Lithium bromide. Accessed: 29-04-2022.* Retrieved from https://www.fishersci.co.uk/store/msds?partNumber=15234674&productDescription=10KG+Lithium+bromide%2C+99%2B%25%2C+for+analysis%2C+anhydrou&countryCode=GB&language=en
266. *Australian Industrial Chemicals Introduction Scheme. Lithium chloride: Human health tier II assessment. Acessed: 27/09/2023.* Retrieved from https://www.industrialchemicals.gov.au/sites/default/files/Lithium%20chloride_Human%20health%20tier%20II%20assessment.pdf
267. *ThermoFisher SCIENTIFIC, SAFETY DATA SHEET, Product Description: Calcium chloride. Accessed: 29-04-2022.* Retrieved from https://www.alfa.com/en/msds/?language=EN&subformat=CLP1&sku=L13191
268. G. Lychnos, *Feasibility of a solar panel-powered liquid desiccant cooling system for greenhouses*. 2010, Aston University.
269. N.H. Abu-Hamdeh and K.H. Almitani, *Solar liquid desiccant regeneration and nanofluids in evaporative cooling for greenhouse food production in Saudi Arabia.* Solar Energy, 2016. **134**: p. 202-210.
270. C. Kittas, T. Bartzanas, and A. Jaffrin, *Temperature gradients in a partially shaded large greenhouse equipped with evaporative cooling pads.* Biosystems Engineering, 2003. **85**(1): p. 87-94.
271. T.L. Oladosu, A.T. Baheta, and A.N. Oumer, *Desiccant solutions, membrane technologies, and regeneration techniques in liquid desiccant air conditioning system.* International Journal of Energy Research, 2021. **45**(6): p. 8420-8447.
272. W. Li and Y. Yao, *Thermodynamic analysis of internally-cooled membrane-based liquid desiccant dehumidifiers of different flow types.* International Journal of Heat and Mass Transfer, 2021. **166**: p. 120802.
273. B. Huang, K. Pu, P. Wu, D. Wu, and J. Leng, *Design, selection and application of energy recovery device in seawater desalination: A review.* Energies, 2020. **13**(16): p. 4150.
274. C. Stanghellini, *Transpiration of greenhouse crops: an aid to climate management*. 1987, IMAG.
275. J. Prenger, R. Fynn, and R. Hansen, *A comparison of four evapotranspiration models in a greenhouse environment.* Transactions of the ASAE, 2002. **45**(6): p. 1779.
276. F. Villarreal-Guerrero, M. Kacira, E. Fitz-Rodríguez, C. Kubota, G.A. Giacomelli, R. Linker, and A. Arbel, *Comparison of three evapotranspiration models for a greenhouse cooling strategy with natural ventilation and variable high pressure fogging.* Scientia Horticulturae, 2012. **134**: p. 210-221.

277. E.B. Smith, *Basic chemical thermodynamics*. Vol. 35. 2004: Imperial College Press.
278. *CAT PUMPS (U.K.) LTD, Pump Catalogue. Accessed: 08-01-2022.* 2018. Retrieved from http://www.www.catpumps.co.uk/products/pdfs/20043%20CAT%20Pump%20Catalog%20UK%2099CATUK001E.pdf
279. S. Bouzid-Lagha and Y. Matrouh, *Optimization of Energy Cost Seawater Desalinization by Reverse Osmosis: Case of Bousmail Station in Algeria.* Exergy for A Better Environment and Improved Sustainability 2: Applications, 2018: p. 739-749.
280. Y.A. Cengel, *Introduction to thermodynamics and heat transfer*. Vol. 846. 1997: McGraw-Hill New York.
281. *BLD Solar Europe GmbH. Datasheet Photovoltaic Modules. Accessed: 08-01-2022.* Retrieved from http://eprints.polsri.ac.id/4627/11/Solar%20Cell.pdf
282. *GEOCLIMA smart HVAC Solutions, TECHNICAL Data Sheet, GHA FC, AIR COOLED CHILLER WITH SCREW COMPRESSORS, AXIAL FANS AND FREE COOLING FOR OUTDOOR INSTALLATION. Accessed: 04-05-2022.* Retrieved from https://www.cooltherm.co.uk/uploads/files/SelDocsGeo/gha.pdf
283. *GEOCLIMA smart HVAC Solutions, TECHNICAL Data Sheet, VHH, WATER COOLED CHILLER WITH SCROLL OR RECIPROCATING COMPRESSORS FOR INDOOR INSTALLATION. Accessed: 04-05-2022.* Retrieved from https://www.cooltherm.co.uk/uploads/files/SelDocsGeo/vhh.pdf
284. *DAIKIN, Air cooled scroll inverter chiller EWAQ-BAWN/BAWP. Accessed: 04-05-2022.* Retrieved from https://www.daikin.eu/content/dam/document-library/catalogues/as/air-cooled-chiller/ewaq-bawn/EWAQ-BAWN_BAWP%20Product%20flyer_ECPEN15-422_1_Product%20Catalogues_English.pdf
285. *ENF Solar. BLD350-72M PV collector. Accessed: 26/09/2023.* Retrieved from https://www.enfsolar.com/pv/panel-datasheet/crystalline/23913
286. A. LaPotin, K.L. Schulte, M.A. Steiner, K. Buznitsky, C.C. Kelsall, D.J. Friedman, E.J. Tervo, R.M. France, M.R. Young, and A. Rohskopf, *Thermophotovoltaic efficiency of 40%.* Nature, 2022. **604**(7905): p. 287-291.
287. M. Salikandi, B. Ranjbar, E. Shirkhan, S.S. Priya, I. Thirunavukkarasu, and K. Sudhakar, *Recent trends in liquid desiccant materials and cooling systems: application, performance and regeneration characteristics.* Journal of Building Engineering, 2021. **33**: p. 101579.
288. R. Yang and P.-L. Wang, *The optimum glazing height of a glazed solar collector/regenerator for open-cycle absorption cooling.* Energy, 1994. **19**(9): p. 925-931.
289. J.-D. Liang, B.-H. Huang, Y.-C. Chiang, and S.-L. Chen, *Experimental investigation of a liquid desiccant dehumidification system integrated with shallow geothermal energy.* Energy, 2020. **191**: p. 116452.
290. P. Mazzei, F. Minichiello, and D. Palma, *HVAC dehumidification systems for thermal comfort: a critical review.* Applied Thermal Engineering, 2005. **25**(5-6): p. 677-707.
291. Y. Luo, S. Shao, H. Xu, and C. Tian, *Dehumidification performance of [EMIM] BF4.* Applied thermal engineering, 2011. **31**(14-15): p. 2772-2777.
292. Y.Y.L.X.L. Weiyi and F.C.Q. Xiling, *EXPERIMENTAL STUDY ON THE CHARACTERISTICS OF SOLAR POWERED LIQUID DEHUMIDIFICATION SYSTEM [J].* ACTA ENERGIAE SOLARIS SINICA, 2000. **2**.
293. J. Zhi, C. Dong, M. Guo, R. Qi, and L.-z. Zhang, *Wettability and performance enhancement with durable super-hydrophilic surfaces for plastic liquid desiccant dehumidification systems.* Energy and Buildings, 2019. **187**: p. 77-85.

294. A.Y. Khan, *Sensitivity analysis and component modelling of a packed‐type liquid desiccant system at partial load operating conditions.* International Journal of Energy Research, 1994. **18**(7): p. 643-655.
295. I.D. Zaytsev and G.G. Aseyev, *Properties of aqueous solutions of electrolytes*. 1992: CRC press.
296. *Bry-Air (Asia) Pvt. Ltd. Moisture and Humidity Control Solution in Pharmaceutical Industry.* Retrieved from https://www.bryair.com/general-pharmaceutical/
297. C.L. Ritt, T. Stassin, D.M. Davenport, R.M. DuChanois, I. Nulens, Z. Yang, A. Ben-Zvi, N. Segev-Mark, M. Elimelech, and C.Y. Tang, *The open membrane database: Synthesis–structure–performance relationships of reverse osmosis membranes.* Journal of Membrane Science, 2022. **641**: p. 119927.
298. A. Ahmad, L. Tan, and S.A. Shukor, *Modeling of the retention of atrazine and dimethoate with nanofiltration.* Chemical Engineering Journal, 2009. **147**(2-3): p. 280-286.
299. C.P. Koutsou and A.J. Karabelas, *Shear stresses and mass transfer at the base of a stirred filtration cell and corresponding conditions in narrow channels with spacers.* Journal of membrane science, 2012. **399**: p. 60-72.
300. I.M. Abdulagatov, A.B. Zeinalova, and N.D. Azizov, *Experimental viscosity B-coefficients of aqueous LiCl solutions.* Journal of molecular liquids, 2006. **126**(1-3): p. 75-88.
301. *LiBrSSC (aqueous lithium bromide) Property Routines, Sorption Systems Consortium at the University of Maryland*.
302. S. Phang and R. Stokes, *Density, viscosity, conductance, and transference number of concentrated aqueous magnesium chloride at 25 C.* Journal of Solution Chemistry, 1980. **9**(7): p. 497-505.
303. V. Lindberg, *Uncertainties and error propagation.* Manual on Uncertainties, Graphing and the Vernier Caliper, Part I. Rochester Institute of Technology, New York, USA., 2000.
304. *STERLITECH Corporation HP4750 ASSEMBLY & OPERATION MANUAL.* 2018.
305. A.O. Olufade and C.J. Simonson, *Characterization of the evolution of crystallization fouling in membranes.* ACS omega, 2018. **3**(12): p. 17188-17198.
306. A.O. Olufade and C.J. Simonson, *Detection of crystallization fouling in a liquid-to-air membrane energy exchanger.* Experimental Thermal and Fluid Science, 2018. **92**: p. 33-45.
307. Z. Wang, M.U. Hassan, F. Nadeem, L. Wu, F. Zhang, and X. Li, *Magnesium fertilization improves crop yield in most production systems: A meta-analysis.* Frontiers in plant science, 2020: p. 1727.
308. L. Wang, C. Violet, R.M. DuChanois, and M. Elimelech, *Derivation of the theoretical minimum energy of separation of desalination processes.* Journal of Chemical Education, 2020. **97**(12): p. 4361-4369.
309. S. Maiti, P. Kane, P. Pandit, K. Singha, and S. Maity, *Zero liquid discharge wastewater treatment technologies*, in *Sustainable Technologies for Textile Wastewater Treatments*. 2021, Elsevier. p. 209-234.
310. R. Schwantes, K. Chavan, D. Winter, C. Felsmann, and J. Pfafferott, *Techno-economic comparison of membrane distillation and MVC in a zero liquid discharge application.* Desalination, 2018. **428**: p. 50-68.
311. M. Turek, K. Mitko, P. Skóra, P. Dydo, A. Jakóbik-Kolon, A. Warzecha, and K. Tyrała, *Improving the Performance of a Salt Production Plant by Using Nanofiltration as a Pretreatment.* Membranes, 2022. **12**(12): p. 1191.
312. M. Mickley, *Survey of high-recovery and zero liquid discharge technologies for water utilities*. 2008: WateReuse Foundation.

313. B. Caldecott, L. Kruitwagen, G. Dericks, D.J. Tulloch, I. Kok, and J. Mitchell, *Stranded Assets and Thermal Coal: An analysis of environment-related risk exposure.* Stranded Assets Programme, SSEE, University of Oxford, 2016.
314. D. Xevgenos, G. Gzyl, K. Panteleaki Tourkodimitri, K. Mitko, G. Tsalidis, A. Skalny, M. Mortou, D. Sapoutzi, and M. Turek. *Redesigning the coal mine wastewater treatment to enable transition to circular economy practices: The ZERO BRINE and Dębieńsko case studies*. in *Proceedings of the 16th Conference on Sustainable Development of Energy, Water, and Environment Systems (SDEWES)*. 2021.
315. K. Mitko and M. Turek, *Membrane-Based Solutions for the Polish Coal Mining Industry.* Membranes, 2021. **11**(8): p. 638.
316. K. Mitko, M. Turek, H. Jaroszek, E. Bernacka, M. Sambor, P. Skóra, and P. Dydo, *Pilot studies on circular economy solution for the coal mining sector.* Water Resources and Industry, 2021. **26**: p. 100161.
317. N.D. Pawar, S. Harris, K. Mitko, and G. Korevaar, *Valorization of coal mine effluents—Challenges and economic opportunities.* Water Resources and Industry, 2022. **28**: p. 100179.
318. G.A. Tsalidis, K.P. Tourkodimitri, K. Mitko, G. Gzyl, A. Skalny, J. Posada, and D. Xevgenos, *Assessing the environmental performance of a novel coal mine brine treatment technique: A case in Poland.* Journal of Cleaner Production, 2022. **358**: p. 131973.
319. M. Yaqub and W. Lee, *Zero-liquid discharge (ZLD) technology for resource recovery from wastewater: A review.* Science of the total environment, 2019. **681**: p. 551-563.
320. A.A. Al-Hajouri, A.S. Al-Amoudi, and A.M. Farooque, *Long term experience in the operation of nanofiltration pretreatment unit for seawater desalination at SWCC SWRO plant.* Desalination and water treatment, 2013. **51**(7-9): p. 1861-1873.
321. A. Hassan, A. Farooque, A. Jamaluddin, A. Al-Amoudi, M. Al-Sofi, A. Al-Rubaian, N. Kither, I. Al-Tisan, and A. Rowaili, *A demonstration plant based on the new NF—SWRO process.* Desalination, 2000. **131**(1-3): p. 157-171.
322. M. Park, J. Park, E. Lee, J. Khim, and J. Cho, *Application of nanofiltration pretreatment to remove divalent ions for economical seawater reverse osmosis desalination.* Desalination and water treatment, 2016. **57**(44): p. 20661-20670.
323. Y. Song, B. Su, X. Gao, and C. Gao, *Investigation on high NF permeate recovery and scaling potential prediction in NF–SWRO integrated membrane operation.* Desalination, 2013. **330**: p. 61-69.
324. E. Laskowska, M. Turek, K. Mitko, and P. Dydo, *Concentration of mine saline water in high-efficiency hybrid RO-NF system.* Desalination and Water Treatment, 2018. **128**: p. 414-420.
325. T.H. Chong and W.B. Krantz, *Process economics and operating strategy for the energy-efficient reverse osmosis (EERO) process.* Desalination, 2018. **443**: p. 70-84.
326. M. Turek, E. Laskowska, K. Mitko, M. Chorążewska, P. Dydo, K. Piotrowski, and A. Jakobik-Kolon, *Application of nanofiltration and electrodialysis for improved performance of a salt production plant.* Desalination and Water Treatment, 2017. **64**: p. 244-250.
327. K.M. Shah, I.H. Billinge, X. Chen, H. Fan, Y. Huang, R.K. Winton, and N.Y. Yip, *Drivers, challenges, and emerging technologies for desalination of high-salinity brines: A critical review.* Desalination, 2022. **538**: p. 115827.
328. N. Ghaffour, J. Bundschuh, H. Mahmoudi, and M.F. Goosen, *Renewable energy-driven desalination technologies: A comprehensive review on challenges and potential applications of integrated systems.* Desalination, 2015. **356**: p. 94-114.

329. K. Mansuriya, B.D. Raja, and V.K. Patel, *Experimental assessment of a small scale hybrid liquid desiccant dehumidification incorporated vapor compression refrigeration system: An energy saving approach.* Applied Thermal Engineering, 2020. **174**: p. 115288.
330. A. Al-Karaghouli and L.L. Kazmerski, *Energy consumption and water production cost of conventional and renewable-energy-powered desalination processes.* Renewable and Sustainable Energy Reviews, 2013. **24**: p. 343-356.
331. J. Gerendás and H. Führs, *The significance of magnesium for crop quality.* Plant and Soil, 2013. **368**: p. 101-128.
332. M. Ishfaq, Y. Wang, M. Yan, Z. Wang, L. Wu, C. Li, and X. Li, *Physiological essence of magnesium in plants and its widespread deficiency in the farming system of china.* Frontiers in Plant Science, 2022. **13**.
333. C. Xiao, L. Xiao, C. Gao, and L. Zeng, *Thermodynamic study on removal of magnesium from lithium chloride solutions using phosphate precipitation method.* Separation and Purification Technology, 2015. **156**: p. 582-587.
334. D. Shi, B. Cui, L. Li, M. Xu, Y. Zhang, X. Peng, L. Zhang, F. Song, and L. Ji, *Removal of calcium and magnesium from lithium concentrated solution by solvent extraction method using D2EHPA.* Desalination, 2020. **479**: p. 114306.
335. N. Mahmud, D.V.F. Alvarez, M.H. Ibrahim, M.H. El-Naas, and D.V. Esposito, *Magnesium recovery from desalination reject brine as pretreatment for membraneless electrolysis.* Desalination, 2022. **525**: p. 115489.
336. F. Vassallo, D. La Corte, N. Cancilla, A. Tamburini, M. Bevacqua, A. Cipollina, and G. Micale, *A pilot-plant for the selective recovery of magnesium and calcium from waste brines.* Desalination, 2021. **517**: p. 115231.
337. C.P. Koutsou, S.G. Yiantsios, and A.J. Karabelas, *A numerical and experimental study of mass transfer in spacer-filled channels: Effects of spacer geometrical characteristics and Schmidt number.* Journal of Membrane Science, 2009. **326**(1): p. 234-251.
338. *Dow Water Solutions, FILMTEC™ Membranes product catalog. Accessed: 01-01-2023.* Retrieved from https://www.lenntech.com/Data-sheets/Filmtec-Reverse-Osmosis-Product-Catalog-L.pdf
339. A. Haidari, S. Heijman, and W. van der Meer, *Visualization of hydraulic conditions inside the feed channel of Reverse Osmosis: A practical comparison of velocity between empty and spacer-filled channel.* Water research, 2016. **106**: p. 232-241.
340. K. Mitko, E. Laskowska, M. Turek, P. Dydo, and K. Piotrowski, *Scaling risk assessment in nanofiltration of mine waters.* Membranes, 2020. **10**(10): p. 288.
341. S. Déon, P. Dutournié, P. Fievet, L. Limousy, and P. Bourseau, *Concentration polarization phenomenon during the nanofiltration of multi-ionic solutions: Influence of the filtrated solution and operating conditions.* Water research, 2013. **47**(7): p. 2260-2272.
342. J.R. Werber, A. Deshmukh, and M. Elimelech, *The critical need for increased selectivity, not increased water permeability, for desalination membranes.* Environmental Science & Technology Letters, 2016. **3**(4): p. 112-120.
343. C. Tang, Y. Zhao, R. Wang, C. Hélix-Nielsen, and A. Fane, *Desalination by biomimetic aquaporin membranes: Review of status and prospects.* Desalination, 2013. **308**: p. 34-40.
344. S. Gravelle, L. Joly, F. Detcheverry, C. Ybert, C. Cottin-Bizonne, and L. Bocquet, *Optimizing water permeability through the hourglass shape of aquaporins.* Proceedings of the National Academy of Sciences, 2013. **110**(41): p. 16367-16372.
345. J. Vrouwenvelder, C. Hinrichs, W. Van der Meer, M. Van Loosdrecht, and J. Kruithof, *Pressure drop increase by biofilm accumulation in spiral wound RO and NF membrane systems: role of substrate concentration, flow velocity, substrate load and flow direction.* Biofouling, 2009. **25**(6): p. 543-555.

346. L. Wang, T. Cao, J.E. Dykstra, S. Porada, P. Biesheuvel, and M. Elimelech, *Salt and water transport in reverse osmosis membranes: beyond the solution-diffusion model.* Environmental Science & Technology, 2021. **55**(24): p. 16665-16675.
347. K.M. Persson, V. Gekas, and G. Trägårdh, *Study of membrane compaction and its influence on ultrafiltration water permeability.* Journal of membrane science, 1995. **100**(2): p. 155-162.
348. D.M. Davenport, L. Wang, E. Shalusky, and M. Elimelech, *Design principles and challenges of bench-scale high-pressure reverse osmosis up to 150 bar.* Desalination, 2021. **517**: p. 115237.
349. M. Date, V. Patyal, D. Jaspal, A. Malviya, and K. Khare, *Zero liquid discharge technology for recovery, reuse, and reclamation of wastewater: A critical review.* Journal of Water Process Engineering, 2022. **49**: p. 103129.
350. Y. Liang, X. Lin, X. Kong, Q. Duan, P. Wang, X. Mei, and J. Ma, *Making waves: Zero liquid discharge for sustainable industrial effluent management.* Water, 2021. **13**(20): p. 2852.
351. L.I. Qrenawi and A. Abuhabib, *A review on sources, types, mechanisms, characteristics, impacts and control strategies of fouling in RO membrane systems.* Water Treat, 2020. **208**: p. 43-69.
352. N.N.R. Ahmad, A.W. Mohammad, E. Mahmoudi, W.L. Ang, C.P. Leo, and Y.H. Teow, *An Overview of the Modification Strategies in Developing Antifouling Nanofiltration Membranes.* Membranes, 2022. **12**(12): p. 1276.
353. H.-J. Lee, M.A. Halali, T. Baker, S. Sarathy, and C.-F. de Lannoy, *A comparative study of RO membrane scale inhibitors in wastewater reclamation: Antiscalants versus pH adjustment.* Separation and Purification Technology, 2020. **240**: p. 116549.
354. A. Sweity, T.R. Zere, I. David, S. Bason, Y. Oren, Z. Ronen, and M. Herzberg, *Side effects of antiscalants on biofouling of reverse osmosis membranes in brackish water desalination.* Journal of Membrane Science, 2015. **481**: p. 172-187.
355. M. Ahmed, M.O. Mavukkandy, A. Giwa, M. Elektorowicz, E. Katsou, O. Khelifi, V. Naddeo, and S.W. Hasan, *Recent developments in hazardous pollutants removal from wastewater and water reuse within a circular economy.* NPJ Clean Water, 2022. **5**(1): p. 12.
356. A. Antony, J.H. Low, S. Gray, A.E. Childress, P. Le-Clech, and G. Leslie, *Scale formation and control in high pressure membrane water treatment systems: A review.* Journal of membrane science, 2011. **383**(1-2): p. 1-16.
357. A. Controls, *Understanding and Using VPD.* Argus Application Note, Argus Control Systems LTD, CANADA, 2009.
358. R. Shamshiri, H. Che Man, A. Zakaria, P.V. Beveren, W. Wan Ismail, and D. Ahmad. *Membership function model for defining optimality of vapor pressure deficit in closed-field cultivation of tomato*. in *III International Conference on Agricultural and Food Engineering 1152*. 2016.
359. H.E. Beck, N.E. Zimmermann, T.R. McVicar, N. Vergopolan, A. Berg, and E.F. Wood, *Present and future Köppen-Geiger climate classification maps at 1-km resolution.* Scientific data, 2018. **5**(1): p. 1-12.
360. I. Hamdi, S. Kooli, A. Elkhadraoui, Z. Azaizia, F. Abdelhamid, and A. Guizani, *Experimental study and numerical modeling for drying grapes under solar greenhouse.* Renewable Energy, 2018. **127**: p. 936-946.
361. O. Asa'd, V.I. Ugursal, and N. Ben-Abdallah, *Investigation of the energetic performance of an attached solar greenhouse through monitoring and simulation.* Energy for Sustainable Development, 2019. **53**: p. 15-29.
362. D. Jani, M. Mishra, and P.K. Sahoo, *Performance analysis of a solid desiccant assisted hybrid space cooling system using TRNSYS.* Journal of Building Engineering, 2018. **19**: p. 26-35.

363. E.W.D.A. 10-12-2022. Retrieved from https://energyplus.net/weather
364. *Agra Tech, Inc, Commercial Greenhouse Manufacturer. Accessed: 24-08-2023.* Retrieved from http://agratech.com/blog-commercial-greenhouse-manufacturer.html
365. *GrowSpan, Commercial Series S-500. Accessed: 24-08-2023.* Retrieved from https://www.growspan.com/structures/commercial-series/s-500/
366. *Gothic Arch Greenhouses, Commercial Greenhouses. Accessed: 24-08-2023.* Retrieved from https://www.gothicarchgreenhouses.com/commercialgreenhouses.html
367. *GGS Structures, GGS Greenhouse. Accessed: 24-08-2023.* Retrieved from https://ggs-greenhouse.com/
368. *Alibaba. Greenhouse Sandwich Panel. Accessed: 24-08-2023.* Retrieved from https://www.alibaba.com/showroom/greenhouse-sandwich-panel.html
369. *Mornglass. Greenhouse Glass Types. Accessed: 24-08-2023.* Retrieved from https://www.mornglass.com/greenhouse-glass-types.html
370. *New South Wales Department of Primary Industries. Greenhouse Structures and Technology: Ventilation. Accessed: 24-08-2023.* Retrieved from https://www.dpi.nsw.gov.au/agriculture/horticulture/greenhouse/structures-and-technology/ventilation
371. S.J. Acquah, H. Yan, C. Zhang, G. Wang, B. Zhao, H. Wu, and H. Zhang, *Application and evaluation of Stanghellini model in the determination of crop evapotranspiration in a naturally ventilated greenhouse.* International Journal of Agricultural and Biological Engineering, 2018. **11**(6): p. 95-103.
372. *World sea water temperatures. Accessed: 14/04/2023.* Retrieved from https://seatemperature.info/
373. I.M.A. Aljubury and H.D.a. Ridha, *Enhancement of evaporative cooling system in a greenhouse using geothermal energy.* Renewable energy, 2017. **111**: p. 321-331.
374. I. Tsafaras, J. Campen, C. Stanghellini, H. De Zwart, W. Voogt, K. Scheffers, A. Al Harbi, and K. Al Assaf, *Intelligent greenhouse design decreases water use for evaporative cooling in arid regions.* Agricultural Water Management, 2021. **250**: p. 106807.
375. *1380mm Heavy Hammer Exhaust Fan for Chicken House/Greenhouse/Poultry Farm Cooling Fan, Made-in-China. Accessed: 24/04/2023.* Retrieved from https://cncoolingpad.en.made-in-china.com/product/SZiTsCAjScpq/China-1380mm-Heavy-Hammer-Exhaust-Fan-for-Chicken-House-Greenhouse-Poultry-Farm-Cooling-Fan.html
376. M. Camporese and M. Abou Najm, *Not All Light Spectra Were Created Equal: Can We Harvest Light for Optimum Food‐Energy Co‐Generation?* Earth's Future, 2022. **10**(12): p. e2022EF002900.
377. K.R. Patil, A.D. Tripathi, G. Pathak, and S.S. Katti, *Thermodynamic properties of aqueous electrolyte solutions. 2. Vapor pressure of aqueous solutions of sodium bromide, sodium iodide, potassium chloride, potassium bromide, potassium iodide, rubidium chloride, cesium chloride, cesium bromide, cesium iodide, magnesium chloride, calcium chloride, calcium bromide, calcium iodide, strontium chloride, strontium bromide, strontium iodide, barium chloride, and barium bromide.* Journal of chemical and engineering data, 1991. **36**(2): p. 225-230.
378. *TESSLibs 17 Component Libraries for the TRNSYS Simulation Environment, Volume 06, HVAC Library Mathematical Reference, TESS – Thermal Energy Systems Specialists. Accessed: 08-01-2022.* Retrieved from http://www.trnsys.com
379. *Occidental Chemical Corporation. Calcium Chloride A Guide to Physical Properties. Accessed: 08-04-2022*.

380. G. Perron, A. Roux, and J.E. Desnoyers, *Heat capacities and volumes of NaCl, MgCl2, CaCl2, and NiCl2 up to 6 molal in water.* Canadian Journal of Chemistry, 1981. **59**(21): p. 3049-3054.
381. A. Zaltash and M.R. Ally, *Refractive indexes of aqueous lithium bromide solutions.* Journal of Chemical and Engineering Data, 1992. **37**(1): p. 110-113.
382. V. Gekas, C. Gonzalez, A. Sereno, A. Chiralt, and P. Fito, *Mass transfer properties of osmotic solutions. I. Water activity and osmotic pressure.* International Journal of Food Properties, 1998. **1**(2): p. 95-112.

Appendix 1: Modelling and validation of the dehumidifier

The moisture absorption is a natural process which equilibrates the vapour pressures of the air and the LD, meaning that a higher dehumidification effectiveness is achieved when the vapour pressure difference is high. For example, the vapour pressure of air ($P_{vap,air}$) at T=30 °C and RH=70% is equal to 2.972 kPa, whereas the vapour pressure of $CaCl_2$ as the LD ($P_{vap,LD}$) at temperatures of 25 and 35 °C and weight concentrations of 25 and 35 wt.% (290 and 430 g/L) is between 1.614 and 4.235 kPa (see Table A1-1). If $P_{vap,LD}$ is higher than $P_{vap,air}$, then the air will absorb moisture from the LD.

Table A1-1. Vapour pressures of $CaCl_2$ as the LD ($P_{vap,LD}$) at temperatures of 25 and 35 °C and weight concentrations of 25 and 35 wt.% (290 and 430 g/L), using the interpolation taken from Patil et al. [377].

$P_{vap,LD}$ [kPa]	25 °C	35 °C
25 wt.%	2.365	4.235
35 wt.%	1.614	2.941

The dehumidifier (HMX) model calculates the outlet conditions of the air and the LD as it follows:

1) Determine input conditions of air and LD

For the air:

- $\dot{m}_{\mathrm{Air}}^{\mathrm{in}}$, mass flow of air entering the HMX [kg/s]
- $T_{\mathrm{Air}}^{\mathrm{in}}$, temperature of air entering the HMX [°C]
- $RH_{\mathrm{Air}}^{\mathrm{in}}$, relative humidity of air entering the HMX
- The enthalpy ($h_{\mathrm{Air}}^{\mathrm{in}}$) [kJ/kg] and the absolute humidity ($x_{\mathrm{Air}}^{\mathrm{in}}$) [$g_v/kg_a$] of air can be calculated from $T_{\mathrm{Air}}^{\mathrm{in}}$ and $RH_{\mathrm{Air}}^{\mathrm{in}}$
- $\dot{m}_{\mathrm{d,Air}}^{\mathrm{in}}$, mass flow of dry air entering the HMX [kg/s], calculated as:

$$\dot{m}_{\mathrm{d,Air}}{}^{\mathrm{in}} = \dot{m}_{\mathrm{Air}}{}^{\mathrm{in}}\left(1 - \frac{1}{10^{-3}x_{\mathrm{Air}}{}^{\mathrm{in}} + 1}\right) \quad (1\text{-}1)$$

- $\dot{m}_{\mathrm{v,Air}}{}^{\mathrm{in}}$, mass flow of moisture entering the HMX [kg/s], calculated as:

$$\dot{m}_{\mathrm{v,Air}}{}^{\mathrm{in}} = \dot{m}_{\mathrm{Air}}{}^{\mathrm{in}} - \dot{m}_{\mathrm{d,Air}}{}^{\mathrm{in}} \quad (1\text{-}2)$$

For the LD:

- $\dot{m}_{\mathrm{LD}}{}^{\mathrm{in}}$, mass flow of LD entering the HMX [kg/s]
- $T_{\mathrm{LD}}{}^{\mathrm{in}}$, temperature of LD entering the HMX [°C]
- $wt_{\mathrm{LD}}{}^{\mathrm{in}}$, weight concentration of LD entering the HMX [wt.%]

2) Calculate the effectiveness of the evaporative cooling pad for LDAC ($\varepsilon_{\mathrm{deh}}$).

$$\varepsilon_{\mathrm{deh}} = -0.0333\left(T_{\mathrm{Air}}{}^{\mathrm{in}} - T_{\mathrm{LD}}{}^{\mathrm{in}}\right) + 0.9667 \quad (1\text{-}3)$$

The proposed equation for $\varepsilon_{\mathrm{deh}}$ gave results in agreement with experiments using an evaporative cooling pad. Future studies could improve the calculation of $\varepsilon_{\mathrm{deh}}$ by also accounting for the geometry of the evaporative cooling pad and other operating parameters.

3) Assume that the outlet LD temperature ($T_{\mathrm{LD}}{}^{\mathrm{in}}$) is equal to the inlet temperature and calculate the outlet air temperature ($T_{\mathrm{Air}}{}^{\mathrm{out}}$) as the mean temperature (between inlet and outlet) of the LD. This calculation is used by TRNSYS® software [378] and agrees with Koronaki et al. experiments [28].

$$T_{\mathrm{Air}}{}^{\mathrm{out}} = \frac{T_{\mathrm{LD}}{}^{\mathrm{out}} + T_{\mathrm{LD}}{}^{\mathrm{in}}}{2} \quad (1\text{-}4)$$

4) Assume that the outlet vapour pressures of the air (${P_{\mathrm{vap,Air}}}^{\mathrm{out}}$) [kPa] and the LD (${P_{\mathrm{vap,LD}}}^{\mathrm{out}}$) [kPa] are equal to their inlet ${P_{\mathrm{vap,Air}}}^{\mathrm{in}}$ and ${P_{\mathrm{vap,LD}}}^{\mathrm{in}}$, respectively. $P_{\mathrm{vap,LD}}$ is calculated based on [377] while $P_{\mathrm{vap,air}}$ as:

$$P_{\mathrm{vap,air}} = 4042.9 \exp\left(23.57712 - \frac{4042.9}{T_{\mathrm{Air}} + 237.57}\right)\frac{RH_{\mathrm{Air}}}{100} \tag{1-5}$$

5) Start a while loop for $\dot{m}_{\mathrm{v}}$ going from 0 to ${\dot{m}_{\mathrm{v,Air}}}^{\mathrm{in}}$ with an increment step $\dot{m}_{\mathrm{v,step}}$. By increasing $\dot{m}_{\mathrm{v}}$, ${P_{\mathrm{vap,Air}}}^{\mathrm{out}}$ and ${P_{\mathrm{vap,LD}}}^{\mathrm{out}}$ change. The while loop is implemented until the difference between ${P_{\mathrm{vap,Air}}}^{\mathrm{out}}$ and ${P_{\mathrm{vap,LD}}}^{\mathrm{out}}$ becomes zero. Therefore, the while loop is as follows:

while ${P_{\mathrm{vap,LD}}}^{\mathrm{out}} < {P_{\mathrm{vap,Air}}}^{\mathrm{out}}$

a) Calculate the new moisture absorption rate [kg/s]:

$$\dot{m}_{\mathrm{v,new}} = \dot{m}_{\mathrm{v}} + \dot{m}_{\mathrm{v,step}} \tag{1-6}$$

b) Calculate the outlet flows of air (${\dot{m}_{\mathrm{Air}}}^{\mathrm{out}}$) and LD (${\dot{m}_{\mathrm{LD}}}^{\mathrm{out}}$):

$${\dot{m}_{\mathrm{Air}}}^{\mathrm{out}} = {\dot{m}_{\mathrm{Air}}}^{\mathrm{in}} - \dot{m}_{\mathrm{v,step}} \tag{1-7}$$

$${\dot{m}_{\mathrm{LD}}}^{\mathrm{out}} = {\dot{m}_{\mathrm{LD}}}^{\mathrm{in}} + \dot{m}_{\mathrm{v,step}} \tag{1-8}$$

c) Calculate the new outlet LD weight concentration [wt.%]:

$${wt_{\mathrm{LD}}}^{\mathrm{out}} = \frac{{\dot{m}_{\mathrm{LD}}}^{\mathrm{in}}\, {wt_{\mathrm{LD}}}^{\mathrm{in}}}{{\dot{m}_{\mathrm{LD}}}^{\mathrm{in}} + \dot{m}_{\mathrm{v,new}}} \tag{1-9}$$

d) Calculate the outlet air absolute humidity [g_v/kg_a]:

$${x_{\mathrm{Air}}}^{\mathrm{out}} = 10^3 \frac{{\dot{m}_{\mathrm{v,Air}}}^{\mathrm{in}} - \dot{m}_{\mathrm{v,new}}}{({\dot{m}_{\mathrm{Air}}}^{\mathrm{in}} - {\dot{m}_{\mathrm{v,Air}}}^{\mathrm{in}})} \tag{1-10}$$

e) The enthalpy (${h_{\mathrm{Air}}}^{\mathrm{out}}$) and the relative humidity (${RH_{\mathrm{Air}}}^{\mathrm{out}}$) of the outlet air can be calculated from ${T_{\mathrm{Air}}}^{\mathrm{out}}$ and ${x_{\mathrm{Air}}}^{\mathrm{out}}$. Then, the heat difference between the inlet and outlet air (Q_{Air}) [kW_{th}] is calculated as:

$$Q_{\mathrm{Air}} = {\dot{m}_{\mathrm{Air}}}^{\mathrm{in}} {h_{\mathrm{Air}}}^{\mathrm{in}} - {\dot{m}_{\mathrm{Air}}}^{\mathrm{out}} {h_{\mathrm{Air}}}^{\mathrm{out}} \tag{1-11}$$

f) Calculate the heat capacity of the inlet LD (${h_{\mathrm{p,LD}}}^{\mathrm{in}}$) [kJ/(kg K)] and outlet LD (${h_{\mathrm{p,LD}}}^{\mathrm{out}}$) [kJ/(kg K)]. The heat capacity depends on the LD temperature and weight concentration. For $CaCl_2$, this can be calculated using data from [379]. Then, the outlet LD temperature ${T_{\mathrm{LD}}}^{\mathrm{out}}$ [°C] is calculated as:

$${T_{\mathrm{LD}}}^{\mathrm{out}} = \frac{Q_{\mathrm{Air}} + {\dot{m}_{\mathrm{LD}}}^{\mathrm{in}} {h_{\mathrm{p,LD}}}^{\mathrm{in}} ({T_{\mathrm{LD}}}^{\mathrm{in}} + 273.15)}{{\dot{m}_{\mathrm{LD}}}^{\mathrm{out}} {h_{\mathrm{p,LD}}}^{\mathrm{out}}} - 273.15 \tag{1-12}$$

g) The outlet LD vapour pressure (${P_{\mathrm{vap,LD}}}^{\mathrm{out}}$) can be calculated from ${T_{\mathrm{LD}}}^{\mathrm{out}}$ and ${wt_{\mathrm{LD}}}^{\mathrm{out}}$, based on [377].

h) Calculate the idealised outlet air temperature (${T_{\mathrm{Air,id}}}^{\mathrm{out}}$) [°C] and the real air temperature when accounting for the effectiveness of the evaporative cooling pad (${T_{\mathrm{Air}}}^{\mathrm{out}}$) [°C], as:

$${T_{\mathrm{Air,id}}}^{\mathrm{out}} = \frac{{T_{\mathrm{LD}}}^{\mathrm{out}} + {T_{\mathrm{LD}}}^{\mathrm{in}}}{2} \tag{1-13}$$

$${T_{\mathrm{Air}}}^{\mathrm{out}} = {T_{\mathrm{Air}}}^{\mathrm{in}} - \varepsilon_{\mathrm{deh}} ({T_{\mathrm{Air}}}^{\mathrm{in}} - {T_{\mathrm{Air,id}}}^{\mathrm{out}}) \tag{1-14}$$

i) The outlet air vapour pressure ($P_{\mathrm{vap,air}}{}^{\mathrm{out}}$) can be calculated from $T_{\mathrm{Air}}{}^{\mathrm{out}}$ and $x_{\mathrm{Air}}{}^{\mathrm{out}}$. Note that $T_{\mathrm{Air}}{}^{\mathrm{out}}$ is referred to as $T_{\mathrm{out}}{}^{\mathrm{deh}}$ in Figure 3-1. Here the terminology is different to distinguish it from $T_{\mathrm{LD}}{}^{\mathrm{out}}$.

6) If $P_{\mathrm{vap,LD}}{}^{\mathrm{out}} = P_{\mathrm{vap,Air}}{}^{\mathrm{out}}$, end the while loop. Otherwise, return to the beginning of the while loop. With this method, the outlet air temperature may converge to a certain value (Figure A1-1), but it may also never converge. For example, this method does not converge when $\dot{m}_{\mathrm{Air}}{}^{\mathrm{in}}$ is more than four times $\dot{m}_{\mathrm{LD}}{}^{\mathrm{in}}$.

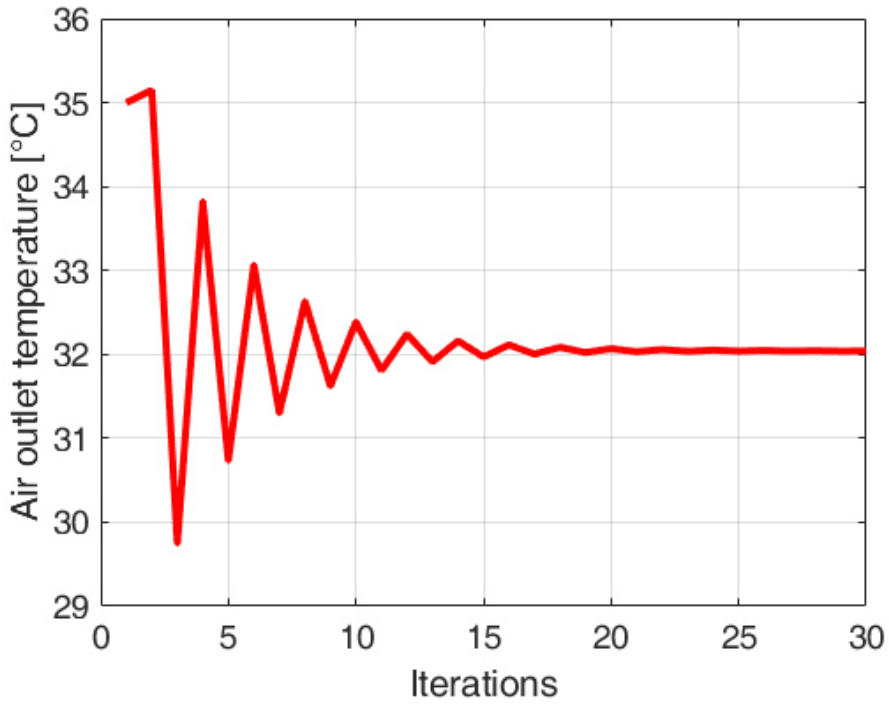

Figure A1-1. Example of convergence of the outlet air temperature using the HMX model.

The HMX model was verified by conducting experiments using an evaporative cooling pad (Figure A1-2) and $CaCl_2$ as the LD.

Figure A1-2. Experimental evaporative cooling pad.

The experimental data and model predictions showed good agreement (see Figure A1-3).

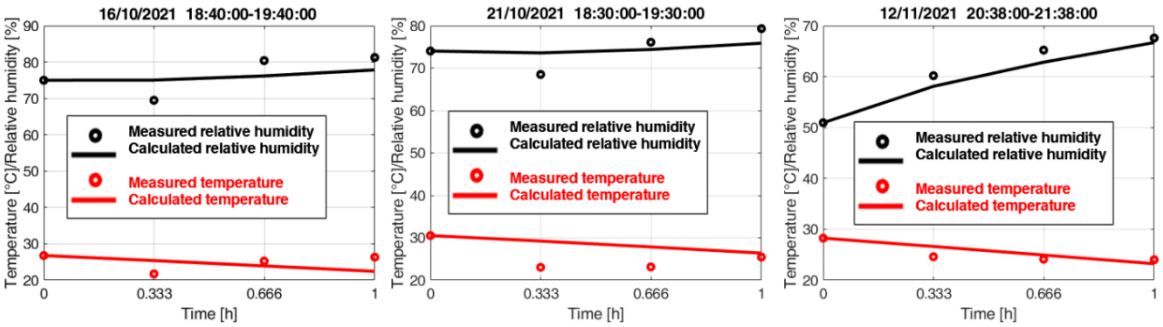

Figure A1-3. Validation of the HMX model using $CaCl_2$ as the liquid desiccant. Black values are for air relative humidity and red values for air temperature. Lines represent the model and points the experimental measurements. Temperature and relative humidity were measured in the closed area in front of the evaporative cooling pad of Figure A1-2.

The HMX model used in Chapter 3 is based on $CaCl_2$ heat capacity data from datasheets. In Chapter 6, the same HMX model is applied to the TRNSYS model, even though Chapter 6 considers $MgCl_2$ as the LD. This is supported by a study [380] that measured heat capacities [q/cm^3] of $MgCl_2$ and $CaCl_2$ at varying concentrations and found almost identical values (see Figure A1-4). Consequently, the heat capacity of $MgCl_2$ was calculated using the equation used for $CaCl_2$. The HMX model used in Chapter 6 is different from that of Chapter 3 in that it calculates the vapour pressure of $MgCl_2$ instead of $CaCl_2$ (both based on [377]).

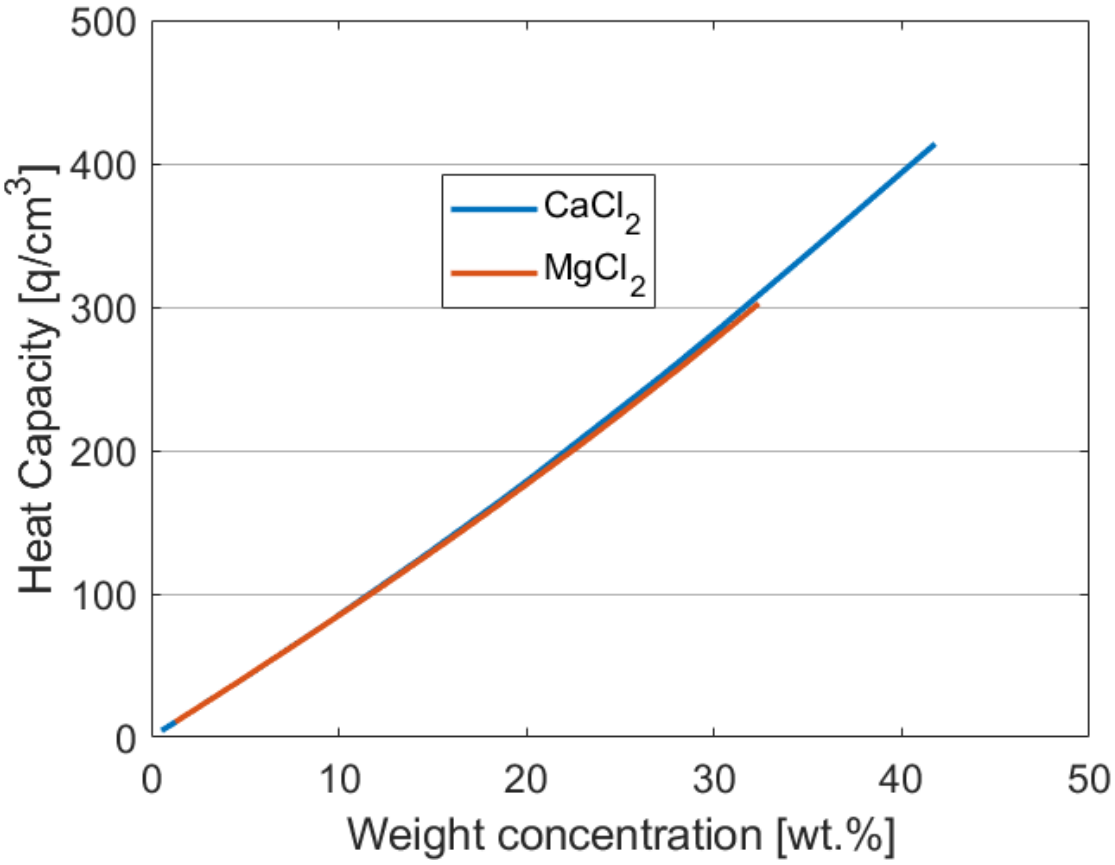

Figure A1-4. Heat capacity of $CaCl_2$ and $MgCl_2$ against liquid desiccant weight concentrations based on [380].

Appendix 2: Equations to calculate crop transpiration

The equations to calculate the parameters of Eq. 2-25 are presented here; equations A2-1 to A2-8 are taken from Acquah et al. [371].

$$\lambda = 2501 - 2.361 T_{\text{cool}} \tag{A2-1}$$

$$\Delta = \frac{4042.9 \exp\left(23.57712 - \frac{4042.9}{T_{\text{cool}} + 237.57}\right)}{10^3 (T_{\text{cool}} + 237.57)^2} \tag{A2-2}$$

$$VPD = 4042.9 \exp\left(23.57712 - \frac{4042.9}{T_{\text{cool}} + 237.57}\right)\left(1 - \frac{RH_{\text{cool}}}{100}\right) \tag{A2-3}$$

$$\rho_{\text{Air}} = \frac{10^5}{287(T_{\text{cool}} + 273.15)} \tag{A2-4}$$

$$r_{\text{R}} = \frac{10^3 \rho_{\text{Air}} c_{\text{p,Air}}}{4\, \sigma_{\text{S-B}} (T_{\text{cool}} + 273.15)^3} \tag{A2-5}$$

$$r_{\text{a}} = \frac{665}{1 + 0.54 Speed_{\text{Air}}} \tag{A2-6}$$

$$R_{\text{n}} = 0.0031 I \tau [1 - \exp(-0.7 LAI)] \tag{A2-7}$$

$$r_{\text{c}} = \frac{2}{LAI[108.5 + 660 \exp(-9I)]} \tag{A2-8}$$

where T_{cool} and RH_{cool} are the temperature [°C] and relative humidity [%] of air leaving the dehumidifier, $Speed_{\text{Air}}$ is the speed of air [m/s], and $\sigma_{\text{S-B}}$ is the constant of Stefan–Boltzmann equal to 5.67 10^{-8} W/(m^2 K^4).

Appendix 3: Iterative method to calculate reflection factor

To yield Eq. 3-18 for the reflection factor (σ), equations 3-6, 3-8, 3-2, and 3-7 must be rearranged as:

Eq. 3-6:

$$R_s - R_s\sigma F = \sigma - \sigma F \Leftrightarrow$$

$$R_s - \sigma = R_s\sigma F - \sigma F = \sigma F(R_s - 1) \Leftrightarrow$$

$$F = \frac{R_s - \sigma}{\sigma(R_s - 1)} \tag{A3-1}$$

Eq. 3-8:

1) $$R_{os} = 1 - \frac{C_p}{C_f} = \frac{C_f}{C_f} - \frac{C_p}{C_f} = \frac{\Delta C}{C_f} \tag{A3-2}$$

2) $$\frac{C_p}{C_f} = 1 - R_{os} \Leftrightarrow C_p = C_f(1 - R_{os}) \tag{A3-3}$$

Eq. 3-2:

$$J_s = P_s\Delta C + (1 - \sigma)C_f J_v$$

using Eq. 3-3:

$$P_s = \frac{J_s}{\Delta C} - \frac{(1 - \sigma)C_f J_v}{\Delta C}$$

using Eq. A3-2

$$P_s = J_v\left(\frac{C_p}{\Delta C} - \frac{(1 - \sigma)C_f}{\Delta C}\right)$$

using Eq. A3-3

$$P_s = J_v\left[\frac{C_f(1-R_{os})}{\Delta C} - \frac{(1-\sigma)C_f}{\Delta C}\right] \Leftrightarrow$$

$$P_s = J_v\left[\frac{(1-R_{os})}{R_{os}} - \frac{(1-\sigma)}{R_{os}}\right] \Leftrightarrow$$

$$P_s = J_v\left[\frac{(\sigma-R_{os})}{R_{os}}\right] \quad \text{(A3-4)}$$

Eq. 3-7 (using equations A3-1 and A3-4):

$$\ln(F) = \frac{(\sigma-1)}{P_s}J_v \Leftrightarrow$$

$$\ln\left[\frac{R_s-\sigma}{\sigma(R_s-1)}\right] = \frac{(\sigma-1)}{\cancel{J_v}\left[\frac{(\sigma-R_{os})}{R_{os}}\right]}\cancel{J_v} \Leftrightarrow$$

$$\ln\left[\frac{R_s-\sigma}{\sigma(R_s-1)}\right] = \frac{(\sigma-1)R_{os}}{\sigma-R_{os}} \Leftrightarrow$$

$$\ln\left[\frac{R_s-\sigma}{\sigma(R_s-1)}\right](\sigma-R_{os}) = \sigma R_{os} - R_{os} \Leftrightarrow$$

$$\ln\left[\frac{R_s-\sigma}{\sigma(R_s-1)}\right](\sigma-R_{os}) + R_{os} = \sigma R_{os} \Leftrightarrow$$

$$\sigma = \ln\left[\frac{\sigma-R_s}{\sigma(1-R_s)}\right]\left(\frac{\sigma}{R_{os}}-1\right)+1 \quad \text{(A3-5)}$$

Appendix 4: Concentration measurement using a refractometer

A refractometer was used to calculate the concentrations of the feed, permeate, and concentrate LD for the experiments conducted in Chapter 4. Solutions with different feed concentrations were prepared using LiCl, LiBr and $MgCl_2$ to correlate their refractive index (output of the refractometer) with their weight concentration (Figure A4-1).

The solutions were prepared with 200 g of deionised water. Gradually, 1 g of desiccant salt was added to the solution. Once the salt was totally dissolved in the solution, the refractive index was measured. The addition of 1 g of desiccant salt was done until a weight concentration of 10 wt.% (105 g/L) was reached. Then, 3 g of desiccant salt was added. During the first additions of desiccant salt, the salts required time to be totally dissolved. As the weight concentration increased, heat was released which facilitated the salt mixing. After reaching 10 wt.% (105 g/L), the solution was hot enough to easily dissolve 3 g of desiccant salt. Even though the temperature of the solution was higher than 25 °C, the automatic J357 refractometer maintained the temperature at 25 °C. The experimental data was in agreement with the data from Zaltash and Ally [381] who measured the refractive index for different LiBr concentrations (see Figure A4-1). Unfortunately, similar studies regarding LiCl and $MgCl_2$ could not be found. The polynomial equations are:

$$wt_{\mathrm{LiCl}} = -443.9Ref_{\mathrm{idx}}{}^{2} + 1667Ref_{\mathrm{idx}} - 1433 \quad \text{(A4-1)}$$

$$wt_{\mathrm{LiBr}} = -1566Ref_{\mathrm{idx}}{}^{2} + 4783Ref_{\mathrm{idx}} - 3592 \quad \text{(A4-2)}$$

$$wt_{\mathrm{MgCl2}} = -667.8Ref_{\mathrm{idx}}{}^{2} + 2182Ref_{\mathrm{idx}} - 1722 \quad \text{(A4-3)}$$

where wt_{LiCl}, wt_{LiBr}, and wt_{MgCl2} are the weight concentrations [wt.%] of LiCl, LiBr, and $MgCl_2$, respectively, and Ref_{idx} is the refractive index.

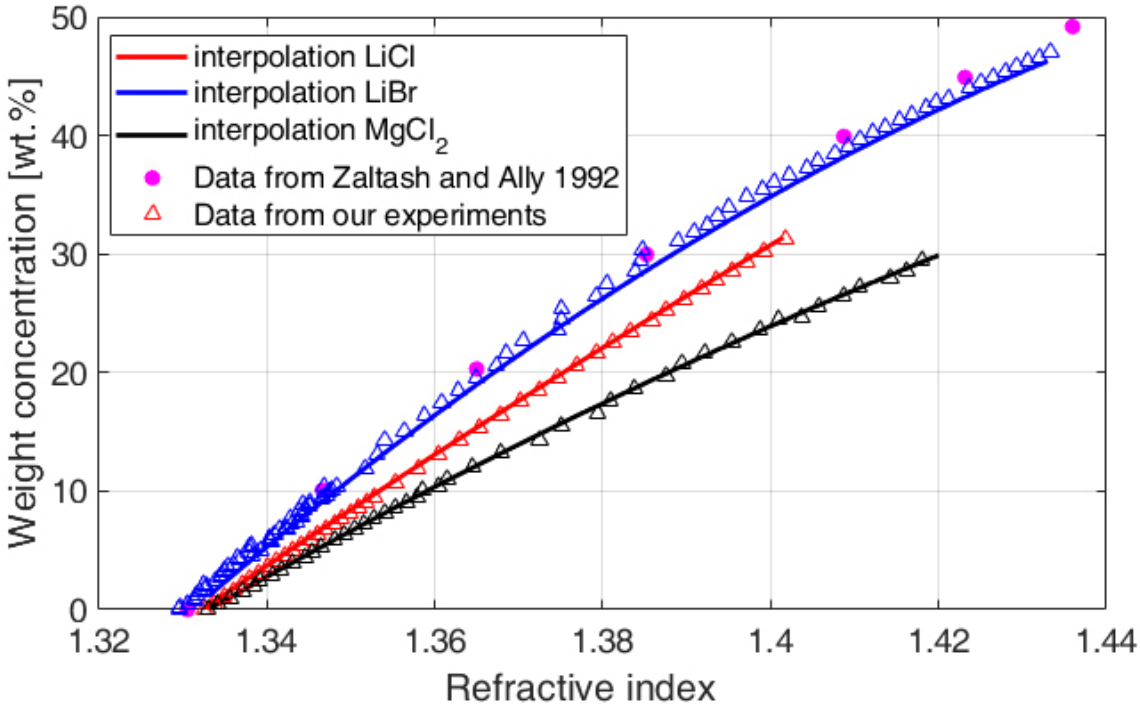

Figure A4-1. Weight concentrations of LiCl, LiBr, and $MgCl_2$ measured at different refractive indexes. The triangles represent the experimental data obtained by using a refractometer, the dots represent the data from Zaltash and Ally [381], and the lines represent interpolations that fit the experimental results. These results are plotted considering a temperature of 25 °C .

Appendix 5. Solution preparation for dead-end filtration experiments

Three solutions were prepared for each LD (LiCl, LiBr, and $MgCl_2$) used for the experiments in Chapter 4. The total volume (V_{tot}) of each solution was equal to 0.2 L. For a given weight concentration (*wt*) [wt.%], the required grams of water (g_{H2O}) and grams of LD (g_{LD}) are calculated as:

$$g_{\text{H}_2\text{O}} = \frac{V_{\text{tot}}}{1 + \frac{wt}{(1-wt)\rho_{\text{LD}}}} \tag{A5-1}$$

$$g_{\text{LD}} = \frac{wt}{(1-wt)} g_{\text{H}_2\text{O}} \tag{A5-2}$$

where ρ_{LD} is the density of the pure desiccant salt [kg/m^3]. The volumes of water ($V_{\text{H}_2\text{O}}$) and LD (V_{LD}) [L] are calculated as:

$$V_{\text{H}_2\text{O}} = g_{\text{H}_2\text{O}} \tag{A5-3}$$

$$V_{\text{LD}} = {}^{g_{\text{LD}}}/_{\rho_{\text{LD}}} \tag{A5-4}$$

For example, the preparation of LiCl solution with a total volume of 0.2 L and a weight concentration of 10 wt.% (105 g/L) requires 189.765 g of water and 21.085 g of LiCl salt. For this case, the total grams are equal to 210.85; the division of g_{LD} with the total grams is equal to *wt*. For the preparation of the solutions, the utilised densities of pure solid anhydrous LiCl, LiBr, and $MgCl_2$ salts were 2060, 3460, and 2320 kg/m^3, respectively.

Appendix 6: Example of accurate osmotic pressure calculation

The van ‘t Hoff formula (Eq. 3-17) is a linear approximation of osmotic pressure (Π) valid for dilute solution. Accurate values of Π for concentrated solutions can be calculated based on Gibbs energy [382] (see Eq. 2-4). Assuming LiCl is the LD, equations 3-17 and 2-4 give similar Π results for concentrations below 10 wt.% (105 g/L), but the results diverge at higher concentrations (Figure A6-1). Since LDAC requires highly concentrated solutions, Eq. 2-4 is better than Eq. 3-17 for calculating Π at high LD concentrations.

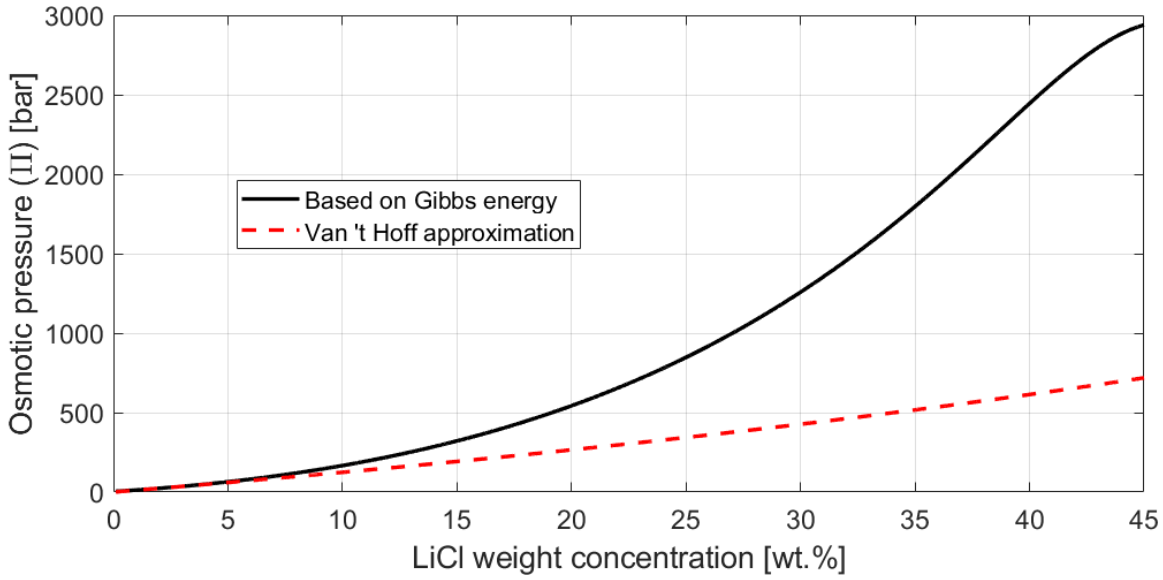

Figure A6-1. Osmotic pressure (Π) calculated for LiCl concentrations up to 45 wt.% (600 g/L) using the van ‘t Hoff linear approximation (dash line) and the equation based on Gibbs energy (continuous line). The plot shows that the approximation is valid for LiCl concentrations below 10 wt.% (105 g/L).

Appendix 7: Multi-stage systems: experimental equations and models

For the experiments in Chapter 5, the weight concentration (*wt*) [wt.%] was measured through the refractive index (Ref_{idx}). For $MgCl_2$ concentrations below 9 wt.% (equivalent to 95 g/L), *wt* is calculated as:

$$wt = \frac{Ref_{\mathrm{idx}} - 1.33299}{0.002572} \tag{A7-1}$$

The osmotic pressure ($\Delta\Pi$) [bar] is calculated by using the van 't Hoff approximation, valid for $MgCl_2$ concentrations below 95 g/L. For $MgCl_2$ *C* concentrations above 95 g/L, *wt* is calculated as:

$$wt = -667.8 Ref_{\mathrm{idx}}{}^2 + 2182 Ref_{\mathrm{idx}} - 1722 \tag{A7-2}$$

and $\Delta\Pi$ by using the Gibbs energy calculation. Two different $\Delta\Pi$ calculations are used because the van 't Hoff approximation calculates a higher $\Delta\Pi$ value than the Gibbs energy when *wt* is below 9 wt.%. Thus, the van 't Hoff approximation is used for *wt* below 9 wt.% as the worst case between the two methods. Experiments in Chapter 5 were carried out with *wt* below 9 wt.%, therefore the van 't Hoff approximation was used to calculate the parameters based on the experimental data. The equations for *wt* above 9 wt.% were used to model the 4-stage systems in Subsections 4.4.3 and 4.4.4.

The hydraulic power ($Power_{\mathrm{hyd}}$) [kW] is calculated as:

$$Power_{\mathrm{hyd}} = \frac{\dot{m}_{\mathrm{f}}\, \Delta P}{60 \rho_{\mathrm{f}}} \tag{A7-3}$$

where $\dot{m}_f$ [kg/min] is the feed flow of the pump ($\dot{m}_{f,NF}$ or $\dot{m}_{f,RO}$), ΔP [bar] is the applied pressure, and ρ_f [kg/m^3] the density of the feed flow. ΔP is calculated as (Eq. 4-5):

$$\Delta P = CP\ \Delta\Pi_b + \frac{J_v}{L_p} + \frac{\Delta P_m}{2} \quad \text{(A7-4)}$$

Following the solution-diffusion equation, L_p is calculated by dividing the flux ($J_{v,}$) [L/(m^2 h)] by the difference between ΔP [bar] and the feed osmotic pressure difference ($\Delta\Pi_f$) [bar], as:

$$L_p = \frac{J_v}{\Delta P - \Delta\Pi_f} \quad \text{(A7-5)}$$

Since ΔP and L_p are interdependent, an iterative method was used for their calculation. The method assumes L_p equal to the pure water permeability, calculates ΔP through Eq. A7-4, and then calculates a new value of L_p by using Eq. A7-5. Equations A7-4 and A7-5 are used iteratively. This iterative method increases ΔP and is stopped when ΔP goes above ΔP_{max}. The penultimate value of ΔP is the output value of the method. Once ΔP is calculated, L_p is calculated through Eq. A7-5. If $\Delta\Pi_f > \Delta P_{max}$, then L_p is assumed equal to zero and ΔP equal to $\Delta\Pi_f$ which accounts that the system is spending energy without producing permeate.

The power required by the motors was modelled using a linear interpolation having R^2 above 95% and RMSE below 0.024 kW. The motor power requirement depended only on pump flow.

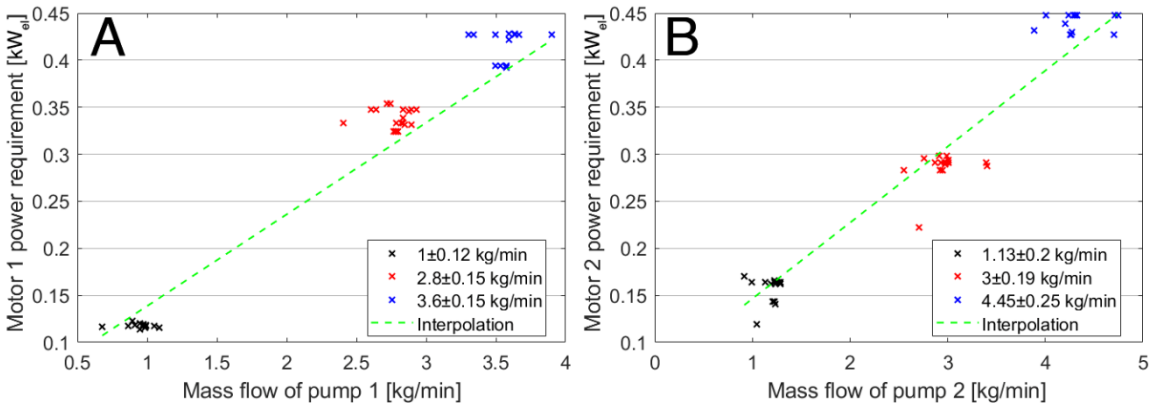

Figure A7-1. A) Electric motor 1 power requirement against pump 1 mass flow. Motor 1 and pump 1 are connected to the nanofiltration membrane. B) Electric motor 2 power requirement against pump 2 mass flow [kg/min]. Motor 2 and pump 2 are connected to the reverse osmosis membrane. The flow of pump 2 shown in B) is the difference between the actual flow and the intermediate recirculation. The intermediate recirculation was much lower than the flow of motor 2. Therefore, the actual pump 2 flow is almost the same as the plotted. A) and B) show experimental results for low, medium, and high pump mass flows in "x," while the interpolation is shown using a dashed line.

The motor power interpolation is based on experiments where the electric power requirements of the motors ($Power_{el}$) [kW_{el}] were measured as:

$$Power_{el} = \frac{I\,Volt}{10^3} \tag{A7-6}$$

where I [A] is the current and $Volt$ [V] the voltage of a motor. The combined motor-pump efficiency ($\eta_{m\text{-}p}$) [%] is given by dividing $Power_{hyd}$ with $Power_{el}$:

$$\eta = 10^2 \frac{Power_{hyd}}{Power_{el}} \tag{A7-7}$$

The total weight change of tanks (Δm_{tot}) [L] is calculated as:

$$\Delta m_{tot} = |\, m_{end} - m_0 \,| \tag{A7-8}$$

where m_{end} and m_0 are the final and initial tank weights, respectively. The absolute value is used because the weight of the feed tank decreased during an experiment.

The recovery (r) is calculated as:

$$r = \frac{\Delta m_{\text{tot,p}}}{\Delta m_{\text{tot,feed tank}}} \tag{A7-9}$$

where $\Delta m_{\text{tot,p}}$ and $\Delta m_{\text{tot,feed tank}}$ are the total weight changes of the permeate tank and the feed tank, respectively. The recovery of the NF membrane (r_{NF}) is calculated as:

$$r_{\text{NF}} = \frac{\Delta m_{\text{tot,second feed tank}}}{\Delta m_{\text{tot,feed tank}}} \tag{A7-10}$$

where $\Delta m_{\text{tot,second feed tank}}$ is the total weight change of the second feed tank. It was not possible to measure the recovery of the RO membrane (r_{RO}) because when pump 2 is active, $\Delta m_{\text{tot,second feed tank}}$ is the difference between $\dot{m}_{\text{pump2}}$ and $\dot{m}_{\text{int}}$ entering the same tank (see Figure 5-2).

The SEC_{el} [$\text{kWh}_{\text{el}}/\text{m}^3$] is defined as the required electric power per cubic metre of permeate, therefore calculated as:

$$SEC_{\text{el}} = 10^3 \frac{Power_{\text{el}}}{\Delta L_{\text{tot,p}}} \tag{A7-11}$$

Similarly, the hydraulic specific energy consumption (SEC_{hyd}) [kWh/m^3] is defined as the required hydraulic power per cubic metre of permeate:

$$SEC_{\text{hyd}} = 10^3 \frac{Power_{\text{hyd}}}{\Delta L_{\text{tot,p}}} \tag{A7-12}$$

For NF-RO, the rejection of the NF membrane (R_{NF}) is calculated as:

$$R_{\text{NF}} = 1 - \frac{C_{\text{int}}}{C_{\text{f,NF}}} \tag{A7-13}$$

For RO-NF, R_{NF} could not be experimentally measured because it was not possible to collect samples for the flow entering the NF membrane. The rejection of the RO membrane (R_{RO}) is calculated as:

$$R_{RO} = 1 - \frac{C_p}{C_{int}} \quad \text{(A7-14)}$$

To avoid confusion in the notation, weight-related parameters (e.g., *m* and derivatives like *r*) refer to tank weights as indicated by subscripts "feed tank", "second feed tank", "permeate tank", and "brine tank" in Figure 5-2. Whereas concentration related parameters (e.g., *C*, *wt*, and derivatives like *R*) refer to concentrations of flows as indicated in Figure 5-2 with "f,NF", "int", "f,RO", "b", and "p". Equations containing different types of concentrations (e.g., ρ, χ, *wt*, and *C*) are derivatives of equations A7-15 to A7-27.

For the concentration-related conversion, equations A7-15 to A7-27 are provided. First, the definitions of concentrations are presented, followed by the equations that correlate the different types of concentrations. Equations A7-15 to A7-27 utilise different nomenclature for weight because *m* is commonly used for Molality in chemistry. Therefore, weight is referred to as *kg*.

Definitions of concentrations:

- Molality:

$$m = \frac{\text{mol of solute}}{1\ \text{kg of water}}\ \left[\frac{\text{mol}}{\text{kg}}\right]$$

- Molarity:

$$M = \frac{\text{mol of solute}}{1\ \text{L of solution}}\ \left[\frac{\text{mol}}{\text{L}}\right]$$

- Weight concentration:

$$wt.\% = \frac{\text{kg of solute}}{\text{kg of solution}}\ [\%]$$

- Parts per million

$$PPM = \frac{\text{mg of solute}}{\text{L of solution}}\ \left[\frac{\text{mg}}{\text{L}}\right]$$

- Molar fraction

$$\chi = \frac{\text{mol of solute}}{\text{mol of solution}}$$

Correlations for a mixture with n solutes and pure water (H_2O) as the solvent:

The total weight of the solution (kg_{sol}) [kg] is calculated as:

$$kg_{\text{sol}} = \sum_{i}^{n} kg_{\text{i}} + kg_{H_2O}$$

Pure water has a density (ρ) of 1000 kg/m^3 (or 1 kg/L), therefore:

$$kg_{\mathrm{H_2O}} = V_{\mathrm{H_2O}} \tag{A7-15}$$

The weight percentage of pure water ($wt.\%_{\mathrm{H_2O}}$) [wt.%] is calculated as:

$$\text{Total weight percentage: } 10^2 = \sum_i^n wt.\%_{\mathrm{i}} + wt.\%_{\mathrm{H_2O}} \Leftrightarrow$$

$$wt.\%_{\mathrm{H_2O}} = 10^2 - \sum_i^n wt.\%_{\mathrm{i}} \tag{A7-16}$$

Due to the property of the percentage, the weight of the j solute (kg_{j}) is correlated with the weight of the pure water ($kg_{\mathrm{H_2O}}$):

$$\frac{kg_{\mathrm{j}}}{wt.\%_{\mathrm{j}}} = \frac{kg_{\mathrm{H_2O}}}{wt.\%_{\mathrm{H_2O}}} \Leftrightarrow$$

$$kg_{\mathrm{j}} = V_{\mathrm{H_2O}} \frac{wt.\%_{\mathrm{j}}}{10^2 - \sum_i^n wt.\%_{\mathrm{i}}} \tag{A7-17}$$

The total volume of the solution (V_{sol}) is calculated as:

$$V_{\mathrm{sol}} = \sum_i^n V_{\mathrm{i}} + V_{\mathrm{H_2O}}\ [L]$$

The volume of the j solute (V_{j}) is calculated through their density (ρ_{j}):

$$V_{\mathrm{j}} = \frac{kg_{\mathrm{j}}}{\rho_{\mathrm{j}}} \Leftrightarrow$$

$$V_{\mathrm{j}} = \frac{V_{\mathrm{H_2O}}\, wt.\%_{\mathrm{j}}}{\rho_{\mathrm{j}}(10^2 - \sum_i^n wt.\%_{\mathrm{i}})} \tag{A7-18}$$

Therefore, V_{sol} is calculated as:

$$V_{\text{sol}} = \sum_{i}^{n} V_{\text{i}} + V_{\text{H}_2\text{O}} \Leftrightarrow$$

$$V_{\text{sol}} = V_{\text{H}_2\text{O}} \left(1 + \frac{\sum_{i}^{n} (wt.\%_{\text{i}}/\rho_{\text{i}})}{10^2 - \sum_{i}^{n} wt.\%_{\text{i}}}\right) \tag{A7-19}$$

The moles of the j solute (mol_{j}) [mol] are calculated as:

$$mol_{\text{j}} = kg_{\text{j}} \frac{10^3}{MM_{\text{j}}} \Leftrightarrow$$

$$mol_{\text{j}} = V_{\text{H}_2\text{O}} \frac{wt.\%_{\text{j}}}{10^2 - \sum_{i}^{n} wt.\%_{\text{i}}} \frac{10^3}{MM_{\text{j}}} \tag{A7-20}$$

where MM_{j} is the relative molecular mass of the j solute [g/mol]. Similarly, the moles of pure water ($mol_{\text{H}_2\text{O}}$) [mol] are calculated as:

$$mol_{\text{H}_2\text{O}} = \frac{10^3 \, V_{\text{H}_2\text{O}}}{MM_{\text{H}_2\text{O}}} \tag{A7-21}$$

where $MM_{\text{H}_2\text{O}}$ is the relative molecular mass of pure water equal to 18.015 g/mol. The molality of the j solute (m_{j}) is calculated by dividing mol_{j} with 1 kg of pure water (equal to 1 L of pure water):

$$m_{\text{j}} = \frac{wt.\%_{\text{j}}}{10^2 - \sum_{i}^{n} wt.\%_{\text{i}}} \frac{10^3}{MM_{\text{j}}} \Leftrightarrow$$

$$m_{\text{j}} = \frac{10^3 wt.\%_{\text{j}}}{MM_{\text{j}}\left(10^2 - \sum_{i}^{n} wt.\%_{\text{i}}\right)} \tag{A7-22}$$

The molarity of the j solute (M_{j}) is calculated by dividing mol_{j} with V_{sol}, which yields:

$$M_{\text{j}} = \frac{\frac{wt.\%_{\text{j}}}{10^2 - \sum_{i}^{n} wt.\%_{\text{i}}} \frac{10^3}{MM_{\text{j}}}}{\left(1 + \frac{\sum_{i}^{n} (wt.\%_{\text{i}}/\rho_{\text{i}})}{10^2 - \sum_{i}^{n} wt.\%_{\text{i}}}\right)} \Leftrightarrow$$

$$M_{\mathrm{j}} = \frac{\left(\frac{wt.\%_{\mathrm{j}}}{10^2 - \sum_i^n wt.\%_{\mathrm{i}}}\right)\frac{10^3}{MM_{\mathrm{j}}}}{1 + \left(\frac{\sum_i^n (wt.\%_{\mathrm{i}}/\rho_{\mathrm{i}})}{10^2 - \sum_i^n wt.\%_{\mathrm{i}}}\right)} \quad \text{(A7-23)}$$

The molar fraction of the j solute (χ_{j}) is calculated as:

$$\chi_{\mathrm{j}} = \frac{mol_{\mathrm{j}}}{\sum_i^n mol_{\mathrm{i}} + mol_{H_2O}} \Leftrightarrow$$

$$\chi_{\mathrm{j}} = \frac{\frac{wt.\%_{\mathrm{j}}}{10^2 - \sum_i^n wt.\%_{\mathrm{i}}}\frac{10^3}{MM_{\mathrm{j}}}}{\sum_i^n \left(\frac{wt.\%_{\mathrm{j}}}{10^2 - \sum_i^n wt.\%_{\mathrm{i}}}\frac{10^3}{MM_{\mathrm{j}}}\right) + \frac{10^3}{MM_{H_2O}}} \Leftrightarrow$$

$$\chi_{\mathrm{j}} = \frac{m_{\mathrm{j}}}{\sum_i^n (m_{\mathrm{i}}) + \frac{10^3}{MM_{H_2O}}} \quad \text{(A7-24)}$$

m_{j} is correlated to M_{j} as:

$$m_{\mathrm{j}} = \frac{mol_{\mathrm{j}}}{V_{H_2O}} \Leftrightarrow mol_{\mathrm{j}} = m_{\mathrm{j}} V_{H_2O}$$

$$M_{\mathrm{j}} = \frac{mol_{\mathrm{j}}}{V_{\mathrm{sol}}} = \frac{mol_{\mathrm{j}}}{V_{H_2O}\left(1 + \frac{\sum_i^n (wt.\%_{\mathrm{i}}/\rho_{\mathrm{i}})}{10^2 - \sum_i^n wt.\%_{\mathrm{i}}}\right)} = \frac{m_{\mathrm{j}}}{\left(1 + \frac{\sum_i^n (wt.\%_{\mathrm{i}}/\rho_{\mathrm{i}})}{10^2 - \sum_i^n wt.\%_{\mathrm{i}}}\right)}$$

m_{j} is correlated to $wt.\%_{\mathrm{j}}$ as:

$$\frac{m_{\mathrm{j}} MM_{\mathrm{j}}}{10^3} = \frac{wt.\%_{\mathrm{j}}}{(10^2 - \sum_i^n wt.\%_{\mathrm{i}})}$$

while M_{j} is correlated to $wt.\%_{\mathrm{j}}$ as:

$$M_{\mathrm{j}} = \frac{m_{\mathrm{j}}}{1 + 10^{-3}\sum_i^n (m_{\mathrm{i}} MM_{\mathrm{i}}/\rho_{\mathrm{i}})} \quad \text{(A7-25)}$$

Thus, m_{j} and M_{j} can be correlated as:

$$m_{\mathrm{j}} = \frac{M_{\mathrm{j}}}{1 - 10^{-3} \sum_{i}^{n} (M_{\mathrm{i}} MM_{\mathrm{i}} / \rho_{\mathrm{i}})} \tag{A7-26}$$

M_{j} is correlated to the *PPM* of the j solute (PPM_{j}) as:

$$M_{\mathrm{j}} = \frac{10^{-3}\, PPM_{\mathrm{j}}}{MM_{\mathrm{j}}} \tag{A7-27}$$

Regarding the 2-stage models, the NF-RO model includes two membrane models, one tee junction model, one ERD model, and two weight models for the feed tank and the second feed tank (see Figure A7-2). The RO-NF model includes two membrane models, one ERD model, one weight model for the feed tank, and one concentration model for the feed tank (see Figure A7-3).

The 4-stage models, i.e., 3NF-RO and RO-3NF, were also modelled using Matlab-Simulink®. The 3NF-RO model (Figure A7-4) is like NF-RO but differs in having three NF membranes before the RO membrane. Whereas RO-3NF (Figure A7-5) has three NF membranes after the RO membrane. Another difference between 2-stage and 4-stage models is that the latter do not include tanks. This is to model continuously operating systems, such as those used in greenhouse LDAC and ZLD systems. The RO-3NF model utilises NaCl instead of $MgCl_2$ to investigate a system as proposed by Wang et al. [73].

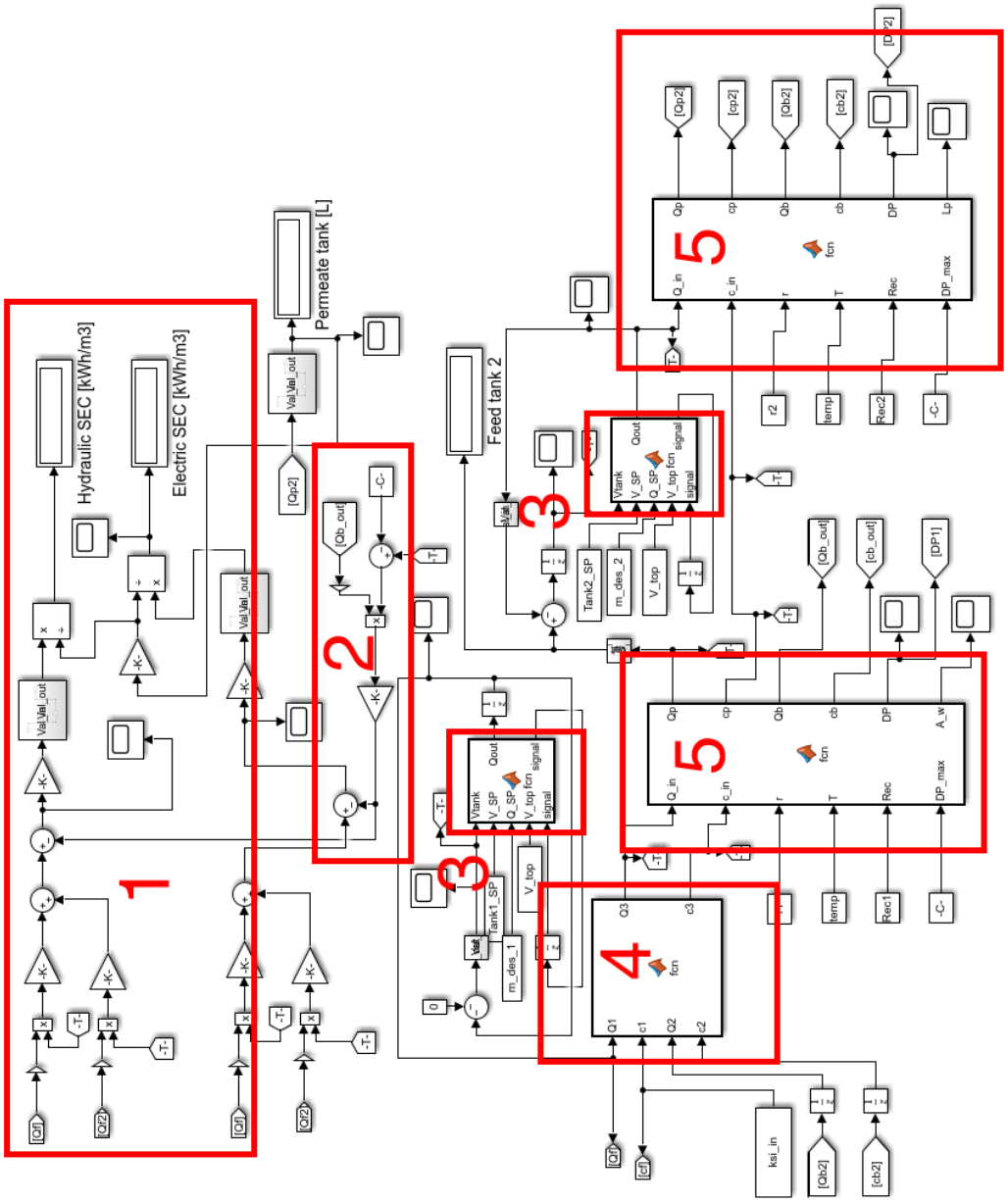

Figure A7-2. Matlab-Simulink® model for NF-RO. The model includes: "1" energy related calculations , "2" the ERD, "3" weight variation models for feed and second feed tanks, "4" the tee junction before the NF membrane, and "5" the membrane stage models.

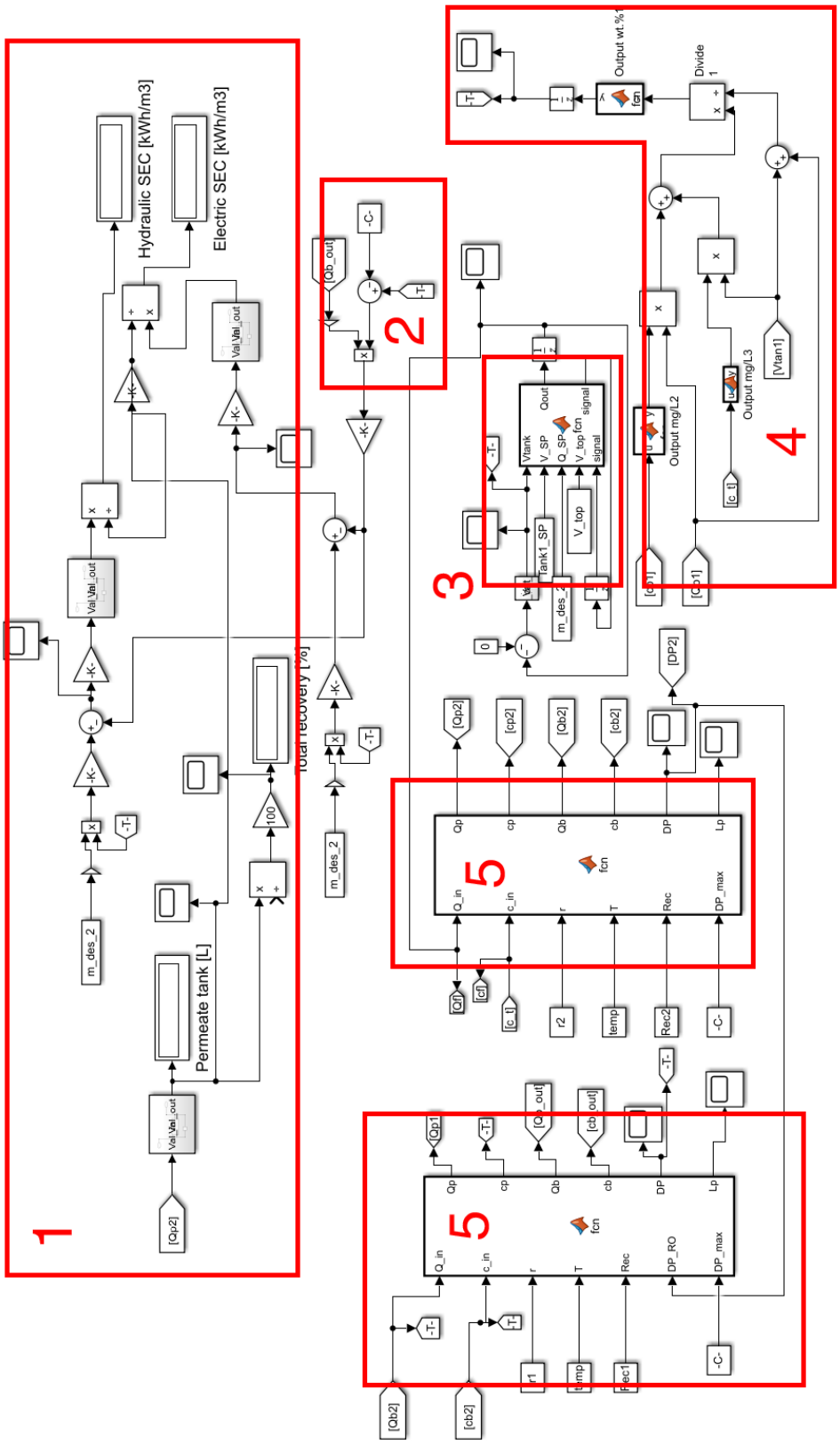

Figure A7-3. Matlab-Simulink® model for RO-NF. The model includes: "1" energy related calculations , "2" the ERD, "3" weight variation model for the feed tank, "4" concentration variation model for the feed tank, and "5" the membrane stage models.

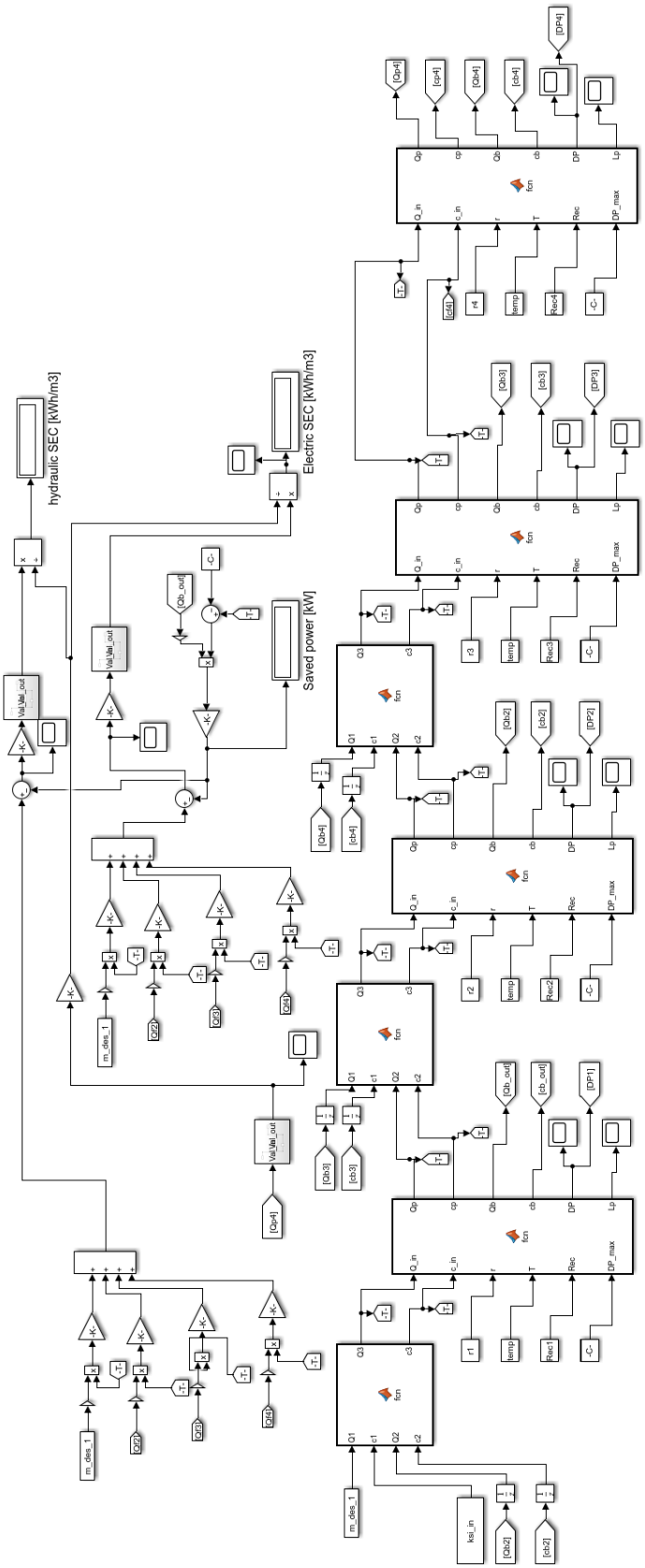

Figure A7-4. Matlab-Simulink® model for 3NF-RO.

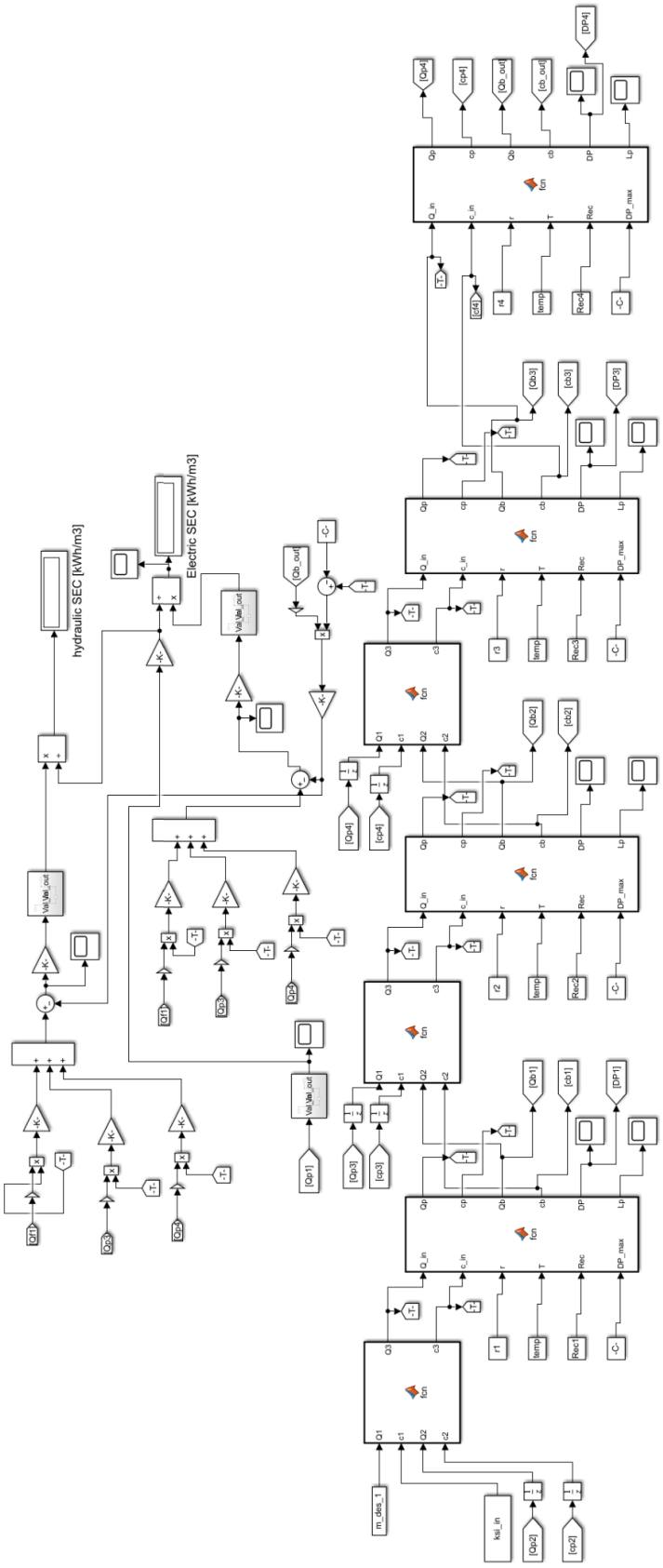

Figure A7-5. Matlab-Simulink® model for RO-3NF.

The RO-3NF model was modified to use NaCl instead of $MgCl_2$. Like the other multi-stage models, the RO-3NF model also utilises both the van 't Hoff approximation and the Gibbs energy to calculate the osmotic pressure. For the van 't Hoff approximation, the NaCl parameters are relative molecular mass of 58.44 g/mol, pure solid anhydrous density of 2160 kg/m^3, diffusion coefficient of 1.47×10^{-9} m^2/s, and van 't Hoff dissociation parameter of 2. For the Gibbs energy, the equilibrium relative humidity of NaCl (ERH_{NaCl}) is calculated as:

$$ERH_{\mathrm{NaCl}} = -1.926x^2 - 0.419x + 1 \quad \text{(A7-28)}$$

where x is the mass fraction of the solution. The van 't Hoff approximation is used for *wt* ≤12.76 wt.% (C ≤137 g/L) because it calculates higher osmotic pressures than Gibbs energy (Figure A7-6). Figure A7-6 shows osmotic pressures against C concentrations because NaCl-based desalination applications typically utilise C instead of *wt*.

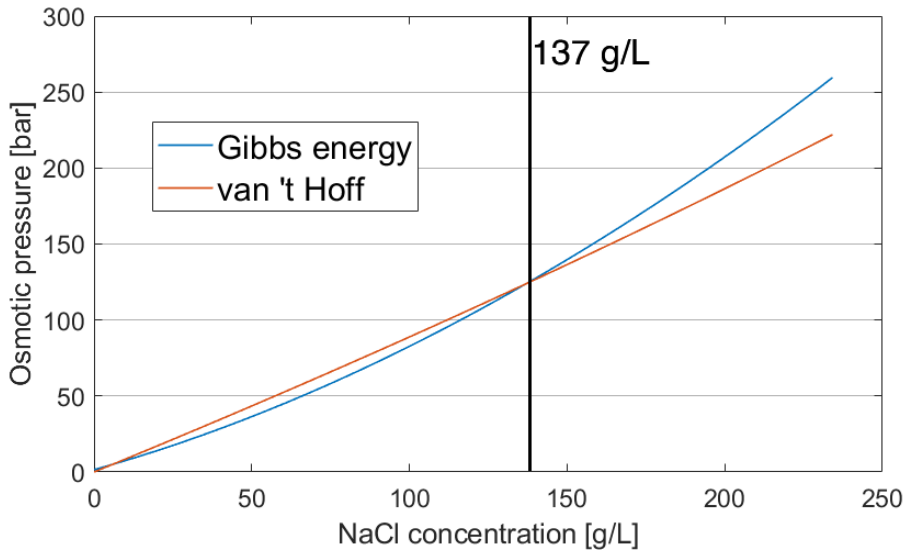

Figure A7-6. Osmotic pressure against NaCl concentration using two calculation methods, Gibbs energy and van 't Hoff.

The Matlab-Simulink model of RO-3NF with the NaCl modification remains as illustrated in Figure A7-5.

Appendix 8: Model validation of 2-stage systems

For the 2-stage models developed in Chapter 5, the model input parameters were set to match the experimental conditions. Thus, r_{NF}, R_{NF}, and R_{RO} were set equal to the average experimental values, solution T was set to 22 °C, and ΔP_{max} was set to 38.5 bar. Since r_{RO} could not be measured during experiments, r_{RO} was varied in the model until the predicted and measured tank weights [kg] matched (Figure A8-1). After matching the tank weights, the NF-RO model predicted flows $\dot{m}$ [kg/min] with error below 8% (Figure A8-2A) and concentrations C [g/L] with error below 2% (Figure 5-10A). Whereas the NF-RO model predicted flows $\dot{m}$ with error below 8% (Figure A8-2B) and concentrations C with error below 3% (Figure 5-10B).

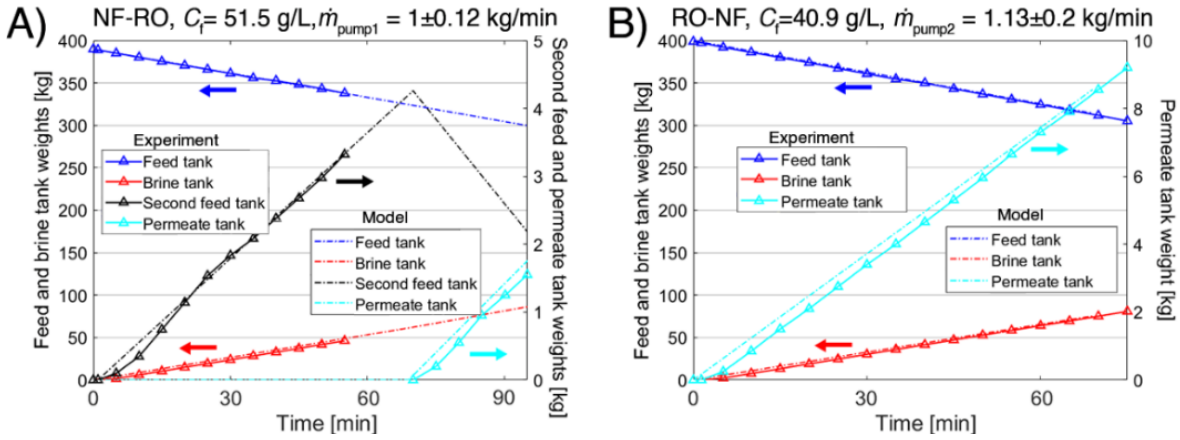

Figure A8-1. A) Weights of feed and brine tanks on the left vertical axis and second feed and permeate tanks on the right vertical axis. Results in triangles are experimental for NF-RO with pump 1 flow of 1±0.12 kg/min and feed concentration (C_f) of 51.5 g/L. Weights of feed, brine, and second feed tanks are shown until brine recirculation was deactivated (model does not include brine recirculation). Model results are shown with dashed lines. Arrows indicate the vertical axis of the plotted parameters. B) Similar to A) but for RO-NF with pump 2 flow of 1.13±0.2 kg/min and C_f of 40.9 g/L.

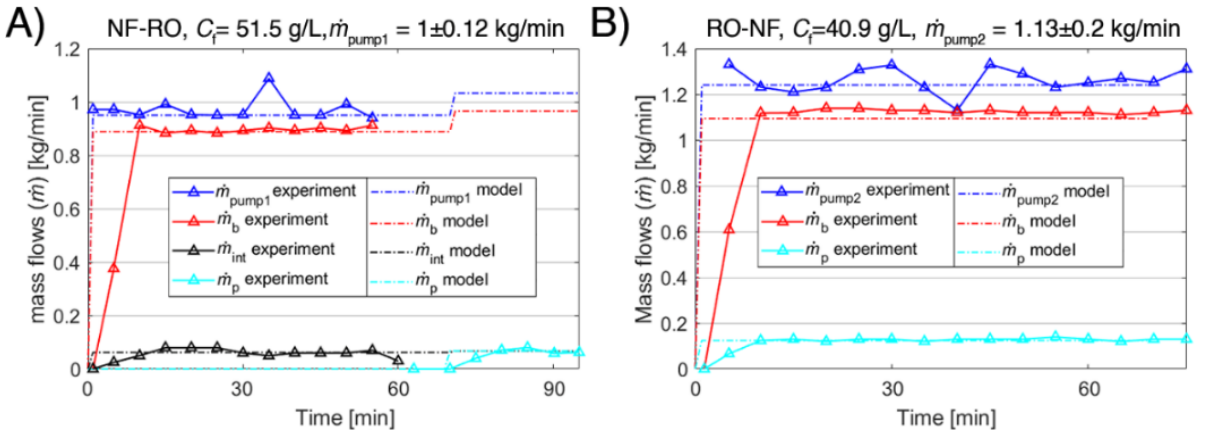

Figure A8-2. A) Flows against time. Results in triangles are experimental for NF-RO with pump 1 flow ($\dot{m}_{pump1}$) of 1±0.12 kg/min and feed concentration (C_f) of 51.5 g/L. Experimental results of $\dot{m}_{pump1}$ and $\dot{m}_b$ are shown until brine recirculation was deactivated (model does not include brine recirculation). Experimental $\dot{m}_{int}$ is shown until pump 2 was deactivated, while experimental $\dot{m}_p$ starts when pump 2 was activated. Model results are shown by dashed lines. B) Similar to A) but for RO-NF with pump 2 flow of 1.13±0.2 kg/min and C_f of 40.9 g/L.

The NF-RO model agreed with experimental ΔP with error below 7% (Figure 5-11A) and L_p with error below 10% (Figure A8-3A). Whereas the RO-NF model had ΔP error below 2% (Figure 5-11B) and L_p error below 7% (Figure A8-3B).

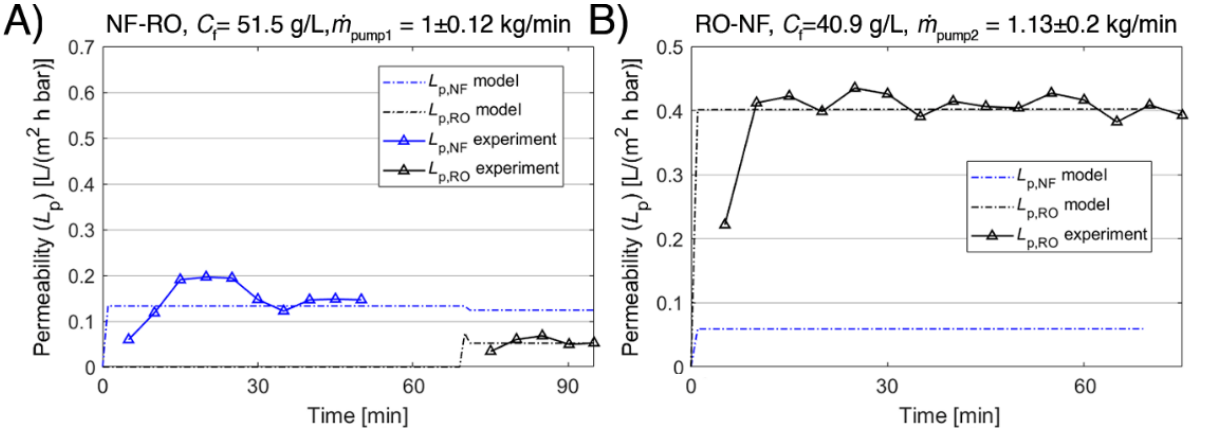

Figure A8-3. A) Permeabilities against time. Results in triangles are experimental for NF-RO with pump 1 flow of 1±0.12 kg/min and feed concentration (C_f) of 33.6 g/L. Experimental $L_{p,NF}$ is shown until pump 2 was deactivated while experimental $L_{p,RO}$ starts when pump 2 was activated. Brine recirculation was active during the time without $L_{p,NF}$ and $L_{p,RO}$. Model results are shown with dashed lines. B) Similar to A) but for RO-NF with pump 2 flow of 1.13±0.2 kg/min and C_f of 40.9 g/L.

For RO-NF, the model of the concentration variation for the feed tank had a maximum error below 3% (Figure A8-4).

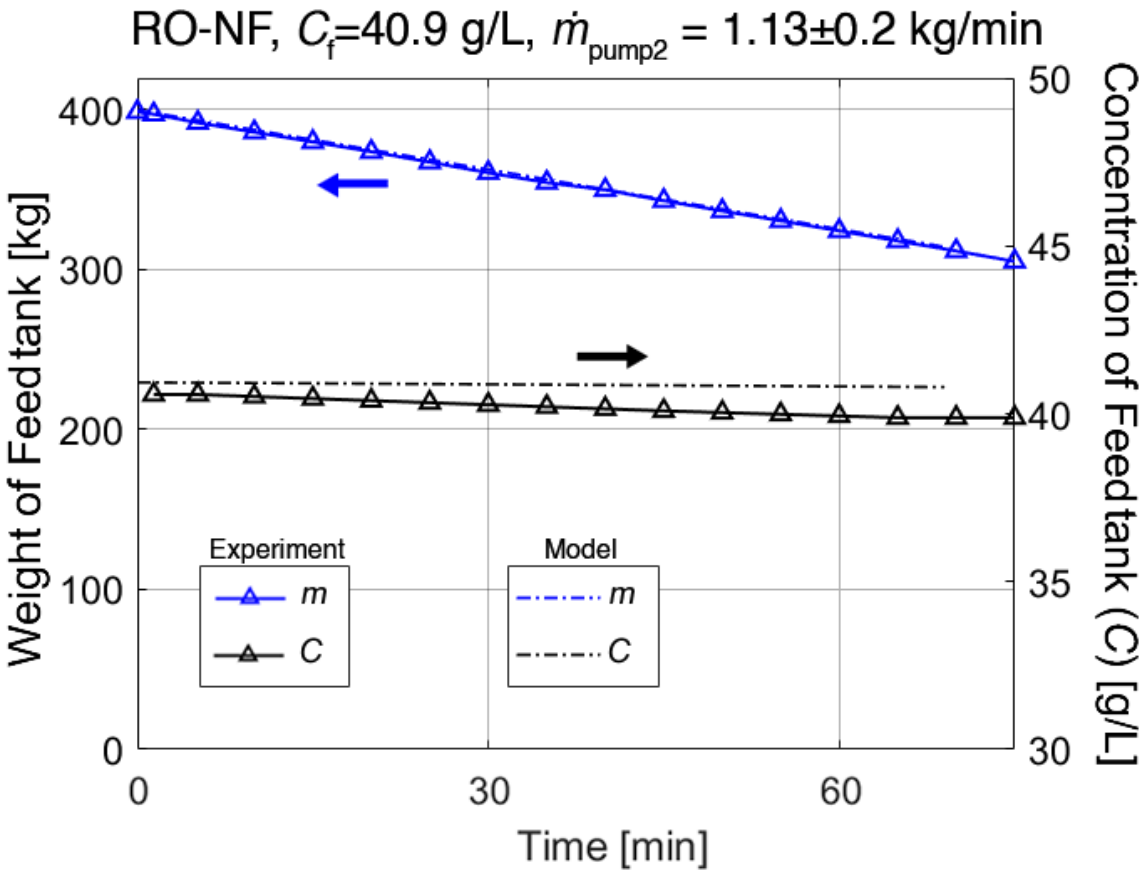

Figure A8-4. Weight of feed tank on the left vertical axis and concentration of feed tank (C) on the right vertical axis. Results in triangles are experimental for RO-NF with pump 2 flow of 1.13±0.2 kg/min and feed concentration (C_f) of 40.9 g/L. Model results are shown with dashed lines. Simulation time does not include experiments with brine recirculation.

Appendix 9: Constant parameters used for the dynamic model

This Appendix summarises the values of parameters used in the TRNSYS model that was developed in Chapter 6. For the PV collectors, the datasheet for the "monocrystalline 325 Wp type BLD350-72M" was used to set the parameters of the TRNSYS component (referred to as "type 103" in TRNSYS). The values are shown in Table A9-1.

Table A9-1. Parameters used in the TRNSYS model for the "PV collectors" component.

Name	Value	Unit
MPPT mode	1	
Module short-circuit current at reference conditions	9.56	A
Module open-circuit voltage at reference conditions	47.24	V
Reference cell temperature	298	K
Reference insolation	1000	W/m^2
Module voltage at max power point and reference conditions	39.11	V
Module current at max power point and reference conditions	8.95	amperes
Temperature coefficient of Isc (ref. cond)	0.07	A/K
Temperature coefficient of Voc (ref. cond.)	-0.36	V/K
Number of cells wired in series	72	
Module temperature at NOCT	293	K
Module area	1.94	m^2
Number of modules in series	32	
Number of modules in parallel	4	

For the HX, the parameters of the TRNSYS component (referred to as "type 657" in TRNSYS) are shown in Table A9-2.

Table A9-2. Parameters used in the TRNSYS model for the "HX" component.

Name	Value	Unit
Effectiveness of Heat Exchanger	0.8	
Specific Heat of Hot-Side Fluid	3.9205	kJ/(kg K)
Specific Heat of Cold-Side Fluid	4.12	kJ/(kg K)
Number of Possible Steps	1000	

For the LD storage, the parameters of the TRNSYS component (referred to as "type 158" in TRNSYS) are shown in Table A9-3.

Table A9-3. Parameters used in the TRNSYS model for the "LD storage" component.

Name	Value	Unit
Tank volume	1000	m^3
Tank height	1.5	m
Number of tank nodes	2	
Top loss coefficient	1	kJ/(hr m^2 K)
Edge loss coefficient	1	kJ/(hr m^2 K)
Bottom loss coefficient	1	kJ/(hr m^2 K)
Fluid specific heat	3.9178	kJ/(kg K)
Fluid density	1.009	kg/m^3
Fluid thermal conductivity	0.591	W/(m K)
Height fraction of inlet 1	1	Fraction
Height fraction of outlet 1	0	Fraction
Height fraction of inlet 2	0	Fraction
Height fraction of outlet 2	1	Fraction
Number of thermostats	1	
Height fraction of thermostat	0.75	Fraction
Number of auxiliary heat inputs	1	
Height fraction of auxiliary input	0.25	Fraction

The monthly wt_{LD} used to regulate the multi-stage regenerator are shown in Table A9-4.

Table A9-4. Monthly wt_{LD} values used for each location.

Location	JAN	FEB	MAR	APR	MAY	JUN	JUL	AUG	SEP	OCT	NOV	DEC
Colombo	17.2	17.2	17.2	17.2	19.2	19.5	17.2	17.2	17.2	19.2	19.8	19.2
Singapore	17.2	17.2	19.2	19.2	19.2	19.8	19.2	17.2	19.2	19.2	19.9	20.2
Chittagong	17.2	17.2	17.2	17.2	19.2	19.2	17.2	17.2	17.2	21.2	22	22
Bamako	17.2	17.2	17.2	17.2	17.2	19.2	18.2	17.2	19.2	19.2	21.1	20
Accra	17.2	17.2	17.2	17.2	20.2	21.5	20.2	20.2	20.2	20.2	20.2	20.2
Mumbai	17.2	17.2	17.5	17.5	19.2	21	17.5	17.2	17.2	20.2	21	20.2
Bangkok	17.2	17.2	17.2	17.2	19.2	19.5	17.2	17.2	20.2	20.2	19.2	17.9
Cairo	17.2	17.2	17.2	20.2	22	22	19.2	17.2	19.2	22	19.2	19.2
Hurghada	17.2	17.2	17.2	22	21	21	17.2	17.2	17.2	20	17.2	19.2
Mecca	17.2	17.2	17.2	17.2	17.2	18.2	17.2	17.2	17.2	17.2	18.2	18.7
Port Sudan	17.2	17.2	17.4	17.2	18.2	19.2	17.2	17.2	17.2	19.2	22	21.2
Djibouti	17.2	17.2	17.2	20.2	18.2	17.9	17.2	17.2	17.2	17.2	21.2	22
Kuwait	17.2	17.2	17.2	19.5	19.5	18.2	17.2	17.2	19.2	22	17.2	17.2
New Delhi	16.2	17.2	17.2	19.2	19.2	19.2	17.2	17.2	17.2	20.2	17.2	17.2
Lahore	17.2	17.2	20.2	20.2	20.2	19.7	17.2	17.2	18.2	20.7	17.2	17.2
Las Palmas	17.2	17.2	17.2	17.2	17.2	17.2	17.2	17.2	17.2	17.2	17.2	17.2
Casablanca	17.2	17.2	17.2	17.2	17.2	17.2	17.2	17.2	17.2	17.2	17.2	17.2

Regarding the water source temperature, hourly values were generated from monthly water temperatures. The parameters p_1, p_2, p_3, and p_4 for the locations are shown in Table A9-5.

Table A9-5. Parameters p_1, p_2, p_3, and p_4 used for the interpolation of the water source temperature.

Location	p_1	p_2	p_3	p_4
Colombo	3.49E-11	-4.58E-07	0.001539	27.41
Singapore City	8.63E-12	-2.11E-07	0.00143	26.8
Chittagong	-6.37E-13	-3.94E-07	0.003956	19.5
Bamako	-7.35E-11	7.77E-07	-0.001172	26.09
Accra	7.63E-11	-8.84E-07	0.002336	26.64
Mumbai	6.15E-12	-2.83E-07	0.002344	23.71
Bangkok	8.91E-12	-3.05E-07	0.00215	25.98
Cairo	-7.35E-11	7.77E-07	-0.001172	26.09
Hurghada	-7.54E-11	8.01E-07	-0.001247	23.24
Mecca	-7.35E-11	7.77E-07	-0.001172	26.09
Port Sudan	-7.35E-11	7.77E-07	-0.001172	26.09
Djibouti City	-7.35E-11	7.77E-07	-0.001172	26.09
Kuwait City	-7.35E-11	7.77E-07	-0.001172	26.09
New Delhi	-7.35E-11	7.77E-07	-0.001172	26.09
Lahore	-7.35E-11	7.77E-07	-0.001172	26.09
Las Palmas	-8.72E-11	8.97E-07	-0.001301	17.59
Casablanca	-8.72E-11	8.97E-07	-0.001301	17.59